STATE OF THE CLIMATE IN 2023

GLOBAL CLIMATE

R. J. H. Dunn, J. Blannin, N. Gobron, J. B. Miller, and K. M. Willett, Eds.

Special Online Supplement to the *Bulletin of the American Meteorological Society*, Vol. 105, No. 8, August 2024

https://doi.org/10.1175/BAMS-D-24-0116.1

Corresponding author: Robert Dunn / robert.dunn@metoffice.gov.uk

STATE OF THE CLIMATE IN 2023

Global Climate

Editors

Jessica Blunden
Tim Boyer

Chapter Editors

Anthony Arguez
Josh Blannin
Peter Bissolli
Kyle R. Clem
Howard J. Diamond
Matthew L. Druckenmiller
Robert J. H. Dunn
Catherine Ganter
Nadine Gobron
Gregory C. Johnson
Rick Lumpkin
Rodney Martinez
Ademe Mekonnen
John B. Miller
Twila A. Moon
Marilyn N. Raphael
Carl J. Schreck III
Laura Stevens
Richard L. Thoman
Kate M. Willett
Zhiwei Zhu

Technical Editor

Lukas Noguchi

BAMS Special Editor for Climate

Timothy DelSole

American Meteorological Society

Cover Credit:
Aerial photo of smoke from wildfires in Alberta, Canada, on 5 May 2023. (Photo credit: Alberta Forestry and Parks)

How to cite this document:
Global Climate is one chapter from the *State of the Climate in 2023* annual report and is available from https://doi.org/10.1175/BAMS-D-24-0116.1. Compiled by NOAA's National Centers for Environmental Information, *State of the Climate in 2023* is based on contributions from scientists from around the world. It provides a detailed update on global climate indicators, notable weather events, and other data collected by environmental monitoring stations and instruments located on land, water, ice, and in space. The full report is available from https://doi.org/10.1175/2024BAMSStateoftheClimate.1.

Citing the complete report:
Blunden, J. and T. Boyer, Eds., 2024: "State of the Climate in 2023". *Bull. Amer. Meteor. Soc.*, **105** (8), Si–S483 https://doi.org/10.1175/2024BAMSStateoftheClimate.1.

Citing this chapter:
Dunn, R. J. H., J. Blannin, N. Gobron, J. B Miller, and K. M. Willett, Eds., 2024: Global Climate [in "State of the Climate in 2023"]. *Bull. Amer. Meteor. Soc.*, **105** (8), S12–S155, https://doi.org/10.1175/BAMS-D-24-0116.1.

Citing a section (example):
Azorin-Molina, C., R. J. H. Dunn, L. Ricciardulli, C. A. Mears, J. P. Nicolas, T. R. McVicar, Z. Zeng, and M. G. Bosilovich, 2024: Land and ocean surface winds [in "State of the Climate in 2023"]. *Bull. Amer. Meteor. Soc.*, **105** (8), S76–S79, https://doi.org/10.1175/BAMS-D-24-0116.1.

Editor and Author Affiliations (alphabetical by name)

Ades, Melanie, European Centre for Medium-Range Weather Forecasts, Reading, United Kingdom

Adler, Robert, University of Maryland, College Park, Maryland

Alexe, Mihai, European Centre for Medium-Range Weather Forecasts, Bonn, Germany

Allan, Richard P., Department of Meteorology and National Centre for Earth Observation, University of Reading, Reading, United Kingdom

Anderson, John, Hampton University, Hampton, Virginia

Anneville, Orlane, National Research Institute for Agriculture, Food and Environment (INRAE), CARRTEL, Université Savoie Mont Blanc, Thonon les Bains, France

Aono, Yasuyuki, Graduate School of Agriculture, Osaka Metropolitan University, Sakai, Japan

Arguez, Anthony, NOAA/NESDIS National Centers for Environmental Information, Asheville, North Carolina

Armenteras Pascual, Dolores, Science Faculty, Universidad Nacional de Colombia, Bogotá, Colombia

Arosio, Carlo, University of Bremen, Bremen, Germany

Asher, Elizabeth, NOAA Global Monitoring Laboratory, Boulder, Colorado

Augustine, John A., NOAA Global Monitoring Laboratory, Boulder, Colorado

Azorin-Molina, Cesar, Centro de Investigaciones sobre Desertificación – Spanish National Research Council (CSIC-UV-GVA), Valencia, Spain

Baez-Villanueva, Oscar M., Hydro-Climate Extremes Lab (H-CEL), Ghent University, Ghent, Belgium

Barichivich, J., Laboratoire des Sciences du Climat et de l'Environnement (LSCE), LSCE/IPSL, CEA-CNRS-UVSQ, Gif-sur-Yvette, France; Instituto de Geografía, Pontificia Universidad Católica de Valparaíso, Valparaíso, Chile

Beck, Hylke E., Physical Science and Engineering Division, King Abdullah University of Science and Technology, Thuwal, Saudi Arabia

Bellouin, Nicolas, University of Reading, Reading, United Kingdom; Institute Pierre Simon Laplace (IPSL), Guyancourt, France

Benedetti, Angela, European Centre for Medium-Range Weather Forecasts, Reading, United Kingdom

Blannin, Josh, Met Office Hadley Centre, Exeter, United Kingdom

Blenkinsop, Stephen, School of Engineering, Newcastle University, Newcastle-upon-Tyne, United Kingdom

Bock, Olivier, Université Paris Cité, Institut de physique du globe de Paris, CNRS, IGN, F-75005 Paris, France; Univ Gustave Eiffel, ENSG, IGN, F-77455 Marne-la-Vallée, France

Bodin, Xavier, Laboratoire EDYTEM, CNRS/Université Savoie Mont-Blanc, Le Bourget-du-Lac, France

Bonte, Olivier, Hydro-Climate Extremes Lab (H-CEL), Ghent University, Ghent, Belgium

Bosilovich, Michael G., Global Modeling and Assimilation Office, NASA Goddard Space Flight Center, Greenbelt, Maryland

Boucher, Olivier, Institute Pierre Simon Laplace (IPSL), Guyancourt, France

Buehler, Stefan A., Universität Hamburg, Hamburg, Germany

Byrne, Michael P., Climate Dynamics Lab, University of St Andrews, St Andrews, United Kingdom

Campos, Diego, Earth Sciences Department, Barcelona Supercomputing Center, Barcelona, Spain

Cappucci, Fabrizio, European Commission Joint Research Centre, Ispra, Italy

Carrea, Laura, University of Reading, Reading, United Kingdom

Chang, Kai-Lan, Cooperative Institute for Research in Environmental Sciences, University of Colorado Boulder, Boulder, Colorado; NOAA Chemical Sciences Laboratory, Boulder, Colorado

Christiansen, Hanne H., Arctic Geophysics Department, University Centre in Svalbard, Longyearbyen, Norway; Geology Department, University Centre in Svalbard, Longyearben, Norway

Christy, John R., University of Alabama in Huntsville, Huntsville, Alabama

Chung, Eui-Seok, Korea Polar Research Institute, Incheon, South Korea

Ciasto, Laura M., NOAA/NWS National Centers for Environmental Prediction Climate Prediction Center, College Park, Maryland

Clingan, Scott, Cooperative Institute for Research in Earth Science, University of Colorado, Boulder, Colorado; NOAA Global Monitoring Laboratory, Boulder, Colorado

Coldewey-Egbers, Melanie, German Aerospace Center (DLR), Oberpfaffenhofen, Germany

Cooper, Owen R., NOAA Chemical Sciences Laboratory, Boulder, Colorado

Cornes, Richard C., National Oceanography Centre, Southampton, United Kingdom

Covey, Curt, Lawrence Livermore National Laboratory, Livermore, California

Crétaux, Jean-Francois, LEGOS (CNES/CNRS/IRD/UPS), Université de Toulouse, Toulouse, France

Crimmins, Theresa, USA National Phenology Network, School of Natural Resources and the Environment, University of Arizona, Tucson, Arizona.

Crotwell, Molly, Cooperative Institute for Research in Earth Science, University of Colorado, Boulder, Colorado; NOAA Global Monitoring Laboratory, Boulder, Colorado

Culpepper, Joshua, Department of Biology, York University, Toronto, Canada

Cusicanqui, Diego, Institut de Géosciences de l'Environnement (IGE), Université Grenoble Alpes, INRAE, CNRS, IRD, Grenoble INP, ISTerre, Grenoble, France

Davis, Sean, NOAA Chemical Sciences Laboratory, Boulder, Colorado

de Jeu, Richard A. M., Planet Labs, Haarlem, The Netherlands

Degenstein, Doug, University of Saskatchewan, Saskatoon, Canada

Delaloye, Reynald, Department of Geosciences, University of Fribourg, Fribourg, Switzerland

DiGangi, Elizabeth, AEM R&D, Germantown, Maryland

Dokulil, Martin T., Research Institute for Limnology, University of Innsbruck, Mondsee, Austria

Donat, Markus G., Barcelona Supercomputing Center, Barcelona, Spain; Catalan Institution for Research and Advanced Studies (ICREA), Barcelona, Spain

Dorigo, Wouter A., Department of Geodesy and Geoinformation, TU Wien, Vienna, Austria

Duchemin, Diane, CESBIO, Université de Toulouse, CNES/CNRS/INRAe/IRD/UPS, Toulouse, France

Dugan, Hilary, Department of Integrative Biology, University of Wisconsin-Madison, Madison, Wisconsin

Dunn, Robert J. H., Met Office Hadley Centre, Exeter, United Kingdom

Durre, Imke, NOAA/NESDIS National Center for Environmental Information, Asheville, North Carolina

Dutton, Geoff, Cooperative Institute for Research in the Earth Sciences, NOAA Global Monitoring Laboratory, Boulder, Colorado

Duveiller, Gregory, Max Planck Institute for Biogeochemistry, Jena, Germany

Estilow, Thomas W., Rutgers University, Piscataway, New Jersey

Estrella, Nicole, Ecoclimatology, Department of Life Science Systems, TUM School of Life Sciences, Technical University of Munich, Freising, Germany.

Fereday, David, Met Office Hadley Centre, Exeter, United Kingdom

Fioletov, Vitali E., Environment and Climate Change Canada, Toronto, Canada

Flemming, Johannes, European Centre for Medium-Range Weather Forecasts, Bonn, Germany

Foster, Michael J., Cooperative Institute for Meteorological Satellite Studies, Space Science and Engineering Center, University of Wisconsin-Madison, Madison, Wisconsin

Frederikse, Thomas, Planet Labs, Haarlem, The Netherlands

Frith, Stacey M., Science Systems and Applications, Inc., Lanham, Maryland; NASA Goddard Space Flight Center, Greenbelt, Maryland

Froidevaux, Lucien, Jet Propulsion Laboratory, California Institute of Technology, Pasadena, California

Füllekrug, Martin, University of Bath, Bath, United Kingdom

Garforth, Judith, Woodland Trust, Grantham, United Kingdom.

Editor and Author Affiliations (continued)

Garg, Jay, ADNET Systems, Inc., Hampton, Virginia

Gobron, Nadine, European Commission Joint Research Centre, Ispra, Italy

Godin-Beekmann, Sophie, Laboratoire Atmosphères, Observations Spatiales (LATMOS), UVSQ, Sorbonne Université, CNRS, IPSL, Guyancourt, France

Goodman, Steven, Thunderbolt Global Analytics, Huntsville, Alabama

Goto, Atsushi, World Meteorological Organization, Geneva, Switzerland

Grimm, Alice, Federal University of Parana, Curitiba, Brazil

Gruber, Alexander, Department of Geodesy and Geoinformation, TU Wien, Vienna, Austria

Gu, Guojun, University of Maryland, College Park, Maryland

Guglielmin, Mauro, Department of Theoretical and Applied Sciences, Insubria University, Varese, Italy

Hahn, Sebastian, Department of Geodesy and Geoinformation, TU Wien, Vienna, Austria

Haimberger, Leopold, University of Vienna, Vienna, Austria

Hall, Brad D., NOAA Global Monitoring Laboratory, Boulder, Colorado

Harlan, Merritt E., U.S. Geological Survey, Denver, Colorado

Harris, I., National Centre for Atmospheric Science (NCAS), University of East Anglia, Norwich, United Kingdom; Climatic Research Unit, School of Environmental Sciences, University of East Anglia, Norwich, United Kingdom

Hemming, Deborah L., Met Office Hadley Centre, Exeter, United Kingdom.; Birmingham Institute of Forest Research, Birmingham University, Birmingham, United Kingdom.

Hirschi, Martin, Institute for Atmospheric and Climate Science, ETH Zurich, Zürich, Switzerland

Ho, Shu-peng (Ben), NOAA/NESDIS Center for Satellite Applications and Research, College Park, Maryland

Holzworth, Robert, University of Washington, Seattle, Washington

Horton, Radley M., Columbia Climate School, Columbia University, New York, New York

Hrbáček, Filip, Department of Geography, Masaryk University, Brno, Czech Republic

Hu, Guojie, Cryosphere Research Station on Qinghai-Tibet Plateau, Northwestern Institute of Eco-Environment and Resources, CAS, Beijing, China

Hurst, Dale, NOAA Global Monitoring Laboratory, Boulder, Colorado

Inness, Antje, European Centre for Medium-Range Weather Forecasts, Reading, United Kingdom

Isaksen, Ketil, Norwegian Meteorological Institute, Oslo, Norway

John, Viju O., EUMETSAT, Darmstadt, Germany

Jones, P. D., Climatic Research Unit, School of Environmental Sciences, University of East Anglia, Norwich, United Kingdom

Junod, Robert, Earth System Science Center, University of Alabama in Huntsville, Huntsville, Alabama

Kääb, Andreas, Department of Geosciences, University of Oslo, Norway

Kaiser, Johannes W., Norwegian Institute for Air Research (NILU), Kjeller, Norway

Kaufmann, Viktor, Institute of Geodesy, Working Group Remote Sensing and Photogrammetry, Graz University of Technology, Graz, Austria

Kellerer-Pirklbauer, Andreas, Institute of Geography and Regional Science, Cascade – The Mountain Processes and Mountain Hazards Group, University of Graz, Graz, Austria

Khaykin, Sergey, Laboratoire Atmosphères, Observations Spatiales (LATMOS), UVSQ, Sorbonne Université, CNRS, IPSL, Guyancourt, France

Kidd, Richard, EODC GmbH, Vienna, Austria

King, Tyler V., U.S. Geological Survey, Boise, Idaho

Kipling, Zak, European Centre for Medium-Range Weather Forecasts, Reading, United Kingdom

Koppa, Akash, Hydro-Climate Extremes Lab (H-CEL), Ghent University, Ghent, Belgium

Kraemer, Benjamin M., University of Freiburg, Freiburg, Germany

La Fuente, R. Sofia, Vrije Universiteit Brussel, Brussels, Belgium

Laas, Alo, Institute of Agricultural and Environmental Sciences, Estonian University of Life Sciences, Tartumaa, Estonia

Lan, Xin, Cooperative Institute for Research in the Earth Sciences, NOAA Global Monitoring Laboratory, Boulder, Colorado; NOAA Global Monitoring Laboratory, Boulder, Colorado

Lantz, Kathleen O., NOAA Global Monitoring Laboratory, Boulder, Colorado

Lapierre, Jeff, AEM R&D, Germantown, Maryland

Lavers, David A., European Centre for Medium-Range Weather Forecasts, Reading, United Kingdom

Leblanc, Thierry, Jet Propulsion Laboratory, California Institute of Technology, Wrightwood, California

Leibensperger, Eric, Department of Physics and Astronomy, Ithaca College, Ithaca, New York

Lennard, Chris, Department of Environmental and Geographical Science, University of Cape Town, Cape Town, South Africa

Liley, Ben, National Institute of Water & Atmospheric Research (NIWA), Lauder, New Zealand

Liu, Yakun, Massachusetts Institute of Technology, Cambridge, Massachusetts

Lo, Y. T. Eunice, Cabot Institute for the Environment, University of Bristol, Bristol, United Kingdom

Loeb, Norman G., NASA Langley Research Center, Hampton Virginia

Loyola, Diego, German Aerospace Center (DLR), Oberpfaffenhofen, Germany

Magnin, Florence, Laboratoire EDYTEM, CNRS/Université Savoie Mont-Blanc, Le Bourget-du-Lac, France

Matsuzaki, Shin-Ichiro, National Institute for Environmental Studies, Tsukuba, Japan

Matthews, Tom, Department of Geography, King's College London, London, United Kingdom

Mayer, Michael, University of Vienna, Vienna, Austria; European Centre for Medium-Range Weather Forecasts, Reading, United Kingdom

McCarthy, Michael, University of Washington, Seattle, Washington

McVicar, Tim R., CSIRO Environment, Canberra, Australian Capital Territory; Australian Research Council Centre of Excellence for Climate Extremes, Sydney, Australia

Mears, Carl A., Remote Sensing Systems, Santa Rosa, California

Menzel, Annette, Ecoclimatology, Department of Life Science Systems, TUM School of Life Sciences, Technical University of Munich, Freising, Germany; Institute for Advanced Study, Technical University of Munich, Garching, Germany

Merchant, Christopher J., University of Reading, Reading, United Kingdom

Merio, Leo-Juhani, Finnish Environment Institute (SYKE), Oulu, Finland

Meyer, Michael F., U.S. Geological Survey, Madison, Wisconsin

Miller, John B., NOAA Global Monitoring Laboratory, Boulder, Colorado

Miralles, Diego G., Hydro-Climate Extremes Lab (H-CEL), Ghent University, Ghent, Belgium

Montzka, Stephan A., NOAA Global Monitoring Laboratory, Boulder, Colorado

Morice, Colin, Met Office Hadley Centre, Exeter, United Kingdom

Morino, Isamu, National Institute for Environmental Studies, Tsukuba, Japan

Mrekaj, Ivan, Technical University in Zvolen, Zvolen, Slovakia

Mühle, Jens, Scripps Institution of Oceanography, University of California San Diego, La Jolla, California

Nance, D., Cooperative Institute for Research in Earth Science, University of Colorado, Boulder, Colorado; NOAA Global Monitoring Laboratory, Boulder, Colorado

Nicolas, Julien P., European Centre for Medium-Range Weather Forecasts, Bonn, Germany

Noetzli, Jeannette, WSL Institute for Snow and Avalanche Research SLF Climate Change, Davos Dorf, Switzerland; Extremes and Natural Hazards in Alpine Regions Research Center CERC, Davos Dorf, Switzerland

Noll, Ben, National Institute of Water and Atmospheric Research (NIWA), Auckland, New Zealand

Editor and Author Affiliations (continued)

O'Keefe, John, The Harvard Forest, Harvard University, Petersham, Massachusetts

Osborn, Tim J., Climatic Research Unit, School of Environmental Sciences, University of East Anglia, Norwich, United Kingdom

Parrington, Mark, European Centre for Medium-Range Weather Forecasts, Bonn, Germany

Pellet, Cécile, Department of Geosciences, University of Fribourg, Fribourg, Switzerland

Pelto, Mauri S., Nichols College, Dudley, Massachusetts

Petersen, Kyle, Cooperative Institute for Research in Earth Science, University of Colorado, Boulder, Colorado; NOAA Global Monitoring Laboratory, Boulder, Colorado

Phillips, Coda, Cooperative Institute for Meteorological Satellite Studies, Space Science and Engineering Center, University of Wisconsin-Madison, Madison, Wisconsin

Pierson, Don, Department of Ecology and Genetics, Uppsala University, Uppsala, Sweden

Pinto, Izidine, Royal Netherlands Meteorological Institute (KNMI), De Bilt, The Netherlands

Po-Chedley, Stephen, Lawrence Livermore National Laboratory, Livermore, California

Pogliotti, Paolo, Environmental Protection Agency of Valle d'Aosta, Saint Christophe, Italy

Polvani, Lorenzo, Columbia University, New York, New York

Preimesberger, Wolfgang, Department of Geodesy and Geoinformation, TU Wien, Vienna, Austria

Price, Colin, Tel Aviv University, Tel Aviv, Israel

Randel, William J., National Center for Atmospheric Research, Boulder, Colorado

Raymond, Colin, University of California, Los Angeles, Los Angeles, California

Rémy, Samuel, HYGEOS, Lille, France

Ricciardulli, Lucrezia, Remote Sensing Systems, Santa Rosa, California

Richardson, Andrew D., School of Informatics, Computing, and Cyber Systems, Northern Arizona University, Flagstaff, Arizona; Center for Ecosystem Science and Society, Northern Arizona University, Flagstaff, Arizona

Robinson, David A., Rutgers University, Piscataway, New Jersey

Rodell, Matthew, Earth Sciences Division, NASA Goddard Space Flight Center, Greenbelt, Maryland

Rodriguez-Fernandez, Nemesio, CESBIO, Université de Toulouse, CNES/CNRS/INRAe/IRD/UPS, Toulouse, France

Rogers, Cassandra D. W., Bureau of Meteorology, Melbourne, Australia

Rohini, P., India Meteorological Department, Ministry of Earth Sciences, Pune, India

Rosenlof, Karen, NOAA Chemical Sciences Laboratory, Boulder, Colorado

Rozanov, Alexei, University of Bremen, Bremen, Germany

Rozkošný, Jozef, Slovak Hydrometeorological Institute, Bratislava, Slovakia

Rusanovskaya, Olga O., Irkutsk State University, Institute of Biology, Irkutsk, Russia

Rutishauser, This, Swiss Academy of Sciences (SCNAT), Bern, Switzerland

Sabeerali, C. T., India Meteorological Department, Ministry of Earth Sciences, Pune, India

Said, Ryan, Vaisala R&D, Louisville, Colorado

Sakai, Tetsu, Meteorological Research Institute, Japan Meteorological Agency, Tsukuba, Japan

Sánchez-Lugo, Ahira, NOAA/NESDIS National Centers for Environmental Information, Asheville, North Carolina

Sawaengphokhai, Parnchai, ADNET Systems, Inc., Hampton Virginia

Schenzinger, Verena, Medical University of Innsbruck, Innsbruck, Austria

Schlegel, Robert W., Laboratoire d'Océanographie de Villefranche, Sorbonne Université, Villefranche-sur-mer, France

Schmid, Martin, Eawag, Department Surface Waters - Research and Management, Kastanienbaum, Switzerland

Seneviratne, Sonia I., ETH Zurich, Department of Environmental Systems Science, Zürich, Switzerland

Sezaki, Fumi, Japan Meteorological Agency, Tokyo, Japan

Shao, Xi, NOAA/NESDIS Center for Satellite Applications and Research, College Park, Maryland

Sharma, Sapna, Department of Biology, York University, Toronto, Canada

Shi, Lei, NOAA/NESDIS National Centers for Environmental Information, Asheville, North Carolina

Shimaraeva, Svetlana V., Irkutsk State University, Institute of Biology, Irkutsk, Russia

Shinohara, Ryuichiro, Regional Environment Conservation Division, National Institute for Environmental Studies, Tsukuba, Japan

Silow, Eugene A., Irkutsk State University, Institute of Biology, Irkutsk, Russia

Simmons, Adrian J., European Centre for Medium-Range Weather Forecasts, Reading, United Kingdom

Smith, Sharon L., Geological Survey of Canada, Natural Resources Canada, Ottawa, Canada

Soden, Brian J., University of Miami, Miami, Florida

Sofieva, Viktoria, Finnish Meteorological Institute, Helsinki, Finland

Soldo, Logan, Cooperative Institute for Research in the Environmental Sciences, University of Colorado, Boulder, Boulder, Colorado

Sreejith, O. P., India Meteorological Department, Ministry of Earth Sciences, Pune, India

Stackhouse, Jr., Paul W., NASA Langley Research Center, Hampton, Virginia

Stauffer, Ryan, Atmospheric Chemistry and Dynamics Laboratory, NASA Goddard Space Flight Center, Greenbelt, Maryland

Steinbrecht, Wolfgang, Deutscher Wetterdienst, Hohenpeissenberg, Germany

Steiner, Andrea K., Wegener Center for Climate and Global Change, University of Graz, Graz, Austria

Stoy, Paul, C., Biological Systems Engineering, College of Agricultural and Life Sciences, University of Wisconsin-Madison, Madison, Wisconsin

Stradiotti, Pietro, Department of Geodesy and Geoinformation, TU Wien, Vienna, Austria

Streletskiy, Dmitry A., Department of Geography, George Washington University, Washington, DC

Taha, Ghassan, Morgan State University, Baltimore, Maryland; NASA Goddard Flight Center, Greenbelt, Maryland

Thackeray, Stephen J., United Kingdom Centre for Ecology & Hydrology, Lancaster, United Kingdom.

Thibert, Emmanuel, Institut de Géosciences de l'Environnement (IGE), Université Grenoble Alpes, INRAE, CNRS, IRD, Grenoble INP, ISTerre, Grenoble, France

Timofeyev, Maxim A., Institute of Biology, Irkutsk State University, Irkutsk, Russia

Tourpali, Kleareti, Aristotle University, Thessaloniki, Greece

Tronquo, Emma, Hydro-Climate Extremes Lab (H-CEL), Ghent University, Ghent, Belgium

Tye, Mari R., National Center for Atmospheric Research, Boulder, Colorado

van der A, Ronald, Royal Netherlands Meteorological Institute (KNMI), De Bilt, The Netherlands

van der Schalie, Robin, Planet Labs, Haarlem, The Netherlands

van der Schrier, Gerard, Royal Netherlands Meteorological Institute (KNMI), De Bilt, The Netherlands

van Vliet, Arnold J. H., Environmental Systems Analysis Group, Wageningen University & Research, The Netherlands

Verburg, Piet, National Institute of Water and Atmospheric Research (NIWA), Wellington, New Zealand

Vernier, Jean-Paul, NASA Langley Research Center, Hampton, Virginia

Vimont, Isaac J., NOAA Global Monitoring Laboratory, Boulder, Colorado

Virts, Katrina, University of Huntsville in Alabama, Huntsville, Alabama

Vivero, Sebastián, Department of Geosciences, University of Fribourg, Fribourg, Switzerland

Vömel, Holger, National Center for Atmospheric Research, Boulder, Colorado

Editor and Author Affiliations (continued)

Vose, Russell S., NOAA/NESDIS National Centers for Environmental Information, Asheville, North Carolina

Wang, Ray H. J., Georgia Institute of Technology, Atlanta, Georgia

Warnock, Taran, University of Saskatchewan, Saskatoon, Canada

Weber, Mark, University of Bremen, Bremen, Germany

Wiese, David N., Jet Propulsion Laboratory, California Institute of Technology, Pasadena, California

Wild, Jeannette D., Earth System Science Interdisciplinary Center, University of Maryland, College Park, Maryland; NOAA/NESDIS Center for Satellite Applications and Research, College Park, Maryland

Willett, Kate M., Met Office Hadley Centre, Exeter, United Kingdom

Williams, Earle, Massachusetts Institute of Technology, Cambridge, Massachusetts

Wong, Takmeng, NASA Langley Research Center, Hampton, Virginia

Woolway, Richard Iestyn, School of Ocean Sciences, Bangor University, Bangor, United Kingdom

Yin, Xungang, NOAA/NESDIS National Centers for Environmental Information, Asheville, North Carolina

Zeng, Zhenzhong, School of Environmental Science and Engineering, Southern University of Science and Technology, Shenzhen, China

Zhao, Lin, School of Geographical Sciences, Nanjing University of Information Science and Technology, Nanjing, China

Zhong, Feng, Hydro-Climate Extremes Lab (H-CEL), Ghent University, Ghent, Belgium

Ziemke, Jerry R., Goddard Earth Sciences Technology and Research, Morgan State University, Baltimore, Maryland; NASA Goddard Space Flight Center, Greenbelt, Maryland

Ziese, Markus, Global Precipitation Climatology Centre, Deutscher Wetterdienst, Offenbach, Germany

Zotta, Ruxandra M., TU Wien, Vienna, Austria

Zou, Cheng-Zhi, NOAA/NESDIS Center for Satellite Applications and Research, College Park, Maryland

Editorial and Production Team

Allen, Jessicca, Graphics Support, Cooperative Institute for Satellite Earth System Studies, North Carolina State University, Asheville, North Carolina

Camper, Amy V., Graphics Support, Innovative Consulting and Management Services, LLC, NOAA/NESDIS National Centers for Environmental Information, Asheville, North Carolina

Haley, Bridgette O., Graphics Support, NOAA/NESDIS National Centers for Environmental Information, Asheville, North Carolina

Hammer, Gregory, Content Team Lead, Communications and Outreach, NOAA/NESDIS National Centers for Environmental Information, Asheville, North Carolina

Love-Brotak, S. Elizabeth, Lead Graphics Production, NOAA/NESDIS National Centers for Environmental Information, Asheville, North Carolina

Ohlmann, Laura, Technical Editor, Innovative Consulting and Management Services, LLC, NOAA/NESDIS National Centers for Environmental Information, Asheville, North Carolina

Noguchi, Lukas, Technical Editor, Innovative Consulting and Management Services, LLC, NOAA/NESDIS National Centers for Environmental Information, Asheville, North Carolina

Riddle, Deborah B., Graphics Support, NOAA/NESDIS National Centers for Environmental Information, Asheville, North Carolina

Veasey, Sara W., Visual Communications Team Lead, Communications and Outreach, NOAA/NESDIS National Centers for Environmental Information, Asheville, North Carolina

2. Table of Contents

2. Table of Contents

2. GLOBAL CLIMATE

R. J. H. Dunn, J. Blannin, N. Gobron, J. B. Miller, and K. M. Willett, Eds.

a. Overview

—R. J. H. Dunn, J. Blannin, N. Gobron, J. B. Miller, and K. M. Willett

Globally, 2023 was the warmest year since records began in the mid-1800s to mid-1900s, according to all seven global temperature datasets. The prolonged La Niña that began in 2020 faded at the start of 2023 and was replaced by a strong El Niño by the end of the year. The change to El Niño conditions contributed to exceptionally high temperatures worldwide, especially in the latter part of the year as the El Niño strengthened. The pervasive warmth was highlighted by widespread and intense temperature extremes, with record numbers of warm days globally and the third-highest land fraction experiencing record numbers of warm days. Also, globally averaged lake surface temperatures in the warm season were the highest since records began in 1995. Over the oceans, night-time air temperatures likewise reached record values. Not only was the near-surface affected, but the lower troposphere average had record temperatures, with particularly exceptional values over the tropics in the latter part of the year. The stratosphere, which usually cools in response to anthropogenic carbon dioxide (CO_2) increases, also warmed this year, reflecting a recovery from the Hunga Tonga–Hunga Ha'apai (HTHH) eruption in 2022.

The unprecedented temperature anomalies over recent years and decades have had worldwide impacts on many essential climate variables covered in this chapter. A sidebar on these impacts in 2023 is included to link the sections and domains where the high global temperatures have driven important changes in Earth's climate system (Sidebar 2.1). The warm temperatures drove consistent changes in the hydrological cycle with greater quantities of water in the atmosphere but also record areas under extreme drought. Glaciers continued to lose mass for the 36th consecutive year, and land surface variables also showed substantial or record-breaking changes.

The fading La Niña in the early part of the year contributed to destructive flooding in New Zealand (e.g., post-Cyclone Gabrielle in February). Later on, the growing El Niño had regional impacts, with increased rainfall in South America leading to flooding in Chile in August, and, conversely, Australia experiencing its driest three-month period on record (August–October). Globally, upper-air winds were also reduced in the second half of the year in a manner typical of El Niño conditions. The impact of the El Niño can even be seen in the high number of thunder hours—a proxy for lightning activity, and which this year replaces the section on lightning flashes—across the eastern Pacific Ocean and southeastern South America.

Atmospheric composition changes both in 2023 and in general are characterized mainly by continued record-breaking atmospheric abundances of long-lived greenhouse gases (LLGHGs). These are the result of continued anthropogenic GHG emissions and year-to-year variability in short-lived species such as water vapor, aerosols, and carbon monoxide related to annual anomalies in emissions and circulation. Globally averaged atmospheric concentrations of CO_2, methane (CH_4), and nitrous oxide (N_2O) for 2023 each reached new annual record-high values of 419.3 ppm, 1922.6 ppb, and 336.7 ppb, respectively. The gases that destroy stratospheric ozone most effectively (i.e., chlorofluorocarbons [CFCs]) continue to decline, and their initial replacements (i.e., hydrochlorofluorocarbons [HCFCs]) may have peaked, although the current replacement compounds (i.e., hydrofluorocarbons [HFCs]) continue to increase, albeit with minimal impact on stratospheric ozone.

Large fires, especially those in eastern and western Canada, led to large anomalies in both carbon monoxide and tropospheric aerosols. In the stratosphere, the HTHH eruption that started in late 2021 still appeared to be impacting levels of water vapor, ozone, and aerosols in 2023. However, stratospheric ozone anomalies are mainly linked to circulation changes, including those related to the onset of El Niño in 2023; the long-term recovery of stratospheric ozone is consistent with model predictions given the decrease in CFCs and related compounds.

Earth's radiation budget at the top-of-atmosphere (approximately 20 km) continued to show a net imbalance. Anomalies for all components were greater than their interannual variability for the first time in the CERES (Clouds and the Earth's Radiant Energy System) record (starting March 2000). The Mauna Loa atmospheric transmission record resumed in July 2023, after being interrupted by the eruption of its volcano in late November 2022.

This year we welcome two new sections to the report: 1) Humid-heat extremes over land (previously introduced in Sidebar 2.1 in *State of the Climate* in 2022), a timely regular addition to the report closely linked to human heat health, and 2) Stratospheric aerosols (previously introduced in Sidebar 2.2 in *State of the Climate* in 2019), which shows the ongoing effects of the HTHH eruption in January 2022.

Another sidebar (Sidebar 2.2) this year discusses near-surface equivalent temperature as a metric to measure changes in the total energy content of the near-surface atmosphere, comprising sensible and latent heat components. A large fraction of the change in near-surface total energy content has been in the latent heat component, which is not captured when measuring surface air temperature. Using the equivalent temperature, this sidebar shows how near-surface atmospheric heating reached record levels in 2023.

As usual, Plate 2.1 shows maps of global annual anomalies for many of the variables and metrics presented herein. Many of these variables are also presented as time series in Plate 1.1. Many sections now use the 1991–2020 climatological reference period, in line with the World Meteorological Organization recommendations, although this newer reference period is not possible for all datasets, depending on their length of record or legacy processing methods.

Sidebar 2.1: **Impacts of extreme global temperatures and events in 2023**

—R. J. H. DUNN, N. GOBRON, AND K. M. WILLETT

The year 2023 saw record-breaking global surface temperatures (section 2b1), especially during the latter half of the calendar year. Record frequencies of extreme temperature days (e.g., by numbers of warm days [TX90p]) were experienced. Near-record spatial extents (in percent of land gridboxes) experienced record warm-day frequencies, while marine heatwaves (in sea-surface temperature) covered the largest total area (in percent of ocean gridboxes) on record (section 2b4). Although significant in its own right, this record warmth resulted in widespread impacts across the essential climate variables (GCOS 2022) presented in this chapter. And, despite being numerically exceptional, this warmth is consistent with globally increasing temperatures over the last decades that are unequivocally the result of human activities (IPCC 2021).

High temperatures and the transition from La Niña to El Niño conditions during 2023 resulted in large quantities of water in the atmospheric column. Evaporation over land reached record levels for the globe, dominated by record values for the Northern Hemisphere (section 2d12). The water vapor content of the near-surface atmosphere was record or near-record high globally, exceeding 2022 levels by a large margin (section 2d1). The energy contribution from the related latent heat component contributed to a record-high global anomaly in equivalent temperature, a measure of the total energy content of the atmosphere (Sidebar 2.2). It was also a record-breaking year for humid-heat indices, as humid-heat intensity doubled the previous record anomaly in 1998, reaching +0.6°C (section 2d2). Three datasets of total column water vapor showed the wettest year on record globally, as well as over the oceans, for all five datasets (section 2d3), with over 1 kg of water vapor extra per square meter across Earth's surface. Despite this increased moisture aloft, 2023 had the lowest cloud area fraction since records began in 1980 (section 2d7) with skies clearer globally. Consequently, the clouds reflected away to space a record small amount of shortwave radiation, but also blocked a record small amount of longwave radiation from leaving Earth. The overall effect was the weakest cooling effect of clouds on record. The clearer skies may have contributed to a lower global mean precipitation total over land surfaces for the year, with 2023 being one of the driest years since 1979 (section

2d5), but global one-day maximum accumulations (Rx1day) were close to average, demonstrating increased intensity of the rain that did fall (section 2d6), as expected under warmer conditions (e.g., Fowler et al. 2021). Global soil moisture, which on average has increased since around 2012, returned to 2020 levels. This return was due to a combination of little change in the Northern Hemisphere and a strong drying in the Southern Hemisphere, likely the result of the shift from La Niña to El Niño conditions (section 2d10). And overall, 2023 saw terrestrial water storage measures reach their second-lowest point since 2002 (section 2d9), leading to 7.9% of global land area being under extreme drought (self-calibrating Palmer Drought Severity Index, scPDSI ≤–4) in July, the first time 7% has been surpassed for this most-severe drought category (section 2d11).

The land surface responded to the elevated temperatures, with a near-record negative anomaly for the visible albedo in the Northern Hemisphere (section 2h1) as the surface darkened. The surface was notably darker for a substantial fraction of Earth's surface (17%), linked to rapid snowmelt in Canada and Siberia. The darkening was also linked to increased plant growth (which causes the absorption of radiation) in other parts of the world, and there were also record positive anomalies for the fraction of absorbed photosynthetically active radiation in the Northern Hemisphere (section 2h2). Plants directly responded to the warmth; early in the year, the full bloom for the cherry trees in the Arashiyama district of Kyoto, Japan, occurred on the earliest date in the over-1200-year-long record, and there was an early start of season in North America. In the latter half of the year, leaf fall in boreal autumn was delayed in North America and Europe as above-average temperatures prevailed (section 2h4).

Glaciers in mountainous regions have continued to lose mass, with the 36th consecutive year of global mass balance loss and the 15th with losses of more than 500-mm water equivalent. This year also marked the highest ratio of negative to positive mass balance observations of any year in the record. In the European Alps, a second consecutive very-warm summer resulted in a 10% decrease in remaining ice volume for Swiss glaciers since 2021 (GLAMOS 2023; WMO 2024; section 2c3). The effects of the warmth penetrated into the ground, with permafrost temperatures at record levels at 10-m and even 20-m depth in the same region. In the Arctic, permafrost temperatures were record high at 9 of the 17 reporting sites, and active-layer thicknesses (the layers in the ground which freeze and thaw each year) also set records for all sites in Svalbard, in some places by up to 5 m (section 2c1).

The exceptional wildfire season in Canada (see Sidebar 7.1 for details), where large-scale fires burned continually from May to September, consumed three times more biomass than the previous record and pushed the global emissions of carbon from biomass burning to the highest annual total since 2015 (section 2h3). Plumes of smoke from these fires elevated aerosol optical depth at 550 nm and increased particulate matter at 2.5 µm in diameter (PM2.5) across North America during 2023, dominating the number of days with extreme (>99.9th percentile) aerosol optical depth globally (section 2g3). Low precipitation amounts and the subsequent drought in central and southern Canada were also contributing factors to the wildfires in those areas (sections 2d5, 2d10). The warm, dry spring resulted in the lowest May snow cover in the satellite record for Canada, and also globally (section 2b5). And finally, above-average thunder hours in the western United States and Canada in 2023 contributed to a greater number of fires ignited by lightning during the year (section 2e4).

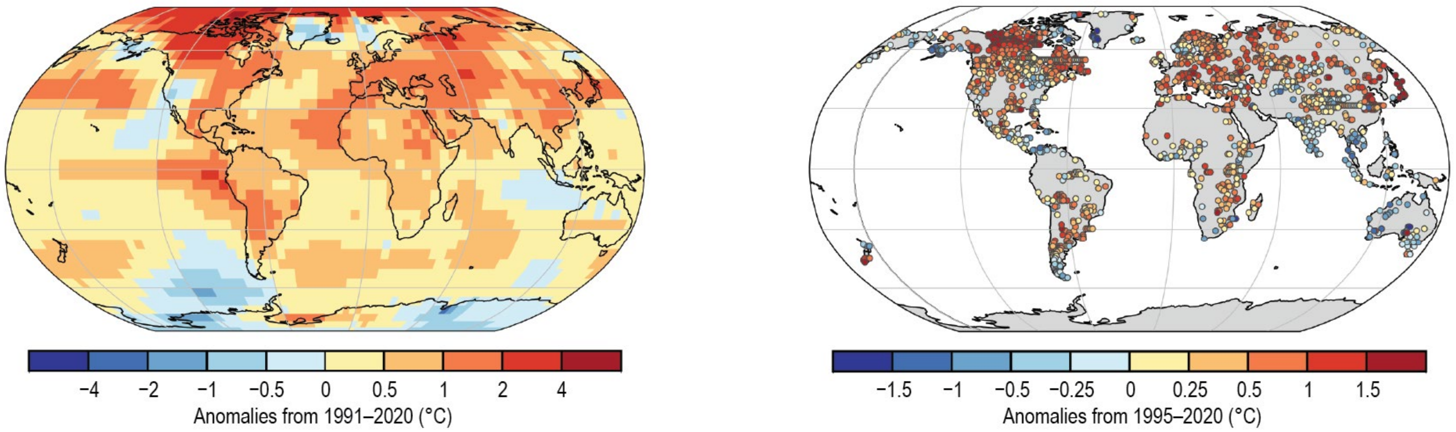
(a) Surface Temperature

(b) Lake Temperature

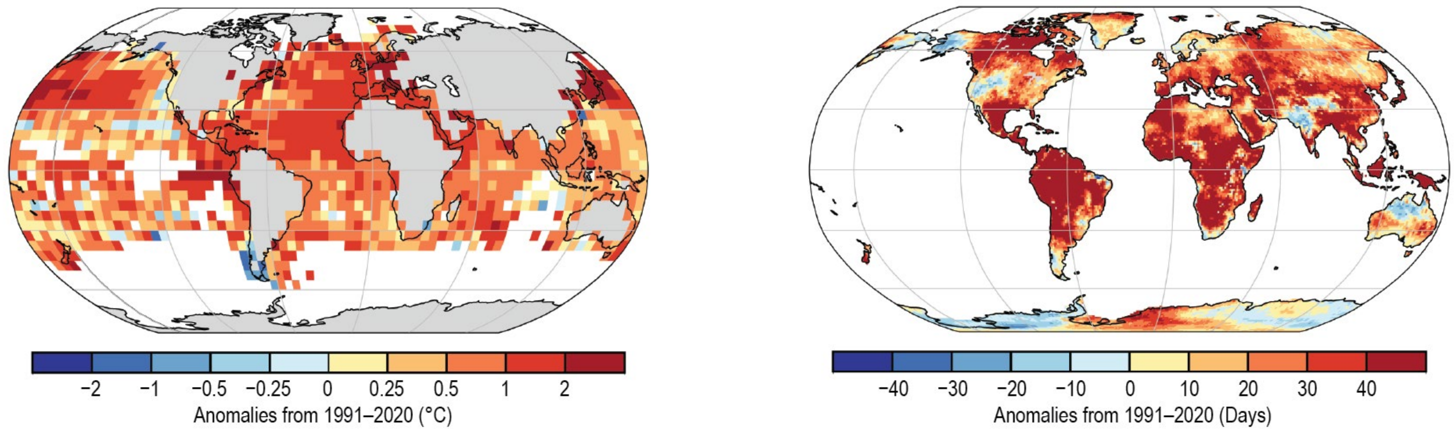
(c) Night Marine Air Temperature

(d) Warm Days (TX90p)

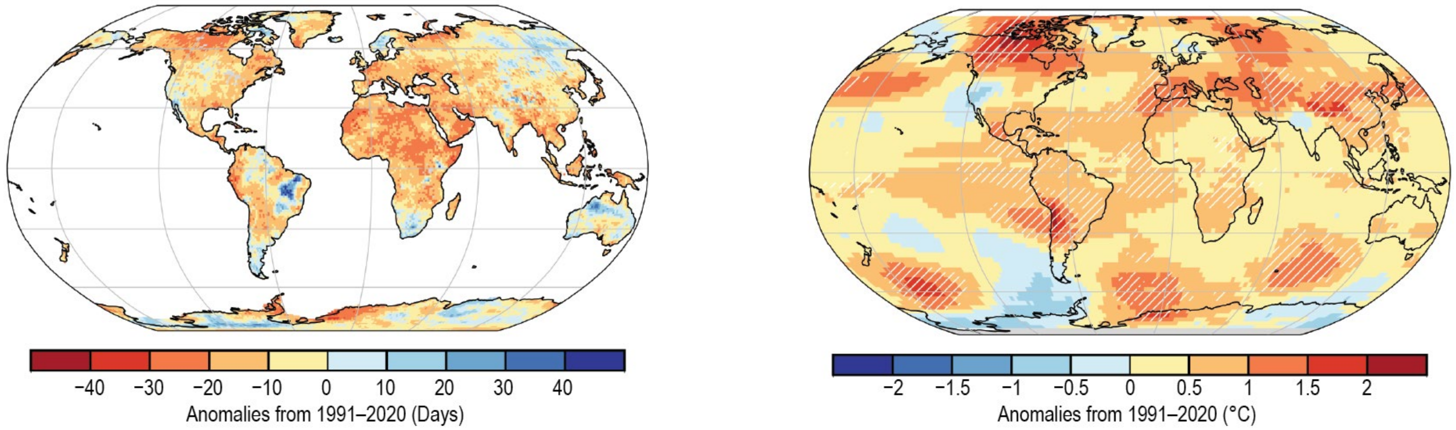
(e) Cool Nights (TX10p)

(f) Lower Tropospheric Temperature

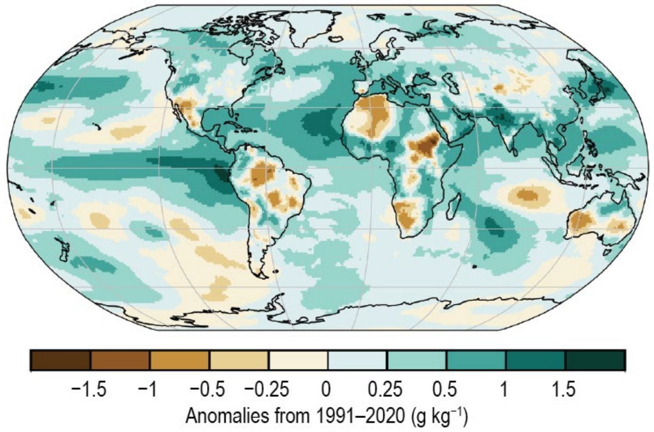
(g) Surface Specific Humidity

Plate 2.1. (a) NOAA NCEI Global land and ocean surface annual temperature anomalies (°C); (b) Satellite-derived lake surface water temperature anomalies, from European Space Agency (ESA) Climate Change Initiative (CCI) LAKES/ Copernicus Climate Change Service (C3S) /Earth Observation Climate Information Service (EOCIS) (°C); (c) CLASSnmat night marine air temperature annual average anomalies (°C); (d) ERA5 warm day threshold exceedance (TX90p); (e) ERA5 cool night threshold exceedance (TN10p); (f) Average of Remote Sensing Systems (RSS) and UAH lower tropospheric temperature anomalies (°C). Hatching denotes regions in which 2023 was the warmest year on record; (g) ERA5 surface specific humidity anomalies (g kg^{-1});

(h) Surface Relative Humidity

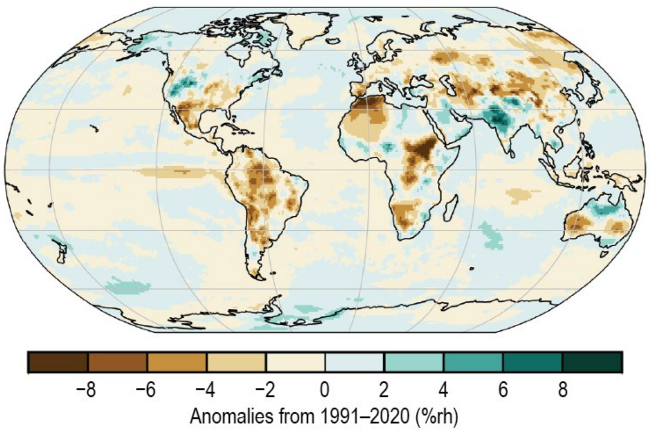

(i) Humid-heat days (TwX90p)

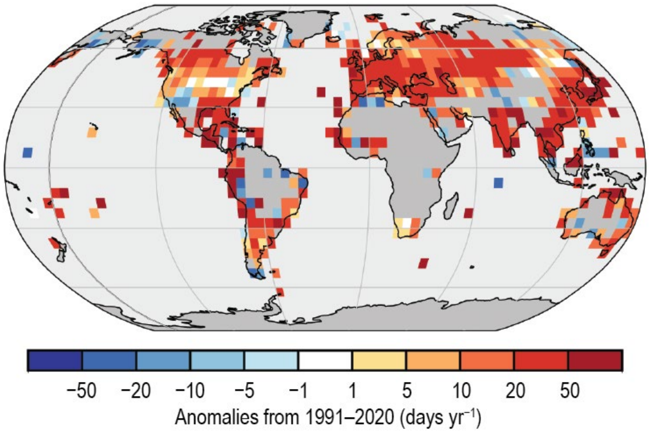

(j) Maximum T_{wet}

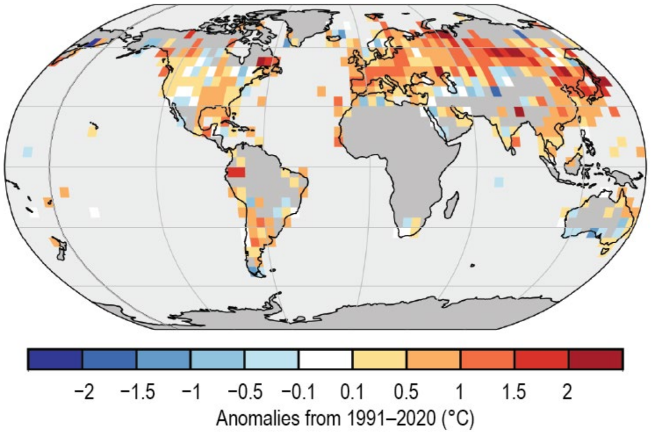

(k) Total Column Water Vapor

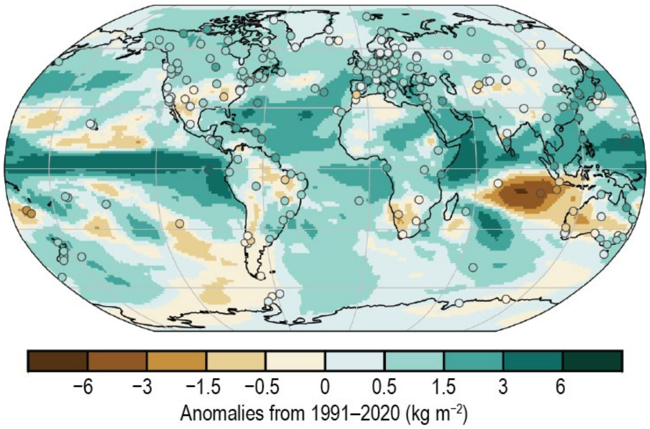

(l) Upper Tropospheric Humidity

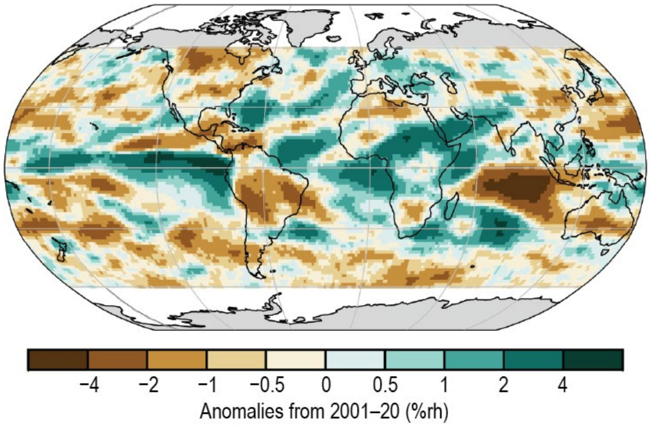

(m) Precipitation

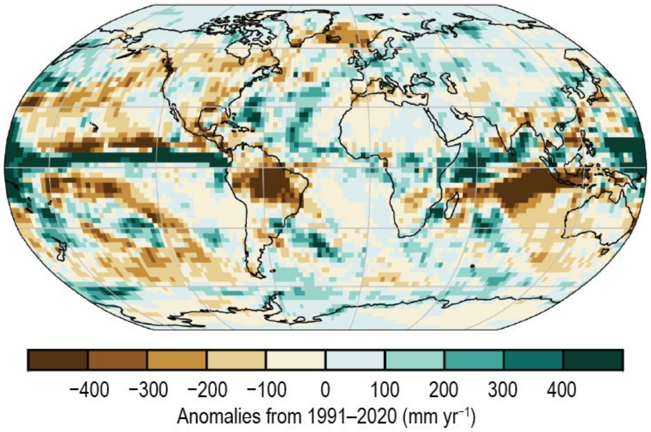

(n) Maximum 5 Day Precipitation Amount

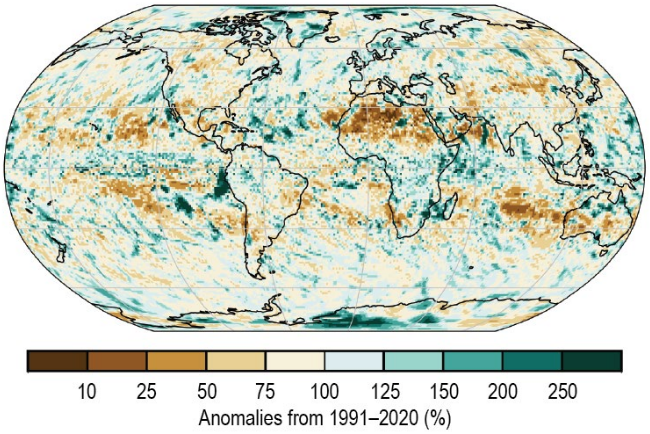

Plate 2.1 (cont.) (h) ERA5 surface relative humidity anomalies (%rh); (i) HadISDH.extremes humid heat frequency anomalies (T_wX90p), measured by the number of days where the daily maximum wet-bulb temperature exceeds the local daily 90th percentile (days yr^{-1}). White gridboxes (over land) represent regions with insufficient data.; (j) HadISDH. extremes humid heat intensity (T_wX), measured by the annual median anomaly of daily maximum wet-bulb temperature (°C). White gridboxes (over land) represent regions with insufficient data. (k) ERA5 TCWV anomalies (%). Data from GNSS stations are plotted as filled circles; (l) Annual microwave-based upper tropospheric humidity (UTH) anomalies (%rh); (m) GPCP v2.3 annual mean precipitation anomalies (mm yr^{-1}); (n) CHIRPS maximum 5-day (Rx5day) annual precipitation anomalies (mm);

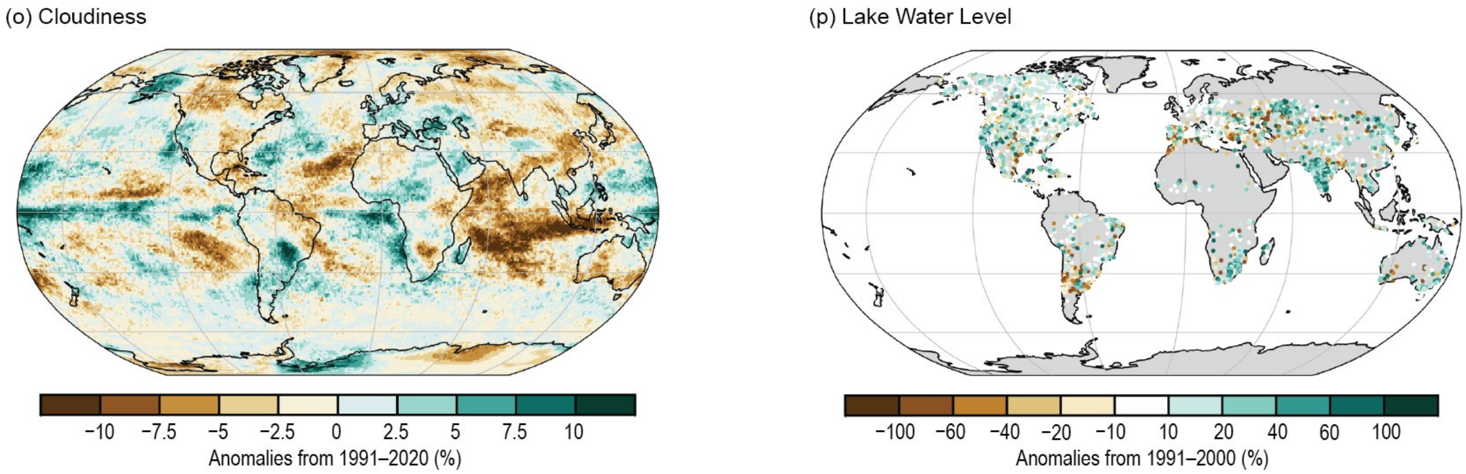
(o) Cloudiness

(p) Lake Water Level

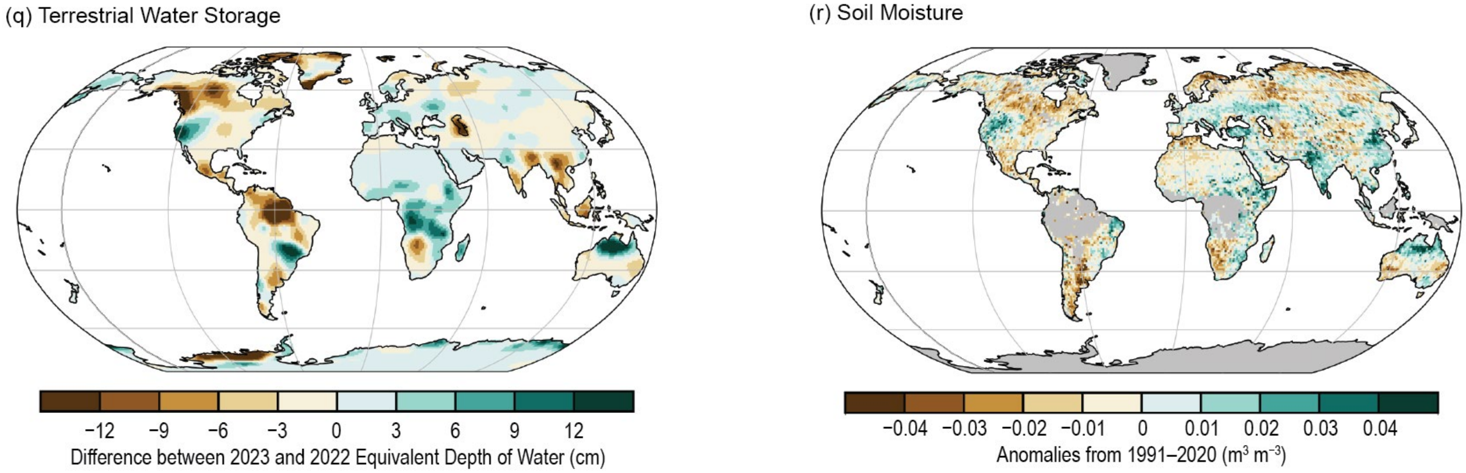
(q) Terrestrial Water Storage

(r) Soil Moisture

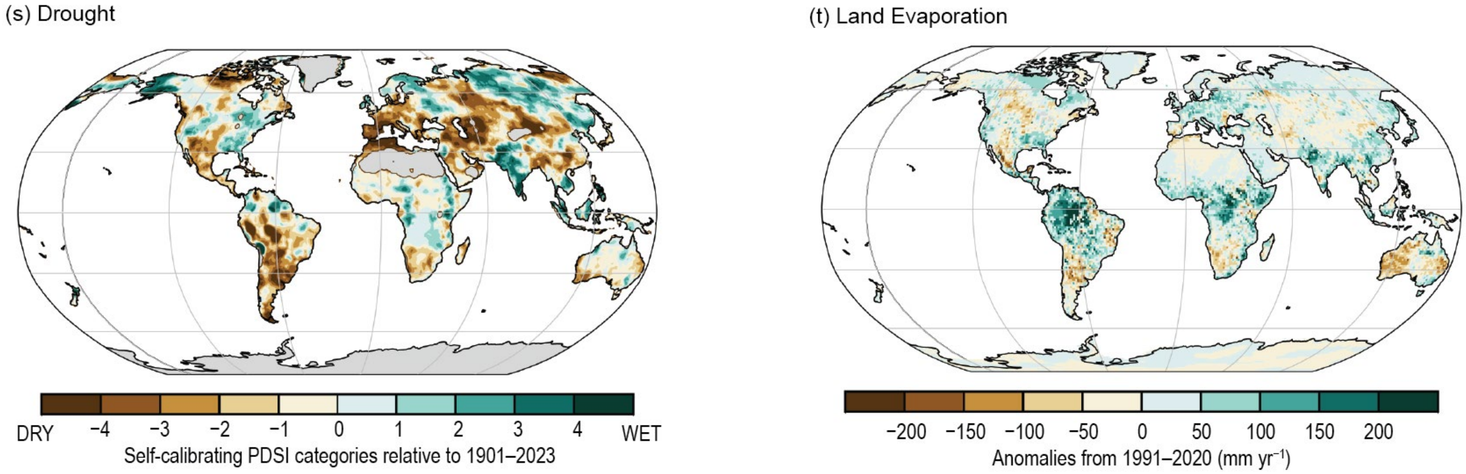
(s) Drought

(t) Land Evaporation

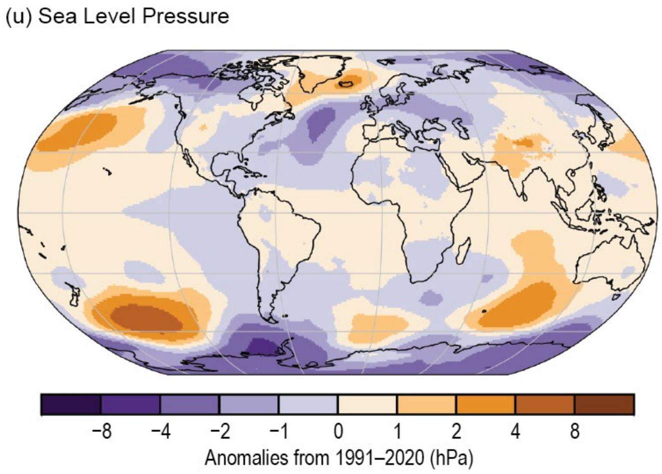
(u) Sea Level Pressure

Plate 2.1 (cont.) (o) PATMOS-x 6.0 cloud fraction annual anomalies (%); (p) GloLakes lake water storage anomalies (%); (q) GRACE-FO difference in annual-mean terrestrial water storage between 2022 and 2023 (cm); (r) Copernicus Climate Change Service (C3S) average surface soil moisture anomalies (m3 m^{-3}). Data are masked where no retrieval is possible or where the quality is not assured and flagged, for example due to dense vegetation, frozen soil, or radio frequency interference; (s) Mean self-calibrating Palmer Drought Severity Index (scPDSI) for 2021. Droughts are indicated by negative values (brown), wet episodes by positive values (green). No calculation is made where a drought index is meaningless (gray areas: ice sheets or deserts with approximately zero mean precipitation); (t) GLEAM land evaporation anomalies (mm yr^{-1}); (u) ERA5 mean sea level pressure anomalies (hPa);

(v) Surface Winds

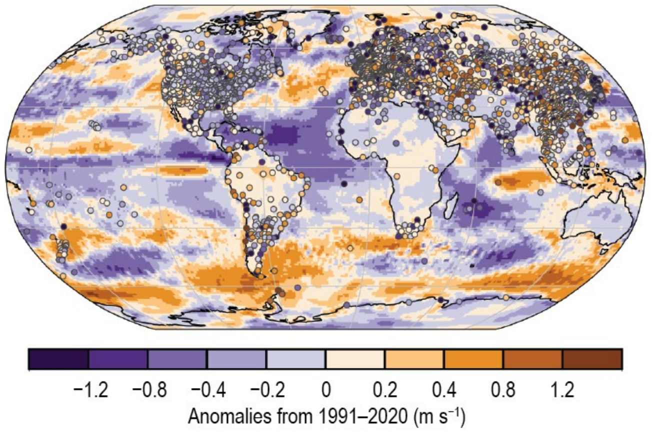

(w) Upper Air (850-hPa) Eastward Winds

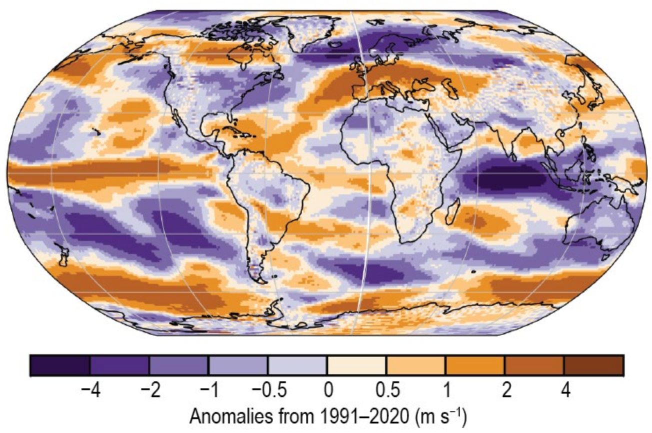

(x) Total Aerosol

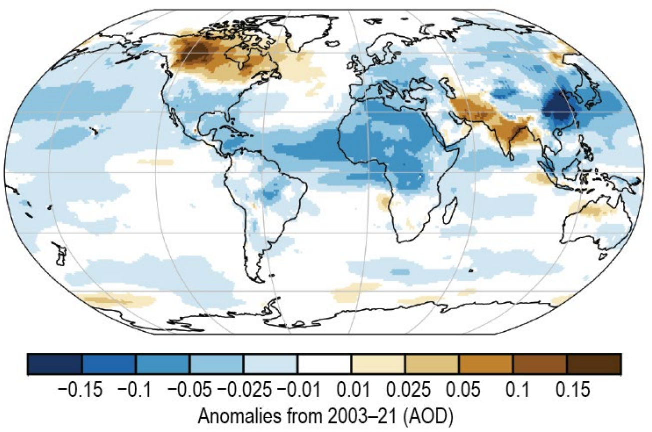

(y) PM25

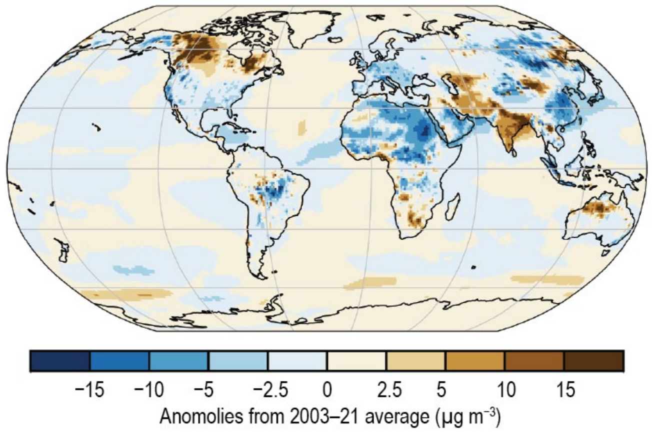

(z) Extreme Aerosol Days

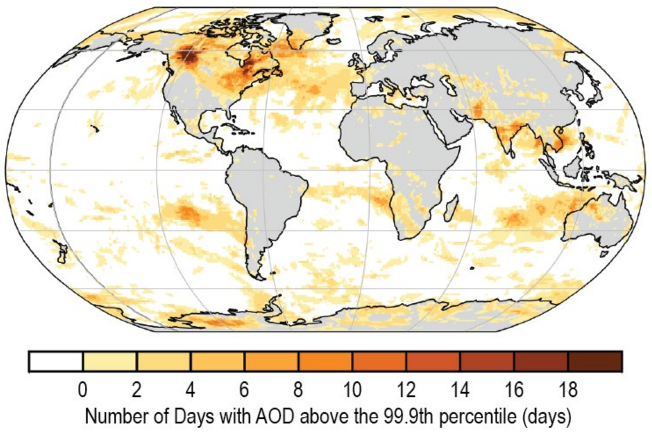

(aa) OMI/MLS Tropospheric Column Ozone

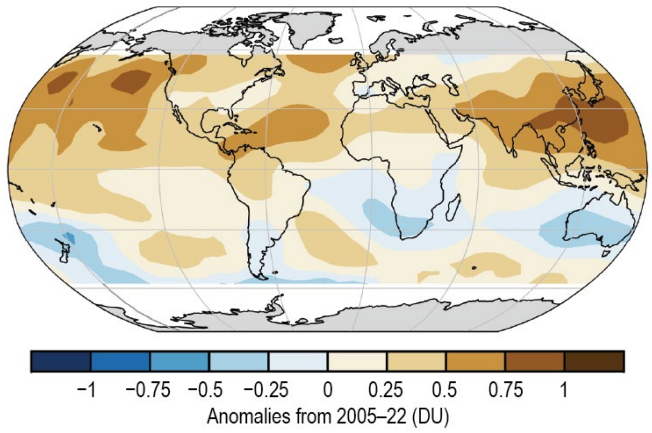

(ab) Stratospheric (Total Column) Ozone

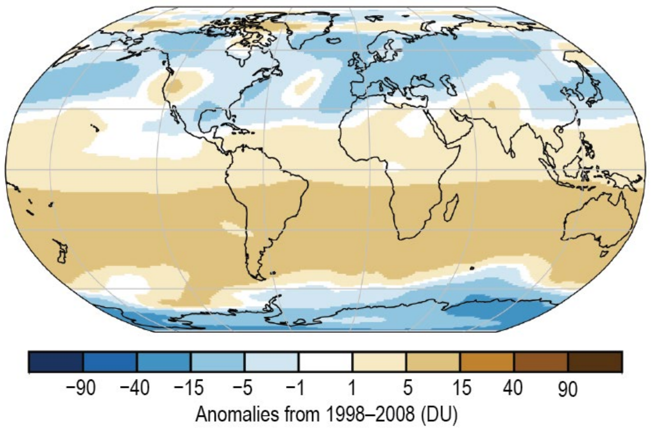

Plate 2.1 (cont.) (v) Surface wind speed anomalies (m s^{-1}) from the observational HadISD3 dataset (land, circles), the ERA5 reanalysis output (land, shaded areas), and Remote Sensing Satellite (RSS) satellite observations (ocean, shaded areas); (w) ERA5 850-hPa eastward wind speed anomalies for Sep–Dec (m s^{-1}); (x) CAMS reanalysis total aerosol optical depth (AOD) anomalies at 550 nm; (y) CAMS reanalysis PM2.5 anomalies (µg m^{-3}) ; (z) Number of days with AOD above the 99.9th percentile from CAMS reanalysis. Areas with zero days appear as the white/gray background; (aa) OMI/MLS tropospheric ozone column anomalies for 60°S–60°N (DU); (ab) total column ozone anomalies determined from TROPOMI aboard Sentinel-5 Precursor (S5P; DU);

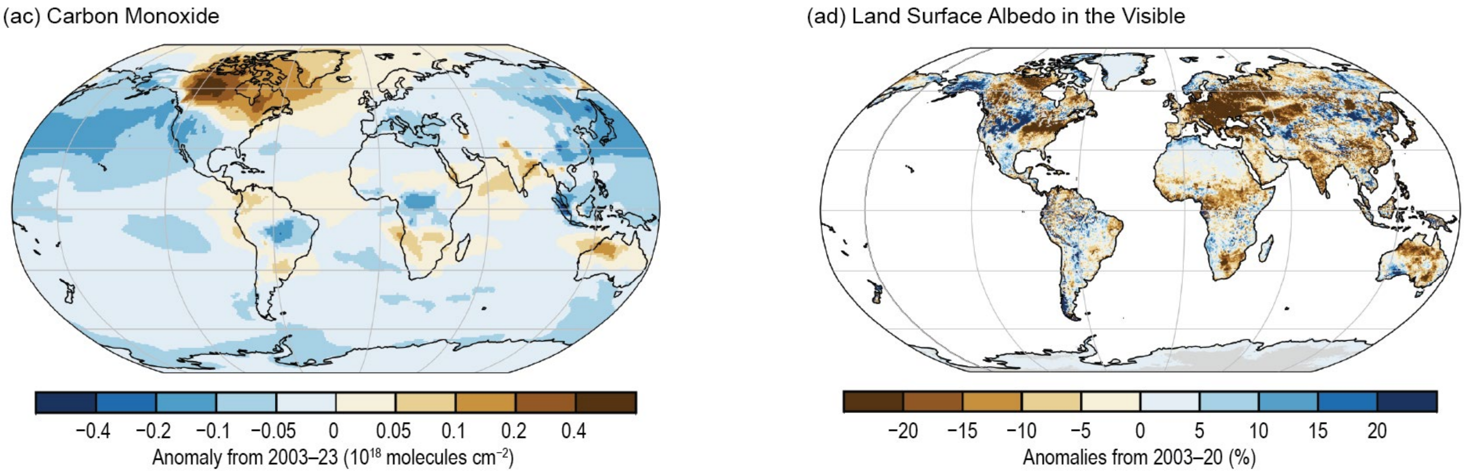

(ac) Carbon Monoxide

(ad) Land Surface Albedo in the Visible

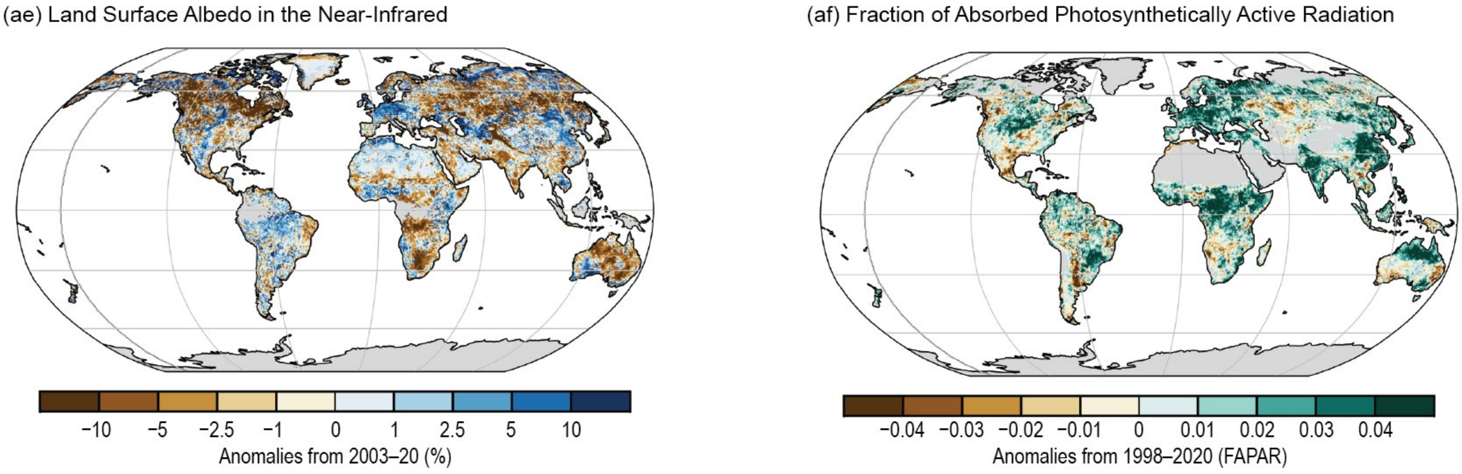

(ae) Land Surface Albedo in the Near-Infrared

(af) Fraction of Absorbed Photosynthetically Active Radiation

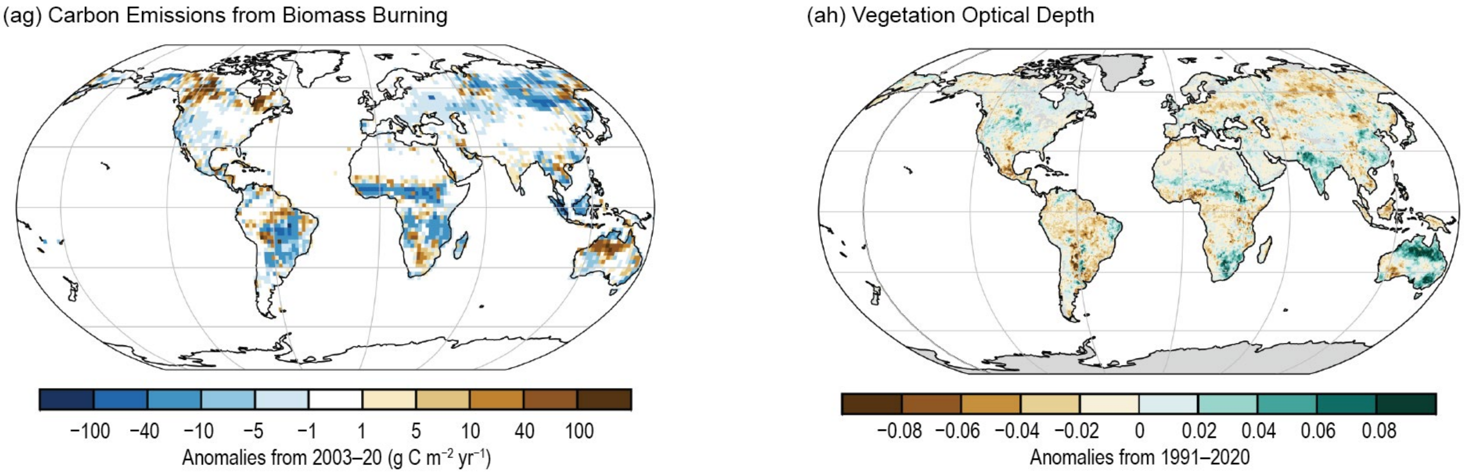

(ag) Carbon Emissions from Biomass Burning

(ah) Vegetation Optical Depth

Plate 2.1 (cont.) (ac) CAMS reanalysis total column carbon monoxide anomalies (× 10^{18} molecules cm^{-2}); (ad) VIIRS land surface visible broadband albedo anomalies (%); (ae) VIIRS land surface near-infrared albedo anomalies (%); (af) FAPAR anomalies; (ag) GFASv1.4 carbonaceous emission anomalies (g C m^{-2} yr^{-1}) from biomass burning; (ah) VODCA CXKu-band VOD anomalies.

b. Temperature

1. GLOBAL SURFACE TEMPERATURE

—A. Sanchez-Lugo, C. Morice, J. P. Nicolas, A. Arguez, F. Sezaki, and A. Goto

The global surface temperature for 2023 was 0.55°C–0.60°C above the 1991–2020 average, according to seven global temperature datasets (Table 2.1; Fig. 2.1). This was the highest value since global records began in the mid-1800s to mid-1900s (with the length of record depending on the dataset), surpassing the previous warmest year on record in 2016 (equal with 2020 in the GISTEMP dataset) by a large margin (+0.13°C to +0.17°C). The datasets consist of four global in situ surface temperature analyses (GISTEMP, Lenssen et al. 2019; HadCRUT5, Morice et al. 2021; NOAAGlobalTemp, Vose et al. 2021; Berkeley Earth, Rhode and Hausfather 2020) and three global atmospheric reanalyses (ERA5, Hersbach et al. 2020; Bell et al. 2021; JRA-55, Kobayashi et al. 2015; JRA-3Q, Kosaka et al. 2024).

Table 2.1. Global temperature anomalies (°C; 1991–2020 base period) for 2023. Note that for the HadCRUT5 column, land values were computed using the CRUTEM.5.0.2.0 dataset (Osborn et al. 2021), ocean values were computed using the HadSST.4.0.1.0 dataset (Kennedy et al. 2019), and global land and ocean values were computed using the HadCRUT.5.0.2.0 dataset (Morice et al. 2021).

Global	NASA-GISTEMPv4	HadCRUT5	NOAA GlobalTemp	Berkeley Earth	ERA5	JRA-55	JRA-3Q
Land	+0.78	+0.73	+0.83	+0.73	+0.85	+0.76	+0.79
Ocean	+0.43	+0.47	+0.43	–	+0.50	+0.48	+0.50
Land and Ocean	+0.56	+0.56	+0.55	+0.57	+0.60	+0.56	+0.58

All seven datasets agree that the last nine years (2015–23) were the nine warmest years since global records began, and the global trends at the short-term (1981–2023; 0.19°C–0.20°C decade^{-1}) and long-term (1880–2023; 0.08°C–0.09°C decade^{-1}) periods for each dataset are comparable to one another. On a trend-adjusted basis, following the Arguez et al. (2020) approach, 2023 was well above the trend in all seven datasets, exceeding the 90th percentile in each. In fact, 2023 registered the highest departure above the trend line (computed for the period 1975–2023) in all four in-situ analyses and the second-highest departure in each reanalysis product, eclipsed only by 1981 in ERA5 and 2016 in JRA-55 and JRA-3Q.

The global surface temperature for 2023 was also 1.35°C–1.54°C above the 1850–1900 average (a period commonly used to represent pre-industrial conditions). The pre-industrial temperature anomaly range was computed using the three datasets that extend back to 1850 (NOAAGlobalTemp, HadCRUT5, Berkeley Earth) using each dataset's own 1850–1900 baseline. The year 2023 marked the ninth consecutive year with a temperature more than 1°C above this average.

After three consecutive years (mid-2020 to early 2023) of La Niña across the tropical

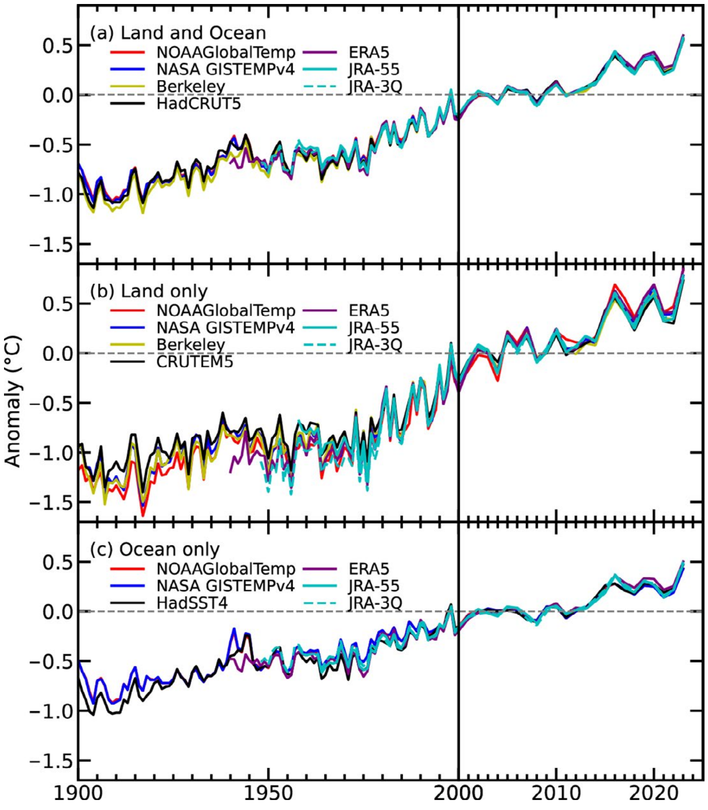

Fig. 2.1. Global average surface-air temperature anomalies (°C; 1991–2020 base period). In situ estimates are shown from NOAAGlobalTemp (Vose et al. 2021), NASA GISTEMPv4 (Lenssen et al. 2019), HadCRUT5 (Morice et al. 2021), CRUTEM5 (Osborn et al. 2021), HadSST4 (Kennedy et al. 2019), and Berkeley (Rhode and Hausfather 2020). Reanalysis estimates are shown from ERA5 (Hersbach et al. 2020; Bell et al. 2021), JRA-55 (Kobayashi et al. 2015), and JRA-3Q (Kosaka et al. 2024).

Pacific Ocean, 2023 quickly transitioned to ENSO-neutral and then to El Niño conditions by May. Monthly global ocean surface temperatures were unusually high (Plate 2.1a; Appendix Figs. A2.1–A2.5), with new global ocean temperature records set each month from June through December 2023. This sustained warmth resulted in a record-high annual global ocean surface temperature that was 0.43°C–0.50°C above the 1991–2020 average. The unusually warm oceans across many basins, along with the presence of El Niño and the long-term warming trend caused by anthropogenic greenhouse gas emissions, were key contributors to the high monthly global surface temperature records observed during the latter half of the year (see also section 3b and Sidebar 3.1 for details). The annual global land surface temperature was also record high, at 0.73°C–0.85°C above average.

Much-warmer-than-average conditions were observed across most of the world's surface, with the largest positive temperature anomalies occurring across parts of the higher northern latitudes (Plate 2.1a; Appendix Figs. A2.1–A2.5). Even with record warmth for the globe as a whole, below-average annual temperatures were observed across parts of Greenland, the southwestern contiguous United States, and parts of the Southern Ocean and Antarctica.

Sidebar 2.2: Near-surface equivalent temperature as a key climate change metric

—T. MATTHEWS, M. BYRNE, P. C. STOY, AND K. M. WILLETT

Only ~1% of the accumulating heat in Earth's system is being stored in the atmosphere (von Schuckmann et al. 2023) and heat has accumulated continuously over the past decades, warming the ocean, the land, the cryosphere, and the atmosphere. According to the Sixth Assessment Report by Working Group I of the Intergovernmental Panel on Climate Change, this planetary warming over multiple decades is human-driven and has resulted in unprecedented and committed changes to the Earth system, with adverse impacts for ecosystems and human systems. The Earth heat inventory provides a measure of the Earth energy imbalance (EEI), yet air temperature has been the de facto metric for communicating climate change. It has therefore been relatively straightforward to estimate global mean temperature change since the pre-industrial period (Hansen et al. 2010; Morice et al. 2021; Rohde and Hausfather 2020). Air temperature trends are also highly relevant to society, not least due to the universal temperature sensitivity observed in the biosphere (Gillooly et al. 2001) and because of the fundamental control of temperature on the hydrological cycle (Held and Soden 2006).

Air temperature alone, however, provides an incomplete perspective of atmospheric heat accumulation (Matthews et al. 2022; Pielke 2003). The total energy content (TEC) of the atmosphere is mostly comprised of sensible heat (~97%) with a minor contribution from latent heat (~3%; Peixoto and Oort 1992). In tracking sensible heat content, air temperature is therefore a good proxy for TEC; however, it is less appropriate for monitoring changes in TEC because almost half of the recent gain in global mean near-surface energy has been channeled into latent heat (Matthews et al. 2022; Stoy et al. 2022), exceeding 75% in some tropical regions. The potential for this increase to be "hidden" by air temperature trends is concerning, as latent heat plays a key role in determining maximum intensities for precipitation extremes (Ali et al. 2018; O'Gorman 2012; Song et al. 2022), near-surface air temperature, and human heat stress (Matthews 2018). Hotspots and hot moments of societally relevant heat accumulation are therefore at risk of being missed by using air temperature alone to track climate change. A metric proportional to TEC could also help constrain assessments of Earth's changing energy budget (von Schuckmann et al. 2023).

$$Teq = T + \frac{L_v}{c_p} q$$

In response to these concerns, the equivalent temperature (*Teq*) has been suggested as an important additional metric for use in climate communications (Matthews et al. 2022; Pielke 2003; Song et al. 2022): in which T is the (dry-bulb) air temperature, L_v is the latent heat of vaporization, c_p is the specific heat capacity of air at constant pressure, and q is the specific humidity. *Teq* therefore tracks the sensible heat content through *T* and the latent heat through $L_v/c_p\, q$. It represents the air temperature that could be reached if all latent heat was converted to sensible heat. A related quantity—the equivalent potential temperature—is conserved under reversible moist adiabatic processes and has been used to explore the land–ocean warming contrast and to help understand the maximum possible intensity of heatwaves (Byrne and O'Gorman 2013; Zhang and Boos 2023).

T, Teq, and the "latent temperature" (*Tq* = *Teq* – *T*) were computed using near-surface air temperature, dewpoint, and surface pressure from ERA5 (Hersbach et al. 2020) following Raymond et al. (2021) to evaluate L_v and c_p. For comparison, *Teq* from the HadISDH near-surface in situ humidity product (land only; Willett et al. 2014, 2013) was also assessed, processing it from hourly observations through to the quality-controlled and homogenized monthly mean gridded fields. Note that both ERA5 and HadISDH data were assessed for the overlapping 1973–2023 period. The 1991–2020 ERA5 climatology illustrates that *Teq* is more variable over Earth's surface than *T*. Both share a minimum slightly below 220 K in Antarctica, while *Teq* climbs to more than 30 K above *T* in the tropics due to the much greater contribution from *Tq* at low latitudes (Figs. SB.2.1a–c). *Teq* therefore exhibits a much steeper poleward reduction (Fig. SB.2.1d).

The ERA5 trends in *T* highlight the familiar warming enhancement over land (Byrne and O'Gorman 2018) and in the Arctic (Figs. SB.2.2a,b). However, *Tq* trends are different, being generally greatest in the northern tropics and subtropics and more similar between land and ocean (Figs. SB.2.2c,d). The weaker trends over subtropical land agree with Simpson et al. (2024) and highlight that latent heat content can fall even as *T* (and hence saturation vapor pressure) climbs due to reductions in relative humidity. The *Teq* trends reflect the combined response of *T* and *Tq* (Figs. SB.2.2e,f), with perhaps the most significant difference from *T* being that Arctic amplification appears more subdued relative to the (densely populated) northern low latitudes. HadISDH agrees with this pattern but suggests even larger low-latitude trend amplification

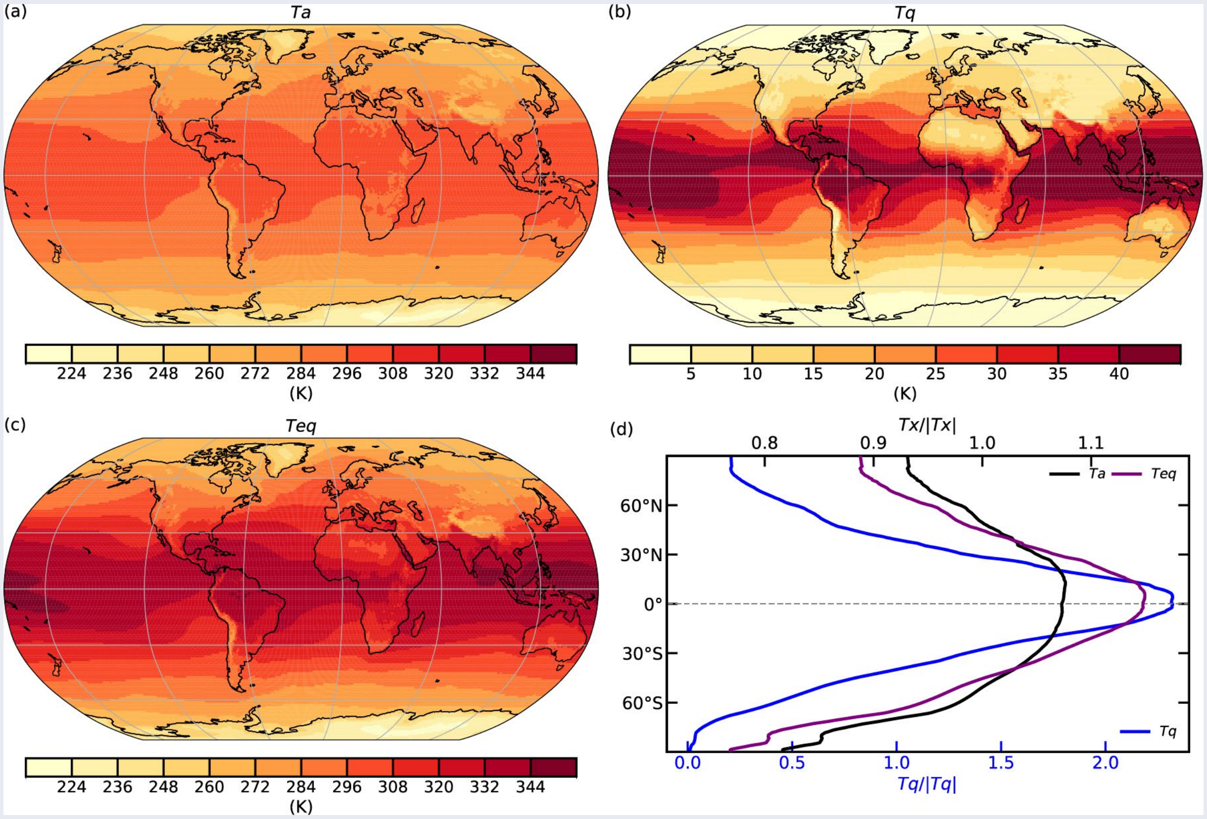

Fig. SB.2.1. The 1991–2020 ERA5 climatology for (a) air temperature (*Ta*), (b) latent temperature (*Tq* = *Teq* – *Ta*), and (c) equivalent temperature (*Teq*). (d) Zonal-mean profiles (*Tx*) normalized to the mean of each series plotted (|*Tx*|). Note that *Tq* is plotted on the bottom x-axis due to its greater variability.

(Fig. SB.2.2f), likely driven by undersampling in those tropical regions (e.g., East Africa) where ERA5 suggests lower *Teq* trends due to drying (Figs. SB.2.2c,e; see Willett et al. 2023).

The ERA5 trend (1973–2023) in global-mean near-surface *Teq* is 0.36±0.03 K decade^{-1} (Fig. SB.2.3). The comparison series from HadISDH indicates a larger trend of 0.55±0.03 K decade^{-1}, likely due to a combination of its land-only nature and incomplete spatial sampling. Disaggregating the *Teq* trend for ERA5 indicates that approximately 58% is explained by the *T* trend (0.21±0.01 K decade^{-1}) and 42% by *Tq* (0.15±0.02 K decade^{-1}). However, because climatological *Tq* is much lower than *T* (Fig. SB.2.1), the *Tq* trend represents a much more significant relative increase. This was well illustrated in 2023: the hottest year on record for *Teq* (in ERA5 and HadISDH:

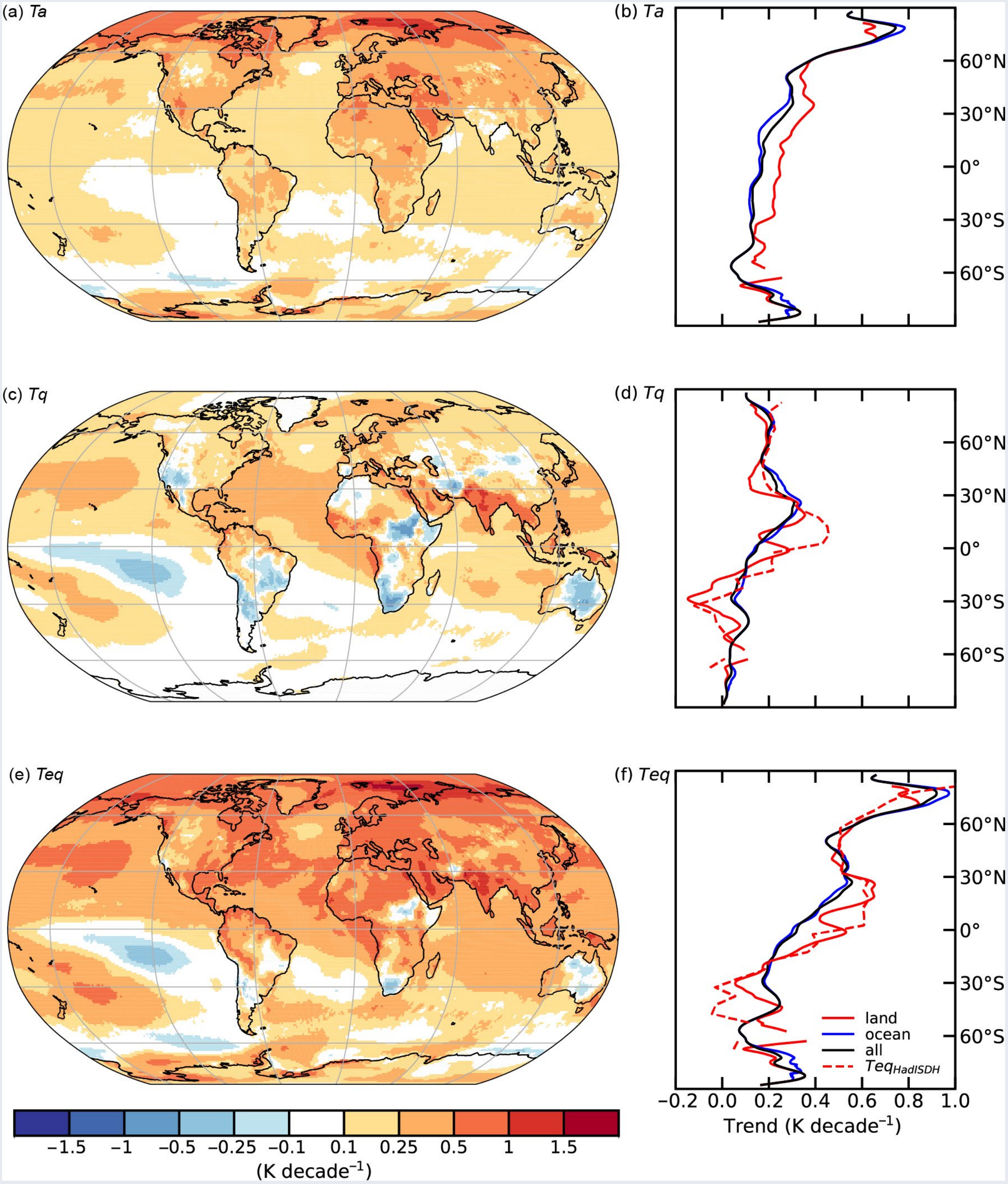

Fig. SB.2.2. The 1973–2023 ERA5 trends and their zonal means (K decade^{-1}; right-hand panels, smoothed with 5° running mean) in (a),(b) air temperature (*Ta*), (c),(d) latent temperature (*Tq* = *Teq* – *T*), and (e), (f) equivalent temperature (*Teq*). In panels (d),(f), (land only) zonal-mean trends for HadISDH are also shown as the dashed line.

Fig. SB.2.3) and for *Ta* and *Tq* individually (Table SB.2.1). The latter both recorded anomalies of 0.6 K relative to the 1991–2020 climatology (see sections 2b1, 2d), but the much lower baseline in *Tq* translates the 0.6 K anomaly to a relative increase of 2.5%—over an order of magnitude larger than for *T* (0.21%). This carries through to *Teq* to some extent, with the relative anomaly in 2023 of 1.2 K representing a rise of 0.38% (Table SB.2.1). As measured by *Teq*, the climate has therefore departed even further from the reference points of human history.

Although *Teq* is a complete physical descriptor of atmospheric heating, its unfamiliarity may present a challenge in climate communications, not least because its absolute values (Fig. SB.2.2) and its variability (Fig. SB.2.3) are much higher than for *T*. However, presenting relative changes as above may be a simple and intuitive solution for overcoming this communication barrier. Such efforts are worth pursuing, as *Teq* is a key indicator of changes to the atmospheric state that are of critical relevance to society.

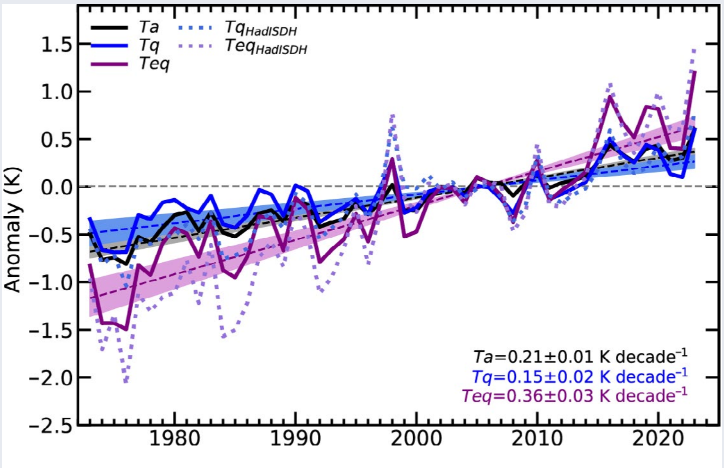

Fig. SB.2.3. 1973–2023 ERA5 and HadISDH trends in global mean air temperature (*Ta*; ERA5 only), latent temperature (*Tq* = *Teq* – *Ta*), and equivalent temperature (*Teq*). Trend lines were computed with simple linear regression, and shading spans 95% confidence intervals. The trends presented on the plot are for ERA5, with ±1 sigma standard error.

Table SB.2.1. Top-10 years for annual mean values in ERA5 (1973–2023). Note that relative anomalies are computed from the 1991–2020 baseline.

Rank	Ta year	Ta (K)	Ta (%)	Tq year	Tq (K)	Tq (%)	Teq year	Teq (K)	Teq (%)
1	2023	0.60	0.21	2023	0.60	2.51	2023	1.20	0.38
2	2016	0.44	0.15	2016	0.50	2.12	2016	0.94	0.30
3	2020	0.43	0.15	2019	0.44	1.85	2019	0.84	0.27
4	2019	0.40	0.14	2020	0.38	1.62	2020	0.82	0.26
5	2017	0.34	0.12	2017	0.34	1.41	2017	0.68	0.22
6	2022	0.30	0.10	1998	0.27	1.14	2015	0.52	0.17
7	2021	0.27	0.10	2015	0.27	1.13	2018	0.52	0.17
8	2018	0.26	0.09	2018	0.25	1.07	2021	0.41	0.13
9	2015	0.26	0.09	2010	0.15	0.63	2022	0.40	0.13
10	2010	0.13	0.05	2021	0.13	0.56	1998	0.29	0.09

2. LAKE SURFACE WATER TEMPERATURE

—L. Carrea, C. J. Merchant, R. I. Woolway, J.-F. Crétaux, T. M. Dokulil, H. Dugan, A. Laas, E. Leibensperger, S.-I. Matsuzaki, L. J. Merio, D. Pierson, O. O. Rusanovskaya, S. V. Shimaraeva, E. A. Silow, M. Schmid, M. A. Timofeyev, and P. Verburg

The globally averaged satellite-derived lake surface water temperature (LSWT) anomaly during the 2023 warm season was +0.46°C with respect to the 1995–2020 baseline, the highest since the record began in 1995 (Fig. 2.2a). The mean LSWT trend during 1995–2023 was 0.20±0.01°C decade^{-1}, broadly consistent with previous analyses even though the number of lakes analyzed has doubled since 2022 (Woolway et al. 2017, 2018; Carrea et al. 2019, 2020, 2021, 2022a; Fig. 2.2a). The 2023 warm-season anomalies for each lake are shown in Plate 2.1b; of the 1949 studied lakes that were not dry, 79% of these were warmer than average and 21% were colder. For 33 lakes, no anomalies could be computed since they were found to be dry.

Large coherent regions of high LSWT were identified in 2023, with 44% of all observed lakes experiencing LSWT anomalies in excess of +0.5°C (Plate 2.1b). The highest anomalies occurred in lakes situated in northern Canada, eastern China, Japan, and Europe. Negative LSWT anomalies were consistently observed in Patagonia, Greenland, Alaska, Australia, northern South America, and southeast Asia.

Four regions were studied in more detail: Europe (number of lakes, *n* = 268, Figs. 2.2b, 2.3a), Canada (*n* = 496, Figs. 2.2d, 2.3c), Tibet (*n* = 144, Figs. 2.2e, 2.3d), and Africa (*n* = 145, Figs. 2.2c, 2.3b). In these regions, the warm-season LSWT anomalies are consistent with the corresponding air temperature anomalies, as compiled by NASA's Goddard Institute for Space Studies (GISS; Lenssen et al. 2019; GISTEMP Team 2023), with an average warming trend of +0.31±0.03°C decade^{-1} in Europe (Fig. 2.2b) and +0.18±0.03°C decade^{-1} in Canada (Fig. 2.2d). In Canada, where the mean LSWT anomaly was +0.83°C in 2023, 92% of observed lakes had positive anomalies. In Europe, the

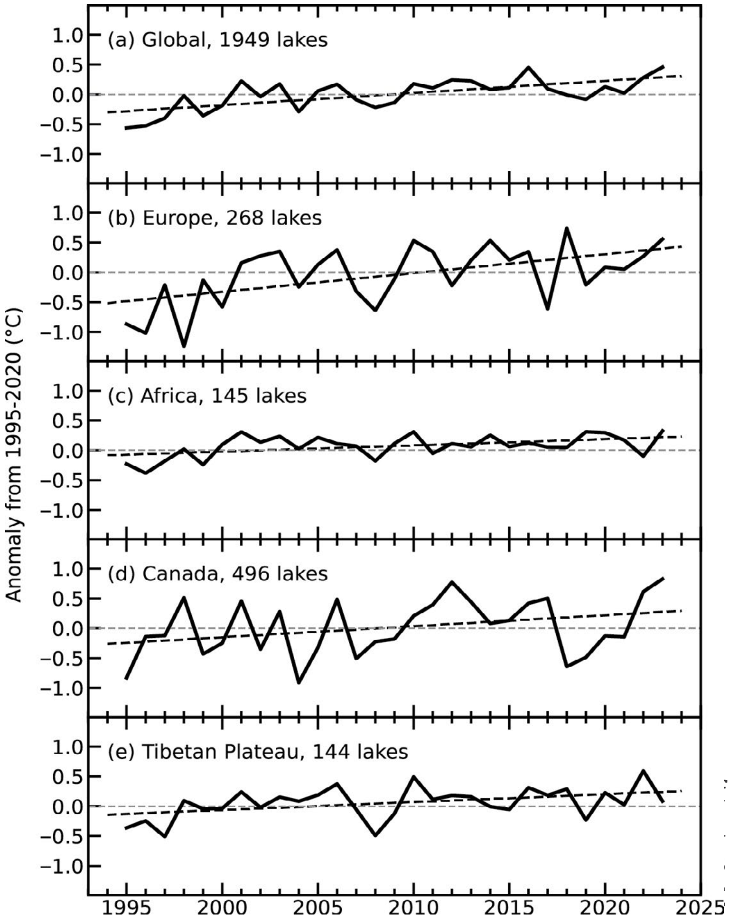

Fig. 2.2. Annual time series of satellite-derived warm-season lake surface water temperature anomalies (°C; 1995–2020 base period) from 1995 to 2023 for lakes distributed (a) globally, and regionally in (b) Europe, (c) Africa, (d) Canada, and (e) the Tibetan Plateau.

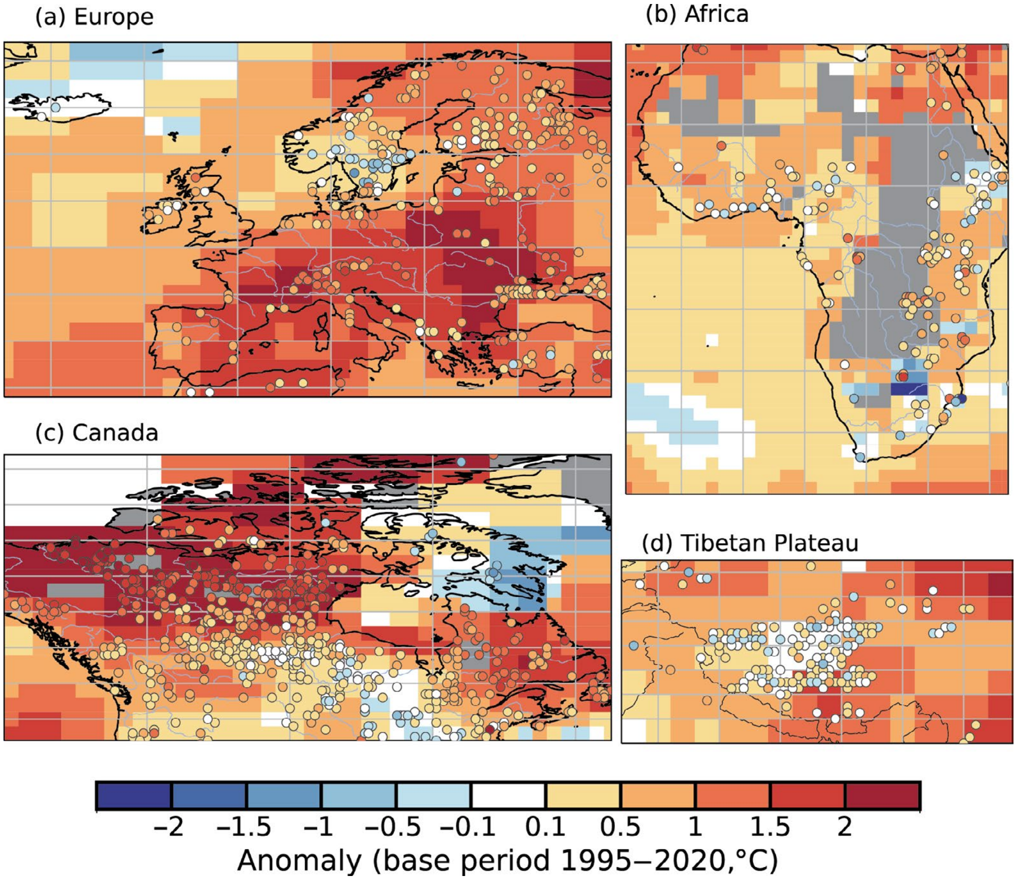

Fig. 2.3. Lake temperature anomalies (°C, colored dots) and 2-m air temperature anomalies (°C) in 2023 for lakes in (a) Europe, (b) Africa, (c) Canada, and (d) the Tibetan Plateau. These values were calculated for the warm season (Jul–Sep in the extratropical Northern Hemisphere; Jan–Mar in the extratropical Southern Hemisphere; Jan–Dec in the tropics) with reference to the 1995–2020 base period.

decade^{-1} and +0.10±0.02°C decade^{-1}, respectively (Figs. 2.2c,e). In Africa, 81% of the 145 lakes had positive LSWT anomalies, and the average anomaly in 2023 was +0.33°C. In Tibet, the average 2023 anomaly was +0.09°C, with 70% of the lakes experiencing positive anomalies.

In situ observations of (single-point) warm season temperature anomalies from 38 lakes are shown in Fig 2.4, 23 of which have measurements for the year 2023, with an average of +0.78°C. The anomalies calculated here differ from those derived from satellite data, which represent lake-wide averages. Five lakes experienced negative anomalies (average of −0.76°C) and 18 lakes had positive anomalies (average of +1.21°C) in 2023. The time series in Fig. 2.4 clearly show that lakes are warming.

The period 1995–2020 is used as a baseline for both in situ (unless no data were available) and satellite temperatures to compute anomalies. The warm-season averages for midlatitude lakes were computed for summers (July–September in the Northern Hemisphere and January–March in the Southern Hemisphere), and January–December averages are presented for tropical lakes (within 23.5° of the equator).

Lake surface water temperature time series were derived from the European Space Agency Climate Change Initiative (ESA CCI) LAKES/Copernicus Climate Change Service (C3S) /Earth Observation Climate Information Service (EOCIS) climate data record (Carrea et al. 2022b, 2023). The LSWT time series has been derived using ATSR2, AATSR, MODIS, AVHRR and SLSTR sensors. For 2023, satellite observations from SLSTR on Sentinel3A and 3B were used. The retrieval method of MacCallum and Merchant (2012) was applied on image pixels filled with water according to both the inland water dataset of Carrea et al. (2015) and a reflectance-based water detection scheme (Carrea et al. 2023).

The satellite-derived LSWT data are spatial averages for each of a total of 1949 lakes. The satellite-derived LSWT data were validated with in situ measurements with an average satellite-minus-in situ temperature difference of less than 0.5°C and standard deviation (robust) of less than 0.7°C (Carrea et al. 2023). Lake-wide average surface temperatures have been shown to give a more representative picture of LSWT responses to climate change compared to single-point measurements (Woolway and Merchant 2018).

The average surface air temperature was calculated from GHCN v4 (250-km smoothing radius) data of the NASA GISS surface temperature analysis (Lenssen et al. 2019; GISTEMP Team 2024).

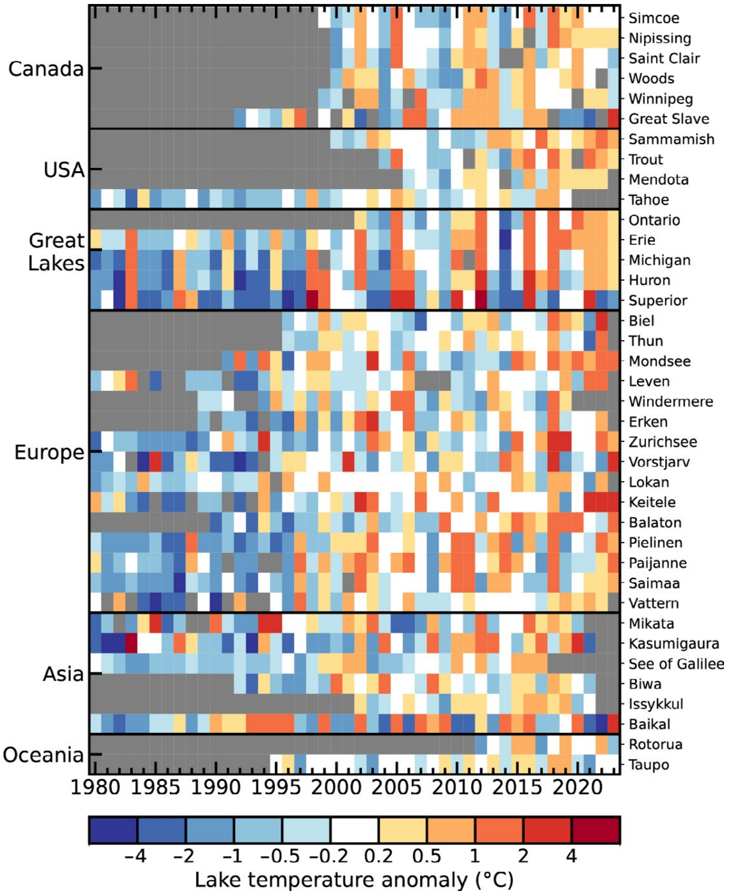

Fig. 2.4. In situ lake surface water temperature observations from 38 globally distributed lakes, showing the annually averaged warm season (Jul–Sep in the Northern Hemisphere; Jan–Mar in the Southern Hemisphere) anomalies (°C; 1995–2020 base period or the available base period).

3. NIGHT MARINE AIR TEMPERATURE

—R. C. Cornes and R. Junod

Two night marine air temperature (NMAT) datasets are routinely updated and used for analysis in this section: UAHNMAT (Junod and Christy 2020) and CLASSnmat (Cornes et al. 2020). These datasets are evaluated in combination with the HadSST4 dataset (Kennedy et al. 2019). Since these datasets are not spatially interpolated, they each have slightly different spatial coverage. In this evaluation the data have been masked to allow comparisons to be made over the common coverage areas, and to the common period of 1900–2023. NMAT and sea-surface temperature

(SST) data are expected to follow each other closely across large spatial scales and over longer time periods. As such, the NMAT data are used here to evaluate the more widely used SST data, which are considered in more detail in section 3b.

In all three datasets, 2023 was the warmest year in the series, with exceptional global annual average temperatures that were 0.50°C, 0.40°C, and 0.47°C above the 1991–2020 baseline in the CLASSnmat, UAHNMAT, and HadSST4 series, respectively (Fig. 2.5a). During the latter half of the year, consistent positive anomalies of >+0.5°C were recorded in the CLASSnmat and HadSST4 datasets (Fig. 2.6). The anomalies in the UAHNMAT were slightly lower, although global average anomalies were consistently above +0.4°C from June to December.

Large-scale averages of the NMAT/SST data are plotted in Figs. 2.5b–d. These results indicate that 2023 was the warmest year in each of the three regions. The largest anomalies were recorded in the northern extratropics (north of 30°N), with average annual anomalies of >+0.7°C in the CLASSnmat and HadSST4 datasets and +0.6°C in UAHNMAT. These results reflect the high frequency of marine heatwaves that occurred globally throughout 2023 (see sections 2b4, 3b, and Sidebar 3.1), although individual events are not evident in those results due to the consideration of annual averages. Examination of the grid-cell values (Plate 2.1c) indicates three areas of marked positive anomalies, which are also present in the UAHNMAT and HadSST data (not shown): the eastern tropical Pacific, the northern Pacific, and the North Atlantic. The pattern across the tropical Pacific reflects the strong El Niño that developed during the latter half of the year.

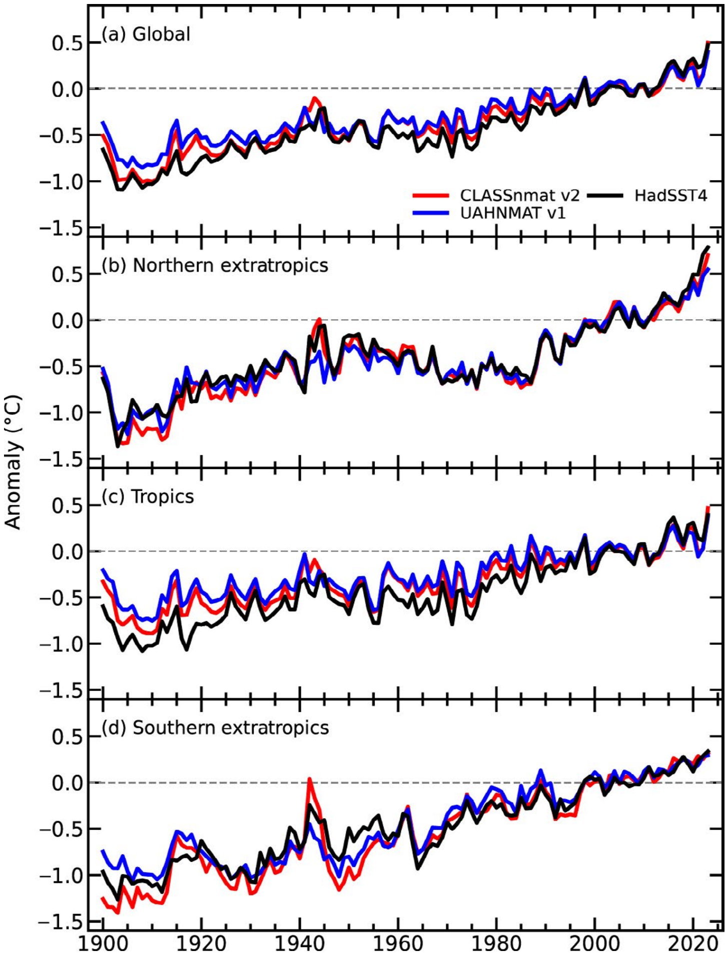

Fig. 2.5. Annual average marine temperature anomalies (°C; 1991–2020 base period) calculated from the CLASSnmat, UAHNMAT, and HadSST4 datasets averaged over the (a) globe, (b) northern extratropics, (c) tropics, and (d) southern extratropics. The tropics is defined as the latitude range 30°S–30°N and the northern (southern) extratropics as >30°N (<30°S). The averages only include values that are common to all three datasets for a given year; since UAHNMAT starts in 1900, only values for the period 1900–2023 are plotted.

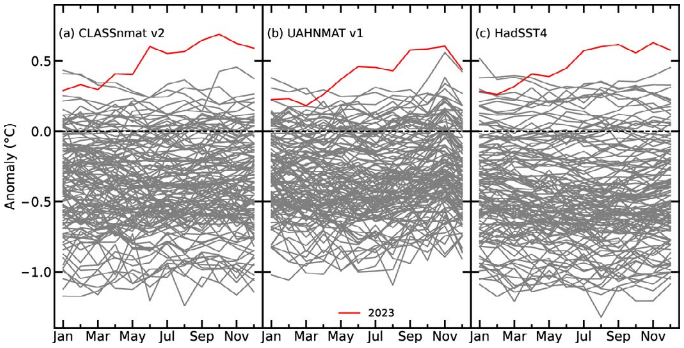

Fig. 2.6. Global monthly average marine temperature anomalies (°C; 1991–2020 base period) in the (a) CLASSnmat, (b) UAHNMAT, and (c) HadSST4 datasets. Each line represents a year of data, and the results for 2023 are shown in red.

Marine air temperature data recorded on board ships have been used for many years for climate monitoring purposes and to evaluate land air temperature and SST datasets (Rayner et al. 2003). However, two main biases exist in these observations: artificial diurnal heating due to the superstructure of the ships (Cropper et al. 2023) and variable temperature observing heights (Kent et al. 2013). To reduce the effect of diurnal heating biases, the daytime observations are removed from the data, resulting in night marine air temperature data. As such, the processing is designed to remove this artefact from the data rather than for quantifying night temperature per se (c.f. terrestrial nighttime temperature extremes in section 2b4). Inhomogeneities arising from changing observation height are removed by adjusting the temperature readings to a common reference height, which is typically 10 m above the sea surface. The UAHNMAT and CLASSnmat datasets examined in this section use different methods to implement the height correction, and they also differ in the quality-control of the data and the approach taken to addressing other biases in the data, notably for the warm bias that exists in the data during the World War II period (Cornes et al. 2020).

4. SURFACE TEMPERATURE EXTREMES

—R. J. H. Dunn, M. G. Donat, R. W. Schlegel, and M. G. Bosilovich

The record-breaking global surface temperatures of 2023 (section 2b1) also translated to record numbers of "warm days" (TX90p; Table 2.2) and, as in the last few years, well-below-average numbers of "cool nights" (TN10p; Table 2.2) over land.

The GHCNDEX dataset of gridded in situ observations (Donat et al. 2013) had a globally averaged number of warm days of 70±7. As this dataset has limited spatial coverage for 2023, several reanalysis products are used (ERA5, Hersbach et al. 2020; Bell et al. 2021; JRA-55, Kobayashi et al. 2015; MERRA-2, Gelaro et al. 2017) to give a globally complete assessment of the land surface extreme temperatures. As shown in Fig. 2.7c and Table 2.2, all reanalysis products reached record values in 2023 for the number of warm days, values which were substantially more than the previous record set in 2016. There is a wide spread in values from these globally complete products, from 70 to 81 warm days in the year (relative to the value over the 1981–2010 reference period of 36.5), with ERA5 showing greater warming than MERRA-2 and JRA-55.

Many areas of the world had their highest number of warm days on record in 2023 (Fig. 2.8a). Globally averaged, 2023 had the third-highest land fraction experiencing record numbers of warm days, following the strong El Niño years of 2010 and 1998 (Fig. 2.8b). Regionally, most of Canada had record numbers of warm days, with a large fraction of South America, and substantial areas of Africa, Europe, and Asia also showing record numbers of warm days (see Chapter 7 for details on regional temperatures). In contrast, Australia had almost no areas of record high values for TX90p (Plate 2.1d). A similar pattern is seen in the anomalies of cool nights (Plate 2.1e). Below-average numbers of warm days occurred in the western United States, Alaska, parts of the Indian subcontinent, and northern Australia.

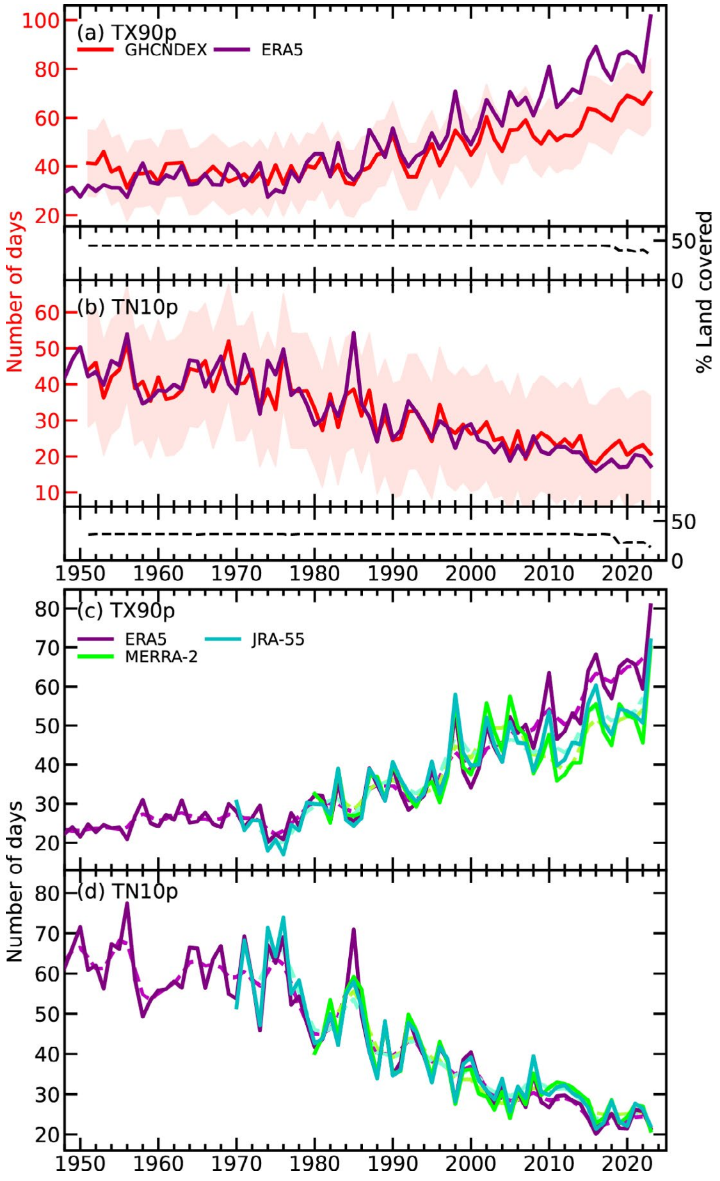

Fig. 2.7. (a),(b) Time series of the (a) annual number of warm days (TX90p) and (b) cool nights (TN10p) averaged over global land regions based on gridded station data from the GHCNDEX dataset (smoothed shown by dashed lines) and ERA5 using 1961–90 as the reference period. The spatial coverage in GHCNDEX is limited, the black dashed lines show the percentage of land area covered (right y-axis). The 2-σ coverage uncertainty (following Brohan et al. 2006; Dunn et al. 2020) is shown by the light red bands in (a),(b). (c),(d) As in (a),(b), for three atmospheric reanalyses (ERA5, MERRA-2, and JRA-55) using 1991–2020 as the reference period.

Table 2.2. Definitions of indices used for land surface temperature extremes, their globally averaged values (days) for 2023, and ranks from the four datasets. Coverage uncertainties are shown for GHCNDEX.

Index	Name	Definition	**GHCNDEX (1951–2023) Value, [rank]** Reference Period 1961–90	**ERA5 (1940–2023) Value, [rank]** Reference Period 1961–90	**ERA5 (1940–2023) Value, [rank]** Reference Period 1991–2020	**MERRA-2 (1980–2023) Value, [rank]** Reference Period 1991–2020	**JRA-55 (1970–2023) Value, [rank]** Reference Period 1991–2020
TX90p	Warm days	The annual count of days when the daily maximum temperature exceeds the 90th percentile	22 [third lowest]	102 [highest]	81 [highest]	70 [highest]	72 [highest]
TN10p	Cool nights	The annual count of nights when the daily minimum temperature falls below the 10th percentile	21±8 [seventh lowest]	17 [fourth lowest]	21 [third lowest]	21 [lowest]	--

Indices recommended by the former World Meteorological Organization Expert Team on Climate Change Detection and Indices (Zhang et al. 2011) characterize temperature extremes using observations of daily maximum and minimum temperatures. These indices are calculated from the daily maximum and minimum temperatures for stations in the GHCN-daily dataset (Menne et al. 2012) and interpolated on to a regular 2.5° grid to form GHCNDEX (Donat et al. 2013). As in previous years' assessments, spatial coverage falls off in recent years, so we use reanalysis products to provide globally complete fields for these indices. A recent comparison of reanalysis and observational products for these indices shows good agreement, especially for the indices presented here (Dunn et al. 2022). These indices use a fixed reference period (1961–90 for GHCNDEX and ERA5; 1991–2020 for ERA5, MERRA-2, and JRA-55), and intercomparison between these is not trivial (Dunn et al. 2020; Yosef et al. 2021; Dunn and Morice 2022).

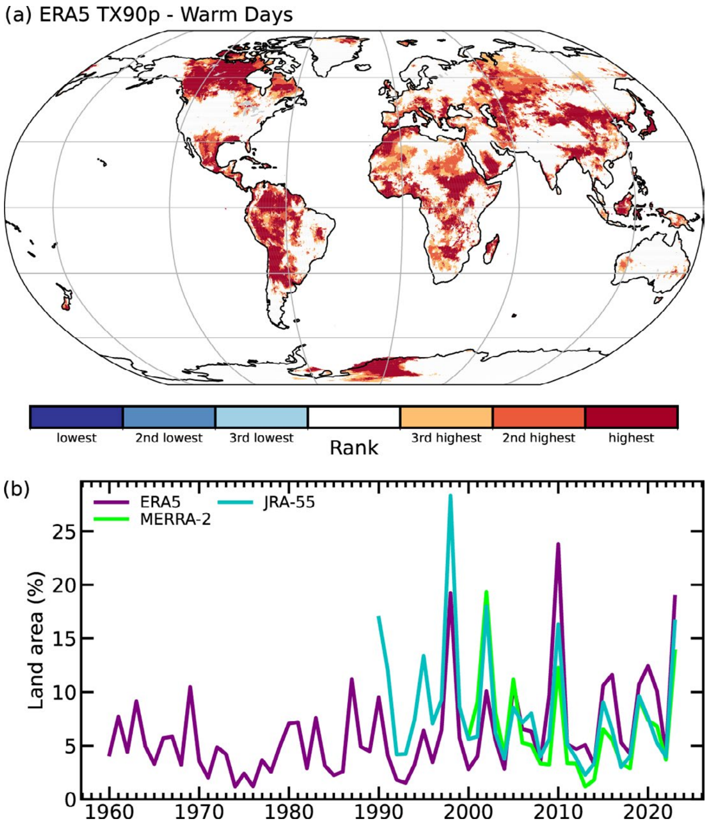

Fig. 2.8. (a) Map indicating grid cells where the warm day index (TX90p) for 2023 ranked in the three highest (orange to red) or three lowest (blue) values based on ERA5 since 1940 using the 1991–2020 reference period. (b) Time series of the percent of land area ranked as the highest value for TX90p in each year for ERA5 (from 1960), JRA-55 (from 1990), and MERRA-2 (from 2000). The ranks from the first 20 years of each reanalysis are not calculated.

A marine heatwave (MHW) is detected when five or more consecutive days of temperature are above a 90th-percentile daily climatology (Hobday et al. 2016). Marine heatwaves are categorized as moderate when the greatest temperature anomaly during the event is less than double the difference between the 90th percentile and the seasonal anomaly. When this value is more than double, triple, or quadruple the difference, the MHW is categorized as strong, severe, or extreme, respectively (see Fig. 2 in Hobday et al. 2018). The direct inverse is used to detect and categorize marine cold spells (MCSs; i.e., days below the 10th percentile). The baseline period used to detect events in this report is 1982–2011, because 1982 is the first full year of the NOAA OISST product (Huang et al. 2021).

The 2023 analysis of NOAA OISST daily v2.1 revealed that 94% of the global ocean surface experienced at least one marine heatwave (Hobday et al. 2016; Figs. 2.9a,b), and 27% experienced at least one MCS (Figs. 2.9c,d). The most common MHW category (Hobday et al. 2018) in 2023 was Category 2 Strong (49%), with the coverage of Category 3 Severe events reaching 10%. Category 1 Moderate MCSs have remained the most common (16%) cool events in all years since 1987. The ocean experienced a new global average record of 116 MHW days in 2023. This is far more than the 2016 MHW record of 86 days (Fig. 2.9a). This equates to a daily average MHW coverage of 32%. In 2023, the global ocean experienced 13 MCS days, far below the record of 37 days in 1982, equating to a daily average coverage of 4% (Fig. 2.9c).

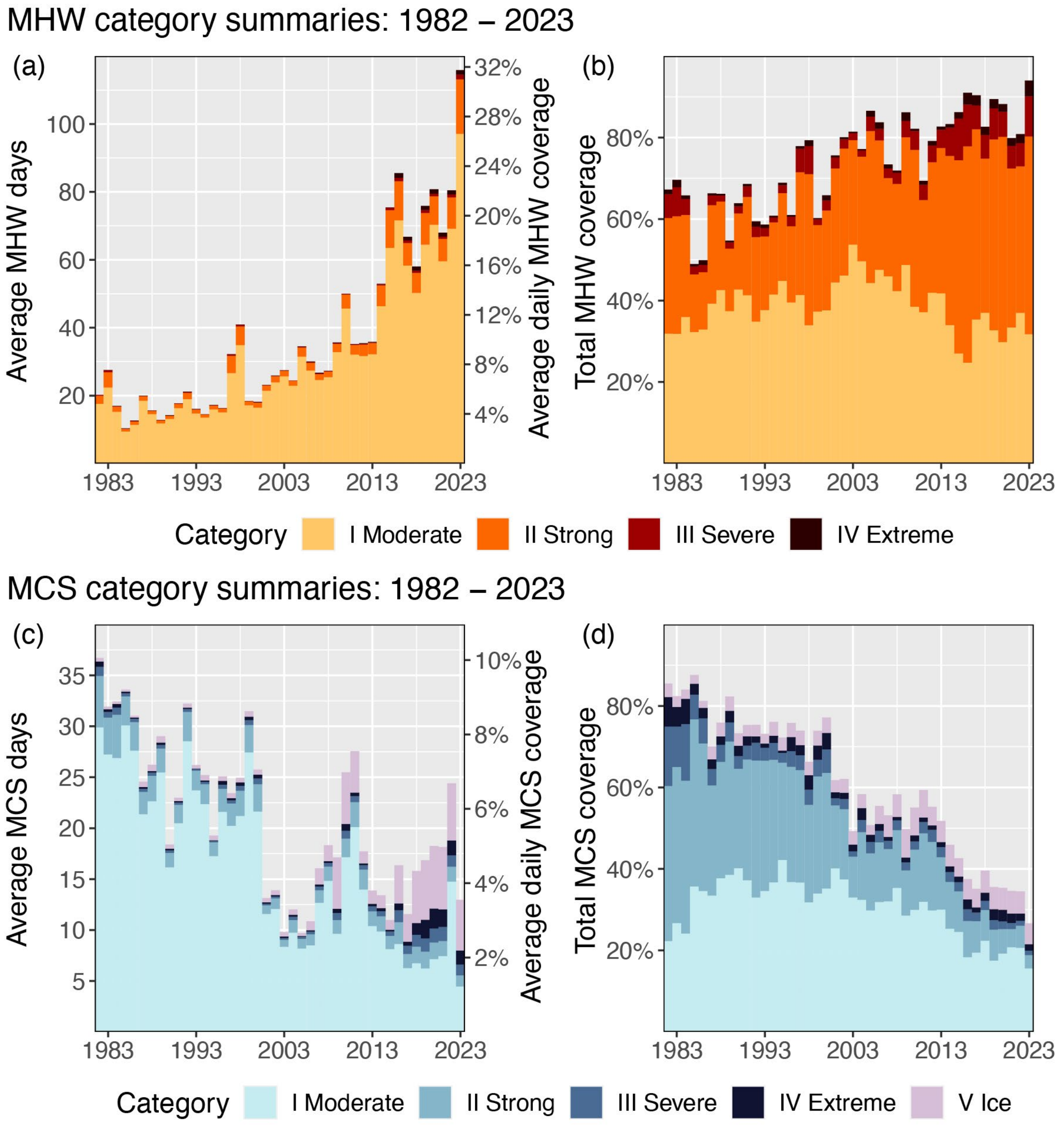

Fig. 2.9. Annual global marine heatwave (MHW; [a],[b]) and marine cold spell (MCS; [c],[d]) occurrence from NOAA OISST v2.1 using a climatology base period of 1982–2011. (a),(c) The average count of MHW/MCS days experienced over the surface of the ocean each year (left y-axis), also expressed as the percent of the surface of the ocean experiencing a MHW/MCS on any given day (right y-axis) of that year. (b),(d) Total percent of the surface area of the ocean that experienced an MHW/MCS at some point during the year. The values shown are for the highest category of MHW/MCS experienced at any point.

5. TROPOSPHERIC TEMPERATURE

—S. Po-Chedley, J. R. Christy, L. Haimberger, C. A. Mears, and C.-Z. Zou

The annual average lower tropospheric temperature (LTT) was record high for 2023, with particularly exceptional values in the tropics during the second half of the year (Fig. 2.10). The annual average LTT was 0.43°C–0.65°C above the 1991–2020 average, depending on the dataset (Fig. 2.11). In the annual average, LTT was above average over approximately 90% of Earth with record-setting temperatures over 17%–20% of the globe (Plate 2.1d). While La Niña conditions during late 2022 into early 2023 depressed global LTT in the first half of the year, El Niño developed in May and strengthened through the year. The El Niño conditions, paired with the underlying global warming trend (Table 2.3), contributed to the record observed tropospheric warmth in 2023 (Fig. 2.10). Continued research is needed to quantify other factors that may have enhanced the exceptional global tropospheric warmth in 2023 (Perkins-Kirkpatrick et al. 2024; Rantanen and Laaksonen 2024; Schmidt 2024).

Long-term records of tropospheric temperature are derived from in situ balloon-borne radiosonde measurements, microwave measurements from satellites, and atmospheric reanalysis models. In this section, we focus on LTT, which represents a weighted vertical average of atmospheric temperature with weight concentrated in the lower troposphere (c.f., Fig. 1 in Christy et al. 2003). Other measures of tropospheric temperature yield broadly consistent results (Po-Chedley et al. 2023). Despite differences in geographic sampling and observation type, the records show excellent agreement on interannual timescales (the minimum correlation coefficient between pairs of annually averaged, global mean, detrended LTT time series is 0.84; Fig. 2.11). While global trend differences are non-negligible (approximately ±0.04°C per decade across datasets, depending on the start date), all datasets exhibit substantial lower tropospheric warming ranging from 0.14°C to 0.22°C per decade. Satellite and reanalysis datasets indicate that 2023 was the warmest year on record for global LTT. 2016 and 2023 were tied as the warmest year in the RATPAC-A radiosonde dataset, and 2023 ranked fourth in the RICH and RAOBCORE radiosonde datasets. Differences in the relative ordering of annual mean global LTT anomalies are due in part to sampling. For example, if we sample reanalysis and satellite LTT values to match RAOBCORE data availability, then 2023 falls behind 2016 as the warmest year on record.

Table 2.3. Global lower-tropospheric temperature (LTT) trends (°C decade^{-1}) over the periods 1958–2023 and 1979–2023. NASA MERRA-2 data begins in 1980 and NOAA STAR v5.0 begins in 1981.

Method	Source	Start Year 1958	Start Year 1979
Radiosonde	NOAA RATPAC vA2 (Free et al. 2005)	0.19	0.22
Radiosonde	RAOBCORE v1.9 (Haimberger et al. 2012)	0.16	0.18
Radiosonde	RICH v1.9 (Haimberger et al. 2012)	0.18	0.20
Satellite	UAH v6.0 (Spencer et al. 2017)	–	0.14[1]
Satellite	RSS v4.0 (Mears and Wentz 2016)	–	0.22
Satellite	NOAA STAR v5.0 (Zou et al. 2023)	–	0.14[1]
Reanalysis	ERA5 (Hersbach et al. 2020)	0.16	0.18
Reanalysis	JRA-55 (Kobayashi et al. 2015)	0.17	0.19
Reanalysis	NASA MERRA-2 (Gelaro et al. 2017)	–	0.20
Median	**N/A**	**0.17**	**0.19**

[1] The retrieval algorithm in UAH and STAR LTT is different from other datasets and results in vertical sampling that is slightly higher in the troposphere (Spencer et al. 2017). As a result, temperature trends are approximately 0.01°C decade^{-1} smaller in UAH and STAR LTT.

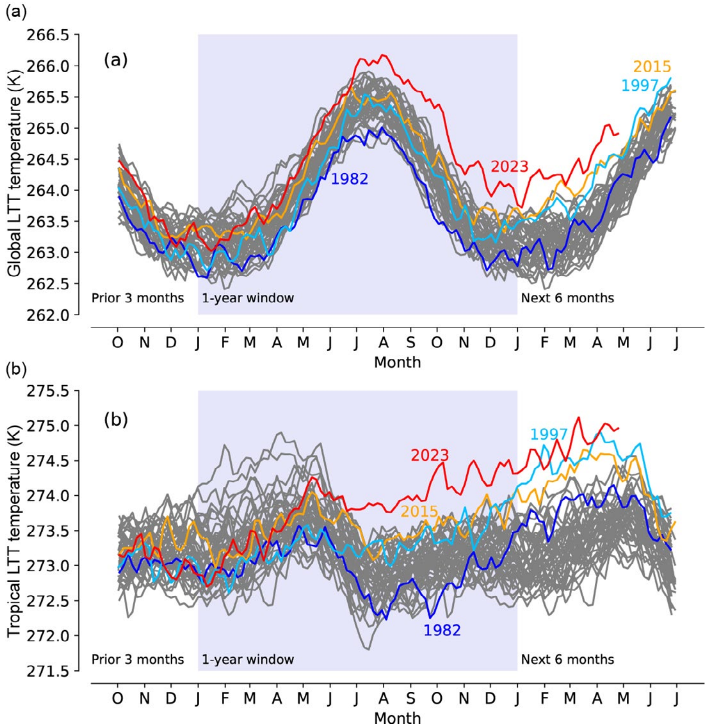

Fig. 2.10. Seasonal cycle of five-day average lower tropospheric temperature (LTT; K) for the (a) global and (b) tropical (20°S–20°N) mean. Each year (1979–2023) is plotted as a different gray line, except for select years that experienced the onset of El Niño (1982, 1997, 2015, and 2023 in blue, cyan, orange, and red, respectively). The full seasonal cycle is shown (shaded blue background) along with data from the preceding three months and following six months. Pentad values are from the UAH LTT dataset.

Over the Southern Hemisphere extratropics, record-high annual average LTT values were recorded over parts of the Southern Ocean into the South Atlantic, South Pacific, and South Indian Oceans. Over the Northern Hemisphere extratropics, record-high values occurred over northwest Canada into the Arctic Ocean, along the northwest coast of Africa and western Europe, and over Central and East Asia. In the tropics, all-time highs were concentrated over tropical South America, eastern Africa, and the tropical Atlantic and eastern tropical Pacific. Most of the tropics (20°S–20°N) set record-high LTT values for the months of July through December (not shown).

In some ways, 2023 appears to be following aspects of the 1997/98 El Niño event (Bell and Halpert 1998), which produced record-high tropospheric temperatures (Figs. 2.10, 2.11). Twenty-five years later, 1998 still ranks as one of the 10 warmest years in most tropospheric temperature datasets. In both 1997 and 2023, El Niño conditions were established by the early summer and strengthened through December. Since there is generally a three- to five-month lag between the warm sea-surface temperatures that accompany an El Niño event and tropical and global tropospheric temperature, record tropospheric warmth occurred in 1998 and, similarly, will likely continue to persist into 2024.

6. STRATOSPHERIC TEMPERATURE

—W. J. Randel, C. Covey, L. Polvani, and A. K. Steiner

Global mean temperatures in the lower, middle, and upper stratosphere increased slightly during 2023, mainly reflecting a recovery from anomalous cooling due to the Hunga Tonga–Hunga Ha‘apai (HTHH) volcanic eruption in early 2022 (Davis et al. 2023). The long-term trends, however, show multi-decadal cooling of the stratosphere due to anthropogenic carbon dioxide (CO_2) increases and ozone (O_3) loss. The Arctic stratospheric polar vortex was disturbed by a major stratospheric warming in February 2023, while the Antarctic polar vortex was strong and persistent during the winter and

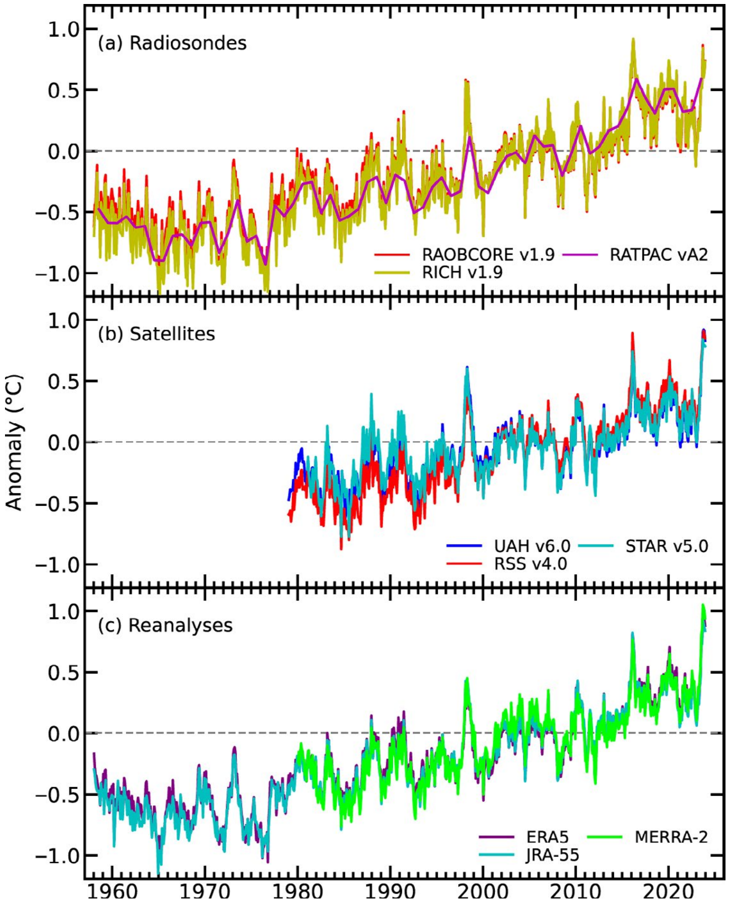

Fig. 2.11. Monthly average global lower tropospheric temperature (LTT) anomalies (°C) for (a) radiosonde, (b) satellite, and (c) reanalysis datasets. Annual averages are displayed for the RATPAC-A dataset. Anomalies are with respect to a 1991–2020 base period.

spring. The stratospheric quasi-biennial oscillation progressed normally in 2023, with equatorial easterly zonal wind shears and cold temperatures descending from the middle to lower stratosphere during the year.

Time series of global monthly temperature anomalies from the middle troposphere to the upper stratosphere based on satellite measurements are shown in Fig. 2.12. In addition to long-term stratospheric cooling and tropospheric warming due to greenhouse gas increases, transient variations arise from a variety of causes, including large volcanic eruptions (e.g., in 1982 and 1991), El Niño–Southern Oscillation (e.g., tropospheric warming events in 1997, 2016, and 2023), and large-scale wildfires (e.g., Australia in 2019/20). The middle stratosphere was anomalously cold in 2022 and early 2023 due to radiative effects of large water vapor (H_2O) anomalies injected by the January 2022 HTHH volcanic eruption (Millan et al. 2022; Wang et al. 2023; Davis et al. 2023; Flemming et al. 2024; Stocker et al. 2024). The HTHH stratospheric H_2O anomalies diffused and propagated upwards during 2023, resulting in smaller stratospheric radiative impacts and leading to a recovery from the anomalous cooling. The 11-year solar cycle was also increasing during 2023 (https://www.swpc.noaa.gov/products/solar-cycle-progression), which may contribute to slightly higher temperatures in the middle and upper stratosphere (Randel et al. 2009).

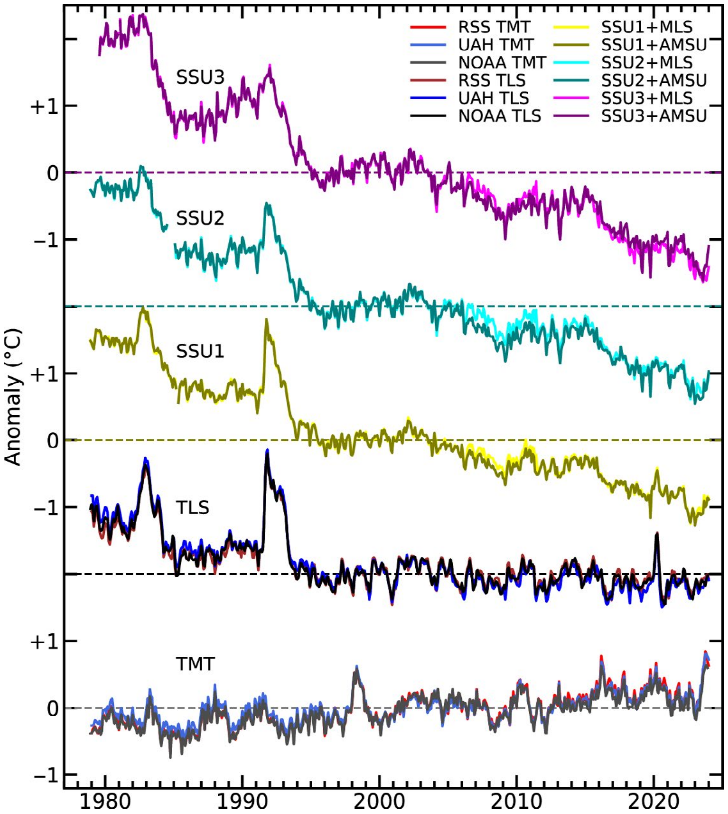

Fig. 2.12. Monthly global temperature anomalies (°C) from the middle troposphere to upper stratosphere (bottom to top). Middle and upper stratosphere data are from the Stratospheric Sounding Unit (SSU) updated with microwave measurements, representing thick-layer averages centered near 30 km, 38 km, and 45 km (SSU1, SSU2, and SSU3, respectively). Lower-stratosphere temperatures (TLS) are ~13-km–22-km layer averages from satellite microwave measurements. Middle troposphere (TMT) data are ~0-km–10-km layer averages and are included for comparison. Satellite data sources and details are discussed in Steiner et al. (2020). Each time series has been normalized to zero for the period 1995–2005, and curves are offset for clarity.

c. Cryosphere

1. PERMAFROST TEMPERATURE AND ACTIVE-LAYER THICKNESS

—J. Noetzli, H. H. Christiansen, M. Guglielmin, F. Hrbáček, G. Hu, K. Isaksen, F. Magnin, P. Pogliotti, S. L. Smith, L. Zhao, and D. A. Streletskiy

In recent decades, permafrost in cold regions worldwide have undergone widespread and persistent change, but the process is mostly slow and not directly visible. Permafrost is ground material with a maximum temperature of 0°C for at least two consecutive years. Its strongest warming was observed in cold high-latitude and high-elevation permafrost, where decadal rates of permafrost temperature increase by up to 1.0°C decade^{-1} at the depth of zero annual amplitude (DZAA, the depth where annual temperature fluctuations become negligible; e.g., Smith et al. 2023; Noetzli et al. 2021; Smith et al. 2022; Etzelmüller et al. 2023; Magnin et al. 2023; PERMOS 2023). In ice-bearing ground in warmer permafrost regions, latent heat effects due to phase change can significantly reduce temperature changes to below 0.1°C decade^{-1}. The layer above the permafrost that thaws during summer is called the active layer. Its annual thickness (active-layer thickness; ALT) has generally increased in all regions as a result of higher air temperatures. ALT increased by a few centimeters per decade in continuous permafrost in the Arctic in sediments and by decimeters per decade in discontinuous permafrost in bedrock in the Arctic, Antarctica, Scandinavia (e.g., Smith et al. 2022; Noetzli et al. 2023; section 5j), and the Qinghai-Tibet Plateau (QTP, Zhao 2024; Hu 2024). ALT changes of several meters were recorded during the past 20 years in the European Alps in bedrock as well as in degrading permafrost sites in talus slopes (e.g., PERMOS 2023, 2024; Magnin et al. 2023; Pogliotti et al. 2023).

Permafrost temperatures in 2023 were the highest on record for 9 of the 17 Arctic sites and higher than those in 2022 for most sites (see section 5j). However, for six sites in northwestern North America, permafrost temperatures were lower in 2023 compared to those in 2022, resulting from the delayed reaction at depth to the lower air temperatures during 2020–22. Similarly, the effect of higher air temperatures in 2023 is not yet observed at depths of 15 m–20 m. In the cold permafrost in Svalbard, the ground temperatures at 20 m were the fifth highest on record in 2023, based on measurements since 1999. Permafrost temperature at 10 m increased only slightly compared to 2022 and 2021 (Fig. 2.13, Janssonhaugen) and was still above the long-term average.

Active-layer thickness observed in 2023 in the Arctic differs between regions (Fig. 2.14; see section 5j): In high-Arctic Svalbard, record ALTs were documented after the record-warm summer of 2023 (see section 5b) for all sites, with values in bedrock of up to nearly 5 m in extreme cases. In 2023, above-average values were measured in Greenland and at sites from the Barents Sea region to West Siberia. In Central, East Siberia, and Chukotka in the Russian Arctic, in Arctic Alaska, western Alaska, and Northwest Canada (in 2022), ALT was close to the long-term average. In North America, the largest positive ALT anomaly in 2023 was observed in interior Alaska.

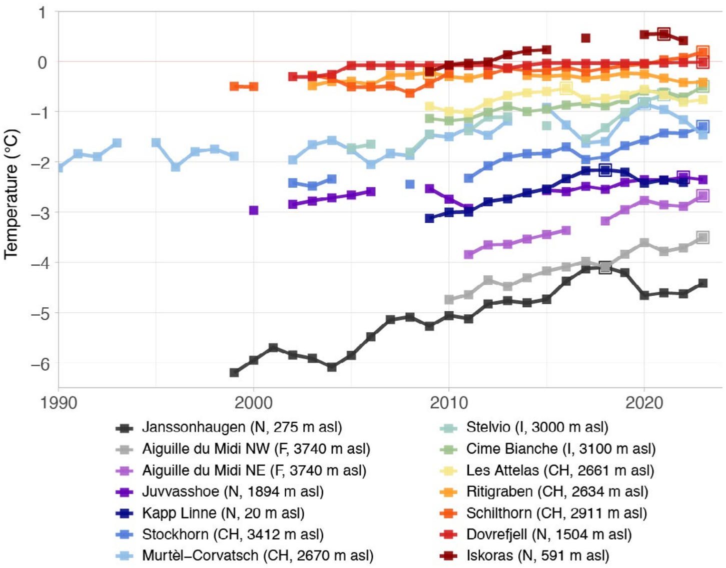

Fig. 2.13. Mean annual ground temperatures (°C) measured in European permafrost boreholes in the Alps, Scandinavia, and Svalbard at a depth of ca. 10 m. Maximum values for each time series are highlighted by a square. (Data sources: Norway: Norwegian Meteorological Institute and the Norwegian Permafrost Database [NORPERM]; Switzerland: Swiss Permafrost Monitoring Network [PERMOS]; France: Magnin et al. 2023; Italy: Pogliotti et al. 2023 and Guglielmin, M. unpublished data.)

Mountain permafrost temperatures near the DZAA in mainland Norway were the highest on record in 2023, meaning reported warming continues (Noetzli et al. 2023; Etzelmüller et al. 2023). In the European Alps, permafrost temperatures at 10-m and 20-m depth were at record levels, particularly for bedrock sites, due to two consecutive hot summers in 2022 and 2023 (as yet, the full effect of the 2023 summer heat cannot be observed at greater depth). In contrast, permafrost temperatures decreased at 10-m depth for several rock glacier stations in

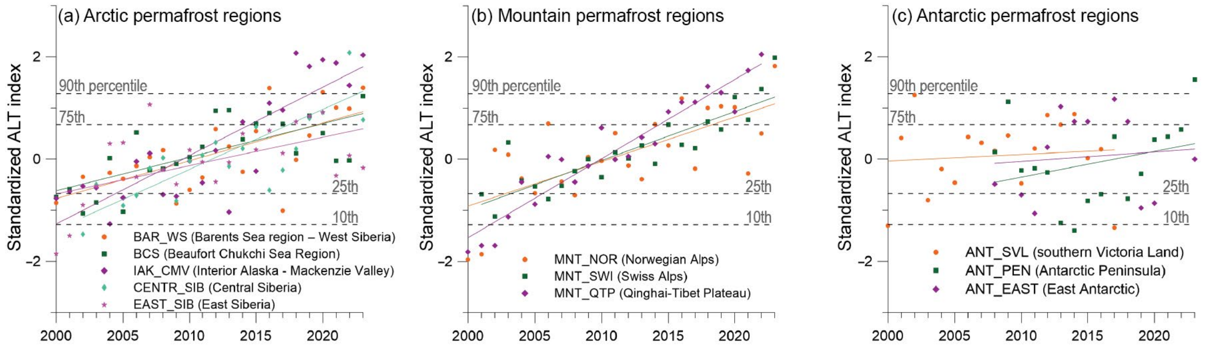

Fig. 2.14. Standardized active-layer thickness (ALT) index relative to 2000–20. (a) Arctic regions: Beaufort Chukchi Sea–Arctic Alaska and Mackenzie Delta region (BCS), Interior Alaska and central Mackenzie Valley, Northwest Territories (IAK_CMV), Barents Sea region–West Siberia (BAR_WS), Central Siberia (CENT_SIB), East Siberia (EAST_SIB); (b) Mountain regions: Norwegian mountains (MNT_NOR), Swiss Alps (MNT_SWI), Qinghai-Tibet Plateau (MNT_QTP); and (c) Antarctic: southern Victoria Land (ANT_SVL), Antarctic Peninsula (ANT_PEN), East Antarctic (ANT_EAST). (Source: Circumpolar Active Layer Monitoring [CALM].)

2023 after a snow-poor winter (Fig. 2.13; PERMOS 2024). The ALT for 2023 at the majority of sites in the Norwegian mountains and in the European Alps were at or close to their previous maximum, or set a new maximum (Fig. 2.14). Degraded permafrost in the upper part of the ground can be observed at several sites in Europe, e.g., by talik formation or active layers that no longer freeze during winter (Etzelmüller 2023; PERMOS 2023, 2024).

Permafrost temperatures at depths of 10 m and 20 m at six sites in the QTP in central Asia (Kunlun mountain pass to Liangdaohe) warmed significantly between 2005 and 2022, with many record values observed in 2021 (Fig. 2.15). For ALT in this region, a large increase was observed at 10 sites from 1981 to 2022 (Fig. 2.14), associated with a significant increase in air temperature.

Active-layer thickness in the Antarctic Peninsula region has increased since 2014, with the 2023 value being the maximum for 2006–23 (Fig. 2.14). Permafrost temperatures at DZAA at Rothera Station and Signy Island have remained stable since 2013 (Grifoni et al., accepted). In East Antarctica and Victoria Land, ALT remains relatively stable without clear detectable trends (Hrbáček et al. 2023).

Permafrost observation relies on field measurements at the national or institutional level and is globally collected in the framework of the Global Terrestrial Network for Permafrost (GTN-P; Streletskiy et al. 2021) as an essential climate variable of the Global Climate Observation System. The global coverage of permafrost monitoring sites is sparse and is mainly available in the Northern Hemisphere. Coverage is particularly limited in regions such as Siberia, central Canada, Antarctica, and the mountains in Central Asia, the Himalayas, and the Andes.

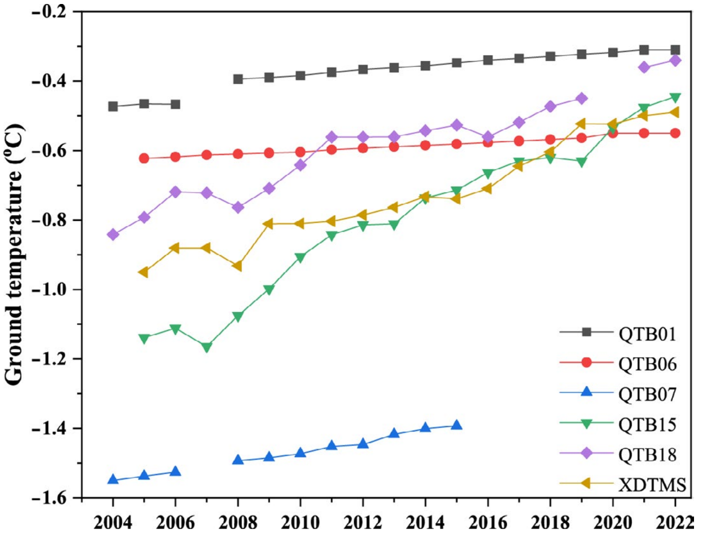

Fig. 2.15. Ground temperatures (°C) measured at 10-m depth in the Qinghai-Tibet Plateau during the period 2005–22. (Source: Cryosphere Research Station on Qinghai-Xizang Plateau, Chinese Academy of Sciences.)

2. ROCK GLACIER VELOCITY

—C. Pellet, X. Bodin, D. Cusicanqui, R. Delaloye, A. Kääb, V. Kaufmann, E. Thibert, S. Vivero, and A. Kellerer-Pirklbauer

Rock glaciers are debris landforms generated by the creep of perennially frozen ground (permafrost) whose velocity changes are indicative of changes in the thermal state of permafrost and associated ground hydrological changes (i.e., increasing temperatures lead to increase in velocity and vice-versa; RGIK 2023a; Staub et al. 2016). Rock glacier velocity (RGV) is a time series of annualized surface velocity values measured/computed on a rock glacier or a part of it (RGIK 2023b). Rock glacier velocities observed in different mountain ranges worldwide have been increasing since the 1950s, with large regional and inter-annual variability. These changes are consistent with the evolution of permafrost temperatures (section 2c1).

Although the hydrological year 2023 (October 2022 to September 2023) was the warmest on record in the European Alps (Fig. 2.16a), RGVs slightly increased in the western part of the Alps and continued to decrease in the east. Compared to 2022, velocity increased in the French Alps (+4% at Laurichard) and western Swiss Alps (+11% at Grosses Gufer and +15% at Gemmi/Furggentälti), whereas velocities continued to decrease in the Austrian Alps (–8% at Dösen and –22% at Hinteres Langtalkar; Fig. 2.16b). These regional evolutions are consistent with different snow conditions, namely exceptionally late onset of the snow cover and low snow depth in the east, which enabled marked cooling of the ground (as confirmed by the permafrost temperature decrease at 10-m depth observed on rock glacier Murtèl-Corvatsch in eastern Switzerland, Fig. 2.16). In the west, slightly later-than-average onset of the snow cover and slightly below-average snow depth were observed (PERMOS 2024). The reported RGV observations in 2023 in the European Alps are part of a general acceleration trend observed at all sites since the 1950s (Cusicanqui et al. 2021; Kellerer-Pirklbauer et al. 2024; PERMOS 2024).

In the Dry Andes in South America, RGVs reconstructed on three rock glaciers showed low velocities from 1950 to 2000, followed by a steady acceleration since the 2000s (Fig. 2.16c), consistent with the slight air temperature increase observed in the region since 1976 (Vivero et al. 2021). The potential effects of the above-average snow depth and longer snow cover duration in this region, associated with the strong El Niño event in 2023, have yet to be quantified.

Rock glacier velocities observed in Central Asia during the period of around 2018–23 show overall high values. Maximum velocities have been observed at Karakoram and Morenny, and

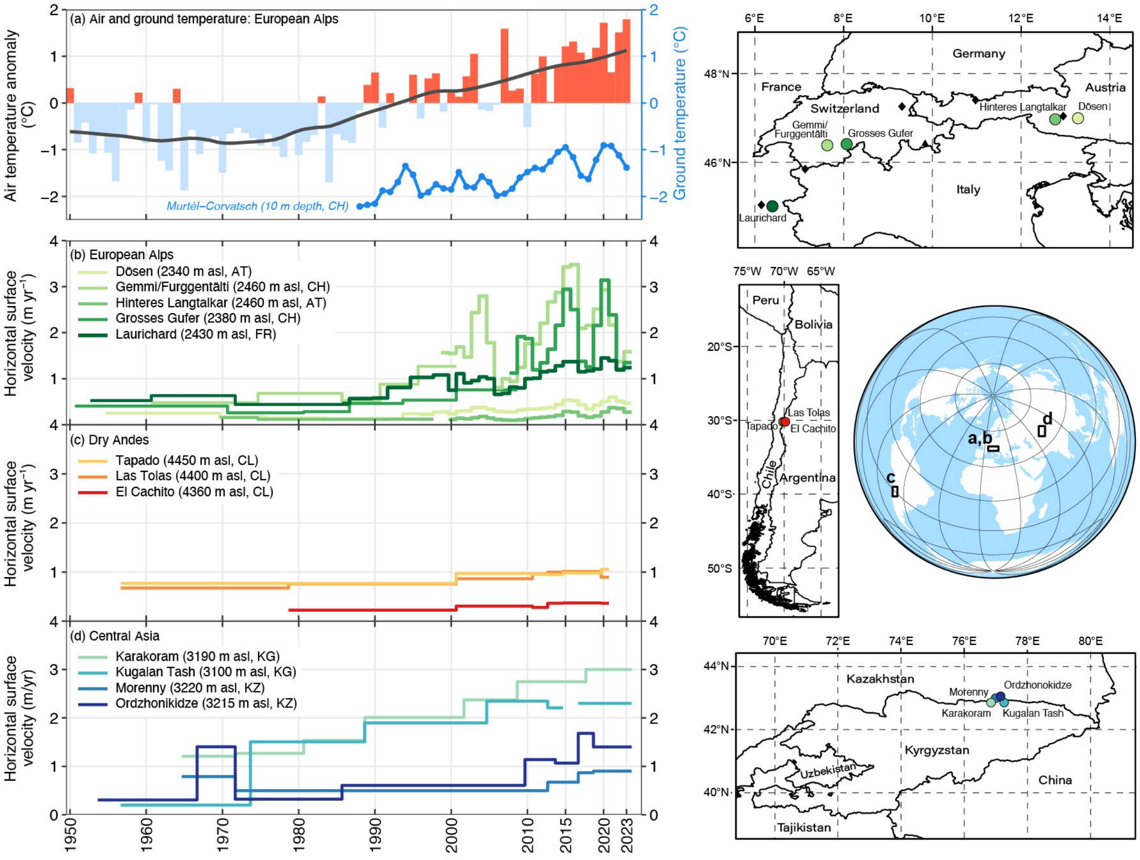

Fig. 2.16. Rock glacier velocity and climate: (a) air and ground temperature (°C) in the European Alps, (b)–(d) rock glacier velocities (m yr^{-1}) at selected sites in the (b) European Alps, (c) Dry Andes (updated from Vivero et al. 2021), and (d) Central Asia (updated from Kääb et al. 2021). Rock glacier velocities are based on in situ geodetic surveys or photogrammetry in the context of long-term monitoring. In situ hydrological mean annual permafrost temperature measured at 10-m depth (blue line) at Murtèl Corvatsch (black triangle on Europe map) and air temperature: composite anomaly to the 1981–2010 base period (bars) and composite 20-year running mean (solid line) at Besse (FR), Grand Saint-Bernard (CH), Saentis (CH), Sonnblick (AT), and Zugspitze (D, black diamonds on Europe map). (Sources: Météo-France, Deutscher Wetterdienst [DWD], MeteoSwiss, GeoSphere Austria, Swiss Permafrost Monitoring Network [PERMOS], University of Fribourg, University of Graz, Graz University of Technology, Université Grenoble Alpes [INRAE], University of Oslo.)

velocities on Kugalan Tash and Ordzhonikidze remain at a high level, although velocity slightly decreased at the latter (Fig. 2.16d; Kääb et al. 2021). This evolution is consistent with increasing air temperatures reported in the region since 1900 (Azisov et al. 2022; Sorg et al. 2015) and with the RGV evolution reported in the European Alps and Dry Andes.

Rock glacier velocity refers to velocities related to permafrost creep, which is a generic term referring to the combination of both internal deformation within the crystalline structure of the frozen ground (creep stricto sensu) and shearing in one or more discrete layers at depth (shear horizon; RGIK 2023b). RGVs are mostly related to the evolution of ground temperature and liquid water content between the upper surface of permafrost (i.e., permafrost table) and the layer at depth of the shear horizon (Cicoira et al. 2019; Frauenfelder et al. 2003; Kenner et al. 2017; Staub et al. 2016). Despite variable size, morphology, topographical and geological settings, and velocity ranges, consistent regional RGV evolutions have been highlighted in several studies (e.g., Pellet et al. 2023; Kellerer-Pirklbauer et al. 2024). Multi-annual long-term RGV time series are reconstructed using repeated aerial or optical satellite images. Horizontal displacements are computed based on cross-correlation feature tracking on multi-temporal ortho-images or digital elevation model matching (Kääb et al. 2021; Vivero et al. 2021). The resulting accuracy strongly depends on the spatial resolution of the images and on the image quality (i.e., presence of snow and shadows). Surface displacements are averaged for a cluster of points/pixels selected within areas considered as representative of the downslope movement of the rock glacier (RGIK 2023b). Annual rock glacier velocities are commonly measured using terrestrial geodetic surveys performed each year at the same time (usually at the end of summer). The positions of selected boulders (10–100 per landform) are measured with an average accuracy in the range of mm to cm (Lambiel and Delaloye 2004; Kellerer-Pirklbauer et al. 2024; PERMOS 2024; Thibert and Bodin 2022).

3. ALPINE GLACIERS

—M. S. Pelto

Mountain-region (i.e., alpine) glacier annual mass balance (sum of accumulation and ablation) observations are reported to the World Glacier Monitoring Service (WGMS). The WGMS reference glaciers each have at least 30 continuous years of mass balance observation, and benchmark glaciers have at least a 10-year mass balance record and are in regions that lack sufficient reference glaciers. In 2023, all 35 reporting reference glaciers had a negative balance, along with all 18 benchmark glaciers. This is the first year that all reference glaciers have had a negative balance. The 2023 dataset includes 109 glaciers from six continents, with 108 having a negative balance and 1 glacier reporting a positive mass balance. This makes 2023 the 36th consecutive year with a global alpine glacier mass balance loss, the 15th consecutive year with a mean global mass balance below –500 mm water equivalent (w.e.), and the year with the highest ratio of negative-to-positive mass balance observations of any year in the record (Fig. 2.17).

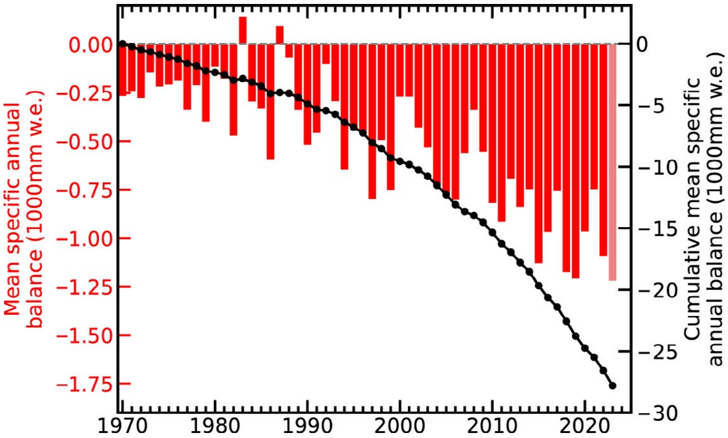

Fig. 2.17. Time series of global mean annual glacier mass balance (mm w.e.) of alpine glaciers from 1970 to 2023 as determined by the World Glacier Monitoring Service, using 19 regional averages from 53 glaciers in total.

The combination of benchmark and reference glaciers is used to generate regional averages (WGMS 2023). Global values are calculated using a single averaged value for each of 19 mountain regions, limiting bias towards well-observed regions (WGMS 2023). In 2023, the mean annual mass balance of the 35 reference glaciers was –1568 mm w.e., and –1590 mm w.e. for all 109 reporting glaciers regardless of record length. In a similar result, 2022 mean annual mass balance was –1475 mm w.e. for 37 reporting reference glaciers and –1568 mm w.e. for all 116 reporting glaciers. The regionally averaged global mass balance was –1090 mm w.e. in 2022; a final value for 2023 has not yet been determined, but the preliminary value is –1219 mm w.e.

The result of the melt in several regions has been an increasing complete loss of glaciers (see below; Huss and Fischer 2016; Fountain et al. 2023). This led to the Global Land Ice Measurements from Space (GLIMS) initiative adding an extinct glacier layer to its Glacier Viewer in 2023 to indicate glaciers that have been lost (GLIMS 2023). The sustained mass balance loss this century is also reducing the drought-buffering capacity of alpine glaciers in most midlatitude mountain ranges (Ultee et al. 2022). In 2023, we continued to see many glaciers across the globe with minimal to no retained snow cover, leading to surface darkening and even greater mass losses (Fig. 2.18).

In the European Alps, all 21 reporting glaciers had annual mass balances below –1300 mm w.e., with an average of –2311 mm w.e. In the Pyrenees, mass balances were also strongly negative. The combination of a snow drought and warm summer temperatures led to this sharp loss in glacier volume.

In High Mountain Asia, 22 of 23 glaciers had negative mass balances across seven nations: China, India, Kazakhstan, Kyrgyzstan, Nepal, Tajikistan, and Uzbekistan. The mean annual mass balance was –1048 mm w.e.

In North America, all 16 glaciers outside of the Arctic had negative mass balances averaging –2700 mm w.e. The combination of limited winter snowpack and a prolonged ablation season across the Pacific Northwest was the most significant contributor to this loss.

In South America, all 10 glaciers had significant negative annual mass balance averaging –1715 mm w.e. Continued drought in the central Andes and a warm melt season across the entire region led to negative mass balances from Ecuador southward to Argentina and Chile. In the central Andes, many glaciers from 32°S to 36°S lost all snow cover.

In Sweden and Norway, all 14 glaciers had negative annual mass balances averaging –1364 mm w.e. Across the Arctic in the Canadian Arctic Islands, Iceland, and Svalbard, all 19 glaciers had negative mass balances averaging –976 mm w.e. (see section 5h).

The rapid volume loss from 2021 to 2023 led to the complete loss of two glaciers in the WGMS mass balance dataset: St. Anna Glacier, Switzerland (reported 2011–23), and Ice Worm Glacier in the United States (reported 1984–2023). These glaciers are indicative of the increasing rate of glacier disappearance.

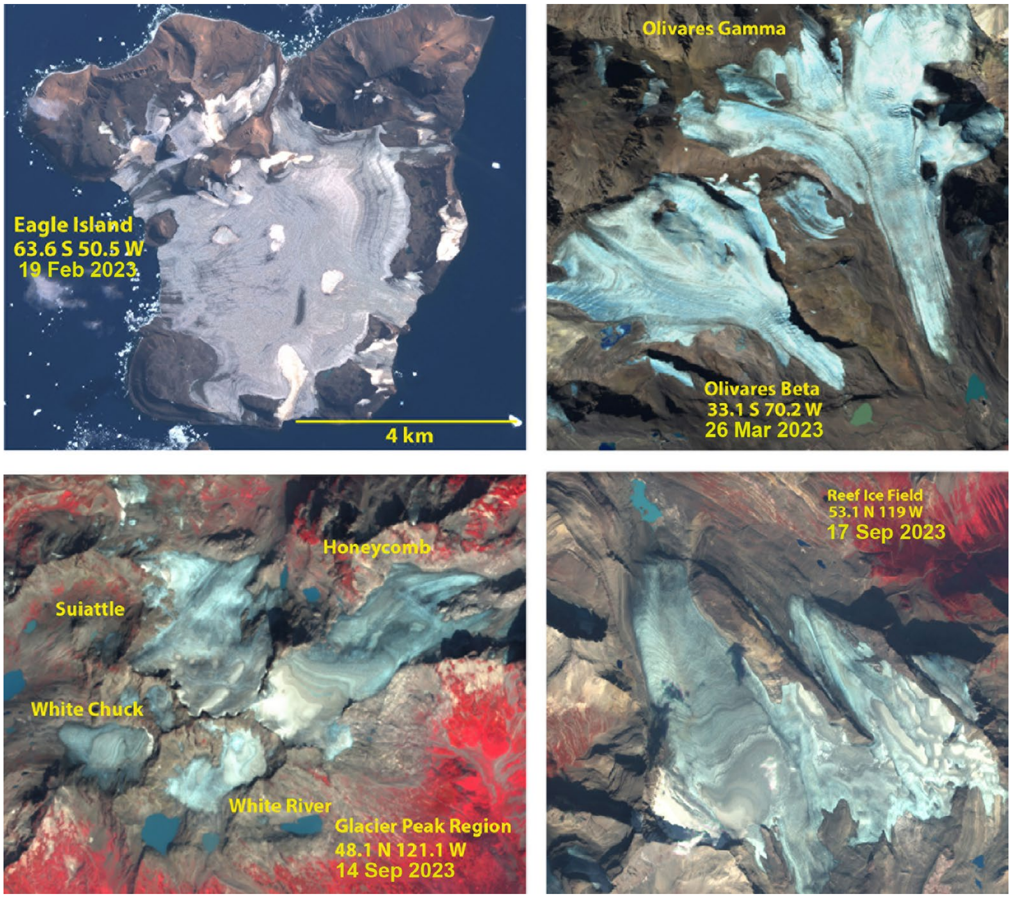

Fig. 2.18. Many alpine glaciers across the globe lost all or nearly all their snow cover in 2023, as illustrated by (a) the 63°S Antarctic Peninsula region, (b) the Andes, (c) North Cascades, and (d) 53°N in the Canadian Rockies. To be in equilibrium, a glacier needs to have at least 50% of its area snow covered throughout the year.

4. LAKE ICE

—S. Sharma, R. I. Woolway, and J. Culpepper

In the 2022/23 winter season (November 2022–April 2023), lake ice phenology (timing of ice-on and ice-off) across the Northern Hemisphere (NH) generally revealed that some lakes had later-than-normal ice-on dates and earlier-than-normal ice-off dates, although most lakes had shorter-than-normal seasonal ice cover. Notably, in situ phenological records revealed that ice-off dates were later for over half (55.8%) of the studied lakes, although the ice season remained shorter.

Across the NH, based on the ERA5 reanalysis data, lakes froze on average four days later and thawed five days earlier, with ice duration nine days shorter relative to the 1991–2020 base period (Fig. 2.19). The ice-on date was the third latest, the ice-off date was the third earliest, and the duration of lake ice cover was the fifth shortest since the start of the record in 1980.

Further, in situ lake ice observations from 157 lakes revealed that, on average, during the 2022/23 winter, ice-on was 2.1 days later, ice-off was 1.6 days later, and ice duration was 1.7 days

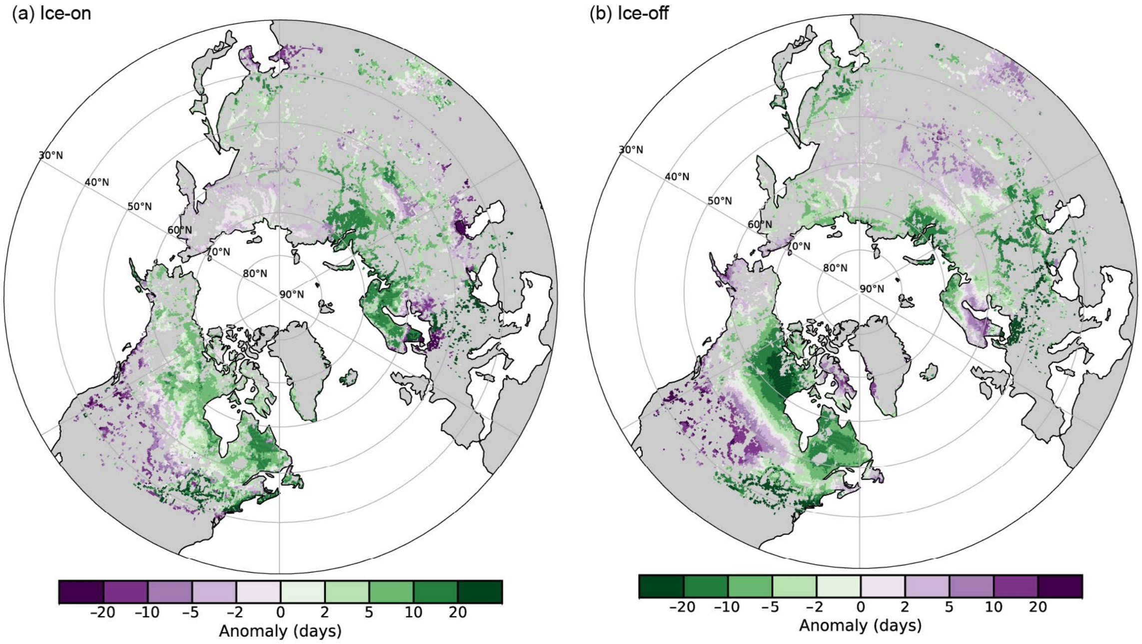
(a) Ice-on

(b) Ice-off

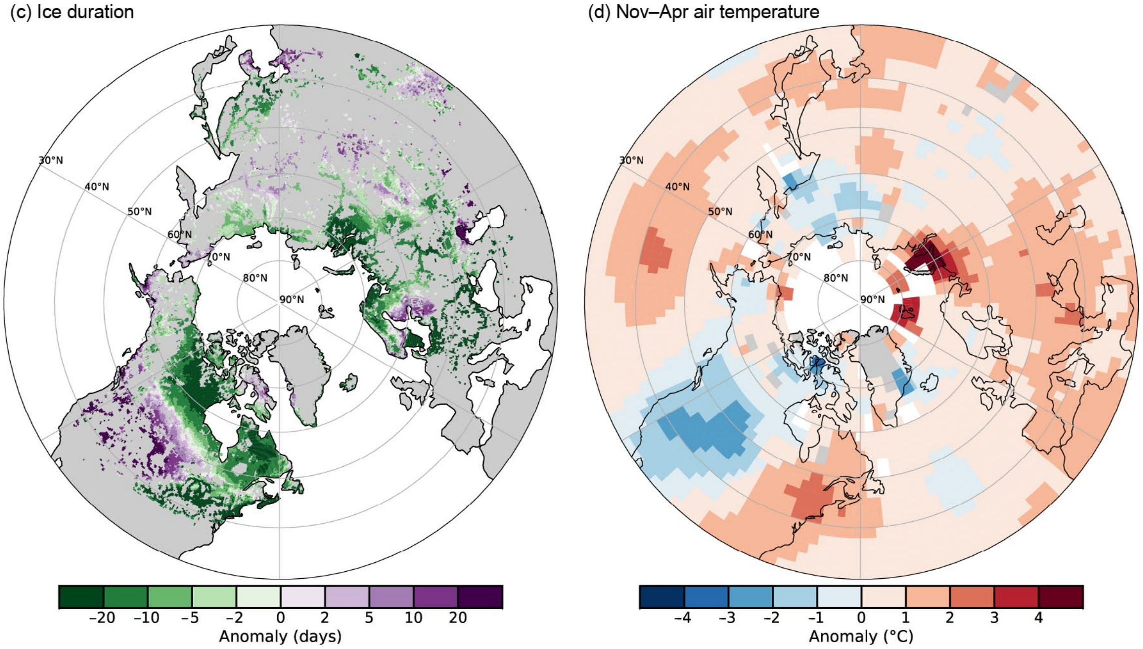
(c) Ice duration

(d) Nov–Apr air temperature

Fig. 2.19. Anomalies (days) for (a) the start of ice cover, (b) end of ice cover, and (c) duration of ice cover for lakes across the Northern Hemisphere (NH), with negative (positive) values being earlier (later) in the year. (d) Surface air temperature anomalies (°C) for the NH cold-season (Nov–Apr average) in 2023. The base period is 1991–2020. (Sources: ERA5, GISTEMPv4.)

shorter relative to the 1991–2020 base period (Fig. 2.20). Notably, Lake Suwa in Japan froze on 26 January 2023, marking the third year in a row this lake froze; three such consecutive freezes have not occurred in at least the past decade. In the last several decades, it has become increasingly rare for Lake Suwa to freeze.

Mountain lakes continue to be underrepresented in global studies of ice phenology (Christianson et al. 2021), owing to challenges in obtaining data and unsafe winter conditions (Block et al. 2019). During winter 2023, the 18 mountain lakes in our dataset (>1000 m a.s.l.) froze 7.8 days later and thawed 3.2 days later on average. Low-temperature anomalies during this winter likely led to later breakup (Fig. 2.20) as well as increased snowfall in the western United States from nine atmospheric rivers throughout December 2022 and January 2023 that impacted the area (NOAA/NCEI 2023c). Castle Lake in northern California, for example, broke up 34.4 days later than its 32-year mean. Despite the overall later breakup dates, ice cover duration continued to show signs of decline, with 10 mountain lakes having shorter ice duration and one lake having a near-zero anomaly. The continued decline in ice-cover duration suggests that generally later formation counteracts the later breakup date.

In North America, the Laurentian Great Lakes had 24.1% less maximal ice coverage during the 2022/23 winter, relative to the winters of 1991–2020. Both Lakes Erie and Superior had approximately 35% less ice coverage in 2023, followed by Lakes Huron (25.5%), Michigan (15%), and Ontario (9.8%; Fig. 2.21). Ice coverage was highest on 4 February—20 days earlier than average—across all of the Great Lakes.

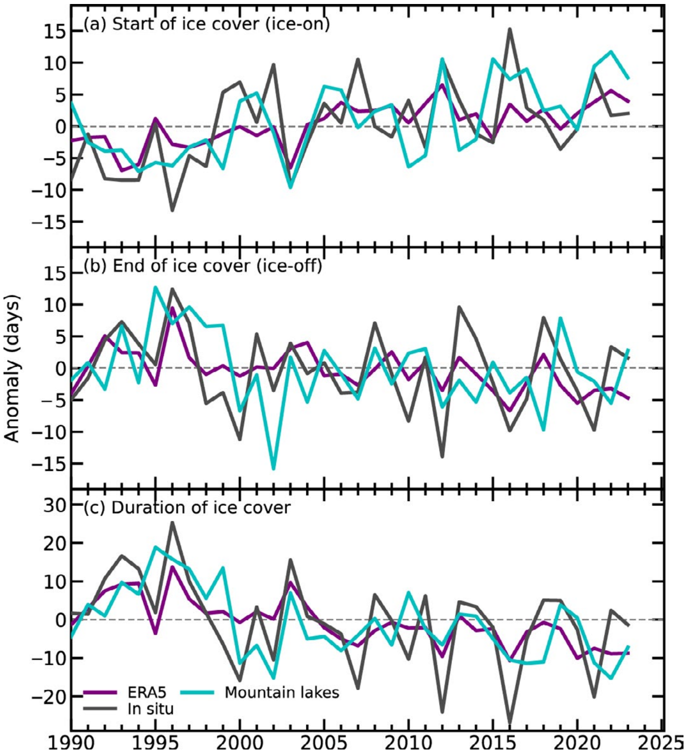

Fig. 2.20. Anomalies (days) in the timing of (a) ice-on, (b) ice-off, and (c) ice duration from 1980 to 2023 derived from ERA5 reanalysis, in situ observations, and mountain lakes. Base period is 1991–2020.

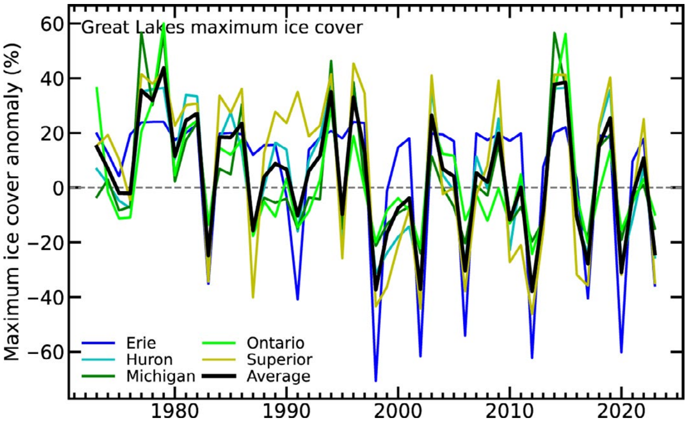

Fig. 2.21. Anomalies in the Laurentian Great Lakes maximum ice cover extent (%) for the period 1973–2023 (base period is 1991–2020) for individual lakes (Erie, Huron, Michigan, Ontario, Superior) and the Great Lakes average.

The ERA5 reanalysis product (Hersbach et al. 2020) was used to calculate ice-on and ice-off dates, in addition to ice-duration dates across NH lakes, following the methodology of Grant et al. (2021). Many citizen scientists, in addition to established monitoring networks, contributed in situ observations for 157 lakes across Canada, the United States, Norway, Finland, and Japan. Citizen scientist networks have been instrumental in sharing their local ice records and can offer extensive, efficient, and cost-effective local in situ environmental monitoring across vast spatial and temporal scales (Fritz et al. 2019; Lopez et al. in press). Furthermore, in situ ice phenology data for eight mountain lakes in the United States and 10 lakes in Europe were obtained and updated through personal correspondence with the data authors (Caine et al. 2023; Chandra et al. 2022; Kainz et al. 2017). Annual maximum ice coverage (%) data for each of the Laurentian Great Lakes were acquired for the period 1973–2023 from the NOAA Great Lakes Environmental Research Laboratory, in addition to the surface air temperature data for the NH cold season (November–April average) from the NASA Goddard Institute for Space Studies' surface temperature analysis (GISTEMP Team 2024). Anomalies for each of our ice metrics were calculated for the 2022/23 winter relative to the 1991–2020 normal base period.

5. NORTHERN HEMISPHERE CONTINENTAL SNOW COVER EXTENT

—D. A. Robinson and T. W. Estilow

Annual snow cover extent (SCE) over NH lands averaged 24.3 million km^2 in 2023. This was 0.8 million km^2 (3.2%) below the full period-of-record (November 1966–December 2023) mean, marking the seventh-least-extensive cover on record (Table 2.4; Fig. 2.22a). Monthly SCE in 2023 ranged from a maximum of 47.1 million km^2 in January to a minimum of 2.9 million km^2 in August.

Northern Hemisphere SCE in January and March ranked in the lower tercile of the 57-year record (1.8% and 2.8% below normal,

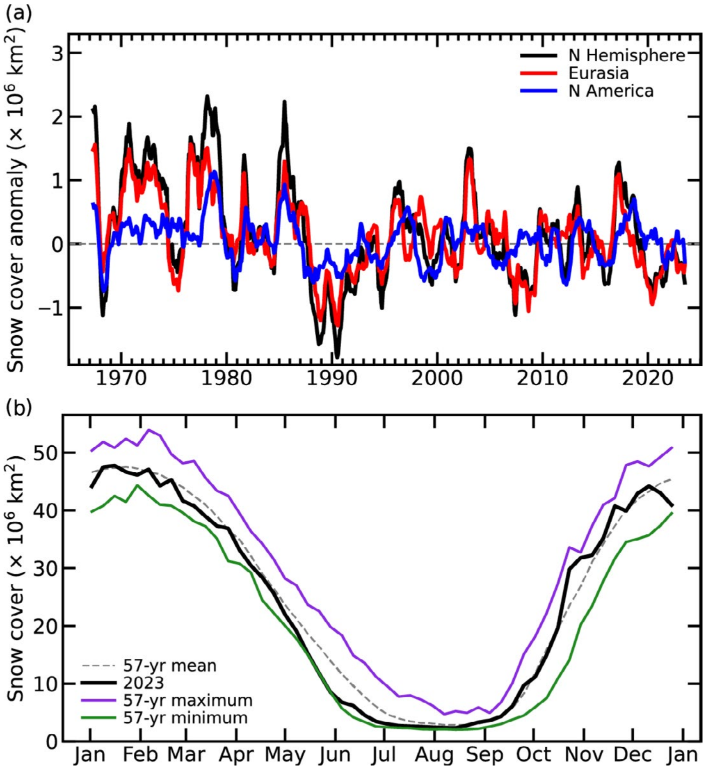

Fig. 2.22. (a) Twelve-month running anomalies of monthly snow cover extent (SCE; × 10^6 km^2, or million km^2) over Northern Hemisphere (NH, black) lands as a whole and Eurasia (red) and North America (blue) separately plotted on the seventh month using values from Nov 1966 to Dec 2023. Anomalies relative to the full period are calculated from NOAA snow maps. Mean NH SCE is 25.1 million km^2 for the full period of record. Monthly means for the period of record are used for nine missing months during 1968, 1969, and 1971 to create a continuous series of running means. Missing months fall between Jun and Oct. (b) Weekly NH SCE time series (× 10^6 km^2) for 2023 (black) plotted with the mean (gray dashed line), maximum (purple), and minimum (green) SCE for each week. Mean weekly SCE and extremes are calculated using the 57-year record from Jan 1967–Dec 2023. Weekly data granules represent SCE for each seven-day period ending on Monday.

Table 2.4. Monthly and annual climatological information on Northern Hemisphere (NH), Eurasia (EUR), and North America (NA) snow cover extent (SCE) between Nov 1966 and Dec 2023. Included are the numbers of years with data used in the calculations, NH anomalies, NH means (Nov 1966–Dec 2023), standard deviations (Nov 1966–Dec 2023), 2023 values, and rankings (highest and lowest). Areas are in millions (× 10^6) of square kilometers (km^2). The years 1968, 1969, and 1971 have one, five, and three missing months, respectively, thus are not included in the annual calculations. NA includes Greenland. Ranks are from most (1) to least extensive (least to most in parentheses)

Month	Yrs	2023 NH Anomaly (× 10^6 km^2)	NH Mean (× 10^6 km^2)	NH Std. Dev.	2023 NH rank	2023 EUR rank	2023 NA rank
Jan	57	–0.9	47.1	1.5	41 (17)	48 (10)	27 (31)
Feb	57	–0.4	45.9	1.8	32 (26)	37 (21)	24 (34)
Mar	57	–1.1	40.4	1.8	43 (15)	52 (6)	4 (54)
Apr	57	–0.2	30.5	1.6	28 (30)	43 (15)	16 (42)
May	57	–2.3	19.0	2.0	50 (8)	35 (23)	57 (1)
Jun	56	–3.3	9.3	2.5	50 (7)	46 (11)	53 (4)
Jul	54	–1.0	3.8	1.2	44 (11)	42 (13)	41 (14)
Aug	55	–0.4	2.9	0.7	39 (17)	39 (17)	29 (27)
Sep	55	–0.1	5.4	0.9	28 (28)	22 (34)	33 (23)
Oct	56	+0.2	18.6	2.6	25 (32)	24 (33)	28 (29)
Nov	58	+1.2	34.4	2.1	17 (42)	16 (43)	28 (31)
Dec	58	–1.2	43.7	1.8	48 (11)	18 (41)	56 (3)
Annual Calculations	**54**	**–0.8**	**25.1**	**0.8**	**48 (7)**	**45 (10)**	**45 (10)**

respectively; Fig. 2.22b), while February (–0.9%) and April (–0.7%) were in the middle. North America (NA) had more extensive snow cover compared to normal than Eurasia (EUR) during each of these four months. In particular, NA had its fourth-most-extensive SCE in March (+7.6%) and its 16th most extensive in April (+4.8%). Thereafter, melt quickly occurred across NA, with May having its least-extensive SCE of the satellite era (–19.5%). Both continents contributed to June having the sixth-least SCE across the NH (–35.6%; Fig 2.23). Across the NH, September and October began the new snow season with SCE in the middle tercile (–1.0% and +0.9%, respectively). SCE was above normal for both continents in November (+3.6%; Fig 2.23). While SCE remained above normal over EUR in December (+2.1%), SCE in NA declined to its third least extensive for the month (–10.8%), contributing to the seventh-least-extensive SCE overall for the NH (–2.8%).

The contiguous United States' (US) SCE (not shown) was close to normal at the beginning of 2023, then became well above normal in March (+45.6%; fourth most extensive) and April (+62.3%, seventh most extensive). In May, the US SCE was below average (–17.6%) while Canadian SCE (not shown) was the lowest on record (–30.7%). Autumn snow cover began early over the US and was the 11th most extensive on record for October (+68.6%), but for the remainder of the year, US SCE was below normal, with December having the sixth-least-extensive SCE on record (–43.4%).

SCE is calculated at the Rutgers Global Snow Lab (GSL) from daily SCE maps produced by meteorologists at the US National Ice Center, who rely primarily on visible satellite imagery to construct the maps (Estilow et al. 2015). Maps depicting daily, weekly, and monthly conditions, anomalies, and climatologies may be viewed at the GSL website (https://snowcover.org).

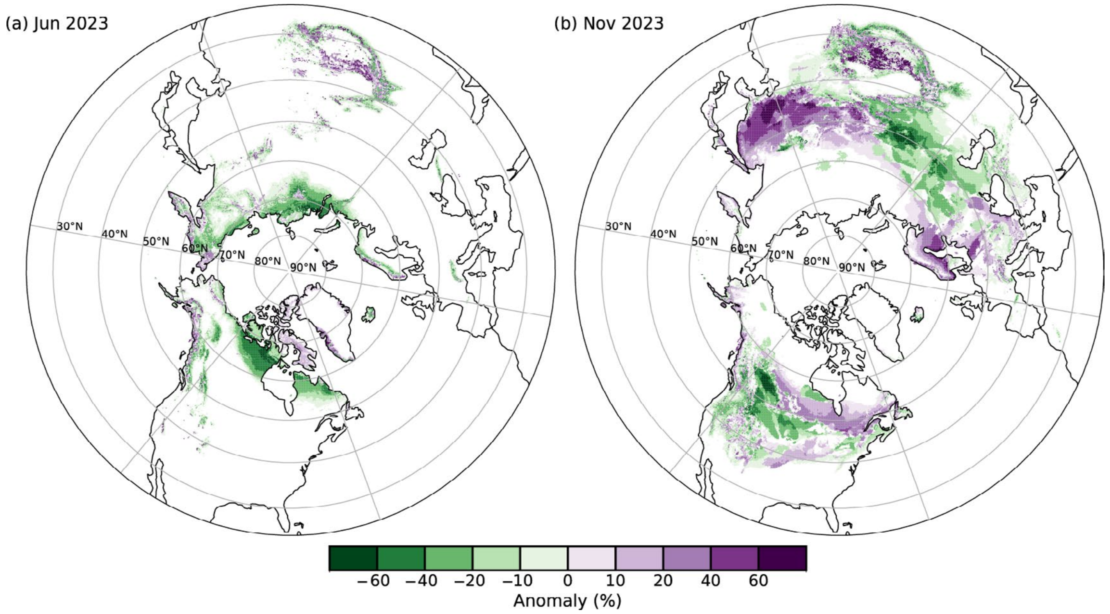

Fig. 2.23. Monthly snow cover extent (SCE) departure (%) maps for (a) Jun and (b) Nov 2023. Jun exhibited the lowest SCE anomaly (–2.17 million km^2) during 2023, while Nov was the highest above normal (+0.53 million km^2). Mean monthly SCE calculated using the 30-yr span from 1991–2020. Negative departures indicate less SCE than normal (green) with positive departures (purple) showing areas of SCE above the 30-yr mean.

d. Hydrological cycle—atmosphere

1. SURFACE HUMIDITY

—K. M. Willett, A. J. Simmons, M. Bosilovich, and D. A. Lavers

The near-surface atmosphere had record or near-record water vapor content for 2023, with global specific humidity (q) anomalies reaching 0.17 g kg^{-1}–0.42 g kg^{-1} across the various datasets (Figs. 2.24a–d; Table 2.5). These anomalies exceeded 2022 q levels by a large margin of 0.14 g kg^{-1} to 0.28 g kg^{-1}. As has been the case since 2011, saturation (relative humidity, RH) remained below average over land, being –0.46%rh to –1.05%rh across datasets. This decline reflects the fact that the temperature over land is rising so quickly that the water-holding capacity is outpacing the actual water vapor content, which is governed largely by local water availability and slower ocean warming rates. Relative humidity over oceans was close to average in 2023, within ±0.1%rh.

Global annual mean q anomalies (relative to 1991–2020; Figs. 2.24a–d; Table 2.5) from HadISDH, MERRA2, JRA-55, and the new JRA-3Q surpassed previous records, with HadISDH and MERRA2 reaching 0.33 g kg^{-1} over land and 0.4 g kg^{-1} and 0.42 g kg^{-1}, respectively, over ocean. Years of previous records differed among datasets. ERA5 had similarly large increases from 2022 (Table 2.5) and record-high q over ocean, reaching 0.24 g kg^{-1}. Masking to HadISDH coverage resulted in higher 2023 anomalies, especially over ocean where HadISDH spatial coverage is very limited. Global annual mean anomalies of RH (Figs. 2.24.e–h; Table 2.5) were lower than those of 2022 over land by between 0.12%rh for ERA5 to 0.32%rh for JRA-3Q. JRA-55 had 2023 as

Table 2.5. Global mean surface-specific (*q*) and relative humidity (RH) anomalies for 2023 and comparison with previous values. Note that no previous record is reported for ocean RH because a long-term trend has not been robustly established. RH values for MERRA-2 are not included in this report. Values in bold type identify new records.

Dataset	*q* (g kg^{-1}) 2023 global mean anomaly	*q* (g kg^{-1}) 2022 global mean anomaly	*q* (g kg^{-1}) Previous record high (year of previous record)	RH (%rh) 2023 global mean anomaly	RH (%rh) 2022 global mean anomaly	RH (%rh) Previous record low (year of previous record)
HadISDH.land	**0.33**	**0.14**	**0.27 (1998)**	–0.46	–0.24	–0.79 (2019)
ERA5 over land	0.17	–0.01	0.21 (2016)	–1.05	–0.93	–1.32 (2021)
ERA5 over land masked	0.22	0.02	0.25 (2016)	–1.01	–0.88	–1.28 (2021)
MERRA-2 over land	**0.33**	**0.19**	**0.27 (2020)**	--	--	--
JRA-55 over land	**0.25**	**0.06**	**0.21 (2016)**	**–0.87**	**–0.62**	**–0.83 (2021)**
JRA-3Q over land	**0.26**	**0.08**	**0.21 (1998/2016)**	–0.91	–0.59	–0.93 (2021)
HadISDH.marine	**0.4**	**0.12**	**0.27 (2020)**	0.06	–0.23	--
ERA5 over ocean	**0.24**	**0.03**	**0.20 (2019)**	–0.08	–0.12	--
ERA5 over ocean masked	**0.40**	**0.19**	**0.34 (2016)**	–0.12	–0.06	--
MERRA-2 over ocean	**0.42**	**0.18**	**0.25 (2019)**	--	--	--
JRA-55 over ocean	**0.34**	**0.09**	**0.19 (2016/2020)**	0.25	0.21	--
JRA-3Q over ocean	**0.34**	**0.09**	**0.19 (2020)**	0.10	0.10	--

record low for land RH but by a very small margin (0.04%rh). Over ocean, where agreement between datasets is much poorer, 2023 values were only slightly higher than in 2022 for ERA5 and JRA-55 (+0.04%rh and +0.03%rh), identical for JRA-3Q, and much larger for HadISDH.marine (+0.29%rh). ERA5 2023 anomalies were slightly drier than average (−0.08%rh) whereas the other datasets were above average (0.06%rh to 0.25%rh). Masking ERA5 to HadISDH coverage resulted in even drier anomalies.

The increases in q relative to 2022 were characteristic of El Niño—this can be seen clearly for 1998, 2010, and 2016 in Figs. 2.24a–d. The La Niña during 2021 and 2022 also likely contributed through its tendency to depress the near-surface water content. Plate 2.1g shows the largest positive q anomalies lying mostly within ±30° latitude over typical El Niño-related wet regions to a large degree. For example, the southern United States, northwestern and southeastern South America, east Africa, and eastern China are broadly positive; the January to December averaging likely dampens these seasonal-scale anomalies. India, Southeast Asia, and northern Australia also show strong positive q anomalies despite El Niño favoring dry conditions over these regions. Over oceans, strong positive q anomalies were present over the typical El Niño–Southern Oscillation (ENSO) region in the tropical Pacific and also over the North Pacific, tropical North Atlantic, and southern Indian Ocean. The latter is associated with the positive phase of the Indian Ocean dipole. These features correspond well to anomalously warm sea-surface temperatures (Plate 2.1a). Figure 2.25a shows that the temporal and latitudinal extent of positive q anomalies in 2023 were unusual in historical context. It also shows that although long-term trends (Fig. 2.25b) are positive over the entire Northern Hemisphere and tropics, there is considerable intra- and inter-annual variability in addition to latitudinal variability.

For RH, the fingerprint of ENSO was less clear in the global and latitudinal mean time series (Figs. 2.24e–h; 2.25c) and the 2023 annual anomaly map (Plate 2.1h). Dry anomalies dominated

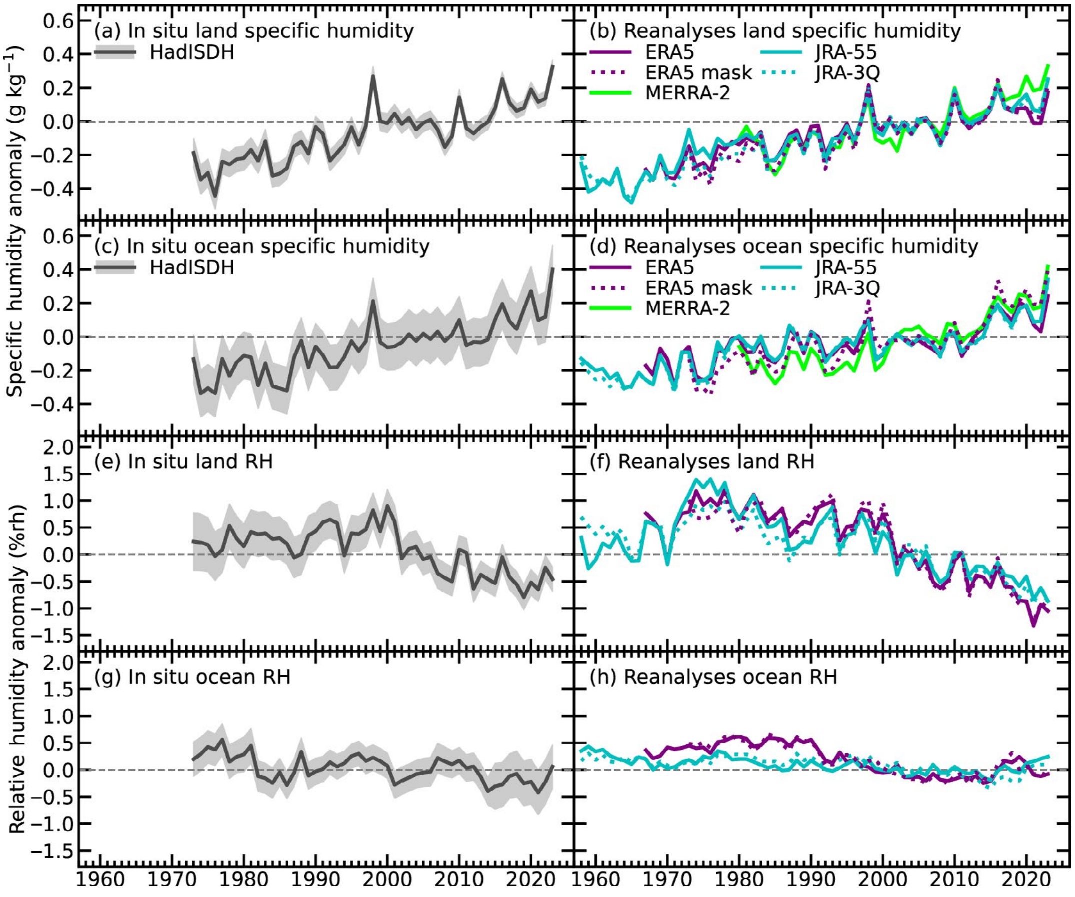

Fig. 2.24. Global average surface humidity annual anomalies (g kg^{-1} for [a]–[d] and %rh for [e]–[h]; 1991–2020 base period). For the in situ datasets, 2-m surface humidity is used over land and ~10-m surface humidity is used over the oceans. For the reanalysis, 2-m humidity is used over the whole globe. For ERA5, ocean series-only points over open sea are selected. ERA5 mask is a version of ERA5 limited to the spatial coverage of HadISDH. Two-sigma uncertainty is shown for HadISDH, capturing the observation, gridbox sampling, and spatial coverage uncertainty. (Sources: HadISDH [Willett et al. 2013, 2014, 2020]; ERA5 [Hersbach et al. 2020]; JRA-55 [Kobayashi et al. 2015]; JRA-3Q [Kosaka et al., 2024]; MERRA-2 [Gelaro et al. 2017].)

over land, despite the strong positive anomalies over the western United States, northwest India/Pakistan, and northern Australia. Dry anomalies were broadly similarly located compared to 2022. Over ocean, the Indian Ocean dipole is apparent with positive RH anomalies spatially matching positive q anomalies. The eastern tropical Pacific had a band of strong negative RH anomalies despite this being a region of strong positive q anomalies, indicating that the warming—and thus water-holding capacity—here (see Plate 2.1a) outpaced the actual water vapor increase.

The lack of in situ data, particularly over oceans, continues to limit our ability to robustly monitor near-surface humidity. The spatial coverage from HadISDH in the Southern Hemisphere is poor, especially over ocean. Figure 2.24 includes ERA5 masked to the lower coverage of HadISDH. This shows improved agreement and that the more positive q anomalies and less negative RH anomalies in HadISDH are partly artifacts of HadISDH undersampling regions where, according to ERA5, drying is stronger. The lower anomalies in ERA5 from 2020 onwards remain substantially lower than in HadISDH and other reanalyses in the masked version, suggesting that this feature is not related to coverage differences. ERA5 suffers from in situ data gaps similar to HadISDH but uses information from satellites and the background model to derive estimates for these regions. All datasets have their own strengths and weaknesses.

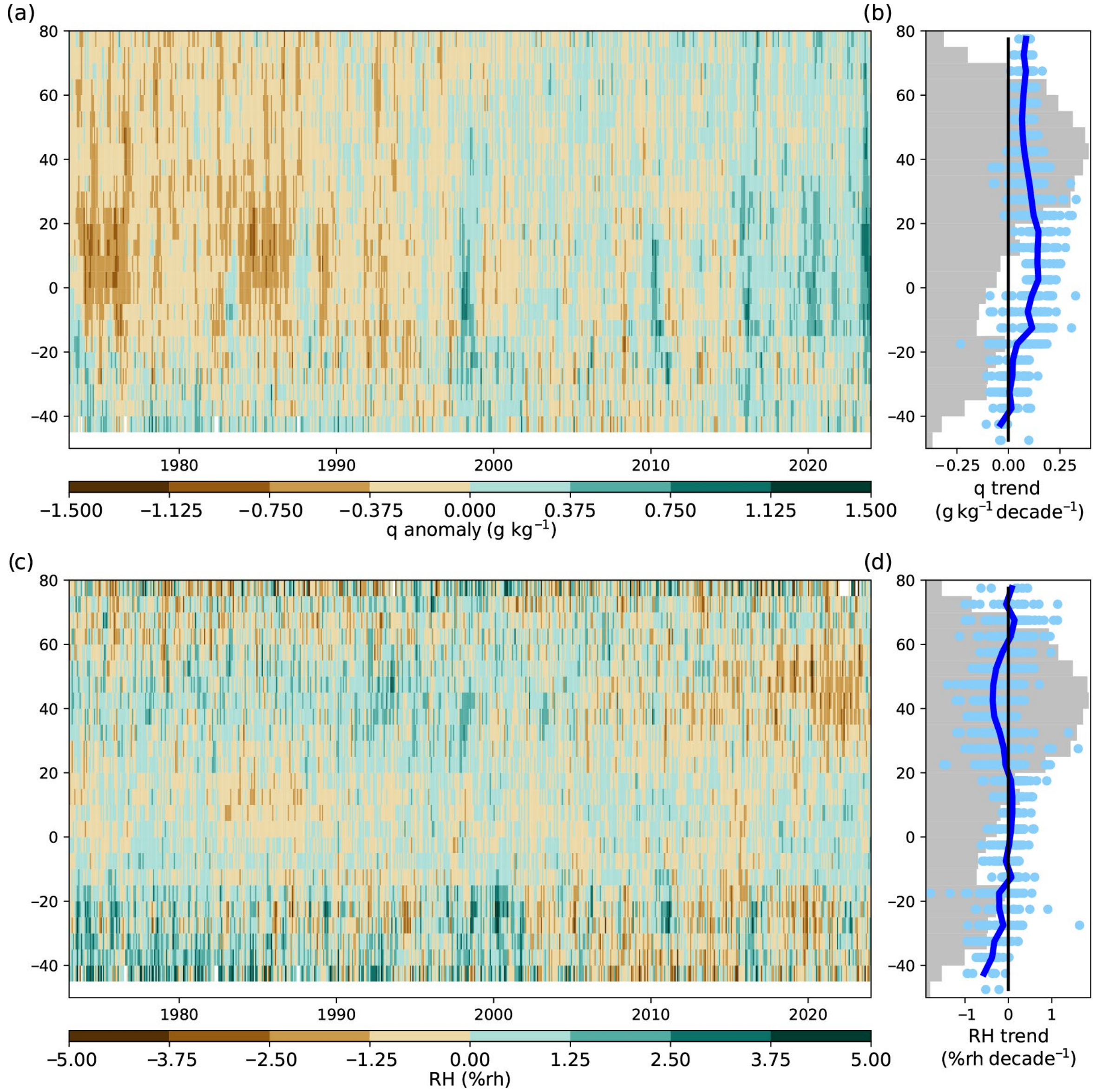

Fig. 2.25. Latitudinal monthly mean anomalies of (a) specific humidity (g kg^{-1}) and (c) relative humidity (%rh; from HadISDH.blend). (b),(d) Decadal trends for each gridbox (dots) and latitude band mean (line), fitted using an ordinary least-squares linear regression following Santer et al. (2008), with gray shading representing the percentage of globe covered by observations (in gridboxes) at each latitude band. Latitude band means are only calculated where there are at least five gridboxes (5° × 5°) at that latitude band.

2. HUMID-HEAT EXTREMES OVER LAND

—K. M. Willett, R. M. Horton, Y. T. E. Lo, C. Raymond, and C. D. W. Rogers

The year 2023 emerged as a record-breaking year by a considerable margin for humid heat over global land, based on daily maximum wet-bulb temperatures ($\mathrm{T_wX}$), for all but one ($\mathrm{T_wX31}$) of the six indices presented herein (see Table 2.6 for definitions of these indices). Humid-heat intensity, measured as the annual anomaly of $\mathrm{T_wX}$, was 0.6°C above the 1991–2020 average (Fig. 2.26a), doubling the previous record of 0.3°C in 1998. Humid-heat frequency also increased by a large margin. The annual $\mathrm{T_wX90p}$ anomaly (Fig. 2.26b), a measure of local extremes, was 26.4 days year–1 above average, far exceeding the previous record of 16.2 days year–1 in 1998. Annual occurrence anomalies for $\mathrm{T_wX25}$, $\mathrm{T_wX27}$, and $\mathrm{T_wX29}$ (Table 2.6) were 6.1, 9.3, and 1.3 days year–1 above average, respectively (Fig. 2.26c). These exceeded the previous records of 4.4, 6.7, and 0.9 days year–1 set in 2020 (equal with 2022 for $\mathrm{T_wX25}$), respectively. For $\mathrm{T_wX31}$, 2023 was equal with the previous record in 1998 at 0.2 days year–1.

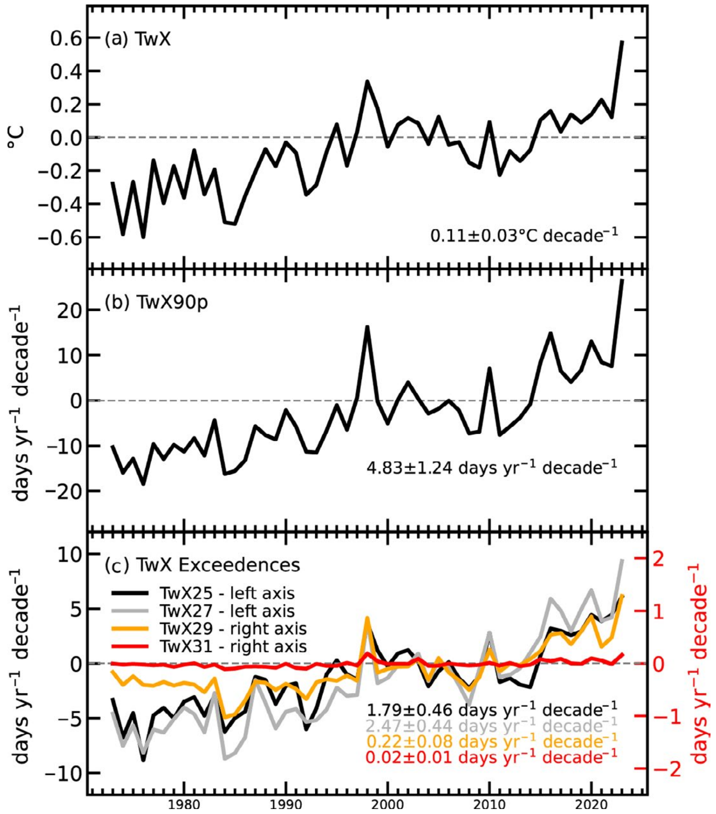

Fig. 2.26. Global land mean annual anomaly time series of various daily maximum wet-bulb temperature indices from HadISDH.extremes relative to a 1991–2020 base period. Decadal trends (significant at $p<0.01$) are also shown. Trends were fitted using an ordinary least-squares linear regression with an autoregressive (1) correction following Santer et al. (2008). (a) Anomaly of the annual median of the monthly maximum wet-bulb temperature (°C). (b) Anomaly of the annual sum of the daily maximum wet-bulb temperature exceedances of the locally defined daily 90th percentile (days yr^{-1}). (c) Anomaly of the annual sums of the daily maximum wet-bulb temperature ≥ 25°C, 27°C, 29°C, and 31°C thresholds (days yr^{-1}). Note that coverage is skewed towards the northern extratropical latitudes with large data gaps over Africa and considerable gaps over South America, Australia, and parts of Central Asia (see Plates 2.1a and 2.1b for spatial coverage).

Table 2.6. Definitions of six humid-heat indices and their respective 2023 global land annual anomalies (1991–2020 base period). The 2023 global annual anomaly for the exceedance indices (not $\mathrm{T_wX}$) is the sum of the monthly spatial mean over the globe. For $\mathrm{T_wX}$, the median is used as a more robust measure in the presence of outliers, averaging first over space for each month and then over time.

Index	Description	Meaning	2023 Global Anomaly
$\mathrm{T_wX}$	Annual median of monthly maximum wet-bulb temperature	Intensity of humid-heat extremes	0.6°C
$\mathrm{T_wX90p}$	Days per year exceeding the 90th percentile of the climatological daily maximum wet-bulb temperature (seasonally varying)	Frequency of humid-heat extremes relative to local climatology	26.4 days
$\mathrm{T_wX25}$	Days per year where the daily maximum wet-bulb temperature ≥25°C	Frequency of moderately high humid-heat extremes	6.1 days
$\mathrm{T_wX27}$	Days per year where the daily maximum wet-bulb temperature ≥27°C	Frequency of high humid-heat extremes	9.3 days
$\mathrm{T_wX29}$	Days per year where the daily maximum wet-bulb temperature ≥29 °C	Frequency of very high humid-heat extremes	1.3 days
$\mathrm{T_wX31}$	Days per year where the daily maximum wet-bulb temperature ≥31°C	Frequency of severe humid-heat extremes	0.2 days

The exceptionally large humid-heat index anomalies are in concert with record anomalies across many other variables in 2023. El Niño, present from May onwards and becoming strong by autumn (see section 4b for details), contributed to record humid-heat anomalies by influencing both atmospheric and sea-surface temperatures. In conjunction with significant positive trends in humid-heat intensity and frequency (Fig. 2.26), these record anomalies are clear indicators of a rapidly changing climate that is impacting society across the globe. Humid heat presents challenges to maintaining comfortable and safe temperatures for humans (Saeed et al. 2022; Wolf et al. 2022; Kjellstrom et al. 2017) and other large mammals (Buzan and Huber 2020) as evaporative cooling (including sweating) is less efficient in hot and humid conditions (Baldwin et al. 2023).

Thresholds of 25°C, 27°C, 29°C, and 31°C T_wX represent moderately high to severe humid-heat extremes. They may be exceeded during midlatitude warm seasons or year-round in the tropics but rarely or never at higher latitudes and elevations. Figure 2.27 shows 2023 anomalies for all indices in historical context, using deciles to identify “unusual” humid heat. Analysis excludes gridboxes with both no 2023 exceedances and <15 years with an exceedance within the 1991–2020 climatological period. “Very unusually high” (10th decile) occurrences for T_wX25 and

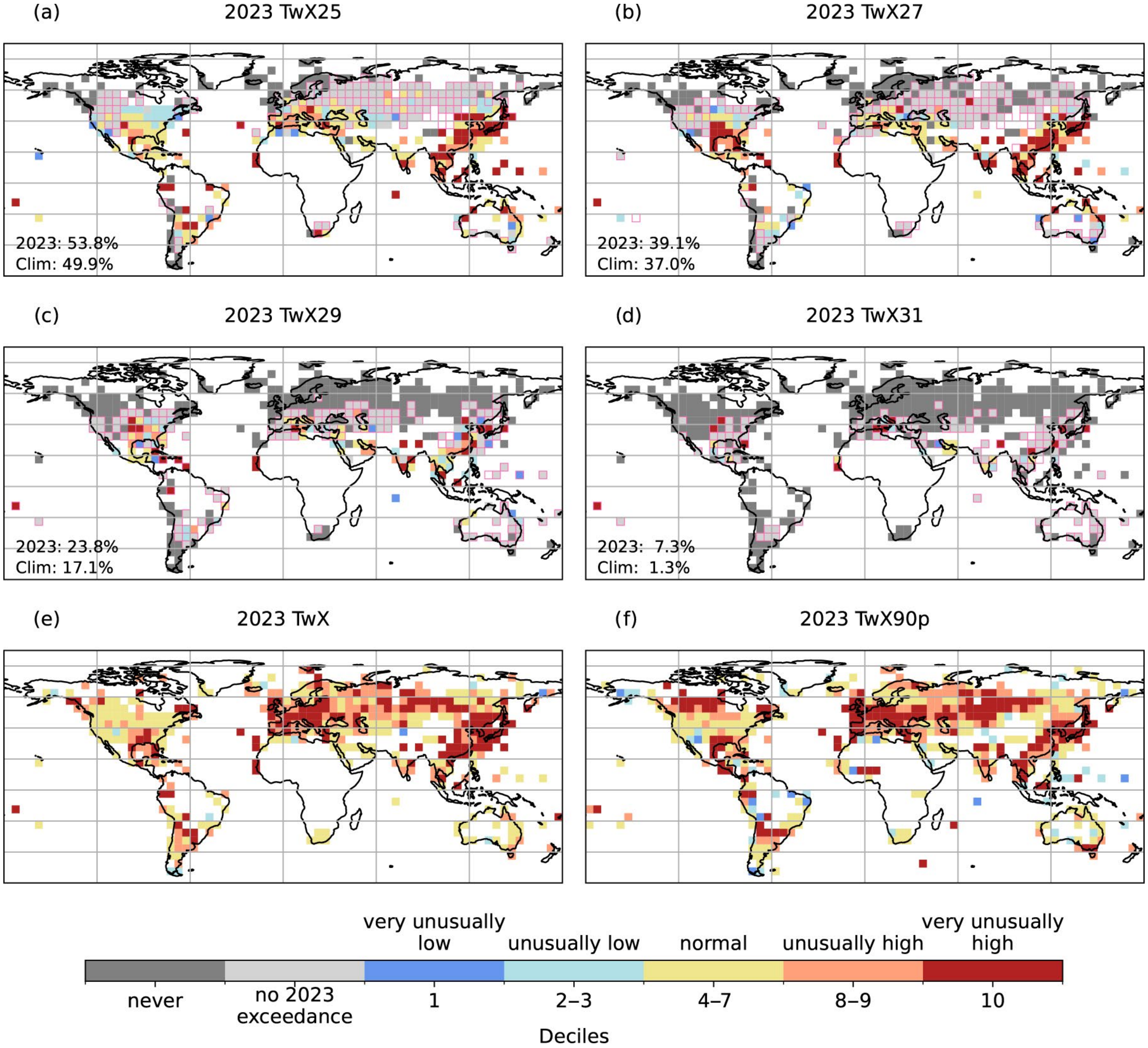

Fig. 2.27. Humid-heat extremes of 2023 as deciles over the period 1973–2023 for various indices. Number of days in 2023 with maximum wet-bulb temperature (T_w) ≥ (a) 25°C (T_wX25), (b) 27°C (T_wX27), (c) 29°C (T_wX29), and (d) 31°C (T_wX31). Gridboxes bounded in pink indicate that <15 years within the 1991–2020 period had an exceedance. These panels are annotated with the percentage of observed area where an exceedance occurred in 2023 and climatologically (≥15 years of at least one exceedance between 1991 and 2020). (e) Annual median anomaly of monthly maximum T_w (T_wX). (f) Number of days in 2023 with maximum T_w > local daily 90th percentile (T_wX90p) relative to a 1991–2020 base period. For (a)–(d) only, gridboxes bounded in pink indicate <15 years within the 1991–2020 period. For (e) and (f), the gray ‘never’ and ‘no 2023 exceedance’ categories are not relevant. Data have been screened to remove gridboxes where temporal completeness is less than 70% (<35 yrs in 51). All valid years have data present for all months.

T_wX27 in 2023 (Figs. 2.27a,b) covered 20.4% and 28.0% of analysis-relevant gridboxes, respectively. This is in contrast to 9.6% and 10.4 %, respectively, for those indices in the "no 2023 exceedance" and "very unusually low" (1st decile) categories combined. These "very unusually high" exceedances were mostly over the southeastern United States (T_wX27 only), eastern China, Japan, and Southeast Asia. In some higher latitudes (e.g., eastern North America, the Caspian Sea), exceedances were "unusually low" (2nd to 3rd deciles), pointing to the inherent interannual variability in rare events and potential differences between dry-bulb and wet-bulb measures of extremes. Sparse occurrences of T_wX29 and T_wX31 (Figs. 2.27c,d) with "very unusually high" frequencies covered 21.9% and 39.4% of analysis-relevant gridboxes, respectively. For T_wX29, these occurred over parts of the tropics, northern India, eastern China, and as far north as Japan and the central United States. "Very unusually high" T_wX31 occurrences were mostly outside the tropics, including over the Mediterranean, near Sicily, and the central United States. The Persian Gulf, a region with climatologically exceptionally high humid heat (Raymond et al. 2020), experienced "normal" (4th to 7th deciles) to "unusually high" (8th to 9th deciles) frequencies in 2023 for T_wX25 to T_wX31. For all absolute threshold indices (T_wX25 to T_wX31, Figs. 2.27a–d), 2023 saw a larger global land area experiencing ≥1 exceedance of +2.1 to +6.7 percent of gridboxes compared to the climatological mean.

The globally applicable measures of T_wX90p and T_wX (Plates 2.1i,j) had positive intensity and frequency anomalies over most of the observed land in 2023. "Unusually high" to "very unusually high" (8th to 10th deciles) local humid-heat intensity (T_wX) and frequency (T_wX90p) covered 57% and 53% of the observed land, respectively (Figs. 2.27e,f), with Europe and eastern Asia standing out. Few gridboxes had "unusually low" or "very unusually low" (1st to 3rd decile) intensities (2.5%) or frequencies (10%). Humid-heat events with notable impacts included those near Rio de Janeiro in November, in Florida and the United States Gulf Coast in June–July, South and Southeast Asia in April, and China in July. A lack of in situ data precludes confident statements about humid heat in many tropical, desert, high-elevation, and high-latitude areas. Absences are most prominent for Africa. The drying out of wet-bulb temperature (T_w) thermometers results in erroneously high readings. Although this is less common now due to the increasing prevalence of humidity probes, its influence in these high-value threshold exceedances cannot be ruled out.

Here, humid heat is explored using the in situ-based monitoring product HadISDH. extremes (Willett 2023a,b) for the period 1973–2023. This product calculates T_w using the Noniterative Evaluation of Wet-bulb Temperature method (Rogers and Warren 2024). Indices are calculated using daily maximum wet-bulb temperature following methods established for dry-bulb indices (section 2b4; https://climpact-sci.org).

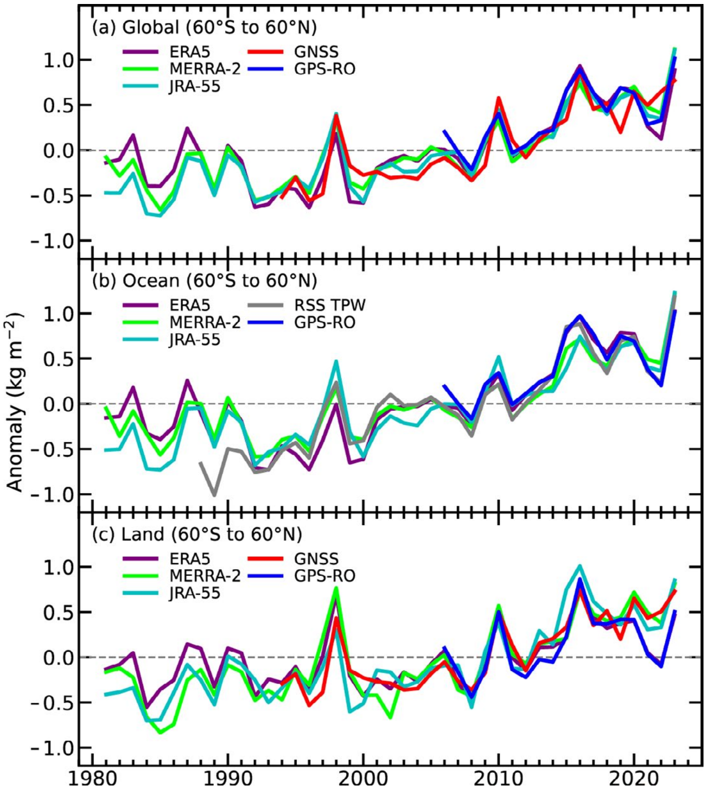

Fig. 2.28. Global mean total column water vapor (TCWV) annual anomalies (kg m^{-2}) over (a) land and ocean, (b) ocean-only, and (c) land-only from observations and reanalyses. The shorter time series from the observations have been adjusted so there is zero mean difference relative to the ERA5 results during their respective periods of record.

3. TOTAL COLUMN WATER VAPOR

—O. Bock, C. A. Mears, S. P. Ho, and X. Shao

In 2023, global (60°S–60°N) mean total column water vapor (TCWV) was between 0.89 kg m^{-2} and 1.12 kg m^{-2} above the 1991–2020 average, according to five datasets (Fig. 2.28a; Table 2.7). Three of the datasets (MERRA2, JRA55, and GPS-RO) determined that 2023 was the wettest year on record. Over oceans (Fig. 2.28b), the moisture excess was even larger, with record-high anomalies between 1.01 kg m^{-2} and 1.23 kg m^{-2} in all five datasets (ERA5, MERRA2, JRA55, RSS TPW

Table 2.7. Global mean (60°S–60°N) total column water vapor (TCWV) anomalies (kg m^{-2}; 1991–2020 base period) for 2023 and linear trends (kg m^{-2} $decade^{-1}$) over the period 1991–2023 (2006–23 for GPS-RO, 1995–2023 for GNSS). The GNSS data include 197 stations over land and ocean islands and 143 stations over land.

TCWV Anomalies (kg m^{-2})

Dataset	ERA5	MERRA2	JRA-55	MWR	GPS-RO	GNSS
Global	0.89	1.12	1.10	--	1.01	0.77
Ocean	1.02	1.21	1.23	1.18	1.01	--
Land	0.46	0.81	0.85	--	0.50	0.73

TCWV Trends (kg m^{-2} $decade^{-1}$)

Dataset	ERA5	MERRA2	JRA-55	MWR	GPS-RO	GNSS
Global	0.38±0.06	0.36±0.05	0.37±0.05	--	0.44±0.14	0.39±0.14
Ocean	0.45±0.06	0.39±0.05	0.38±0.05	0.43±0.06	0.44±0.16	--
Land	0.19±0.06	0.30±0.08	0.32±0.07	--	0.29±0.16	0.33±0.16

v7.0, and GPS-RO). Over land (Fig. 2.28c), TCWV was well above average, but ranked as the second- to fourth-wettest year in four datasets (ERA5, JRA55, GNSS, and GPS-RO) where 2016 holds the record. MERRA-2 ranked 2023 as the wettest. All global anomalies exceeded the linear trend estimate for 2023, coinciding with the El Niño–Southern Oscillation (ENSO) transition to a strong El Niño (see section 4b for details). This contrasts with 2021 and 2022 anomalies, when La Niña conditions prevailed, which were below the linear trend.

On average, moist anomalies were mainly located along the equatorial Pacific Ocean and in a C-shaped pattern extending from the east coast of equatorial Africa to China in the north and into the southern Indian Ocean to the south (Plate 2.1k; Fig. 2.29a). These patterns are typical of El Niño states (Fig. 2.29b; Timmermann et al. 2018), where 2023 resembled other strong October–December El Niños (e.g., 1997 [Fig. 2.29c] and 2015 [Fig. 2.29d]). Similar to 2015, several regions experienced wetter-than-average conditions in 2023 (central Africa, northern North America, Europe, and the Middle East), while other regions experienced drier-than-average conditions, leading to rainfall deficiencies and droughts (Australia and Indonesia, northwest and southwest Africa, and Brazil).

Global mean TCWV variations are strongly constrained by lower tropospheric temperature (LTT) variations following the Clausius-Clapeyron relation, with a typical rate of change in water vapor of ~7% per 1°C (O'Gorman and Muller 2010). This tight relation holds at interannual and longer time scales. The global TCWV trends lie between 0.36 kg m^{-2} $decade^{-1}$ and 0.44 kg m^{-2} $decade^{-1}$ (Table 2.7) or 1.30% $decade^{-1}$ and 1.67% $decade^{-1}$, considering a global mean TCWV of 26.3 kg m^{-2}. When related to the median LTT trend of ~0.18°C $decade^{-1}$ to 0.22°C $decade^{-1}$ reported in Table 2.3, the estimated rate of change of water vapor is in the range 7.6%–9.3% per °C, which is consistent with the Clausius-Clapeyron relation given the uncertainty in the trend estimates (Po Chedley et al. 2023). Superposed on the long-term trend are positive and negative excursions, which coincide with the warm (e.g., 1998 and 2016) and cold (e.g., 2021 and 2022) phases of ENSO.

This assessment used observations from satellite-borne microwave radiometers over the oceans (RSS TPW v7.0; Mears et al. 2018), GPS-RO observations from several satellite missions (Ho et al. 2020; Shao et al. 2023), both over land and oceans, and ground-based GNSS observations over land and islands (Bock 2022). Three global reanalysis products were used: ERA5 (Hersbach et al. 2020), MERRA-2 (Gelaro et al. 2017), and JRA-55 (Kobayashi et al. 2015). All three reanalyses assimilate satellite microwave radiometer data (in the form of radiances) and GPS-RO data (in the form of bending angles), but not ground-based GNSS measurements, which serve as an independent validation dataset.

There is reasonable agreement across datasets, both on interannual timescales and trends in the base period (1991–2020), but this deteriorates prior to 1991 (Figs. 2.28a–c) and in some extreme El Niño years (1997/98, 2010, 2015/16; Figs. 2.28b,c). The divergence from the linear trend and significant scatter between reanalyses prior to 1993 may be due to changes in the global observing system (Allan et al. 2014). Differences in the observations assimilated, in the assimilation systems, as well as in model physics, may all contribute to differences in the reanalysis products, especially in data-sparse regions and in the pre- and early-satellite era (before 1980). Few validation datasets are available prior to 1993. The microwave radiometers included here do not diverge from the linear trend (Fig. 2.28b), suggesting common structural inhomogeneities in the reanalyses. Furthermore, TCWV over land in ERA5 has been low since 2020 (Fig. 2.28c), almost halving the linear trend estimate compared to other datasets (Table 2.8). Comparison with ground-based GNSS data (Plate 2.1k) reveals that ERA5 has a widespread dry bias of 0.5 kg m^{-2}–1 kg m^{-2} in the tropical land areas and smaller wet anomalies (~0.5 kg m^{-2}) in the midlatitudes, consistent with a previous version of the reanalysis (Bock and Parracho 2019). MERRA2 also exhibits a dry bias of ~1 kg m^{-2}, mainly located over the Maritime Continent, which is compensated in the global mean by small wet biases in other regions (not shown).

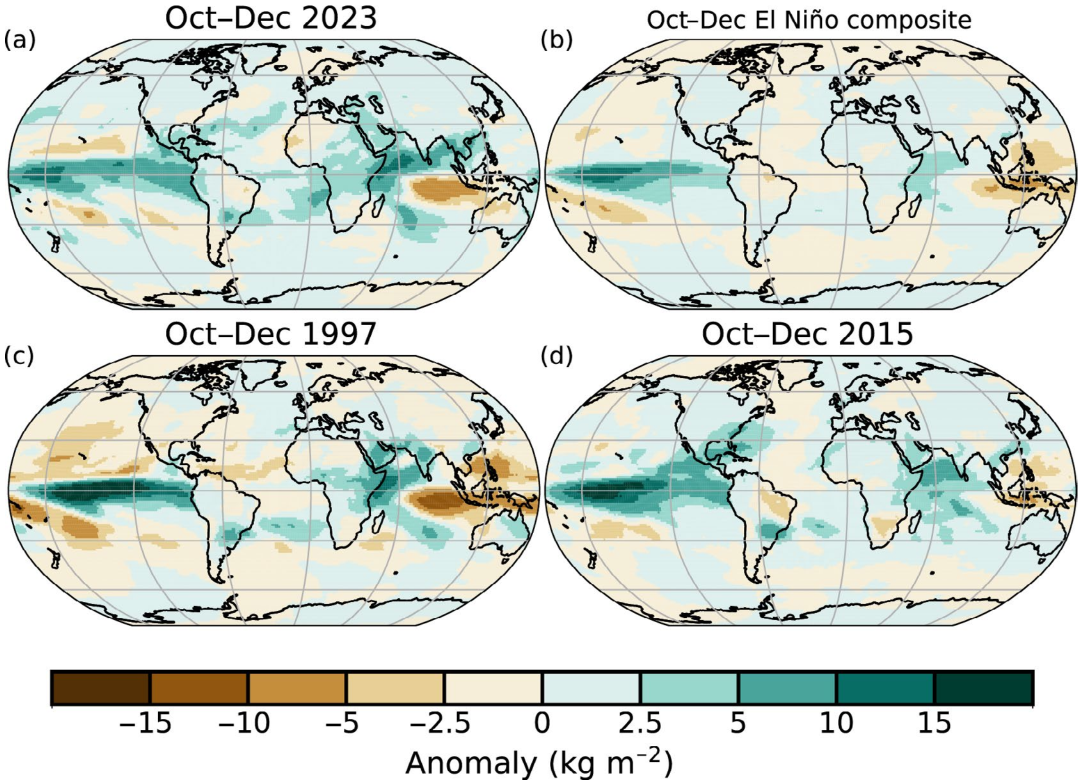

Fig. 2.29. (a) Oct–Dec 2023 mean total column water vapor (TCWV) anomaly from ERA5, compared to (b) Oct–Dec composite for six strong (1957, 1965, 1972, 1987, 1991, 2023) and three very-strong (1982, 1997, 2015) El Niño events (according to the Oceanic Niño Index from NOAA's Climate Prediction Center) and two individual recent very-strong events in (c) 1997 and (d) 2015. Units are given by kg m^{-2}.

4. UPPER-TROPOSPHERIC HUMIDITY

—V. O. John, L. Shi, E.-S. Chung, R. P. Allan, S. A. Buehler, and B. J. Soden

In 2023, the global mean upper-tropospheric humidity (UTH) anomaly, shown using relative humidity in Fig 2.30a, was slightly above normal in the first half of the year but below in the second half. The UTH exhibited expected behavior during El Niño, with regions of large drier-than-average relative humidity anomalies at subtropical latitudes over the Pacific Ocean. These were only partly balanced by more-than-humid anomalies near the equator (McCarthy and Toumi 2004), as depicted in Plate 2.1l. The mean and standard deviation of the global monthly anomalies in 2023 were −0.08±0.32%rh for the microwave-based data (Chung et al. 2013), 0.03±0.32%rh for the infrared-based data (Shi and Bates 2011), and −0.24±0.59%rh for ERA5 reanalysis data (Hersbach et al. 2020).

All datasets show near-zero and statistically insignificant global mean trends, which is in line with the theoretical consideration that the large-scale relative humidity in the upper troposphere remains approximately constant (Ingram 2010); however, this does not mean that the absolute humidity (amount of water vapor) in the upper troposphere remains unchanged in a warming upper troposphere. This is illustrated in Fig 2.30b, which shows the difference between mid-to-upper-tropospheric mean layer temperature (MSU T2; Zou et al. 2023) and the measured brightness temperature of the 6-µm water vapor channel (HIRS T12), which is sensitive to the upper-tropospheric relative humidity. The mid-to-upper-tropospheric mean layer temperature is derived from the brightness temperature of the 60-GHz oxygen channel. As the change of oxygen concentration is insignificant, the emission level in the troposphere of the oxygen channel remains constant and, therefore, the measurements correctly reflect tropospheric warming (Simmons 2022), and the time series of the measurements shows a positive trend (not shown, see tropospheric mean temperature in section 2b5). If there were no change in water vapor amount in the mid-to-upper troposphere, the time series of the upper-tropospheric water vapor channel would have a similar positive warming trend, and the time series of the difference between the two should have a nearly zero trend. On the contrary, the difference time series shows a positive trend. This is because as the amount of water vapor in the upper troposphere (UT) increases, the emission level of the water vapor channel shifts higher in the troposphere and measures water vapor emissions with a lower temperature, diverging from the oxygen emission levels. Therefore, the trend in the difference time series is from the moistening of the UT (Soden et al. 2005; Chung et al. 2014). The 2023 differences were larger than any other points within the record, pointing to record-high UT absolute humidity (water vapor).

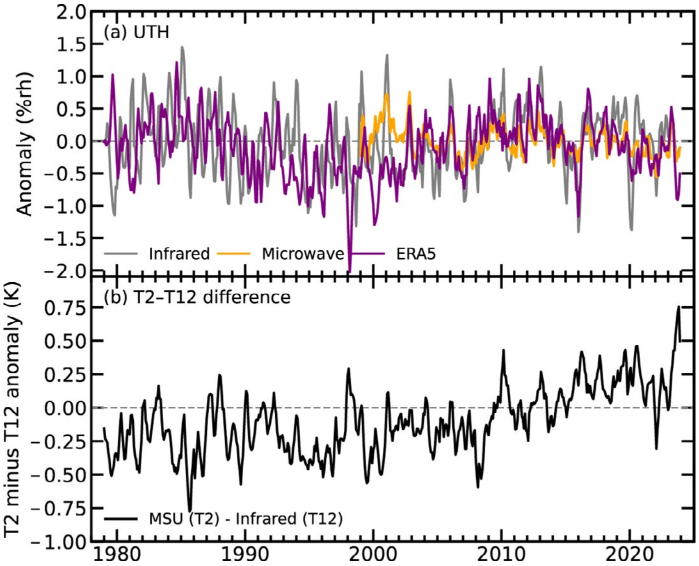

Fig. 2.30. Time series of (a) global monthly mean anomaly upper-tropospheric humidity (UTH) for the three datasets (%rh; see text for details) and (b) the difference between upper-tropospheric temperature (T2) and water vapor channel (T12) brightness temperatures (K). Anomalies are with respect to the 2001–20 base period.

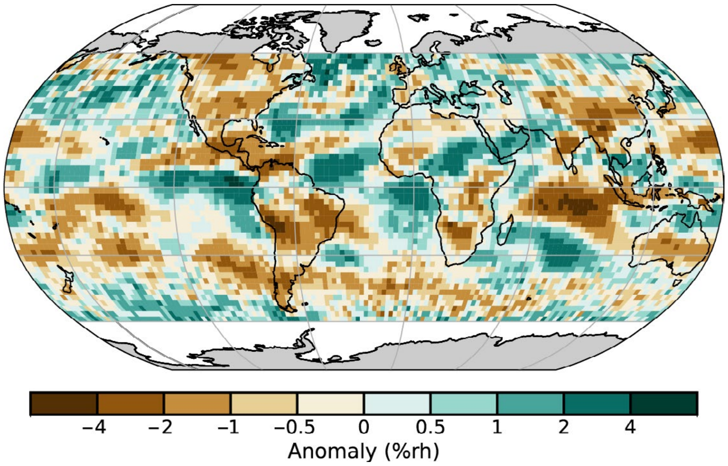

Fig. 2.31. Upper-tropospheric humidity anomaly map (%rh) for 2023 from the infrared data record (2001–20 base period).

Plate 2.1l shows the annual average anomaly map of relative UTH in 2023 derived from the microwave data, and the infrared equivalent is shown in Fig 2.31. The UTH anomalies reflect the large-scale circulation patterns. El Niño-like features were clearly represented, with a large positive anomaly in the eastern Pacific. The strong positive phase of the Indian Ocean dipole can also be seen. Here, the cooler-than-normal eastern Indian Ocean and warmer-than-normal western Indian Ocean led to reduced convection in the east and enhanced convection into the west. There were generally dry conditions over the North and South American continents, and moistening signatures in the UT over Africa.

5. PRECIPITATION

—R. S. Vose, R. Adler, G. Gu, X. Yin, and M. Ziese

Precipitation over global land areas in 2023, as estimated from two different monitoring products, was much below the 1991–2020 long-term average (Fig. 2.32a). In particular, the gauge-based product from the Global Precipitation Climatology Centre (GPCC; Becker et al. 2013) had an anomaly of –31.5 mm for 2023 (GPCC land mean is 780 mm), and the blended gauge–satellite product from the Global Precipitation Climatology Project (GPCP; Adler et al. 2018) had an anomaly of –28.1 mm. Both products indicate that mean global land precipitation in 2023 was much lower than in 2022 and that 2023 was one of the driest years on record (i.e., from 1979 to present). In contrast, precipitation over the global ocean (Fig. 2.32b) was 9.7 mm above the long-term average, according to the GPCP product, which resulted in near-average precipitation for the globe as a whole (Fig. 2.32c).

Over the global land surface, the highest positive precipitation anomalies in 2023 were concentrated in relatively small areas, including equatorial Africa and eastern Asia, though larger regions such as Europe and northern Asia were also wetter than the long-term average. The biggest negative precipitation anomalies over land were spread across a broad swath of the Americas (especially over the Amazon basin) as well as parts of southern Europe, southern Africa, southern Asia, and most of Australia (Plate 2.1m). Over the global oceans, high positive precipitation anomalies were apparent across the northern Indian Ocean, the western Pacific Ocean, and along the Pacific Intertropical Convergence Zone (ITCZ, the narrow band of heavy precipitation across the tropical Pacific just north of the equator). In contrast, large negative precipitation anomalies were evident over much of the southern Indian Ocean and the eastern Pacific Ocean (except along the ITCZ as noted above).

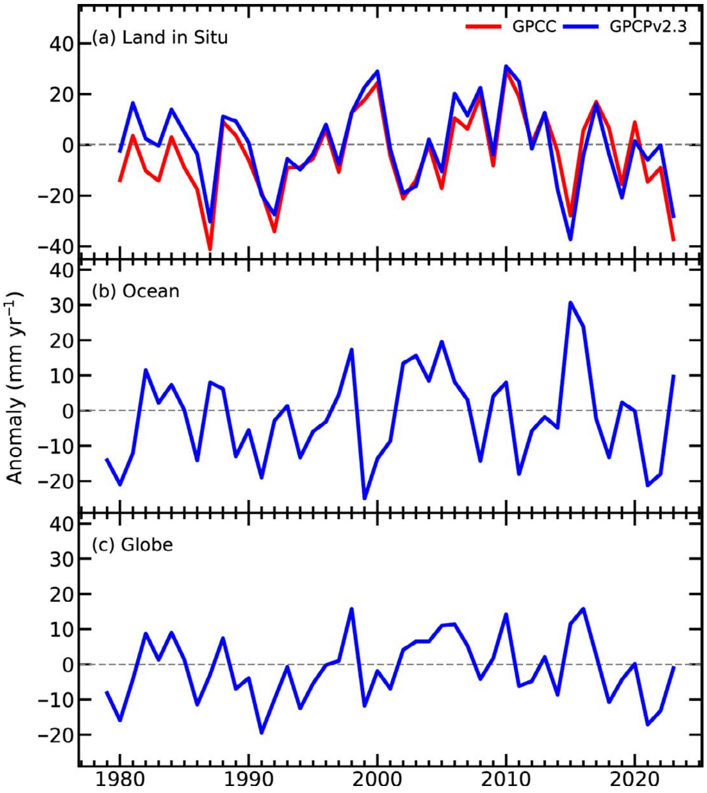

Fig. 2.32. Globally averaged precipitation anomalies (mm yr^{-1}) relative to the 1991–2020 base period over (a) land areas, (b) ocean areas, and (c) the globe. Land and ocean time series were created using a proportional land/sea mask at the 1° × 1° scale.

Consistent with the transition from La Niña to El Niño, anomaly patterns evolved substantially over the course of the year. The pattern for January–March contained a number of typical La Niña features (e.g., a large rainfall deficit over the central equatorial Pacific, a V-shaped positive anomaly over the Maritime Continent, a mostly dry Indian Ocean), but other typical features were absent (e.g., the Amazon was not wet), likely because La Niña was weakening. The pattern for April–June included positive anomalies along the Pacific ITCZ and in the western Pacific, a reflection of the emergence of El Niño. This trend continued to develop from July through December, with the strong El Niño pattern arising by the last three months of the year (e.g., negative anomalies in northern South America, southern Africa, and Australia). The establishment of the El Niño pattern was associated with occurrences of floods and landslides, for example, over Somalia and eastern Africa, and the continuation of the drought over the Amazon.

6. LAND SURFACE PRECIPITATION EXTREMES

—M. R. Tye, S. Blenkinsop, M. G. Bosilovich, M. G. Donat, I. Durre, C. Lennard, I. Pinto, A. J. Simmons, and M. Ziese

The year 2023 transitioned from La Niña to strong El Niño conditions (see section 4b), intensifying one-day/accumulated five-day maxima (Rx1day/Rx5day) in regions surrounding the Pacific and Indian Oceans. Meanwhile, severe drought coincided with a reduction in extreme precipitation over the Amazon basin. While global mean land precipitation was below the long-term (1991–2020) average (section 2d5), global mean Rx1day was close to average (Fig. 2.33). Positive one-day and/or five-day extremes covered large areas of Asia, Europe, northeastern Africa, and isolated locations in North and South America (Fig. 2.33; Plate 2.1n). Other heavy precipitation events were anomalous within regions surrounded by low precipitation (e.g., Brazil) or after long-lasting drought (e.g., Somalia). Some notable local meteorological extremes are listed below and in Appendix Table A2.1 but are not necessarily those with the greatest impact.

Here, Rx1day and Rx5day are derived from gauge-based (GHCNDEX; Donat et al. 2013; HadEX3, Dunn et al. 2020; GPCC, Ziese et al. 2022) and reanalysis (ERA5, Hersbach et al. 2020) data.

Late (January–March) and early (December) summers in Australasia brought notable precipitation extremes. Post-Cylone Gabrielle crossed New Zealand in February, bringing the wettest start to the year since records began (Murray 2023). In one location, 24-hour accumulations of 175.8 mm were recorded, more than three times the average February total. Northwestern Australia received record-breaking Rx5day in January and March. In December, ex-tropical Cyclone Jasper resulted in a concentration of record-breaking Rx1day and Rx5day over Queensland, with Rx5day exceeding 1000 mm at several locations, nearly triple previous records (Fig. 2.34), making Jasper the wettest tropical cyclone on record to affect Australia (Bureau of Meteorology 2024; Bowen et al. 2024; section 7h4).

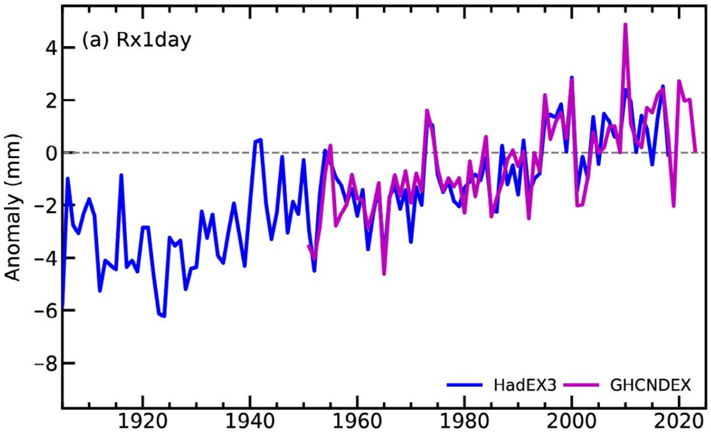

(b) GPCC Rx1day - Maximum 1 day precipitation total

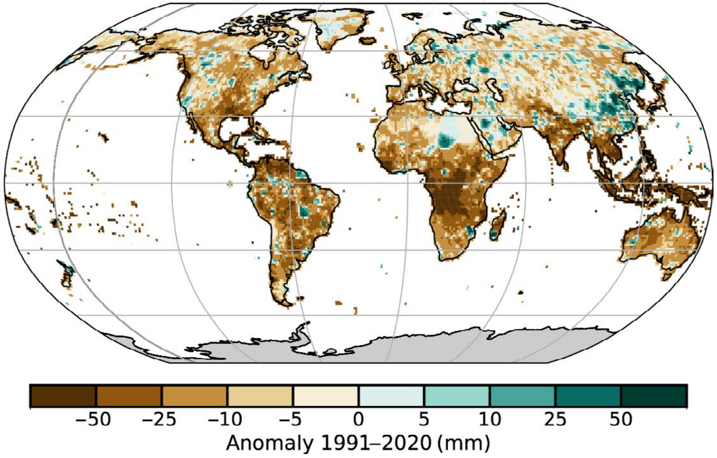

Fig. 2.33. (a) Global mean anomaly of Rx1day (mm) over land from HadEX3 (Dunn et al. 2020) and GHCNDEX gridded observations. (b) Global Rx1day anomalies (mm day^{-1}) in 2023 with respect to the 1991–2020 mean from the Global Precipitation Climatology Centre (GPCC).

Several notable events occurred over East Asia despite fewer-than-average western Pacific typhoons. Super Typhoon Betty (also named Mawar) brought flooding to the Philippines, Guam, and Japan in June, with record precipitation over Japan exceeded again in September. In July, Typhoon Doksuri generated intense precipitation over Beijing with many stations breaking records, while September's Typhoon Haikui generated record one-hour precipitation over Hong Kong.

The dominant modes of variability resulted in high storm and cyclone activity over the Indian Ocean (section 2e1). April–June monsoon rains included isolated exceptionally heavy events causing flash floods in Pakistan. Flood conditions were then exacerbated in India by Tropical Storm Biparjoy (see section 7g4). Cyclone Mocha brought flooding to Myanmar in May, while Tropical Cyclone Tej made landfall in Yemen in October. Long-term drought over East Africa was ended by exceptional flooding during October and November. Long-lived Tropical Cyclone Freddy compounded the effects from January's storm Cheneso over Madagascar, also bringing catastrophic flooding to Mozambique, Zimbabwe, and Malawi after causing damage and fatalities in Mauritius and

La Reunion (see Sidebar 4.2 for details). An extreme cut-off low-pressure system that was isolated from the main atmospheric flow over the Western Cape province of South Africa resulted in widespread flooding, with many stations reporting record daily rainfall amounts during the event, as well as record September totals.

In contrast, intense precipitation events around the Atlantic were isolated within exceptionally dry regions. In Africa, eastern Ghana experienced severe flooding during October. The area around São Paulo, Brazil, recorded its highest 24-hour precipitation totals in February, with high cyclone activity in September affecting Rio Grande do Sul. The percentage of the northeast United States with a much-greater-than-normal proportion of precipitation derived from extreme one-day precipitation was in the top 10th percentile of a 122-year record (NOAA NCEI 2024), although few events were record breakers. On the opposite coast, atmospheric rivers brought record precipitation to California in January–March (section 2d9), while Tropical Storm Hillary also brought persistent heavy rain to the southwest United States in August. In South America, Chile was affected by extreme precipitation in February, June, and, most significantly, August when a frontal system and atmospheric river coincided over the Ñuble region (section 2e1).

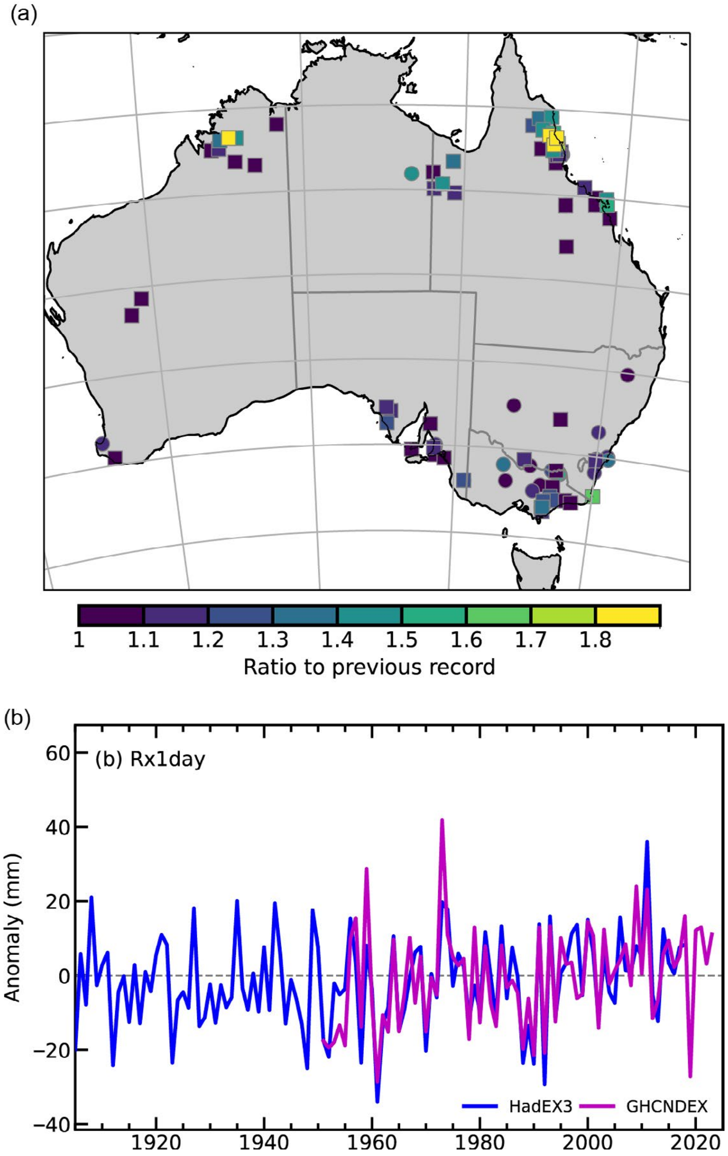

Fig. 2.34. (a) Ratio of new Rx1day (circles) and Rx5day (squares) records set over Australia in 2023 with respect to the previous record. (b) Regional mean anomaly of Rx1day (mm) over north Australia from HadEX3 and GHCNDEX gridded observations.

Storm Daniel formed in the eastern Mediterranean in September, causing flooding in Greece, Türkiye, and Bulgaria, resulting in the loss of at least 27 lives before making landfall in Libya. Here, 414.1 mm of rain was recorded over a 24-hour period in Bayda with an estimated 150 lives lost across the country. Other parts of Europe also experienced summer flooding and fatalities, including Italy in May, followed by a total of 60 new Rx1day and Rx5day records across Scandinavia, the Baltic States, Russia, and Slovenia in August.

7. CLOUDINESS

—C. Phillips and M. J. Foster

Global cloud area fraction in 2023 was 0.16% less than in 2022, the lowest fraction measured in the entire PATMOS-x record, which starts in 1980. A trend of −0.62% decade^{-1} has been observed since the start of the record, increasing the likelihood of record minimum years like 2023. This lower-than-average cloudiness (Plate 2.1o) was distributed globally, with the Indian Ocean, Arctic, and Northern Hemisphere land being especially low in cloudiness in 2023. In 2022, there was a notable increase over the equatorial western Pacific associated with La Niña (Phillips and Foster 2022) that did not appear in 2023 as La Niña ended and El Niño conditions emerged in Northern Hemisphere spring.

These PATMOS-x observations are consistent with independent measurements of cloud radiative effect (CRE) from CERES EBAF 4.2 (Loeb et al. 2018), which started in March 2000. Note that CRE is the "all sky" value minus the "clear sky only" value in this analysis. This shows a record-high global shortwave CRE annual mean anomaly (SWCRE, 1.20 W m^{-2}) and record-low global longwave CRE annual mean anomaly (LWCRE, −0.62 W m^{-2}) in 2023, relative to a 2000–20 base period (Fig. 2.35).

In most cases, the shortwave effect of clouds is to reflect sunlight, which results in cooling, whereas the longwave effect of clouds is to insulate the lower atmosphere, resulting in heating. The sign convention here is that positive anomalies imply heating, so the decrease of clouds in 2023 caused both heating by reflecting less sunlight (+1.20 W m^{-2}) and cooling by insulating less (−0.62 W m^{-2}). In absolute terms, the SWCRE is negative and the LWCRE is positive. The annual mean SWCRE of −44.53 W m^{-2} was the least negative on record, and the annual mean LWCRE of 27.28 W m^{-2} was the least positive on record. Hence, the effect of clouds could be considered weaker than average as both shortwave (negative) and longwave (positive) were closer to zero. This represents the continuation of a decade-long trend (Phillips and Foster 2022), leading to five of the weakest SWCRE and LWCRE years occurring in the past six years.

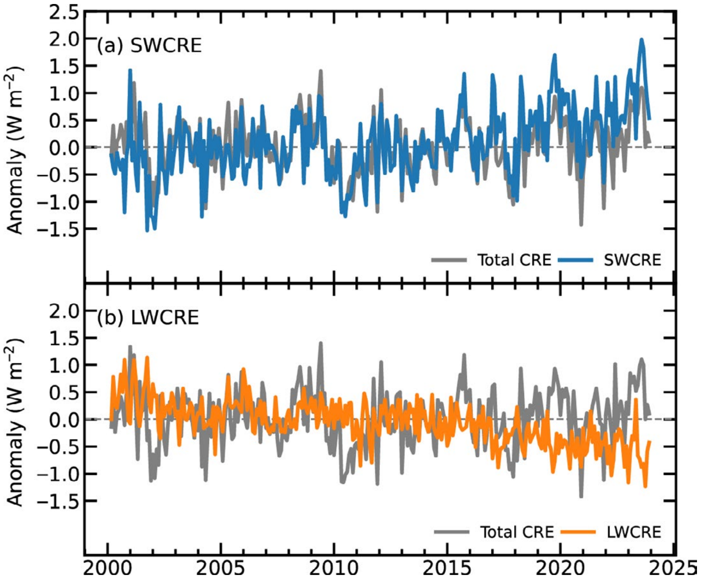

Fig. 2.35. Cloud radiative effect anomalies (W m^{-2}; 2000–20 base period) from CERES EBAF Ed4.2 (Loeb et al. 2018) representing the changes in top-of-atmosphere radiative forcing that are attributable to clouds (which could include both changes to clouds themselves and surface changes masked by clouds). Positive values indicate cloudiness-related warming through more radiation reaching the surface and less being reflected back out to space (shortwave cloud radiative effect [SWCRE]) or more being trapped close to the surface rather than escaping out to space (longwave cloud radiative effect [LWCRE]). Negative values indicate cloudiness-related cooling. Note that these are monthly anomalies whereas annual mean anomalies and absolute values are quoted in the main text.

Adding the shortwave and longwave CRE together, the annual mean total CRE in 2023 was record high at −17.25 W m^{-2} (0.58 W m^{-2} greater than the 2000–20 average). This means that, globally, clouds still had an overall cooling effect, but it was the weakest global cooling effect of any year measured. Unlike its components, total CRE does not exhibit a significant trend—the global long-term deviations SWCRE and LWCRE appear balanced. Related analysis of the radiative flux and energy budget can be found in section 2f1.

The El Niño–Southern Oscillation transitioned from La Niña in January to El Niño in May. Hence, for analysis, 2023 is split into two periods: January–April and May–December. Figures 2.36a–d show the average anomalies (relative to 1991–2020; deseasonalized) for PATMOS-x cloud area fraction compared to a composite of all La Niñas and El Niños. Composites use the thresholds of Multivariate ENSO Index version 2 <−1 for La Niña and >1 for El Niño. The January–April and May–December averages show good agreement with the La Niña and El Niño composites, respectively. The La Niña cloud climate is characterized by about 5% more cloud cover over the Maritime Continent (MC) and about 5% less cloud cover directly to the east. During El Niño, anomalies are typically stronger, with up to 10% less MC cloud cover and 10% more cloud cover over the rest of the equatorial Pacific.

These anomalies in the PATMOS-x cloud area fraction are mirrored by CRE anomalies (from CERES EBAF Ed4.2, Figs. 2.36e–h). Regions with decreased cloud fraction are correlated with negative LWCRE anomalies and positive SWCRE anomalies, meaning that in absolute terms, these CRE quantities are closer to zero. For the most part, these large anomalies are balanced such that total CRE is unaffected. The strongest anomalies for the total CRE (not shown) are located off the coast of Ecuador, where both the SWCRE and LWCRE are positive (heating) during the El Niño period from May to December 2023.

PATMOS-x v6.0 provides twice-daily observed cloud products, including cloud area fraction, from each satellite from the set of NOAA Polar Orbiting Environmental Satellite series and

EUMETSAT Polar System (Foster et al. 2023). Producing a global cloud area fraction anomaly necessitates combining these individual observations into a single value representing the diurnal average. This is done by averaging the data for every observed local hour, month of the year, and gridbox to produce a joint diurnal-seasonal-regional climate average. This multidimensional average can be indexed for any individual observation to find the expected bias compared to the desired reference, which is then subtracted out. CERES EBAF Ed4.2 is an energy-balanced-and-filled dataset with top-of-atmosphere radiative flux derived from the CERES instruments onboard the Aqua, Terra, and NOAA-20 satellites (Loeb et al. 2018).

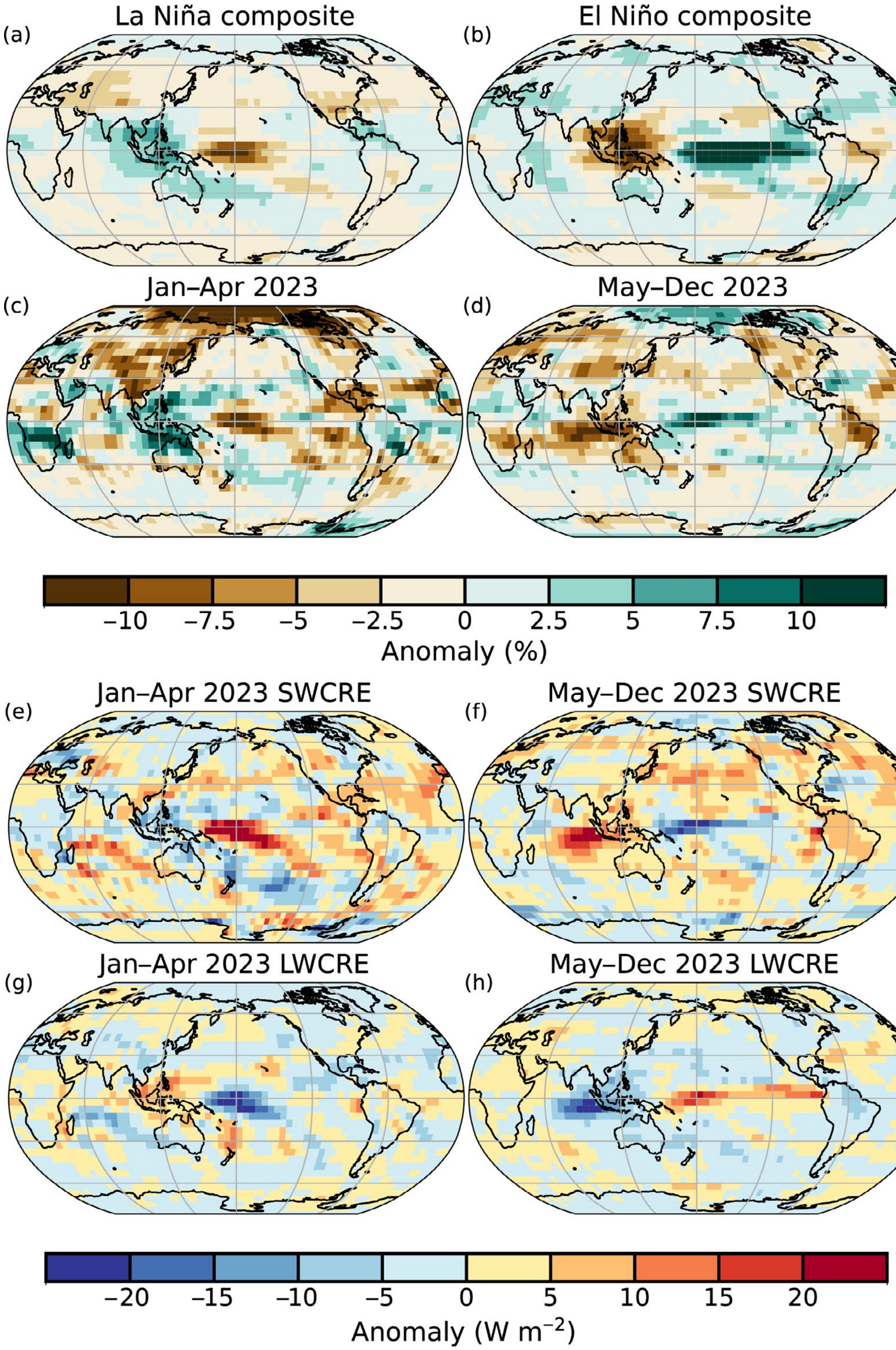

Fig. 2.36. (a) La Niña and (b) El Niño cloud area fraction anomaly composite compared to time averages for (c) Jan–Apr 2023 and (d) May–Dec 2023, respectively (%). PATMOS-x v6.0 composite cloud area fraction anomaly from 1991 to 2022. (e),(f) CERES EBAF-TOA Ed4.2 shortwave cloud radiative effect (SWCRE) anomalies and (g),(h) longwave cloud radiative effect (LWCRE) anomalies (W m^{-2}) for 2023 relative to 2000–20. All anomalies are implicitly deseasonalized.

8. LAKE WATER STORAGE

—M. E. Harlan, B. M. Kraemer, T. V. King, R. S. La Fuente, and M. F. Meyer

Water storage data for 5764 of the world's lakes, provided by a recently published dataset (GloLakes; Hou et al. 2024), reveals a complex picture of hydrological shifts in 2023 (Plate 2.1p). Cumulative lake water storage (LWS) was 1.2% higher in 2023 compared to the baseline period of 1991–2020, demonstrating a slight increase over average historical conditions. Collectively, the lakes with rising LWS increased by a total of 4828 million cubic meters (MCM) whereas those with declining LWS decreased by 2624 MCM. This led to a net increase of 2204 MCM in 2023 (Fig. 2.37). Notably, 64% of the lakes analyzed exhibited higher-than-average water levels relative to their 1991–2020 baseline, reflecting a partial reversal of the recently reported decline in global LWS (Yao et al. 2023; Fig. 2.38). These global, yet heterogenous anomalies underscore the influence of varying climatic and anthropogenic factors on LWS, including precipitation patterns, evaporation rates, and water management practices (Yao et al. 2023; Zhao et al. 2022).

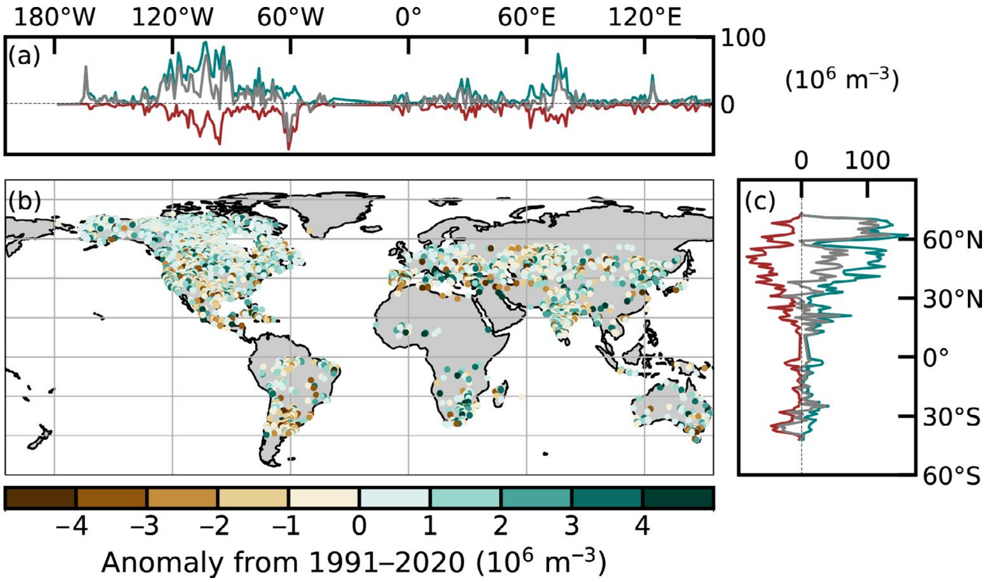

Fig. 2.37. Volumetric water level anomalies (× 10^6 m^3) relative to 1991–2020. The latitudinal and longitudinal insets show the cumulative increase (teal), cumulative decrease (brown), and the net change (gray) across one-degree latitudinal and longitudinal bins.

Excessive LWS fluctuations caused by droughts or floods can have major implications for the availability of essential resources like drinking water, irrigation, food, energy, and transportation, and they pose significant socio-economic challenges (Zohary and Ostrovsky 2011). Importantly, excessive fluctuations in lake volume can also cause considerable ecosystem disturbances, affecting key physical processes, community composition, and biodiversity (Jeppesen et al. 2015), underscoring the need for sustainable water management and conservation strategies in the face of changing global conditions.

While most LWS anomalies were positive, some countries, including Argentina, Algeria, Morocco, Spain, and Türkiye, experienced widespread decreases in lake water volume, with reductions ranging from 10% to 35%. Conversely, Mali, Cambodia, Australia,

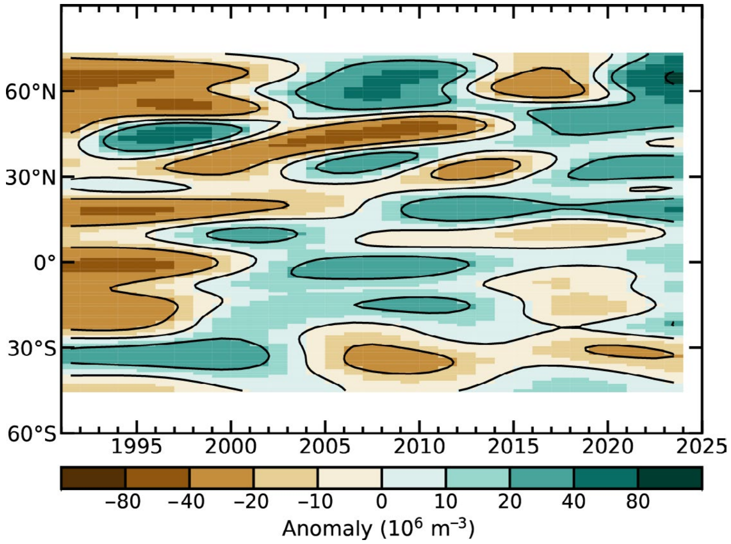

Fig. 2.38. Long-term change in volumetric water level anomalies (× 10^6 m^3) relative to the 1991–2020 mean for each one-degree latitudinal bin. Values are smoothed with a General Additive Model to aid in visualization where the cumulative lake storage anomaly was modeled as a function of an interactive smoothing function between both year and latitude.

South Africa, and India saw their lake volumes increase on average by 43%. The positive LWS anomalies at 60°N observed here contrast with reported water losses at these latitudes due to permafrost thaw (Webb et al. 2022), although previous analyses focused on 2000–20 trends rather than 2023 relative to a baseline of 1991–2020.

To identify changes in lake levels, we used the "GloLakes" lake and reservoir storage dataset (Hou et al. 2024), which combines altimetry and reflectance satellite data across Landsat (Pekel et al. 2016), ICESat2 (Jasinski et al. 2023), the Global Reservoirs and Lakes Monitor (Birkett et al. 2011), and Sentinel-2 (https://www.blue-dot-observatory.com/) to estimate LWS over recent decades. The data were generated using a geostatistical model (Messager et al. 2016) paired with innovative gap-filling methods (Hou et al. 2022). Here, we relied on a subset of the lakes from GloLakes (5764) with data from at least 20 years in the period of 1991 through 2023, with no more than a three-year gap of observations and at least three observations of lake storage in 2023. While the GloLakes dataset allowed us to expand our analysis from altimetry-based water levels in previous reports that focused solely on altimetry data (Kraemer et al. 2022) to include lake water storage, and to include many more lakes (5764 lakes compared to 264 in 2022), the dataset is still restricted in its spatiotemporal coverage. Additionally, the incorporation of optical remote sensing adds challenges such as those posed by clouds, atmospheric interferences, and vegetation, potentially reducing the accuracy of water detection. These challenges could be further mitigated in future years using technologies like passive microwave sensors, synthetic-aperture radars, and wide-swath altimetry (e.g., the Surface Water and Ocean Topography mission).

9. GROUNDWATER AND TERRESTRIAL WATER STORAGE

—M. Rodell and D. N. Wiese

Various regions of the world experienced large increases or decreases in terrestrial water storage (TWS) in 2023, with the global mean approaching a 21-year low. Changes in mean annual TWS between 2023 and 2022 are plotted in Plate 2.1q. Europe, which has been in a state of drought more often than not since 2019, experienced a partial respite in 2023, with TWS increasing slightly across much of the continent while remaining below the long-term average. TWS in parts of southeastern Asia declined from above normal to below normal, while wetness across the rest of Asia, excluding the ever-receding Caspian Sea, remained fairly stable.

Heavy rains in March caused flooding and contributed to TWS increases that exceeded 12 cm across a large area of northern Australia, with some parts experiencing record highs. Total water storage has been well above normal across most of sub-Saharan Africa since 2019, and 2023 was no different, with wet weather raising TWS, especially in the Congo River basin. This multi-year wet event is by far the most intense worldwide (in terms of extent, duration, and TWS anomaly) since satellite observations of TWS changes began in 2002 (Rodell and Li 2023). To the south, drought caused water-level declines across a region centered near the southeastern corner of Angola.

In North America at the start of the year, atmospheric rivers delivered heavy rains to California and parts of adjacent states, resulting in floods and reservoirs being filled to capacity. Despite this, TWS remained near or slightly below the long-term mean in southern California because the slowly recharging aquifers have not fully recovered after years of drought and an associated heavy reliance on groundwater for crop irrigation (Liu et al. 2022). Drought caused TWS to decrease to record lows in central and southern Canada and contributed to their worst year for wildfires on record. Drought also affected TWS in southern Mexico and the central Mississippi River basin, the former which continued into a second year. In South America, a major drought caused TWS to decline by more than 12 cm over a large area of the Amazon River basin, leading to record lows for both that basin and South America as a whole. Northern Argentina and Uruguay also saw water levels decline. On the other hand, a swath of southern Brazil gained a large amount of water.

Deseasonalized time series of monthly zonal-mean and global-mean TWS anomalies are plotted in Figs. 2.39 and 2.40. Data gaps occur when satellite observations are not available. Excluded from the calculation of these means are regions where TWS declines are dominated by ice sheet and glacier ablation: Antarctica, Greenland, the Gulf Coast of Alaska, polar islands, High Mountain Asia, alpine western Canada, and the southern Andes. Land in the zone between about 25°N and 45°N has been drying gradually (roughly 0.5 cm yr^{-1} to 1.0 cm yr^{-1} on average) since the early 2000s, if not before, and that tendency seems to have gained momentum in recent years. This drying aligns with droughts in the central United States and Europe and the long-term declines of the Caspian Sea and groundwater levels in northern India. The latter two are ultimately attributable to agricultural irrigation (Rodell et al. 2018). A zone of elevated TWS between about 8°S and 15°N first appeared around 2019 and persisted in 2023. At its root is the ongoing wet event in sub-Saharan Africa, while contributions from excess TWS in eastern Brazil and southern India abated in 2023. Just south of that latitude band, TWS returned to normal levels within a ~10° latitude zone after having been low during the preceding four years. That zone includes wetting regions of Argentina and Uruguay, southern Africa, and northern Australia as seen in Plate 2.1q. Figure 2.40 shows that in 2023, global mean TWS, excluding ice sheet and glacier losses, reached its second lowest level since 2002, as declines in northern Brazil, Canada, Mexico, southeastern Asia, the Caspian Sea, and elsewhere outweighed gains in Africa, California, northern Australia, and southern Brazil. The three lowest levels of global mean, non-ice TWS—in 2016, 2023, and 2019—all occurred during El Niño events.

Since 2002, TWS anomalies have been derived from Gravity Recovery and Climate Experiment (GRACE) and GRACE Follow-On (GRACE-FO) satellite observations of Earth's time-varying gravity field (Tapley et al. 2004; Landerer et al. 2020). In situ networks do not observe the components of TWS (groundwater, soil moisture, surface waters, snow, and ice) with sufficient density to infer regional to global changes, hence the reliance on remote sensing. Uncertainty in the monthly TWS anomaly observations is about 1 cm–2 cm equivalent height of water over a 500,000 km^2 region at midlatitudes (Wiese et al. 2016). Groundwater is commonly the largest component of variations in TWS over periods longer than a year and outside of the humid tropics (surface water) and high-latitude and alpine regions (ice and snow; Getirana et al. 2017).

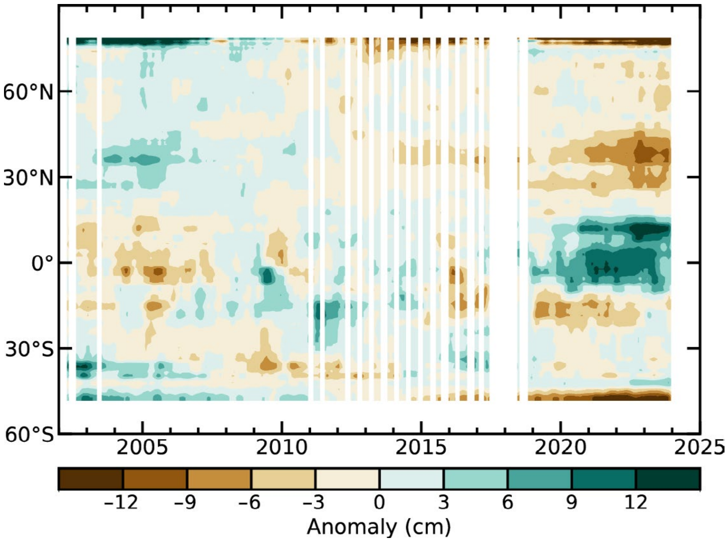

Fig. 2.39. Zonal means of monthly terrestrial water storage anomalies, excluding those in Antarctica, Greenland, the Gulf Coast of Alaska, polar islands, and major glacier systems (e.g., High Mountain Asia, alpine western Canada, and the southern Andes), in cm equivalent height of water, based on gravity observations from the Gravity Recovery and Climate Experiment (GRACE) and Gravity Recovery and Climate Experiment Follow-On (GRACE-FO). The anomalies are relative to a 2003–20 base period.

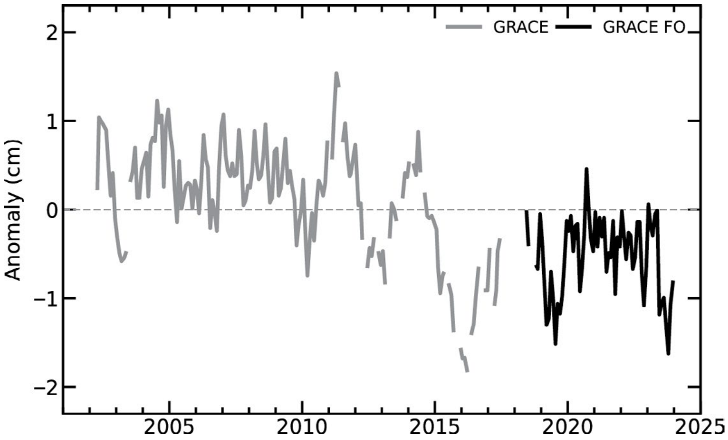

Fig. 2.40. Global average terrestrial water storage anomalies from the Gravity Recovery and Climate Experiment (GRACE; gray) and Gravity Recovery and Climate Experiment Follow-On (GRACE-FO; black), excluding those in Antarctica, Greenland, the gulf coast of Alaska, polar islands, and major glacier systems (e.g., High Mountain Asia, alpine western Canada, and the southern Andes), in cm equivalent height of water, relative to a 2003–20 base period.

10. SOIL MOISTURE

—M. Hirschi, P. Stradiotti, W. Preimesberger, R. van der Schalie, T. Frederikse, D. Duchemin, N. Rodriguez-Fernandez, A. Gruber, S. Hahn, W. A. Dorigo, R. A. M. de Jeu, S. I. Seneviratne, and R. Kidd

Due to its importance in the water, energy, and carbon cycles, soil moisture plays a crucial role in the land–atmosphere interaction (Seneviratne et al. 2010), with impacts on surface air temperature, precipitation generation, and extreme events such as heatwaves and forest fires. The increase in global soil moisture observed over the previous four years (van der Schalie et al. 2022; Stradiotti et al. 2023) reversed in 2023, and the soil moisture values declined back to 2020 levels (Fig. 2.41). While soil moisture in the Northern Hemisphere remained at a similar level to 2022, soil moisture in the Southern Hemisphere strongly decreased after the recent pronounced wetting tendency that began in 2020. This may be a sign of the transition of the ENSO from La Niña to El Niño conditions that occurred in 2023 (see section 4b). This transition is consistent with the occurrence of more widespread below-average soil moisture conditions in the Southern Hemisphere in 2023 (Fig. 2.42; e.g., Zhang et al. 2023). Accordingly, soil moisture in the Southern Hemisphere shifted from a wet to a dry anomaly in 2023, while soil moisture in the Northern Hemisphere remained slightly wetter than normal. Overall, the global soil moisture conditions were close to the 1991–2020 average.

Wetter-than-normal conditions were present throughout most of the year in northern Australia, with wet anomalies that were particularly widespread in January, April, and July (up to 200% of normal in some places; Plate 2.1r, Appendix Fig. A2.6). Similarly strong wet anomalies were also observed in southern and northwestern India, particularly from January to July. Also, parts of East Asia experienced noticeable wetter-than-normal conditions in 2023, similar to 2022. In the Horn of Africa, the drought conditions of 2022 gave way to wet anomalies around March, which intensified again in November due to heavy rain (e.g., Kimutai et al. 2023; section 2d6). This change from a long-term drought in the region to flooding coincided with a switch of the Indian Ocean dipole (IOD) from a negative to positive mode in 2023 (see section 4f). This mode is associated with above-average rainfall in East Africa (Nicholson 2017; Marchant et al. 2007; see also section 2d5). Further areas of above-average soil moisture were also noticeable in parts of eastern Europe and Central Asia, in Türkiye, and in the western United States. Northeast Brazil

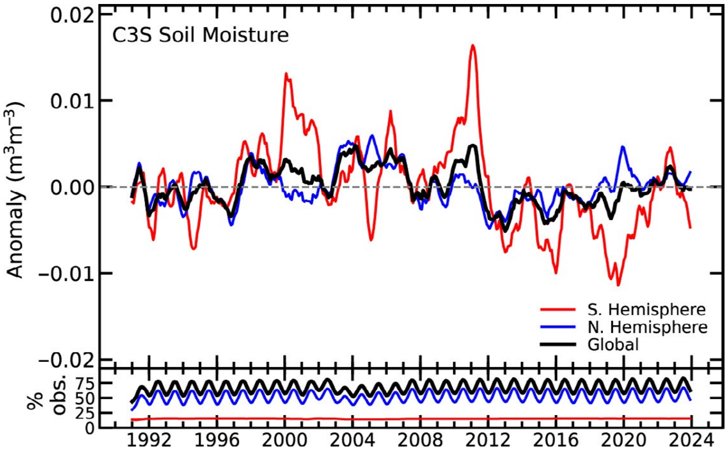

Fig. 2.41. (top) Time series of global (black), Northern Hemisphere (blue), and Southern Hemisphere (red) monthly surface soil moisture anomalies (m³ m⁻³) for the period 1991–2023 (1991–2020 base period) and (bottom) the valid observations as a percentage (%) of total global land surface. Data are masked where no retrieval is possible or where the quality is not assured and flagged, for example due to dense vegetation, frozen soil, permanent ice cover, or radio frequency interference. (Source: Copernicus Climate Change Service [C3S] Soil Moisture.)

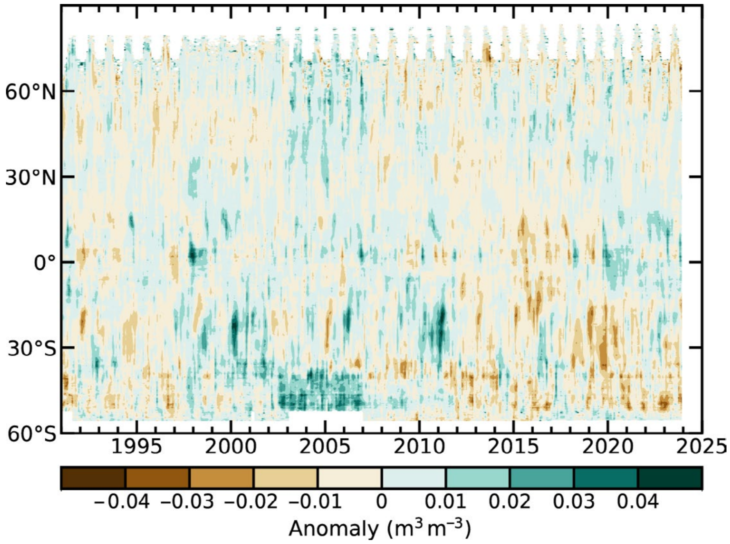

Fig. 2.42. Time–latitude diagram of monthly surface soil moisture anomalies (m³ m⁻³; 1991–2020 base period). Data are masked where no retrieval is possible or where the quality is not assured and flagged, for example due to dense vegetation, frozen soil, permanent ice cover, or radio frequency interference. (Source: C3S Soil Moisture).

started the year with strong wet anomalies that persisted for most of the year, while in the central and southeast part of the country, severe below-normal conditions started to emerge at the end of 2023 (e.g., Clarke et al. 2024; see section 7d2).

In contrast to these regionally confined wet soil moisture anomalies of 2023, dry conditions were observed in numerous regions (Plate 2.1r). The most pronounced dry anomaly was observed in southern South America, especially in the River Plate basin and Patagonia (below 50% of normal soil moisture in some areas). This region has been suffering from a multi-year drought since 2019 (Naumann 2021). Pronounced dry conditions also persisted in the Canadian Prairies for the third consecutive year (see section 7b1; van der Schalie et al. 2022; Stradiotti et al. 2023). Although soil moisture remained below normal, drought conditions in the Great Plains of central North America weakened in 2023 compared to 2022. Mexico experienced drier-than-normal conditions during June–September (Appendix Fig. A2.6). Similarly, below-normal soil moisture was observed in southwestern Africa (including South Africa and Namibia), with the most pronounced dry anomalies recorded from February to May. Many of the regions around the Mediterranean Sea (including Spain, northern Morocco, Algeria, and Tunisia) also experienced moderately dry conditions in 2023. In addition, widespread mild-to-moderate negative soil moisture anomalies were observed over much of inland China, southern Central Asia, northern Asia, and in the higher latitudes in general. In southeast Australia, the strong positive soil moisture anomalies of 2022 (Stradiotti et al. 2023) turned into widespread dry anomalies covering most of the southern part of the continent (except for parts of Victoria), but with intermittent periods of wetter-than-normal conditions in January, April, June, and July.

Soil moisture was observed by microwave satellite remote sensing of the surface soil layer down to approximately 5-cm depth, as provided by the COMBINED product of the Copernicus Climate Change Service (C3S) version 202212 (Dorigo et al. 2023). C3S combines multi-sensor data in the 1978–2023 period through statistical merging (Dorigo et al. 2017; Gruber et al. 2017, 2019). Wet and dry anomalies here refer to the deviation from the 1991–2020 climatological average. Note that changes in spatiotemporal coverage (also between product versions, e.g., resulting from the inclusion of additional sensors) can introduce uncertainties in the domain-averaged soil moisture time series (e.g., Bessenbacher et al. 2023).

11. MONITORING GLOBAL DROUGHT USING THE SELF-CALIBRATING PALMER DROUGHT SEVERITY INDEX

—J. Barichivich, T. J. Osborn, I. Harris, G. van der Schrier, and P. D. Jones

The self-calibrating Palmer Drought Severity Index (scPDSI; Wells et al. 2004; van der Schrier et al. 2013) over the period 1950–2023 shows that the increasing trend in severity and extent of global drought, which has been ongoing since mid-2019 (Barichivich et al. 2020, 2021, 2022), reached a new historical peak during the second half of 2023 (Fig. 2.43). During June–September, extreme drought conditions (scPDSI ≤−4) surpassed 7% of the global land area for the first time in the record, peaking at a new historical maximum of 7.9% in July. Similarly, the extent of severe plus extreme drought conditions (scPDSI ≤−3) in 2023 exceeded 16% of the global land area for the first time during the same period, reaching a historical maximum of 16.8% in July. Moderate or worse drought conditions (scPDSI ≤−2) peaked in September at a historical maximum of 29.7% of the global land area.

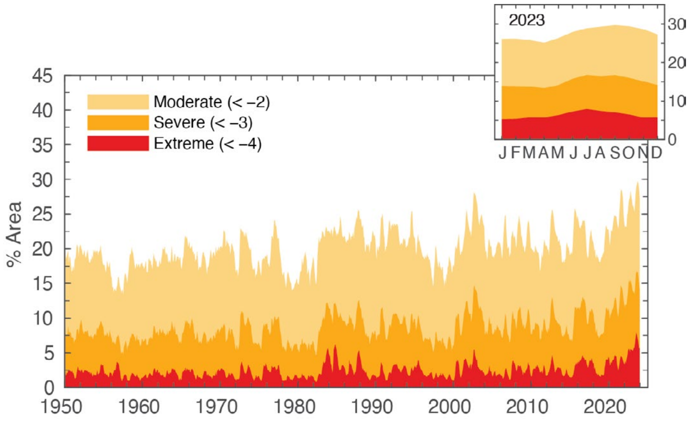

Fig. 2.43. Percentage of global land area (excluding ice sheets and deserts) with self-calibrating Palmer Drought Severity Index (scPDSI) indicating moderate (≤−2), severe (≤−3), and extreme (≤−4) drought for each month during the period 1950–2023. Inset: each month of 2023.

The global pattern of regional droughts seen in 2022 largely persisted through 2023, with the most extensive severe-to-extreme drought conditions occurring over South America, parts of North America, the Mediterranean, and the midlatitudes of Asia (Plate 2.1s). Drought severity eased through western North America and parts of northern and eastern Europe but worsened in tropical South America and the midlatitudes of Asia (Fig. 2.44). In western North America, California experienced a shift from dry to wet conditions, but the overall west–east moisture contrast observed across the United States since 2017 continued as Arizona and New Mexico were under moderate drought (Plate 2.1s). Moderate drought conditions also affected Mexico and Central America. In South America, El Niño conditions during the latter half of 2023 led to extremely wet conditions in coastal areas of Peru and extreme drought through the Amazon basin to the La Plata basin and central Chile. By the end of October, the Rio Negro at Manaus, a major tributary of the Amazon River (Barichivich et al. 2018), fell to its lowest water level since records began in 1902. The megadrought of central Chile reached its 14th consecutive year in 2023, but an increase in winter rainfall broke the drought in the south-central part of the country (section 2d5).

Although precipitation was above normal in parts of northern, central, and eastern Europe in 2023 (section 2b5), most of the southern part of the continent, particularly countries around the Mediterranean, continued under severe-to-extreme drought (Plate 2.1s). In northern Africa, previous extreme drought conditions along the Mediterranean coast from Morocco to Tunisia continued through 2023 (Plate 2.1s). Most of the Middle East from eastern Türkiye to Pakistan also saw a continuation of severe-to-extreme drought conditions.

Although uncertain due to sparse in situ data, moisture patterns in Africa did not change much in 2023 (Plate 2.1s). Tropical Africa saw a continuation of moderate wet conditions that were observed since 2019. Southern Africa saw a continuation of drought conditions that began in 2018, and its severity remained mostly as moderate. In Australia, drought eased in many northern regions, was sustained in the southwest, and worsened in the easternmost parts during 2023; some parts of the country continued under moderate drought (Plate 2.1s). Wet conditions seen through most of India and southeast Asia in 2022 continued during 2023. In contrast, severe-to-extreme drought conditions extended farther through China, Mongolia, and Kazakhstan. Previous severe-to-extreme drought continued through part of northeastern Siberia (Plate 2.1s).

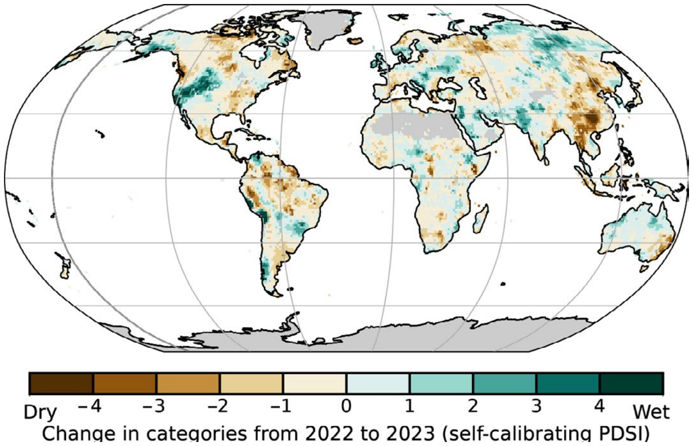

Fig. 2.44. Change in drought categories from 2022 to 2023 (mean self-calibrating Palmer Drought Severity Index [scPDSI] for 2023 minus mean scPDSI for 2022). Increases in drought severity are indicated by negative values (brown) and decreases by positive values (green). No calculation is made where a drought index is meaningless (gray areas: ice sheets or deserts with approximately zero mean precipitation).

Hydrological drought results from a period of abnormally low precipitation, sometimes exacerbated by a concurrent increase in evapotranspiration (ET). Its occurrence can be apparent in reduced river discharge, soil moisture, and/or groundwater storage, depending on the season and duration of the event. Here, the scPDSI is calculated, using gridded global precipitation and Penman-Monteith Potential ET from an early update of the CRU TS 4.08 dataset (Harris et al. 2020). A simple water balance at the core of the scPDSI estimates actual evapotranspiration, soil moisture content, and runoff based on the input precipitation and potential loss of moisture to the atmosphere. Estimated soil moisture categories are calibrated over the complete 1901–2023 period to ensure that "extreme" droughts and pluvials (wet periods) relate to events that do not occur more frequently than in approximately 2% of the months. This calibration affects direct comparison with other hydrological cycle variables in Plate 2.1s that use a different baseline period.

12. LAND EVAPORATION

—D. G. Miralles, O. M. Baez-Villanueva, A. Koppa, O. Bonte, E. Tronquo, F. Zhong, and H. E. Beck

Understanding the spatial and temporal dynamics of evaporation is crucial for agriculture and water management, as well as for diagnosing the influence of short-term climate variability and long-term climate trends on water resources. The year 2023 saw a mix of positive and negative evaporation anomalies across different regions, reflecting a complex interplay of meteorological variables and land surface processes (Plate 2.1t). Notably, semiarid regions of Australia, South America, and North America experienced negative anomalies, particularly towards the end of the year, consistent with the reversal of La Niña to El Niño conditions (Martens et al. 2018; Miralles et al. 2014). Meanwhile, positive anomalies were prevalent over the U.S. East Coast, most of Europe, boreal latitudes, tropical forests, and large parts of India and China. These anomalies mostly reflected regional climatic conditions, with high temperatures driving increased evaporation rates over the U.S. East Coast and Europe (section 2b1), while in tropical forests, positive anomalies were mostly attributed to enhanced precipitation (section 2d4), which increased interception loss, a primary component of evaporation in forested regions. Similarly, in northern India, positive anomalies correlated with higher-than-usual precipitation volumes. The high regional heterogeneity underscores the need for continued monitoring of evaporation for agriculture and water management applications. For example, in semiarid regions experiencing negative anomalies, such as parts of Australia and the Americas, decreased evaporation reflects reduced water availability (section 2d9), with potential implications for crop yields and freshwater security. Conversely, in regions with positive anomalies, like central Europe and parts of Asia, higher-than-usual evaporation rates may contribute to decreased water resources in following dry seasons.

Despite El Niño conditions usually being associated with lower-than-usual global mean evaporation due to the occurrence of persistent droughts in several global regions (Miralles et al. 2014), the average evaporation values in 2023 reached unprecedented high levels due to the high air temperatures (section 2b1), marking the highest on record for the Northern Hemisphere and the globe as a whole (Fig. 2.45). The global mean evaporation in 2023 was above the linear trend of +0.5 mm yr^{-1}, which can be attributed to positive anomalies in both hemispheres. The positive multidecadal trend has been attributed to the ongoing rise in global temperatures (Brutsaert 2017) and terrestrial greening (Yang et al. 2023; see also section 2h2). Arguably due to the positive temperature anomalies in 2023 in the Northern Hemisphere and tropics, particularly towards the end of the year (section 2b1), evaporation was consistently higher than usual in those latitudes (Fig. 2.46). Meanwhile, in the Southern Hemisphere, drought conditions led to negative anomalies in semiarid regions at latitudes between 25°S to 40°S during the second half of the year (Fig. 2.46).

In recent years, land evaporation has been gaining recognition as an essential climate variable by the World Meteorological Organization, and today multiple satellite-based approaches are advancing global evaporation monitoring. The results shown here correspond to the latest version of GLEAM, a set of algorithms dedicated to estimating evaporation based on satellite and reanalysis data (Miralles et al. 2011).

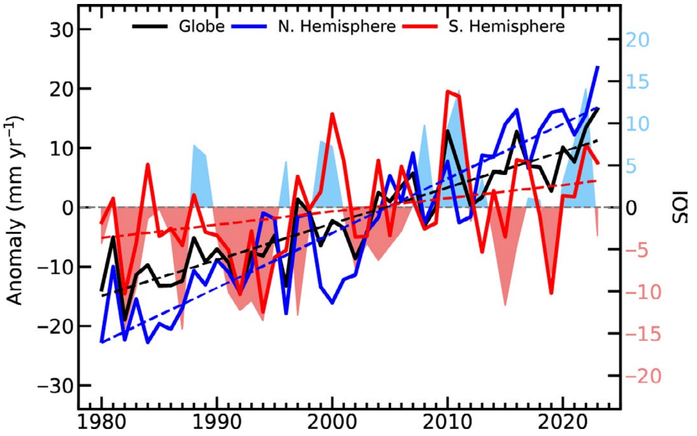

Fig. 2.45. Land evaporation anomaly (mm yr^{-1}; 1991–2020 base period) for the Northern Hemisphere, Southern Hemisphere, and the entire globe (blue, red, and black solid lines, respectively). Linear trends in evaporation (dashed lines) and the Southern Oscillation Index (SOI) from the Climatic Research Unit (right axis, shaded area) are also shown. (Source: Global Land Evaporation Amsterdam Model [GLEAM].)

Despite improvements in global evaporation monitoring in recent years, challenges persist, particularly those related to the accurate depiction of ecosystem responses to drought stress and the representation of interception loss in forests (Fisher et al. 2017; McCabe et al. 2019). Efforts to further advance land evaporation monitoring are ongoing, with future advancements expected to leverage emerging technologies from thermal missions like ECOSTRESS (Fisher et al. 2020) and TRISHNA (Lagouarde et al. 2018), as well as hyper-resolution optical remote sensing facilitated by cubesat constellations (McCabe et al. 2017). These innovations hold promise for enhancing our understanding of evaporation dynamics and their implications for water resources, climate, and ecosystems.

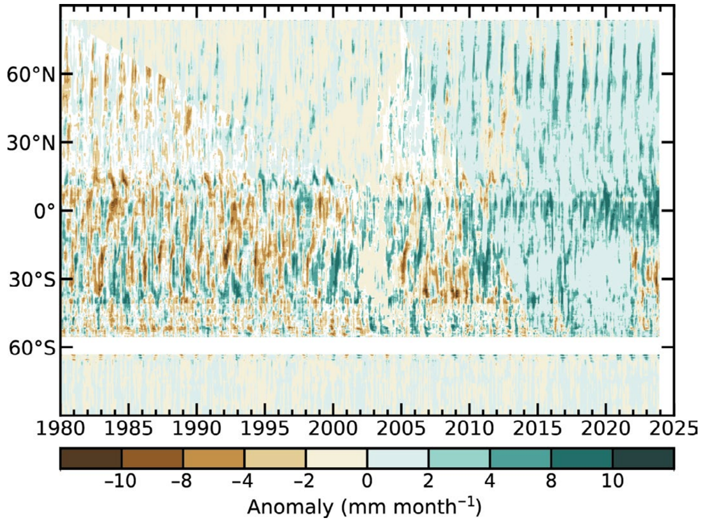

Fig. 2.46. Zonal-mean terrestrial evaporation anomalies (mm month^{-1}; 1991–2020 base period). (Source: Global Land Evaporation Amsterdam Model [GLEAM].)

e. Atmospheric circulation

1. MEAN SEA LEVEL PRESSURE AND RELATED MODES OF VARIABILITY

—B. Noll, D. Fereday, and D. Campos

Mean sea-level pressure (MSLP) variability is characterized by large-scale modes that drive weather and climate anomalies and extremes. These modes include the Arctic Oscillation, the North Atlantic Oscillation (NAO), and the Pacific/North American (PNA) in the Northern Hemisphere (NH) as well as the Southern Annular Mode (SAM)/Antarctic Oscillation in the Southern Hemisphere (SH; Kaplan 2011). Because of its direct impact in the tropics and important extratropical teleconnections to both hemispheres (Capotondi et al. 2015), the El Niño–Southern Oscillation (ENSO) is one of the most significant and well-tracked global climate drivers. ENSO can be described by the Southern Oscillation Index (SOI), the normalized MSLP difference between Tahiti and Darwin (Allan et al. 1996; Kaplan 2011).

The SOI was variable in early 2023, coinciding with a decaying La Niña, before turning consistently negative from July onward as El Niño became established (see section 4b). Early in the year, La Niña contributed to destructive floods and ex-tropical cyclones in New Zealand (see sections 4g8, 7h5), while the emerging El Niño contributed to seven consecutive months of record-breaking global warmth from June to December (section 2b1; C3S 2024), elevated wildfire activity in Canada (see section 7b1, Sidebar 7.1), and caused record-low annual maximum and minimum sea-ice extents in Antarctica (see section 6d). From June to August, the development of anomalous low pressure in the subtropical South Pacific, closely related to the strengthening El Niño, allowed an enhanced atmospheric river season across southern South America (e.g., Campos and Rondanelli 2023) and led to flooding in central Chile (DMC 2023a).

The Indian Ocean dipole (IOD) is an important mode of climatic variability in the Eastern Hemisphere (Saji et al. 1999). The positive IOD phase, which developed in September 2023 (see section 4f), comprises warm ocean temperatures in the tropical western Indian Ocean and cool ocean temperatures in the east. The IOD is often driven by ENSO via the Walker Circulation (Behera et al. 2006). The concurrent strongly positive IOD and El Niño contributed to Australia's driest three-month period of record from August to October 2023 (see section 7h4). It also strengthened the descending branch of the Walker Circulation over Indonesia and western Australia, which likely delayed the northern Australian monsoon (BoM 2024b; Lisonbee and Ribbe 2021).

In the NH, the NAO index was positive in January and February, consistent with mild winter conditions in Europe. Summer saw low pressure over the eastern United States, contributing to increased rainfall there (see section 7b2). A pressure dipole was seen over northwestern Europe, strongly projecting onto the summer NAO pattern (Fig 2.47c). This pattern is defined as the leading empirical orthogonal function (EOF) mode of variability in the North Atlantic/European region in July/August (Folland et al. 2009). The 2023 summer NAO index was the lowest in the time series back to 1959, in contrast to the second-highest value seen in 2022 (Fig 2.47e). Low pressure persisted across the North Atlantic, Europe, and east into Asia in autumn, and was associated with increased rainfall in these regions (see sections 2d5, 7f, 7g). Consistent with the positive ENSO phase in late 2023, the December PNA and NAO were both positive (Livezey et al. 1997; Ayarzagüena et al. 2018).

The SAM, which explains 22%–34% of the variability in extratropical SH atmospheric circulation (Fogt and Marshall 2020), was positive for 53% of days during 2023, fewer days than each year from 2020 to 2022. Annual MSLP was much above normal in the midlatitude South Pacific east of New Zealand and southwest of Australia, and below normal in the Bellingshausen Sea (Plate 2.1u; Fig. 2.48). Overall, this resembled the negative phase of the Pacific–South American (PSA) pattern (Irving and Simmonds 2016). The atmospheric circulation anomalies and blocking (e.g., Renwick and Revell 1999) associated with this pattern likely contributed to wetter conditions in northern New Zealand and the country's second-warmest year on record (see section 7h5) as well as to wetter conditions in late winter and spring over south-central Chile (see section 7d3). They also likely contributed to drier conditions in western and southern Western Australia (see section 7h4), as well as extremely low Antarctic sea-ice extent for most of the year (see section 6d), which was linked to strengthened westerly winds around the continent. This pattern was also associated with a stronger-than-normal subtropical jet stream extending from eastern Australia to Chile and Argentina (e.g., Montecinos et al. 2011). The negative phase of the PSA showed a statistically significant increasing trend on an annual basis from 1979 to 2014 and is consistent with positive trends in the SAM, making it an important SH diagnostic (Irving and Simmonds 2016).

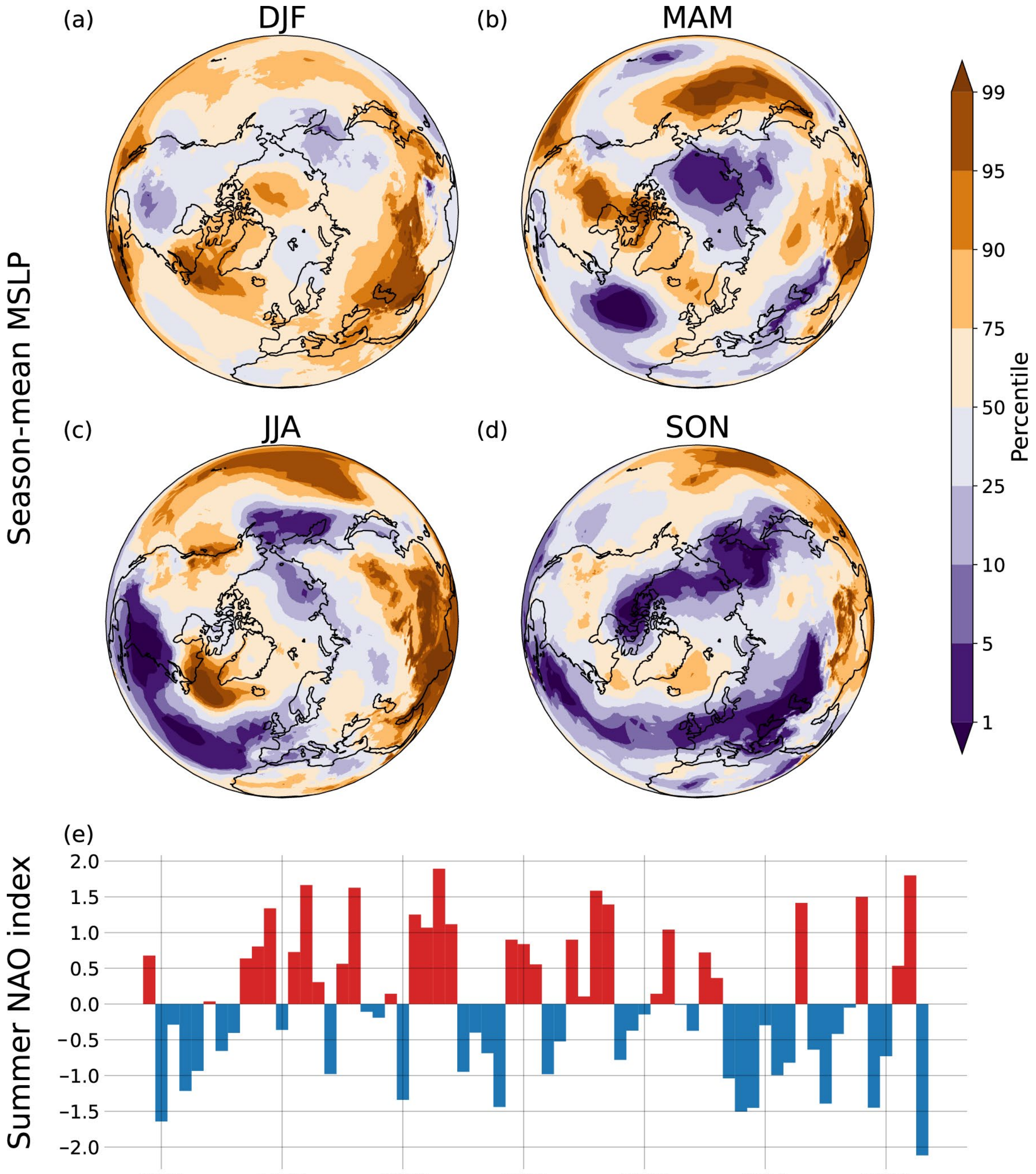

Fig. 2.47. Northern Hemisphere circulation in 2023. (a)–(d) seasonal mean sea level pressure (MSLP) anomalies with respect to the 1991–2020 base period, shown as percentiles based on the 1959–2023 period. (e) Jul/Aug summer North Atlantic Oscillation (NAO) index for the period 1959–2023 (Source: ERA5 [Hersbach et al. 2020].)

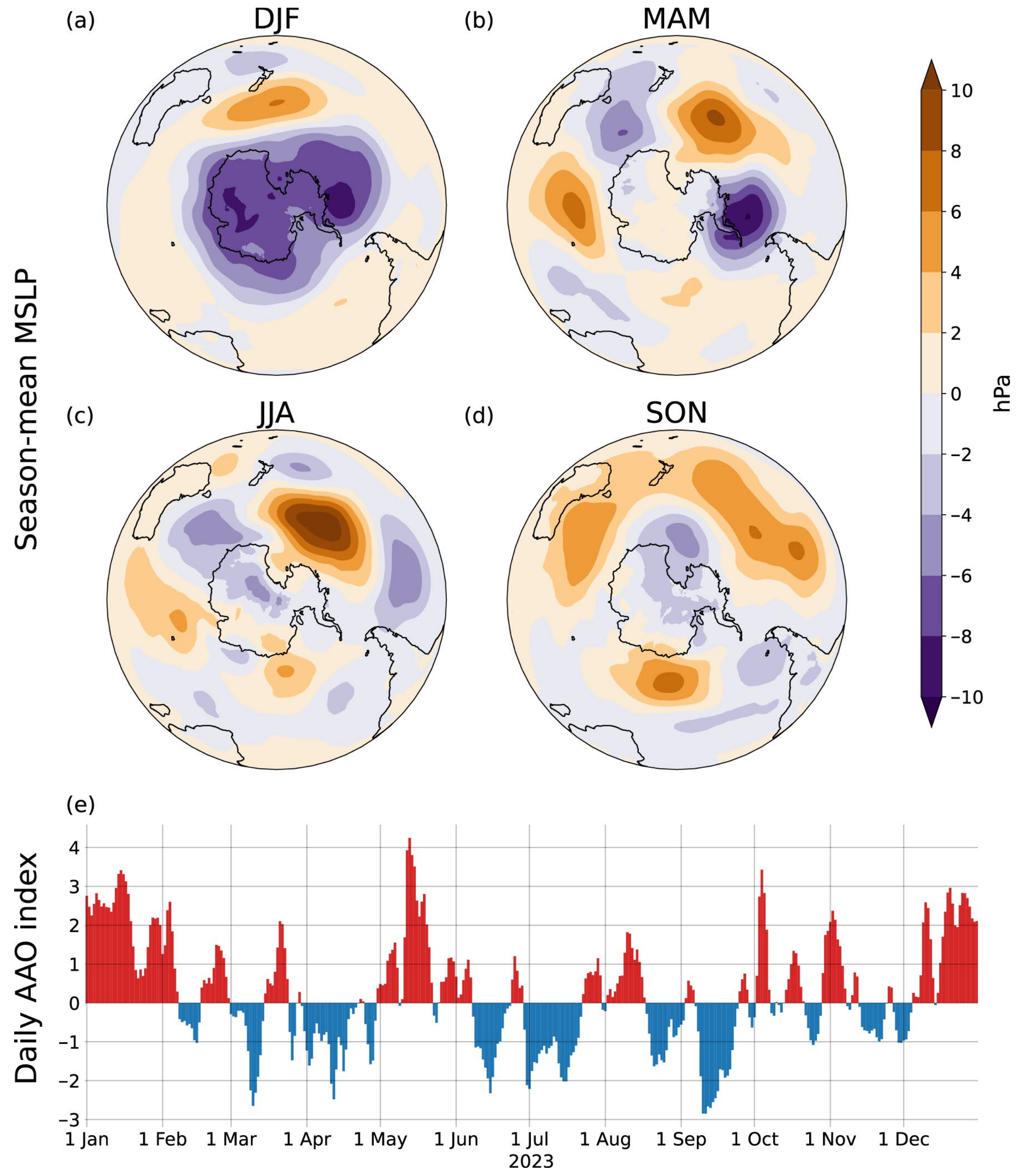

Fig. 2.48. Southern Hemisphere circulation in 2023. Seasonal mean sea-level pressure (MSLP) anomalies (hPa; 1991–2020 base period) for (a) DJF 2022/23, (b) MAM 2023, (c) JJA 2023, and (d) SON 2023. (Source: ERA5 reanalysis.) (e) Daily Antarctic Oscillation (AAO) index time series (Source: NOAA Climate Prediction Center.)

2. LAND AND OCEAN SURFACE WINDS

—C. Azorin-Molina, R. J. H. Dunn, L. Ricciardulli, C. A. Mears, J. P. Nicolas, T. R. McVicar, Z. Zeng, and M. G. Bosilovich

Annual mean wind speed at ~10 m above the ground was anomalously low over Northern Hemisphere lands in 2023 (−0.035 m s^{-1}) with respect to the 1991–2020 climatology (Table 2.8). This negative anomaly was primarily driven by the decline in winds observed in North America (−0.168 m s^{-1}) and, secondarily, in Europe (−0.011 m s^{-1}). This contrasts with the interhemispheric asymmetry of positive anomalies in South America (+0.145 m s^{-1}) and Central (+0.076 m s^{-1}) and East (+0.032 m s^{-1}) Asia (Plate 2.1v). After decades of "stilling" (McVicar et al. 2012), a weak "reversal" of winds occurred around the 2010s (Zeng et al. 2019) with almost neutral anomalies dominating the last decade (Fig. 2.49a). Moreover, the observed changes are dominated by a declining frequency of winds at >3 m s^{-1} (Fig. 2.49c) and particularly at >10 m s^{-1} (Fig. 2.49d), which in 2023 reached the third lowest frequency value during the 1973–2023 record.

The assessment of terrestrial surface wind speed anomalies, trends, and multidecadal variability is based on: 1) the HadISD3 observational dataset (1973–2023; Dunn et al. 2012, 2016, 2019) with stations selected for completeness; 2) the ERA5 reanalysis (1979–2023; Hersbach et al. 2020; Bell et al. 2021); and 3) the MERRA-2 reanalysis (1980–2023; Gelaro et al. 2017). Reanalyses underestimated anomalies and failed in reproducing the decadal variability of both the observed "stilling" and "reversal"; however, their agreement with station observations improved since the mid-1990s (Fig. 2.49b; e.g. Torralba et al. 2017; Wohland et al. 2019).

The average land wind speed has declined across the Northern Hemisphere over the last 45 years (−0.053 m s^{-1} decade^{-1} for the period 1979–2023), with a noticeable inter-hemispheric asymmetry of surface winds changes (Zha et al. 2021). Table 2.8 reports this opposite sign in trends between the northern continents, where the strongest negative trend is recorded in North America (−0.072 m s^{-1} decade^{-1}) and the strongest positive trend in South America (+0.052 m s^{-1} decade^{-1}). Due to the cessation of the "stilling" over the last decade, the global negative trend is of lesser magnitude compared to previous reports (Azorin-Molina et al. 2023a). The asymmetric trends between hemispheres are partly captured by the ERA5 reanalysis (Fig. 2.50a; Deng et al. 2021).

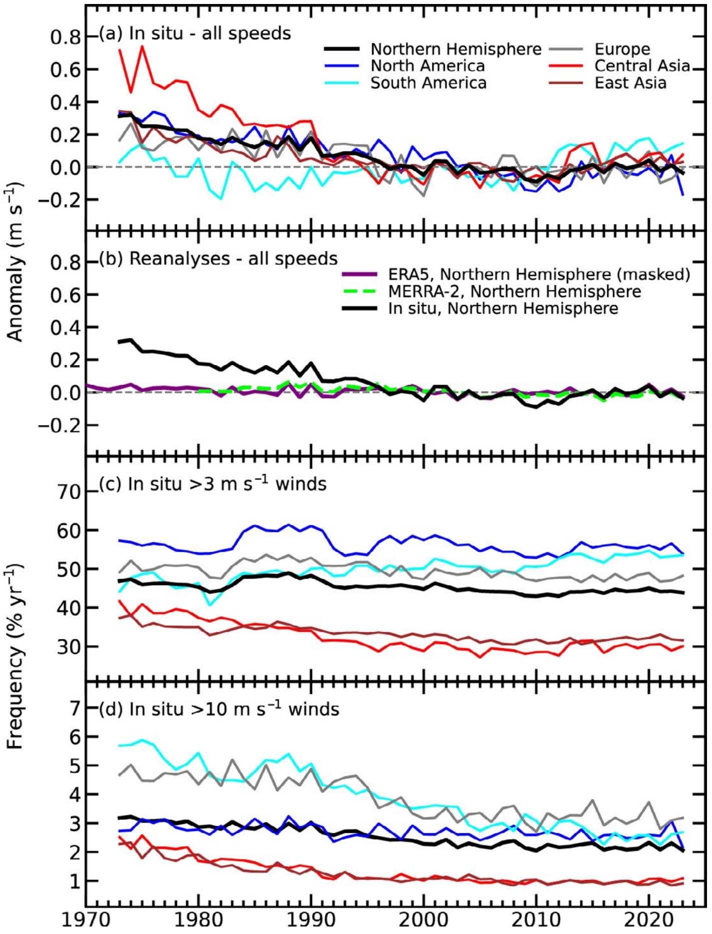

Fig. 2.49. Land surface Northern Hemisphere (20°N–70°N) and regional surface wind speed anomaly time series (m s^{-1}; 1991–2020 reference period): (a) HadISD3 observational dataset (1973–2023), (b) ERA5 (1970–2023 masked to only those grid boxes which contain one of the HadISD stations used in this section), and MERRA-2 (1980–2023 complete land surface) reanalyses. (c),(d) The HadISD3 occurrence frequencies (% yr^{-1}) for wind speeds (c) >3 m s^{-1} and (d) >10 m s^{-1}.

Table 2.8. Northern Hemisphere (20°N–70°N) and regional statistics for land surface wind speed (m s^{-1}) using the observational HadISD3 dataset for 1979–2023.

Region	Mean Wind Speed 1991–2020 (m s^{-1})	Wind Speed Anomaly 2023 (m s^{-1})	Wind Speed Trend 1979–2023 (m s^{-1} decade^{-1}), and 5th to 95th percentile confidence range	Number of stations
Northern Hemisphere	3.302	−0.035	−0.053 (−0.067 → −0.040)	2874
North America	3.642	−0.168	−0.072 (−0.086 → −0.053)	841
Europe	3.644	−0.011	−0.049 (−0.069 → −0.033)	931
Central Asia	2.738	+0.076	−0.069 (−0.105 → −0.041)	304
East Asia	2.711	+0.032	−0.027 (−0.042 → −0.013)	540
South America	3.452	+0.145	+0.052 (+0.036 → +0.071)	101

Changes in ocean surface winds for the period 1988–2023 were assessed using two products: 1) ERA5 and 2) satellite-based products as the merged radiometer winds (including Special Sensor Microwave/Imager [SSM/I], the Special Sensor Microwave Imager/Sounder [SSMIS], the Advanced Microwave Scanning Radiometer for the Earth Observation Satellite [AMSRE] and Advanced Microwave Scanning Radiometer 2 [AMSR2], Tropical Rainfall Measuring Mission's [TRMM] Microwave Imager [TMI], and WindSat), and the scatterometers Quick Scatterometer (QuikSCAT) and Advanced Scatterometer (ASCAT; Wentz 1997; Wentz et al. 2007, 2015; Ricciardulli and Wentz 2015; Ricciardulli and Manaster 2021), all processed at Remote Sensing Systems (RSS). Ocean wind speed anomalies were slightly negative in 2023: satellite radiometers (RSS, –0.055 m s^{-1}), satellite scatterometers (ASCAT, –0.038 m s^{-1}), and reanalyses (ERA5, –0.050 m s^{-1}, MERRA-2, –0.132 m s^{-1}; Fig. 2.51). Spatially (Plate 2.1v), there was a localized weak positive anomaly in the southern equatorial eastern Pacific, and a large negative anomaly in the tropical Atlantic, almost unprecedented over the past 30 years (2010 being the closest). The strong positive anomaly pattern seen in 2022 in the western and central equatorial Pacific Ocean (Azorin-Molina et al. 2023a) reversed to a weak negative pattern in 2023 (due to El Niño, albeit much weaker than in 1997 and 2015). Much smaller positive anomalies, or even negative ones, were observed in the Southern Ocean. Over the Indian Ocean, negative anomalies dominated except in a strip west of Sumatra. Due to the weak ocean surface winds in 2023, long-term trends (1988–2023) are of lesser magnitude with respect to previous reports (RSS Radiometers: <+0.1 m s^{-1} decade^{-1}; ERA5: +0.03 m s^{-1} decade^{-1} over 60°S–60°N) but have similar spatial patterns (Fig. 2.50a). Positive trends dominate over the south Pacific trade winds, the Southern Ocean, the Bering Sea, and near coastlines, while negative trends persist across midlatitude ocean areas and the whole Indian Ocean.

Widespread warm sea-surface temperatures (coincident with El Niño, sections 2b1, 2b3, 3b) might have weakened pressure gradients and driven negative wind speed anomalies in 2023. Changes in both land and

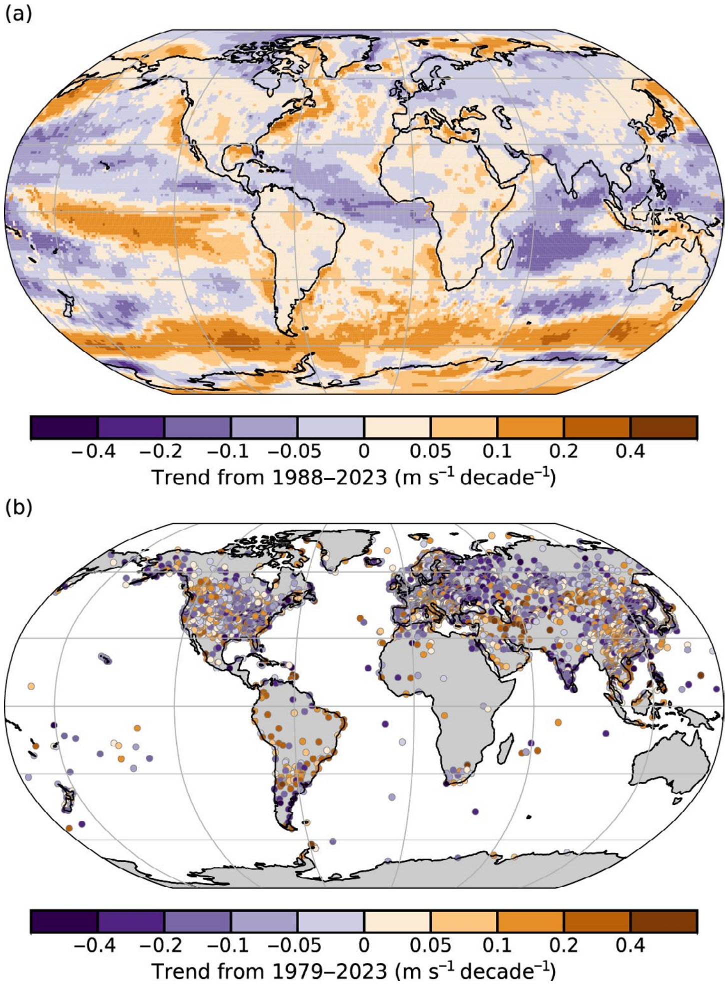

Fig. 2.50. Wind speed trends (m s^{-1} decade^{-1}) from the (a) ERA5 reanalysis output over land/ice and Remote Sensing Systems (RSS) satellite radiometers (Special Sensor Microwave/Imager [SSM/I], Special Sensor Microwave Imager / Sounder [SSMIS], Tropical Rainfall Measuring Mission's Microwave Imager [TMI], Advanced Microwave Scanning Radiometer 2 [AMSR2], Advanced Microwave Scanning Radiometer for the Earth Observing System [ASMR-E], and WindSat) over ocean for the period 1988–2023 (shaded areas) and (b) observational HadISD3 dataset over land (circles) for the period 1979–2023.

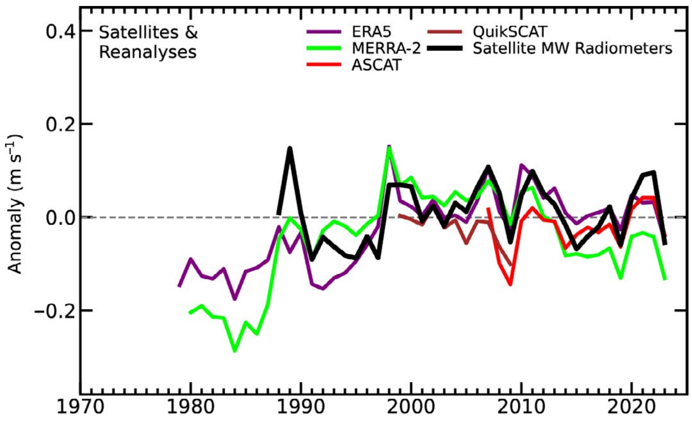

Fig. 2.51. Annual global mean wind speed anomalies (m s^{-1}; 1991–2020 baseline) over the ocean from satellite radiometers and scatterometers, ERA5, and MERRA-2 reanalyses.

ocean winds have been mainly attributed to decadal ocean–atmosphere oscillations characterized as the decadal variations of climate indices such as the tropical North Atlantic, North Atlantic Oscillation, and Pacific Decadal Oscillation (Zeng et al. 2019); however, changes in the pressure gradient (Zhang et al. 2021) forced by the anthropogenic warming partly explain the interhemispheric asymmetry with negative (positive) trends in the Northern (Southern) Hemisphere (Zha et al. 2021). Secondary drivers are linked to anemometer biases (Azorin-Molina et al. 2023b; Liu et al. 2024), encoding data issues (Dunn et al. 2022), and land cover changes (Minola et al. 2022).

3. UPPER AIR WINDS

—L. Haimberger, M. Mayer, P. Rohini, C. T. Sabeerali, V. Schenzinger, and O. P. Sreejith

Anomalies such as the El Niño–Southern Oscillation have profound impacts on upper-level circulation. Climate projections predict changes of upper-level wind patterns, such as the Hadley cell or jet stream intensity. Therefore, it is important to monitor the observed upper air winds. The 2023 global mean wind speed anomaly at 850 hPa (Fig. 2.52a) became negative (–0.1 m s^{-1}) in the second half of the year in a manner typical of El Niño conditions. Hence, linear trends decreased very slightly (0.02 m s^{-1} decade^{-1} to 0.04 m s^{-1} decade^{-1} for the period 1991–2023).

The Southern Annular Mode (SAM) Index (Marshal 2003) stayed high in 2023 (0.77) whereas the closely related Antarctic Oscillation index returned toward normal albeit still-positive values (0.24). This is consistent with the zonal 850-hPa wind speed anomalies between 70°S and 50°S (Fig. 2.52b), which were more than +1 m s^{-1} in the first and last months of the year (consistent with mostly positive values in this belt in Plate 2.1w), but were near zero or even slightly negative during austral winter. The positive wind speed trend in this latitude belt remained highly significant for the period 1991–2023, between 0.2 m s^{-1} decade^{-1} and 0.26 m s^{-1} decade^{-1}, consistent with section 2e1.

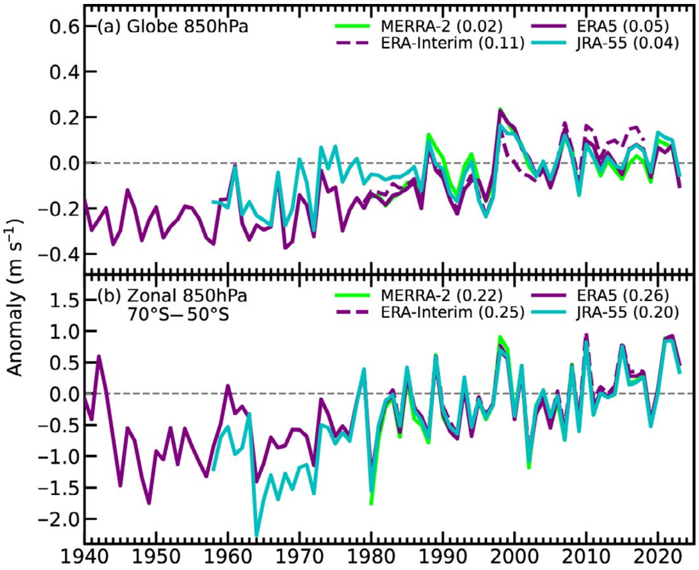

Fig. 2.52. Annual anomalies of (a) global mean, (b) 70°S–50°S belt mean wind speed (m s^{-1}; 1991–2020 base period) at 850 hPa from four reanalyses (ERA5 [Hersbach et al. 2020], ERA-Interim [Dee et al. 2011], MERRA-2 [Gelaro et al. 2017], and JRA-55 [Kobayashi et al. 2015]). The numbers in parentheses are linear trends in m s^{-1} decade^{-1} for the period 1991–2023. The ERA-Interim time series ends in 2019.

The pattern of strong easterlies (negative anomalies in a region with negative wind climatology) wind at 850 hPa over September–December in 2023 (Plate 2.1w; fourth strongest in 50 years over the area 60°E–90°E, 10°S–10°N, stronger only in 2019, 2010, 1997) over the equatorial Indian Ocean is related to both strongly positive Indian Ocean dipole (IOD) (see section 4f) and El Niño (see section 4b) indices during that time. Due to El Niño, the easterlies were weaker (positive anomalies) in the tropical central and east Pacific. There was a relatively prominent westerly wind anomaly (positive anomaly) over western and central Europe during the whole year, but it was strongest in the summer and autumn months, which likely contributed to above-average precipitation over west-central Europe at the same time.

We investigate the impact of major tropical climate anomalies on the upper-air divergent circulation by assessing the anomalous 200-hPa velocity potential in October–December (OND) 2023 (Fig. 2.53a). A strong positive anomaly was present over the Indo-Pacific warm pool, indicative of upper-air convergence and sinking motion associated with the strongly positive IOD and Oceanic Niño Index (ONI). Combined with ascending motion over the tropical west Indian Ocean and connected by strong anomalous easterly (negative) flows over the central Indian Ocean (Plate 2.1w), this anomaly resulted in strong zonal-vertical circulation.

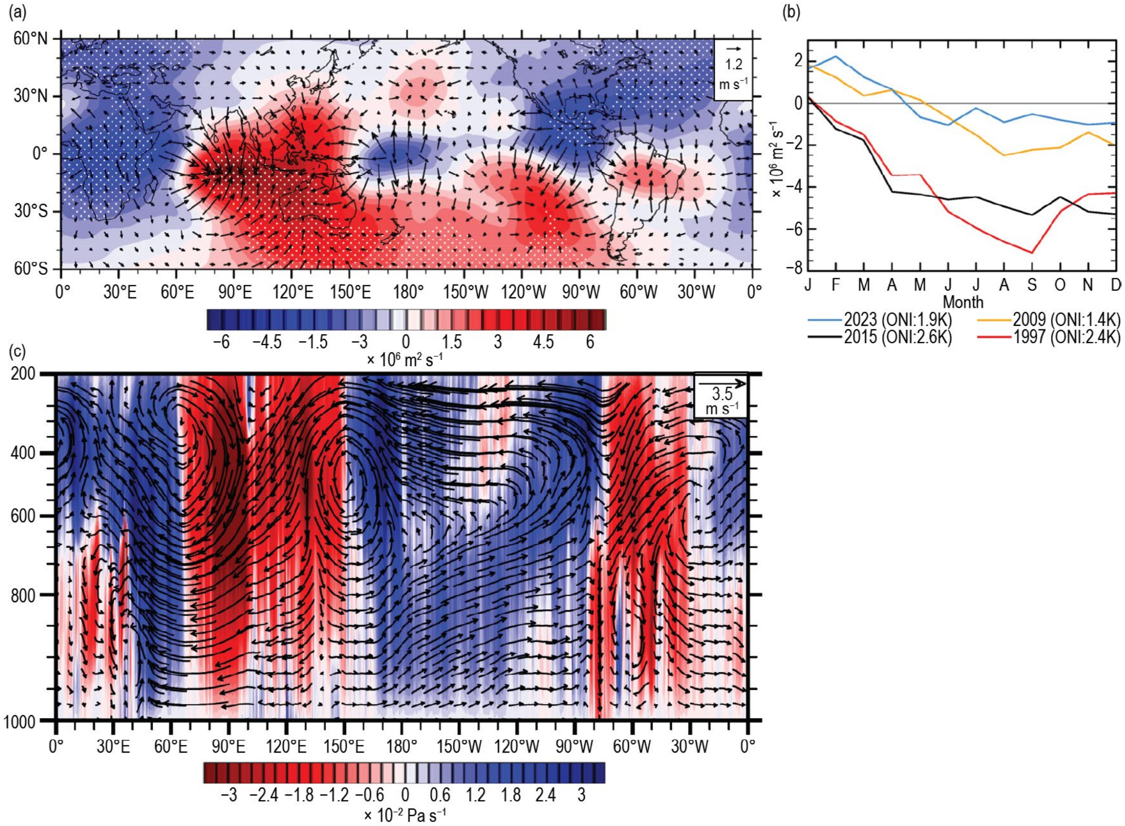

Fig. 2.53. (a) 200-hPa (colors) velocity potential ($\times 10^6$ m² s^{-1}) and (arrows) divergent wind anomalies (m s^{-1}; 1991–2020 base period) for OND 2023; stippling indicates regions with anomalies exceeding 1.65 std. dev. of the seasonal anomalies; (b) evolution of anomalous velocity potential ($\times 10^6$ m² s^{-1}) in the equatorial central Pacific (5°S–5°N, 170°E –130°W) for the four strongest El Niño years since 1991. The Nov Oceanic Niño Index (ONI) for the four years is provided in the legend. (Source: ERA5.) (c) Anomalies of pressure vertical velocity (shaded; units: $\times 10^{-2}$ Pa s^{-1}) and u/w anomalies (arrows) averaged over the region 10°S–10°N (zonal wind anomaly [u] unit: m s^{-1}, pressure vertical velocity anomaly [w] unit: $\times 10^{-2}$ Pa s^{-1}).

The IOD is also associated with the negative velocity potential anomaly over the western Indian Ocean and central Africa, and the ONI is associated with a negative anomaly over the central equatorial Pacific (both related to enhanced convection in their respective regions). Although the 2023 El Niño event was one of the strongest of the past decades, the velocity potential anomaly in the central Pacific was rather weak. The region was chosen based on the location of the typically strongest precipitation response to El Niño (see, e.g., Fig. 3b in Mayer et al. 2013). The relatively weak upper-air wind response to the 2023 El Niño conditions (also noted in section 2e2) is consistent with the surprisingly weak coupling of Pacific equatorial surface winds to central-to-eastern Pacific warm sea-surface temperature (SST) anomalies during the development phase of the event. Thus, the weakening of the Pacific Walker cell was modest during 2023 despite the strong warm Pacific SST anomalies.

There was a strong negative velocity potential anomaly over the far eastern tropical Pacific and Central America, which is consistent with the highly active eastern North Pacific hurricane season (see section 4g3). Together with high oceanic heat content, it likely contributed to the explosive development of Hurricane Otis that made landfall near Acapulco on 25 October (see section 4g3 and Sidebar 4.1 for details).

Figure 2.53c depicts anomalies in pressure vertical velocity and zonal/vertical velocities averaged over the region spanning from 10°S to 10°N in OND 2023. Consistent with Fig. 2.53a, positive anomalies in pressure vertical velocity were observed over the tropical central/east Pacific, indicating ascending motion associated with El Niño. Particularly noteworthy is the stronger ascending motion observed during OND compared to the June–August season, suggesting the intensification of El Niño as the season progressed.

In 2023, the quasi-biennial oscillation (QBO) of stratospheric zonal-mean zonal winds completed its regular westerly phase after 12.7 months. It reached its maximum value of 16.1 m s^{-1} at the 40-hPa level in April. The newly formed easterly descended from the 10-hPa pressure level to

60-hPa at a rate of 1.1 ± 0.5 km month^{-1}, which is quite fast. Descent tends to stall between 40 hPa and 50 hPa in many years, but this did not happen in 2023. A new westerly had already formed at the 10-hPa level in late November, starting a new QBO cycle for 2024.

4. THUNDER HOURS

—M. Füllekrug, E. Williams, C. Price, S. Goodman, R. Holzworth, J. Lapierre, E. DiGangi, R. Said, M. McCarthy, K. Virts, A. M. Grimm, and Y. Liu

The lifetime of an ordinary thunderstorm is about one hour, and thunder can be heard over a ~15 km radius. Based on this, the definition of a thunder hour is that at least two lightning flashes occurred within one hour and 15 km from a given location. The mapping of thunder hours enables the characterization of thunderstorm frequencies around the world (DiGangi et al. 2021) that are indicative of high-impact weather including high wind speeds, intense rainfall, large hail, and lightning hazards. (Füllekrug et al. 2022 and references therein). Thunder hours can be derived from optical, radio, and sonic remote sensing and result in maps that offer a statistically robust measure of the frequency of deep convection—on time scales ranging from hours to decades—that is suitable for climate studies.

This contribution describes the first global climatic thunder hour anomaly map calculated from composite radio remote sensing using three different ground-based global lightning detection networks for comparison with optical remote sensing using the Geostationary Lightning Mapper (GLM) on board the NOAA GOES-16 (Rudlosky and Virts 2021). Vaisala's Global Lightning Detection Network (GLD360; Said et al. 2013), Earth Network's Total Lightning Network (ENTLN; Zhu et al, 2022), and the University of Washington's World-Wide Lightning Location Network (WWLLN; Holzworth et al. 2021) radio-locate lightning flashes around the world. The lightning occurrence times and locations are subsequently used to calculate the total number of thunder hours separately for each network and for each year from 2018 to 2023 with a geographic resolution of 0.05° × 0.05°, which corresponds to a spatial resolution of ~5.56 km × 5.56 km at the equator. Subsequently, the total number of thunder hours in 2023 is averaged across all three networks, revealing up to ~500 thunder hours in the Americas, Central Africa, and the Maritime Continent in Southeast Asia (Fig. 2.54a). The global thunder hour anomaly within the field of view of GLM in 2023 (Fig. 2.55) exhibits remarkable agreement with the anomaly calculated from the ground-based global lightning detection networks (Fig. 2.54b).

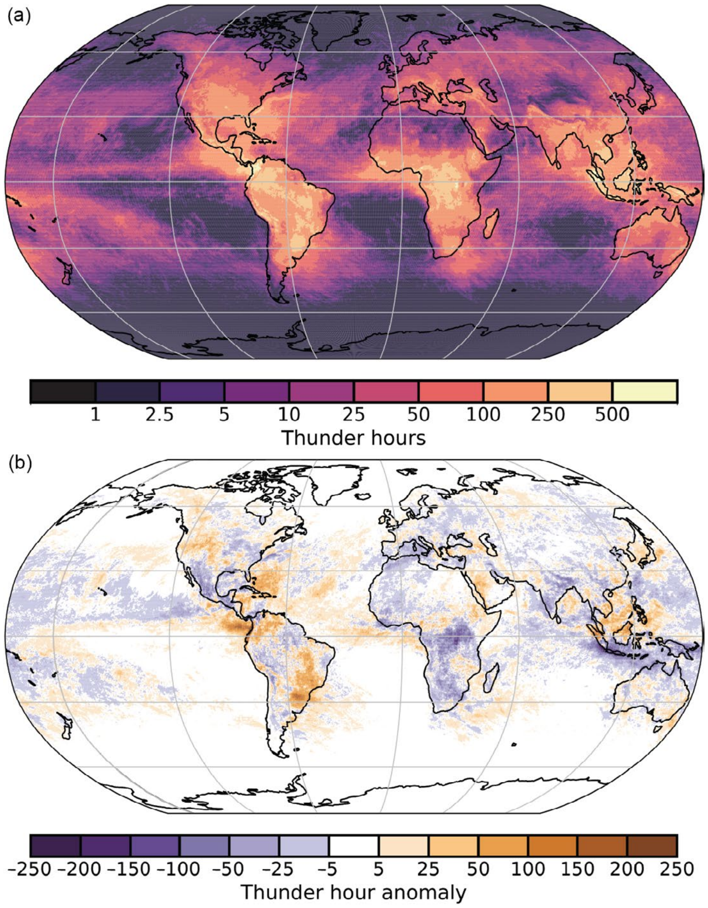

Fig. 2.54. (a) Total number of thunder hours for 2023 averaged from three ground-based global lightning detection networks (Vaisala Global Lightning Detection Network [GLD360], Advanced Environmental Monitoring Earth Networks Total Lightning Network [AEM ENTLN], and the University of Washington's World Wide Lightning Location Network [UW WWLLN]) and (b) thunder hour anomalies for 2023 (base period is 2018–22).

Thunder hour anomalies in 2023 were calculated against the preceding five-year average of annual thunder hours (2018–22). The anomaly of up to ~200 additional thunder hours over the eastern tropical Pacific (Fig. 2.54b) is attributed to increased convection associated with above-average SSTs (see sections 2b2, 3b) and El Niño (see sections 2d5, 4b).

Above-average numbers of thunder hours and precipitation in southeastern South America has been attributed to a teleconnection between weather patterns in northwestern and southeastern South America in austral spring, albeit before the peak of El Niño's SST anomaly (Grimm 2003; Grimm and Natori 2006; Adler et al. 2017). The similarity of this feature with an increased number of days and hours with lightning during the 1997/98 El Niño along the northern Gulf of Mexico basin (Goodman et al. 2000) suggests a common physical mechanism. However, negative thunder hour anomalies prevailed along the northern Gulf of Mexico in 2023, possibly because the impact of El Niño on the location of the subtropical jet stream over North America is largest in Northern Hemisphere winter (Manney et al. 2021, Fig. 11 top row).

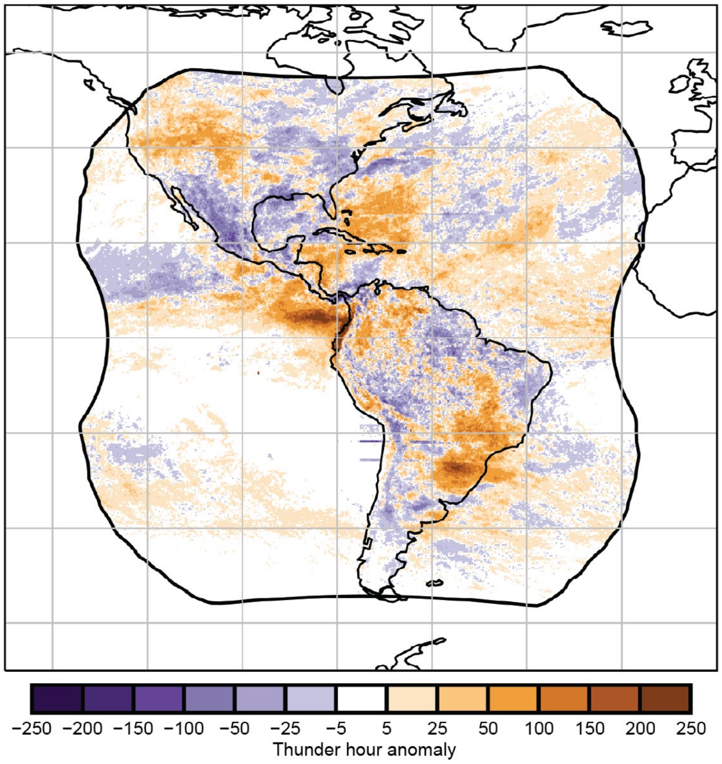

Fig. 2.55. Thunder hour anomaly for 2023 calculated from NOAA's Geostationary Lightning Mapper on GOES-16. This compares well to the 2023 anomalies calculated from ground-based lightning detection networks (Fig 2.54b).

A third area of above-average numbers of thunder hours in 2023 is evident in the northern part of the Maritime Continent, where previous studies have shown maximum lightning responsiveness to "Super El Niño" events (Hansen et al. 2006; Williams et al. 2021), which are declared when the SST anomaly exceeds 2°C. The negative anomaly in the southern portion of the Maritime Continent is potentially attributed to a cold anomaly in SSTs (sections 2b3, 3b). A more detailed characterization of thunder hour anomalies over land and ocean is the subject of ongoing research.

Finally, our analysis shows a positive anomaly in thunder hours in the western United States and Canada during 2023. This was coincident with extreme wildfires in Canada over the summer (sections 2h3; Sidebar 7.1). Thunder hours are indicative of high-impact weather as part of weather and climate disasters documented for the United States (Bartow-Gillies et al. 2023).

f. Earth radiation budget

1. EARTH RADIATION BUDGET AT TOP-OF-ATMOSPHERE

—P. W. Stackhouse Jr., T. Wong, P. Sawaengphokhai, J. Garg, and N. G. Loeb

The Earth radiation budget (ERB) at top-of-atmosphere (TOA) involves the exchange of incoming total solar irradiance (TSI) and outgoing radiation from Earth given by the sum of reflected shortwave (RSW) and outgoing longwave radiation (OLR). This balance is crucial in understanding Earth's climate system and global temperature variations. Over the last 20 years, the observed climate system has been experiencing an increasing net positive imbalance, representing a surplus of energy to the Earth–atmosphere system (Loeb et al. 2022; von Schuckmann et al. 2023). This observed net positive imbalance continued in 2023, albeit with significant changes in all ERB components corresponding to the transition from La Niña to El Niño.

An analysis of CERES (Clouds and the Earth's Radiant Energy System) TOA ERB measurements (Table 2.9) shows that the global annual mean OLR, TSI, and net radiation increased by 0.60 W m^{-2}, 0.10 W m^{-2}, and 0.30 W m^{-2}, respectively, in 2023 relative to 2022 (rounded to the nearest 0.05 W m^{-2}). In contrast, the global annual mean RSW decreased by 0.80 W m^{-2} over the same period. Relative to the 2001–22 climatology, the 2023 global annual mean anomalies for all TOA radiative flux components (Table 2.9) are greater than their corresponding 2-sigma interannual variability; this is the first time this has occurred in the CERES record. These large TOA radiative flux anomalies are indicative of the extremely large climate anomalies that occurred in 2023. The TOA radiative impact of the La Niña to El Niño transition is shown in Fig. 2.56 as regional annual mean difference maps in OLR and RSW between 2023 and 2022.

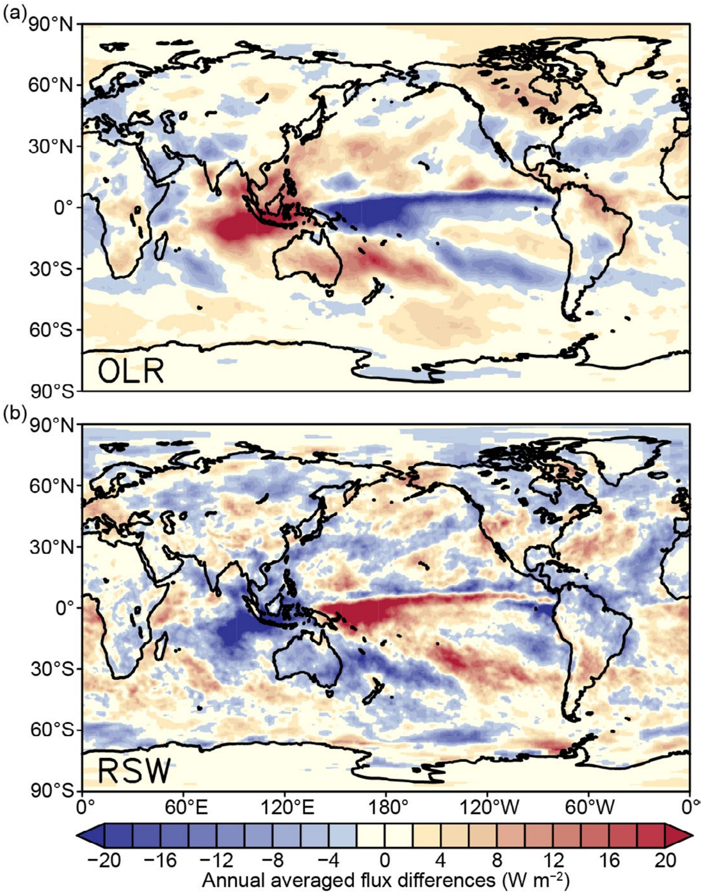

Fig. 2.56. Annual average top-of-atmosphere flux differences (W m^{-2}) between 2023 and 2022 for (a) outgoing longwave radiation (OLR) and (b) reflected shortwave radiation (RSW). The annual mean maps for 2023 were derived after adjusting Dec 2023 FLASHFlux version 4B data using the difference between CERES EBAF Ed4.2 and CERES FLASHFlux version 4B data in 2022.

Table 2.9. Global annual mean top-of-atmosphere (TOA) radiative flux changes between 2022 and 2023, the 2023 global annual mean radiative flux anomalies relative to their corresponding 2001–22 mean climatological values, the mean 2001–22 climatological values, and the 2-sigma interannual variabilities of the 2001–22 global annual mean fluxes (all units in W m^{-2}) for the outgoing longwave radiation (OLR), total solar irradiance (TSI), reflected shortwave (RSW), absorbed solar radiation (ASR, determined from TSI – RSW), and total net fluxes. All flux values have been rounded to the nearest 0.05 W m^{-2} and only balance to that level of significance.

Global	One Year Change (2023 minus 2022) (W m^{-2})	2023 Anomaly (Relative to 2001–22) (W m^{-2})	Climatological Mean (2001–22) (W m^{-2})	Interannual Variability (2001–22) (W m^{-2})
OLR	+0.60	+0.85	240.35	±0.65
TSI	+0.10	+0.25	340.20	±0.15
RSW	–0.80	–1.50	99.00	±1.05
ASR	+0.90	+1.75	241.20	±1.05
Net	+0.30	+0.90	0.85	±0.85

The largest reductions in OLR and increases in RSW, indicative of the increases in deep convection, are observed spanning from the tropical western Pacific (north of Australia) eastward in the equatorial region and southeastward into the South Pacific Ocean. The largest increases in OLR and decreases in RSW are observed over the Indian Ocean and the Maritime Continent, extending northeastward into the subtropical northern Pacific and southeastward over Australia in the subtropical southern Pacific Ocean.

The global monthly mean TOA OLR anomaly showed large variability in 2023 (Fig. 2.57), dropping to a minimum of −0.70 W m^{-2} for May, then peaking in October at +1.90 W m^{-2}. This is the largest range in monthly OLR anomaly for the CERES climatology for a given year. This variability is consistent with NOAA HIRS (Lee and NOAA CDR Program 2018) and NASA AIRS (Susskind et al. 2012) OLR datasets (not shown). The 2023 global annual mean TOA OLR anomaly was +0.85 W m^{-2}. The global monthly mean TOA absorbed solar radiation (ASR, determined from TSI minus RSW) anomaly increased throughout 2023, peaking at +2.35 W m^{-2} in August before slightly decreasing over the last few months. For the year as a whole, the 2023 global annual mean TOA ASR anomaly was +1.75 W m^{-2}. The global monthly mean TOA total net anomaly, which is calculated from ASR anomaly minus OLR anomaly, also stayed positive throughout 2023, peaking at +1.80 W m^{-2} in April, but decreasing strongly to about +0.15 W m^{-2} by October. The global annual mean TOA total net anomaly for 2023 was +0.90 W m^{-2}, representing a continuation of positive net imbalance in 2023 (known as the Earth energy imbalance) that has been observed through the 2020s (Loeb et al. 2021, 2022; von Schuckmann et al. 2023). That positive net imbalance continued to grow in early 2023 but appears to have been interrupted by the onset of the strong El Niño. Further analyses are needed to understand the significances and impacts of these observed global changes.

The TSI data are from a "Community-Consensus TSI Composite" using the methodology defined by Dudok de Wit et al. (2017). The TOA RSW and TOA OLR data come from two different CERES datasets. The data for March 2000–November 2023 are based on the CERES EBAF edition 4.2 product (Loeb et al. 2009, 2012, 2018), which are constructed with measurements from the CERES instruments (Wielicki et al. 1996, 1998) aboard *Terra*, *Aqua*, and NOAA-20 spacecraft. The data for December 2023 comes from the CERES FLASHFlux version 4B product (Kratz et al. 2014), which are created using CERES measurements from *Terra* and NOAA-20 spacecraft. The FLASHFlux to EBAF data normalization procedure (Stackhouse et al. 2016) results in 2-sigma monthly uncertainties of ±0.40 W m^{-2}, ±0.00 W m^{-2}, ±0.30 W m^{-2}, and ±0.45 W m^{-2} for the OLR, TSI, RSW, and total net radiation, respectively (rounded to nearest 0.05 W m^{-2}).

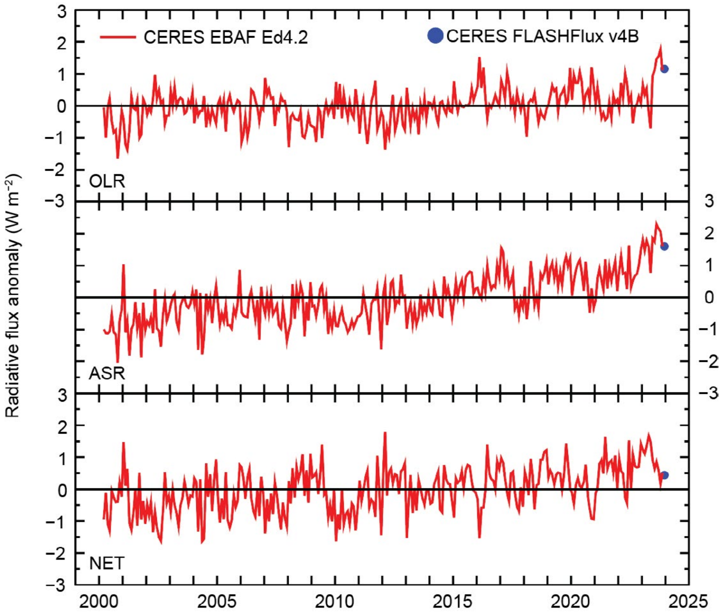

Fig. 2.57. Time series of global monthly mean deseasonalized anomalies (W m^{-2}) of top-of-atmosphere Earth radiation budget for outgoing longwave radiation (OLR; top), absorbed solar radiation (ASR, determined from total solar irradiance [TSI] minus reflected shortwave [RSW]; middle), and total net (TSI-RSW-OLR; lower) from Mar 2000 to Dec 2023. Anomalies are relative to their calendar month climatology (2001–22). Time series show the CERES EBAF Ed4.2 1-Deg data (Mar 2000–Nov 2023) in red and the CERES FLASHFlux version 4B data (Dec 2023) marked by the blue dot; see text for merging procedure. (Sources: https://ceres-tool.larc.nasa.gov/ord-tool/jsp/EBAFTOA42Selection.jsp and https://ceres-tool.larc.nasa.gov/ord-tool/jsp/FLASH_TISASelection.jsp.)

2. MAUNA LOA APPARENT TRANSMISSION RECORD

—J. A. Augustine, K. O. Lantz, J.-P. Vernier, and L. Soldo

The time series of monthly mean apparent atmospheric transmission from pyrheliometer measurements at NOAA's Mauna Loa Observatory (MLO) in Hawaii (19.536°N, 155.576°W, 3397 m a.s.l.) is one of the longest geophysical records, dating back to 1958. However, its extension to 2023 is abbreviated due to damage sustained from the eruption of Mauna Loa on 27 November 2022. Ten meters of lava buried approximately a mile of the road leading to the station and demolished the power lines. Power was restored in July 2023.

The apparent atmospheric transmission time series through 2023 is shown in Fig. 2.58. Lack of operations in the first half of the year precluded sampling of the perennial springtime passage of Asian dust that usually causes a reduction in transmission (Augustine et al. 2023; Bodhaine et al. 1981). Until November 2023, transmission levels are maintained at the relatively low levels (0.926±0.0026) that have been observed since 2018. A composite of Stratospheric Aerosol and Gas Experiment (SAGE) limb sounder imagery (Leckey et al. 2021; https://sage.nasa.gov/sageiii-iss/browse_images/expedited/) suggests that this long period of relatively low transmission may have been sustained by a series of volcanic eruptions, including Ambae-1 and -2 in 2018, Raikoke and Ulawun in 2019, Taal in 2020, Soufriere in 2021, and Hunga Tonga–Hunga Ha'apai (HTHH) in 2022. Although SAGE imagery covers only +10° to –10° latitude, Yu et al. (2023) attribute elevated stratospheric aerosols at 15.5 km and 18.5 km from balloon-borne Portable Optical Particle Spectrometer soundings at Boulder, Colorado (40°N), and the Tibetan Plateau (25°N–36°N) to those eruptions, indicating that the volcanic aerosols did spread northward over Mauna Loa.

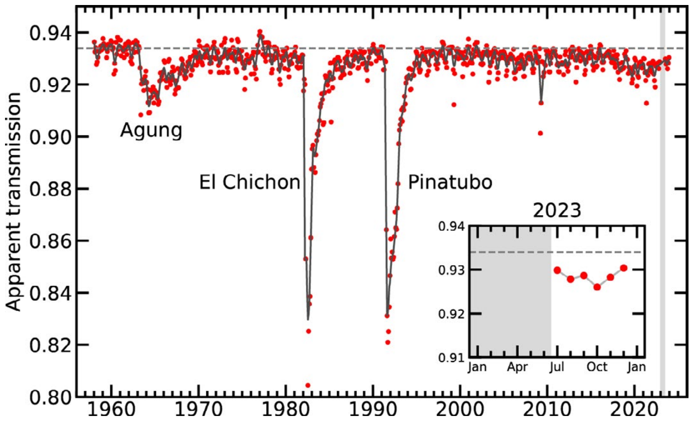

Fig. 2.58. Apparent transmission at Mauna Loa, Hawaii, from 1958 through 2023. Red dots are monthly averages of morning apparent transmission, and the gray curve is a lowess fit with a six-month smoother applied. Inset shows new data for 2023. The gray horizontal dashed line represents the average transmission of the clean period (Ammann et al. 2003; Solomon et al. 2011) before the eruption of Agung. Transmission is not available from Jan through Jun 2023 (gray areas in main figure and inset) because lava from the eruption of Mauna Loa in late Nov 2022 cut power to the station.

High levels of stratospheric water vapor from HHTH may have also contributed to the low transmission after January 2022. However, successive upticks in November and December of 2023 (to 0.93) may hint at the onset of a recovery. That tendency continued into January 2024, when the MLO transmission remained >0.93 (not shown). A possible cause is the switching of the quasi-biennial oscillation to an easterly phase around October 2023, and the significant drying of the lower stratosphere thereafter, which has been confirmed by integrated water vapor measurements at Mauna Loa. Less absorption in the near-infrared from that drying likely contributed to the increase in transmission from November 2023 through January 2024.

According to the Smithsonian/U.S. Geological Survey Weekly Volcanic Activity Report, 72 eruptions occurred in 2023. Of those, only one, specifically Lascar in Chile, attained a Volcanic Explosivity Index (VEI) of 3, with two others registering VEIs of 2 and 1. Other 2023 eruptions were, or have so far been too weak to be classified as explosive. Analyses of the CALIPSO data show that the plume from the January 2022 explosive eruption of HTHH remains in the lower stratosphere but is confined mainly to the Southern Hemisphere. However, CALIPSO and SAGE continue to show a weak but diminishing presence of that plume at the latitude of MLO at least through June and October 2023, respectively.

The primary aerosol event of 2023 was unprecedented wildfires across Canada from May through September that impacted air quality throughout the Northern Hemisphere (Wang et al. 2023; see Sidebar 7.1 for details). Pyrocumulus thunderstorms generated by some of those fires as well as solar heating of black carbon within initial plumes likely lofted smoke into the lower stratosphere; however, a Copernicus Atmospheric Monitoring Service (CAMS) global analysis of daily mean organic matter aerosol optical depth at 550 nm (Garrigues et al. 2022) from May through September shows that smoke was confined mostly north of 40°N. A modeling study by Wang et al. (2023) shows very low concentrations of particulate matter (PM2.5) aerosol (<1 μg m^{-3}) over Hawaii from late June through September from wildfires in Canada and East Asia, but no presence of it there in the other months of the year. This evidence indicates that wildfire smoke may not have had a significant impact on MLO transmission in 2023.

To calculate apparent atmospheric transmission, three ratios of successive clear-morning pyrheliometer measurements made near the summit at solar air masses of 2, 3, 4, and 5 are averaged to get a representative daily transmission (Ellis and Pueschel 1971). The mean of daily transmissions for a particular month is considered to be a representative monthly transmission. It is referred to as "apparent" because atmospheric variability at longer pathlengths increases the uncertainty of the measurements.

g. Atmospheric composition

1. LONG-LIVED GREENHOUSE GASES

—X. Lan, B. D. Hall, G. Dutton, and I. Vimont

In 2023, the atmospheric burdens of the long-lived greenhouse gases (LLGHGs) carbon dioxide (CO_2), methane (CH_4), and nitrous oxide (N_2O), that are largely responsible for increasing global temperature (Forster et al. 2023; IPCC 2013), continued to rise to record-high levels. CO_2 is the most important and abundant anthropogenic GHG, and in 2023, globally averaged CO_2—as derived from remote marine boundary layer measurements made by NOAA's Global Monitoring Laboratory—reached 419.3±0.1 ppm (parts per million by moles in dry air; Fig. 2.59a; Table 2.10; uncertainties are reported as one sigma in this section). This is a 50% increase from the pre-industrial level of ~278 ppm (Etheridge et al. 1996). Annual growth in global mean CO_2 has risen from 0.6±0.1 ppm yr^{-1} in the early 1960s to an average of 2.5 ppm yr^{-1} during 2014–23 (Fig. 2.59a; Lan et al. 2024a). CO_2 growth in 2023 was 2.8 ppm, the fourth highest in the record since the 1960s.

The main driver of increasing atmospheric CO_2 is fossil fuel (FF) burning, with emissions increasing from 3.0±0.2 Pg C yr^{-1} in the 1960s to 9.6±0.5 Pg C yr^{-1} (including cement production) in the past decade (2013–22; Friedlingstein et al. 2023). Together with the measured atmospheric increase, we can conclude that about 45% of the FF-emitted CO_2 since 1958 has remained in the atmosphere, with the remaining portion entering the oceans and terrestrial biosphere (Friedlingstein et al. 2023). While increasing emissions of CO_2 from FF combustion are roughly monotonic, the CO_2 growth rate varies from year to year (standard deviation = 0.4 ppm in 2014–23) with variability mostly driven by terrestrial biosphere exchange of CO_2, as confirmed by measurements of the ^{13}C:^{12}C ratio in atmospheric CO_2 (e.g., Keeling et al. 1985; Alden et al. 2010). The El Niño–Southern Oscillation (ENSO) is the main driver of this interannual variability (Betts et al. 2016; Liu et al. 2017), which impacts photosynthetic CO_2 uptake, respiratory release, and fires.

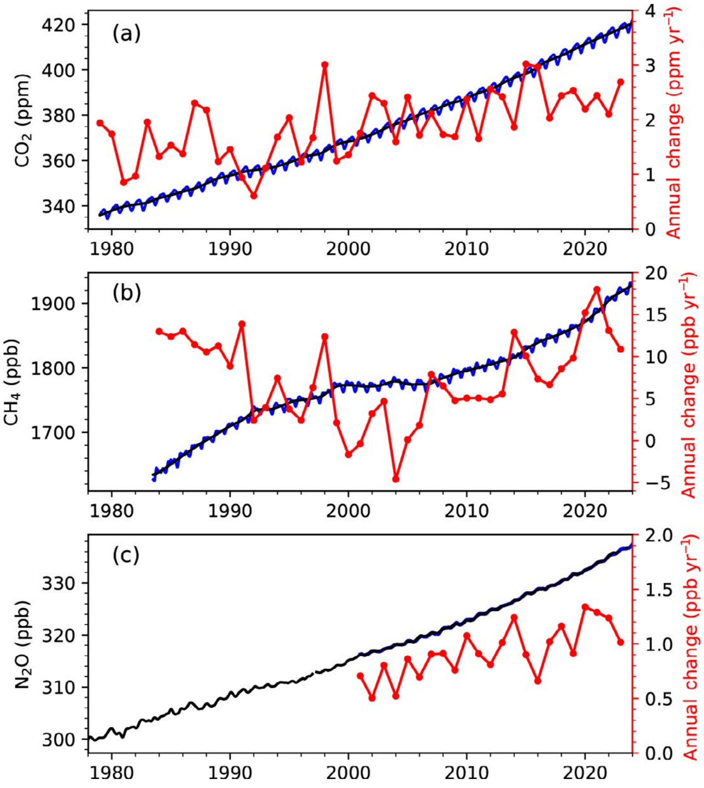

Fig. 2.59. Global mean dry air remote surface mole fractions (approximately weekly data in blue and the deseasonalized trend in black [see Dlugokencky et al. 1994 for methods]; left axis) and annual change (red, right axis) of (a) CO_2 (ppm), (b) CH_4 (ppb), and (c) N_2O (ppb) derived from the NOAA Global Greenhouse Gases Reference Network. N_2O data prior to 2000 are insufficient to accurately calculate its growth rate.

Atmospheric CH_4 is the second most important LLGHG, and in 2023 its atmospheric abundance reached 1922.6±0.6 ppb (parts per billion by moles in dry air; Lan et al. 2024b), about 2.6 times its pre-industrial level of 729±9 ppb (Mitchell et al. 2013). Global CH_4 increased by an average rate of 11.7±1.4 ppb yr^{-1} between 1984 and 1991, followed by a smaller increase of 4.4±1.8 ppb yr^{-1} between 1992 and 1998, and further reduced to near zero (0.5±3.0 ppb yr^{-1}) during 1999–2006. Atmospheric CH_4 growth restarted in 2007 and has accelerated since 2014 and further accelerated in 2020–22 with an average rate of increase of 15.4±2.0 ppb yr^{-1} (Fig. 2.59b). Its growth remained high in 2023 at about 11.1±0.4 ppb, which was the fifth-highest annual growth rate since the renewed growth started in 2007.

Atmospheric CH_4 is emitted by anthropogenic sources such as fossil fuel exploitation, livestock, waste and landfill, and rice cultivation, as well as natural sources such as wetlands and shallow lakes. The ongoing reduction in atmospheric $\delta^{13}C$-CH_4 since 2008 (Michel et al. 2022) indicates increased emissions from microbial sources (Basu et al. 2022), including emissions from livestock as well as natural wetland and lakes, which have more negative $\delta^{13}C$-CH_4 signatures. Small increases in FF emissions may also play a role in the post-2006 global CH_4 increase (Oh et al. 2023; Lan et al. 2019, 2021; Basu et al. 2022). The contribution of hydroxyl radical, the main sink for CH_4, is still uncertain, but it is less likely to be a major contributor (Zhao et al. 2019; Lan et al. 2021). Recent studies suggest a dominant role of increased tropical wetland emissions in the post-2020 CH_4 surge (Feng et al. 2021; Peng et al. 2022), and sustained increases in wetland CH_4 emissions may be an indication of an emerging carbon climate feedback (Nisbet et al. 2023; Zhang et al. 2023). An increased contribution from wetland emissions is also consistent with the acceleration in the decline of atmospheric $\delta^{13}C$-CH_4 in 2020–22 (Michel et al. 2022).

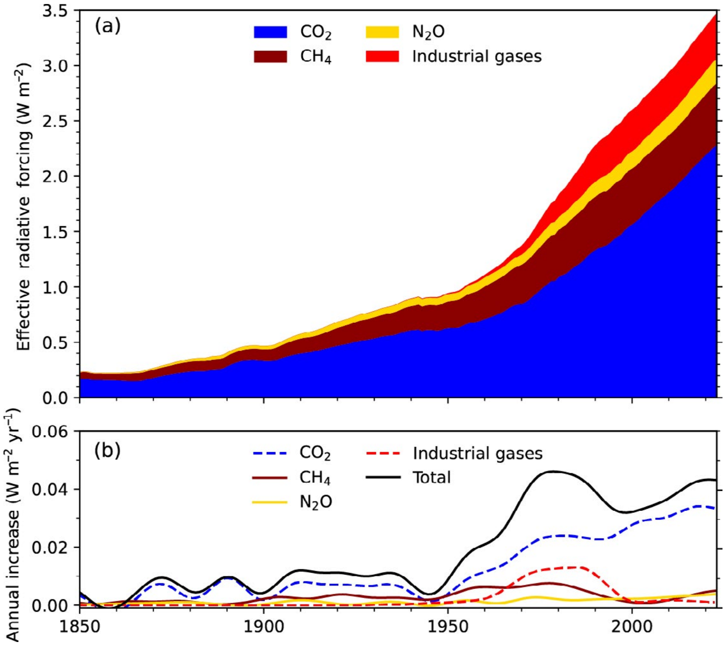

Fig. 2.60. (a) Effective radiative forcing (W m^{-2}) due to long-lived greenhouse gases (LLGHGs; see Table 2.10 for details on industrial gases). (b) Annual increase in direct radiative forcing (W m^{-2}).

Nitrous oxide (N_2O) is a potent greenhouse gas with an atmospheric lifetime of 120 years (Tian et al. 2023). It is produced by microbes that rely on nitrogen substrates from natural and agricultural soils, animal manure, and the oceans (Davidson 2009), and increased agricultural emissions related to fertilizer usage are the major source of its long-term increase (Tian et al. 2023). The mean global atmospheric abundance of N_2O in 2023 was 336.7±0.1 ppb, a 25% increase over its pre-industrial level of 270 ppb (Rubino et al. 2019). Recent growth reached an average rate of 1.3±0.1 ppb yr^{-1} from 2020 to 2022 (Fig. 2.59c), larger than the average rate between 2010 and 2019 (1.0±0.2 ppb yr^{-1}), strongly suggesting increased emissions. The N_2O growth rate in 2023 was 1.0±0.1 ppb.

The impacts of LLGHGs on global climate can be estimated using the effective radiative forcing (ERF) of LLGHGs, the change of radiative energy caused by added LLGHGs to the atmosphere, following the Intergovernmental Panel on Climate Change's Sixth Assessment Report (Forster et al. 2021). Increasing atmospheric CO_2 has accounted for 64% of the increase in ERF by LLGHGs, reaching 2.28 W m^{-2} in 2023 (Fig. 2.60) compared with preindustrial times (1750). The increase in CH_4 contributed a 0.56 W m^{-2} increase in ERF between 1750 and 2023 while the CH_4-related production of tropospheric ozone and stratospheric water vapor also contributes to ~0.30 W m^{-2} indirect radiative forcing (Myhre et al. 2014). The increase in atmospheric N_2O abundance contributed to a 0.22 W m^{-2} increase in ERF between 1750 and 2023.

Table 2.10. Summary table of long-lived greenhouse gases for 2023 (CO_2 mole fractions and changes from prior year, in brackets, are in ppm; N_2O and CH_4 in ppb; and all others in ppt).

Compound Class	Industrial Designation or Common Name	Chemical Formula	ERF[a]	Rad. Efficiency (W m^{-2} ppb^{-1})[b]	Rad. Forcing[a] (ERF/SARF) (W m^{-2})	Mean surface mole fraction, 2023 [change from prior year][c]	Lifetime (yrs)[b]
Acidic oxide	Carbon Dioxide	CO_2	Y	1.33×10^{-5}	2.28	419.3 [2.2]	
Alkane	Methane	CH_4	Y	3.88×10^{-4}	0.56	1922.6 [10.6]	9.1
Nitride	Nitrous Oxide	N_2O	Y	3.2×10^{-3}	0.22	336.7 [1.0]	123
Chlorofluorocarbon	CFC-11	CCl_3F	N(Y)[e]	0.26	0.057(0.064)	217.1 [−2.4][d]	52
Chlorofluorocarbon	CFC-12	CCl_2F_2	N(Y)[e]	0.32	0.156(0.174)	485.4 [−4.3][d]	102
Chlorofluorocarbon	CFC-113	CCl_2FCClF_2	N	0.30	0.020	67.1 [−0.6][d,f]	93

Compound Class	Industrial Designation or Common Name	Chemical Formula	ERF[a]	Rad. Efficiency ($W\ m^{-2}\ ppb^{-1}$)[b]	Rad. Forcing[a] (ERF/SARF) ($W\ m^{-2}$)	Mean surface mole fraction, 2023 [change from prior year][c]	Lifetime (yrs)[b]
Hydrochlorofluorocarbon	HCFC-22	$CHClF_2$	N	0.21	0.052	247.5 [–1.3]	11.9
Hydrochlorofluorocarbon	HCFC-141b	CH_3CCl_2F	N	0.16	0.004	24.5 [–0.1]	9.4
Hydrochlorofluorocarbon	HCFC-142b	CH_3CClF_2	N	0.19	0.004	21.0 [–0.2]	18
Hydrofluorocarbon	HFC-134a	CH_2FCF_3	N	0.17	0.021	129.5 [5.0]	14
Hydrofluorocarbon	HFC-152a	CH_3CHF_2	N	0.10	<0.001	7.4 [0.0]	1.6
Hydrofluorocarbon	HFC-143a	CH_3CF_3	N	0.17	0.005	28.4 [1.7]	51
Hydrofluorocarbon	HFC-125	CHF_2CF_3	N	0.23	0.009	38.8 [3.7]	30
Hydrofluorocarbon	HFC-32	CH_2F_2	N	0.11	0.002	28.3 [3.7]	5.4
Hydrofluorocarbon	HFC-23	CHF_3	N	0.18	0.007	36.8 [0.9]	228
Hydrofluorocarbon	HFC-365mfc	$CH_3CF_2CH_2CF_3$	N	0.22	<0.001	1.07 [0.00]	8.9
Hydrofluorocarbon	HFC-227ea	CF_3CHFCF_3	N	0.26	<0.001	2.20 [0.16]	36
Chlorocarbon	Methyl Chloroform	CH_3CCl_3	N	0.07	<0.001	0.98 [–0.12]	5.0
Chlorocarbon	Carbon Tetrachloride	CCl_4	N	0.17	0.013	73.8 [–0.9][d]	32
Chlorocarbon	Methyl Chloride	CH_3Cl	N	0.01	<0.001	549.9 [2.7]	0.9
Bromocarbon	Methyl Bromide	CH_3Br	N	0.004	<0.001	6.47 [–0.05]	0.8
Bromocarbon	Halon 1211	$CBrClF_2$	N	0.29	0.001	2.84 [–0.09]	16
Bromocarbon	Halon 1301	$CBrF_3$	N	0.30	0.001	3.32 [0.01]	72
Bromocarbon	Halon 2402	$CBrF_2CBrF_2$	N	0.31	<0.001	0.396 [–0.001]	28
Fully fluorinated species	Sulfur Hexafluoride	SF_6	N	0.57	0.006	11.40 [0.38]	>600
Fully fluorinated species	PFC-14	CF_4	N	0.09	0.005	89.4 [0.09]	~50,000
Fully fluorinated species	PFC-116	C_2F_6	N	0.25	0.001	5.24 [0.09]	~10,000
Fully fluorinated species	PFC-218	C_3F_8	N	0.28	<0.001	0.76 [0.02]	~2600
Fully fluorinated species	PFC-318	$c\text{-}C_4F_8$	N	0.32	<0.001	2.10 [0.11]	~3200

[a] Effective Radiative Forcing (ERF) calculated by multiplying the stratospheric-temperature adjusted radiative efficiency (SARF) by the global mole fraction (in ppb) and then applying a tropospheric adjustment factor for the species indicated based on recommended values from chapters 6 and 7 in the Intergovernmental Panel on Climate Change Sixth Assessment Report Working Group I (IPCC AR6 WGI) Report. The Radiative Forcing column is either ERF (where indicated) or SARF. The adjustments to the SARF are CO_2: 5% ± 5%, CH_4: –14% ± 15%, N_2O: 7% ±13%–16%.

[b] Radiative efficiencies and lifetimes were taken from Appendix A in WMO (2018) and Hodnebrog et al. (2020a), except for SF_6 lifetime from Ray et al. (2017), CH_4 lifetime from Prather et al. (2012). For CO_2, numerous removal processes complicate the derivation of a global lifetime. AGGI = Annual Greenhouse Gas Index. For radiative forcing, see https://www.esrl.noaa.gov/gmd/aggi/aggi.html.

[c] Mole fractions are global, annual, midyear surface means determined from the NOAA cooperative global air sampling network (Hofmann et al. 2006), except for PFC-14, PFC-116, PFC-218, PFC-318, and HFC-23, which were measured by the Advanced Global Atmospheric Gases Experiment (AGAGE; Mühle et al. 2010; Miller et al. 2010). Changes indicated in brackets are the differences between the 2023 and 2022 means, the relevant quantities for calculating radiative forcing. These changes are somewhat different from the 2023 annual increases reported in Section 2.g.1, which are determined as the difference between 1 Jan 2023 and 1 Jan 2024. All values are preliminary and subject to minor updates.

[d] Global mean estimates derived from multiple NOAA measurement programs ("Combined Dataset").

[e] ERF-calculated values for CFC-11 and CFC-12 are highly uncertain but recommended by the IPCC AR6 WGI Report. Thus, they are included in parentheses here as the lower confidence value. The adjustment to the SARF for these values is 12%±13% (Hodnebrog et al. (2020b).

[f] Measurements of CFC-113 are known to be a combination of CFC-113 and CFC-113a, with CFC-113a contributing approximately 0.4 ppt to CFC-113.

2. OZONE-DEPLETING SUBSTANCES

—I. J. Vimont, B. D. Hall, G. Dutton, S. A. Montzka, J. Mühle, M. Crotwell, K. Petersen, S. Clingan, and D. Nance

Since 1987, the Montreal Protocol and its Amendments (The Protocol; https://ozone.unep.org/treaties/montreal-protocol) have regulated the production and consumption of ozone-depleting substances (ODSs) and their replacement compounds. The broad categories of these compounds are the chlorofluorocarbons, hydrochlorofluorocarbons, hydrofluorocarbons, and perfluorocarbons (CFCs, HCFCs, HFCs, and PFCs, respectively), as well as halons and methyl bromide. While the primary goal of controlling ODSs through The Protocol was to limit damage to the ozone layer by limiting production for dispersive uses, these controls (and the subsequent amendments controlling the replacement compounds) have also reduced their radiative impact. Through the 2016 Kigali Amendment, The Protocol also addresses some HFCs that do not destroy stratospheric ozone, but are strong greenhouse gases. As of 2023, 155 nations have ratified the Kigali Amendment, which will aid the global effort to reduce the impacts of these gases on the climate.

Phase-out of the production for dispersive use is not the end of emissions of a chemical, nor are emissions the only factor controlling the atmospheric abundance of a trace gas species. Existing reservoirs of gases, such as those in insulating foams, are known as banks and continue to emit controlled chemicals for years after the final phase-out has occurred. The atmospheric lifetime, or rate of destruction, of a chemical in the atmosphere dictates how quickly a compound is removed, and these lifetimes vary over a large range between different species. As an example, CFC-11 and CFC-12 were reported to be globally phased out in 2010, but have long atmospheric lifetimes and large banks that continue to emit both compounds. These two gases have declined by only 18% and 10%, respectively, from their peak atmospheric abundances in 1994 and 2003 (Fig. 2.61). Conversely, methyl chloroform (CH_3CCl_3) has relatively few banks and a short lifetime and, despite having been phased out in 2015, has declined by 99% from its peak abundance in the atmosphere.

While the transition from CFCs to HCFCs resulted in an increase in the atmospheric abundance of several HCFCs during the 1990s and 2000s, the mole fractions of two of the three most abundant HCFCs (HCFC-22 and HCFC-141b) have not increased from 2021 to 2023, suggesting that their mole fractions may have peaked (Fig. 2.61; Table 2.10). The third most abundant HCFC, HCFC-142b, has been declining since about 2020 (Fig. 2.61; Table 2.10). Mole fractions of several HFCs, used as replacements for HCFCs, have increased substantially since their introduction in the mid-1990s, in particular HFC-134a, HFC-32, and HFC-23 (Fig. 2.61; Table 2.10).

Additionally, chemicals controlled under The Protocol are still allowed to be used as feedstocks for newer-generation products. Feedstock use may play a role in renewed release of ozone-depleting substances, such as CFC-112, CFC-113a, CFC-114a, and CFC-115 (e.g., Western et al. 2023). While these new releases do not yet pose a risk to the recovery

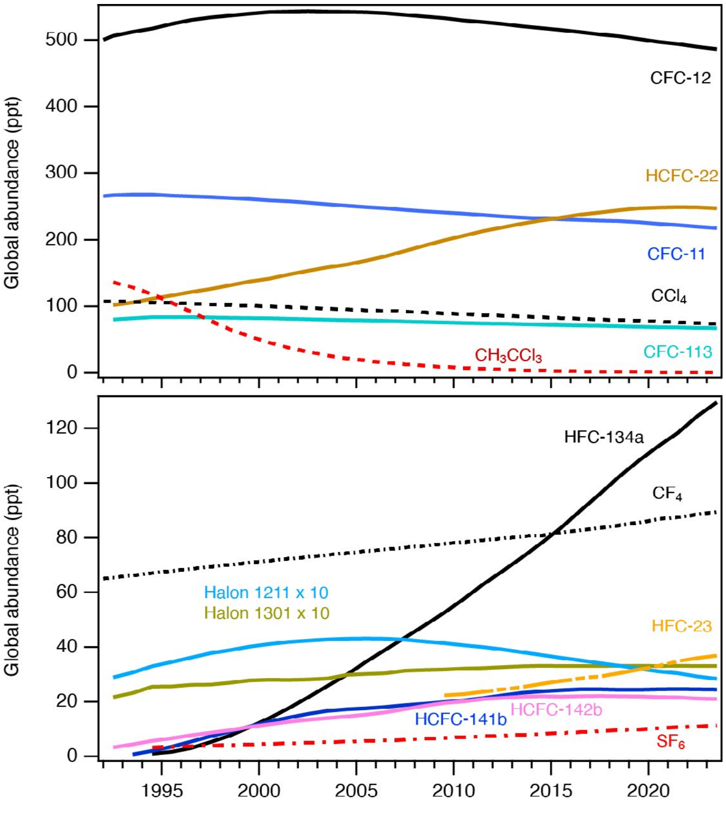

Fig. 2.61. Global mean abundances (mole fractions) at Earth's surface (ppt = nmol mol^{-1} in dry air) for several halogenated gases, many of which also deplete stratospheric ozone. See Table 2.10 for the 2023 global mean mole fractions of these and other gases.

of the ozone layer, continued emissions could begin to impact ozone layer recovery in the future (Western et al. 2023).

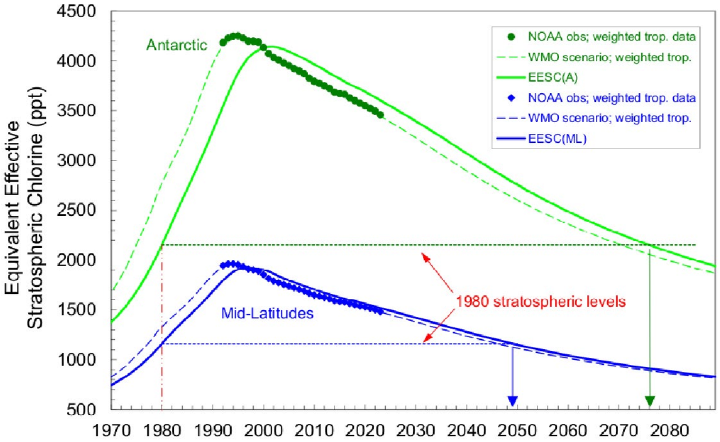

Fig. 2.62. The values of equivalent effective stratospheric chlorine in the Antarctic and midlatitudes (EESC[A] and EESC[ML], respectively) represent EESC on 1 Jan of each year since 1970. Dashed lines represent tropospheric measurement-derived scenarios, based on past measurements and, for the future, full adherence to all controls from The Protocol based on the World Meteorological Organization (WMO)/United Nations Environment Programme 2018 Ozone Assessment. Solid arrows indicate currently predicted dates for the return of EESC to 1980s levels. Solid lines depict inferred stratospheric changes based on the measured tropospheric curves. In 2023, midlatitude and Antarctic EESC were 1526 ppt and 3610 ppt, respectively, which represents a respective reduction of 21% and 13% in stratospheric reactive halogen loading from its peak. Translating this to the Ozone Depleting Gas Index (ODGI), the midlatitude ODGI is 47.1 and the Antarctic ODGI is 72.8, meaning the stratospheric reactive halogen loading has declined by 52.9% and 27.2%, respectively, relative to the 1980 benchmark reactive halogen abundance.

While global measurements of ODSs mainly represent the composition of the planetary boundary layer close to Earth's surface, destruction of the ozone layer is dependent on the amount of reactive halogen in the stratosphere. In order to track progress towards the ozone layer's recovery, equivalent effective stratospheric chlorine (EESC) is used as a measure of the reactive halogen loading in the stratosphere based on global tropospheric measurements, atmospheric transport (i.e., estimates of the mean age of the air in different parts of the stratosphere), and chemical reactivity (Daniel et al. 1995; Montzka et al. 1996; Newman et al. 2007). The destruction of the CFCs is the primary source of stratospheric reactive halogen and strongly contributes to the overall EESC. However, it is useful to scale the EESC relative to a benchmark by using the Ozone Depleting Gas Index (ODGI) to provide a more intuitive measure of the progress towards ozone layer recovery. The ODGI assesses the EESC relative to 1980, where an ODGI of 0 represents the EESC level in 1980, and an ODGI of 100 represents peak EESC (Hoffmann and Montzka 2009). The EESC, and therefore also the ODGI, are reported for the midlatitudes and the Antarctic, which spans the range of ozone layer recovery due to differences in transport processes in the stratosphere. The midlatitude EESC is expected to return to 1980 levels around 2045, while the Antarctic EESC is expected to recover by the 2070s (Fig. 2.62; https://gml.noaa.gov/odgi/).

3. TROPOSPHERIC AEROSOLS

—S. Rémy, N. Bellouin, M. Parrington, M. Ades, M. Alexe, A. Benedetti, O. Boucher, and Z. Kipling

Aerosols represent a serious public health issue in many countries and are subject to monitoring and forecasting as part of air quality policies. They also impact weather and climate by scattering and absorbing radiation and by affecting the life cycle, optical properties, and precipitation activity of clouds (IPCC AR6, chapter 6; Szopa et al. 2021).

The Copernicus Atmosphere Monitoring Service (CAMS, https://atmosphere.copernicus.eu) produces a reanalysis of global aerosols and trace gases that covers the years 2003–23 (i.e., CAMSRA; Inness et al. 2019) by combining state-of-the-art numerical modeling and aerosol remote sensing retrievals from the Moderate-Resolution Imaging Spectroradiometer (MODIS; Levy et al. 2013) and the Advanced Along Track Scanning Radiometer (AATSR; Popp et al. 2016). This analysis uses data exclusively from the CAMS reanalysis, focusing on aerosol optical depth at 550 nm and surface particulate matter (PM2.5) concentrations.

Aerosol optical depth (AOD) at 550 nm and PM2.5 in 2023 show maxima over the polluted regions of India and China, as well as from dust over the Sahara and the Middle East (Figs. 2.63a,b). High values arose from seasonal vegetation fires in equatorial Africa and occasional extreme fires, most notably across large parts of high-latitude North America, eastern Siberia, and parts of the Amazon basin (section 2h3; see Sidebar 7.1). Figure 2.63c shows the time series of monthly and yearly globally averaged total AOD during 2003–23. There is strong seasonality in AOD, driven mainly by dust episodes between March and July in the Sahara, Middle East, and the Taklamakan/Gobi deserts as well as seasonal biomass burning in Africa, South America, and Indonesia. Globally averaged AOD in 2023 was the lowest on record, on par with 2022. The summer maximum was slightly higher than in 2022 and significantly lower than in 2021, as the large fires in Canada in 2023 (see Sidebar 7.1) were compensated by lower-than-usual fire emissions elsewhere (section 2h3).

The AOD anomalies at 550 nm and PM2.5 anomalies (Plates 2.1x,y) are dominated by the exceptional fire events during summer 2023 over western and eastern Canada (section 2h3; see Sidebar 7.1) and the associated transported plumes over the North Atlantic. Positive anomalies due to fires are also seen over eastern Siberia, while the number of fires and associated emissions from equatorial Africa continued the downward trend of the last two decades. Dust storm activity was lower than usual over Northern Hemisphere (NH) deserts. The negative anomalies

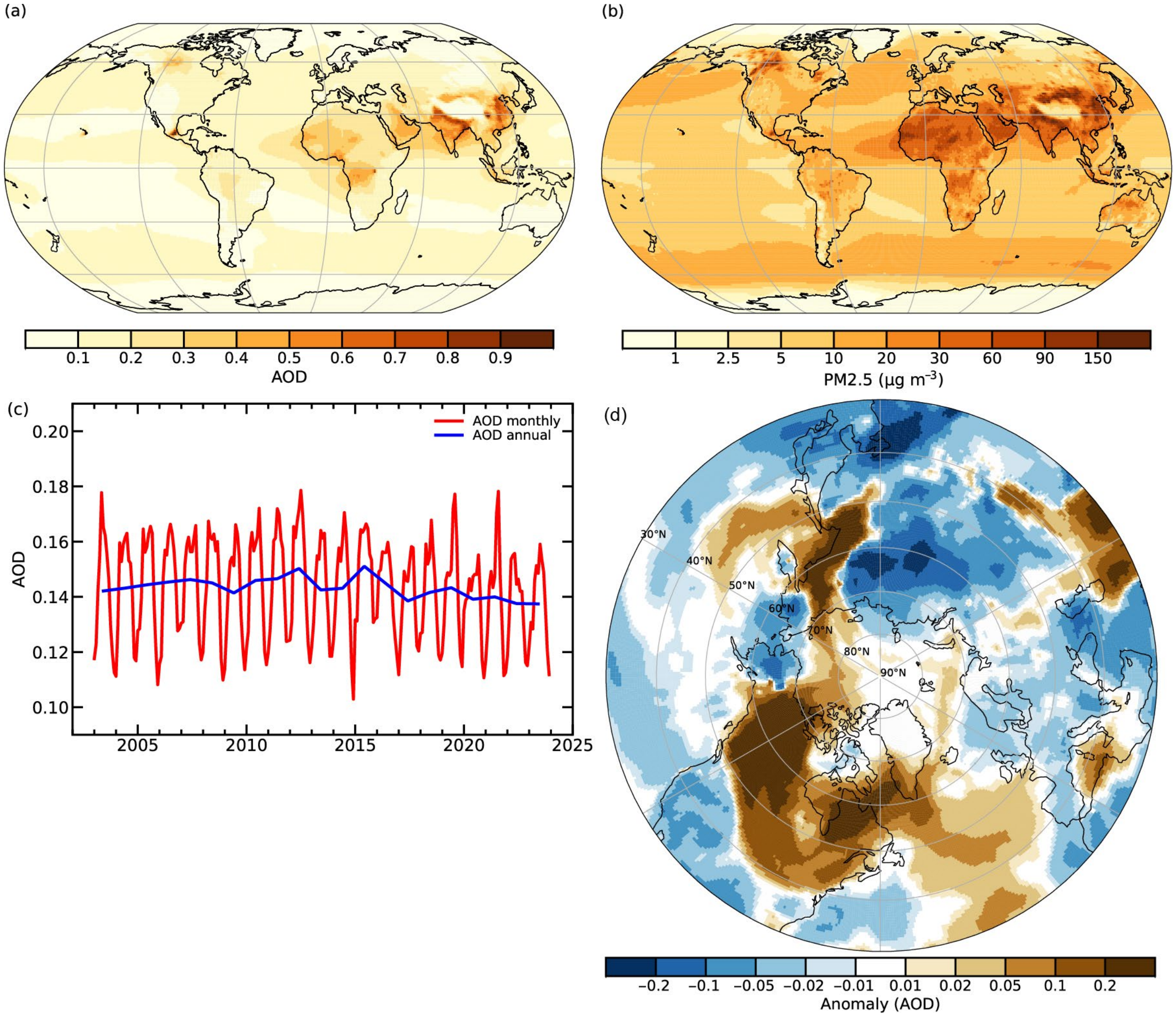

Fig. 2.63. (a) Global aerosol optical depth (AOD) at 550 nm in 2023; (b) global surface fine particulate matter (PM2.5) concentrations (μg m^{-3}) in 2023; (c) global average of total AOD at 550 nm averaged over monthly (red) and annual (blue) periods for 2003–23; and (d) monthly AOD anomalies at 550 nm for Jul 2023 compared to the Jul 2003–22 average, highlighting the extreme nature of the Canadian fires.

of AOD and PM2.5 over East Asia, Europe, and the Amazon basin (positive anomalies over India and Iran) can be explained by ongoing decreasing (increasing) trends in these regions. The exceptional nature of the summer 2023 Canada fires is highlighted by Plate 2.1z, which shows the number of extreme AOD days in 2023, and by Fig. 2.63d , which focuses on the AOD 550 nm anomaly in July 2023 over the North Hemisphere.

The AOD at 550 nm and PM2.5 trends for 2003–23 and 2012–23 are shown in Figs. 2.64a–d. The trends in AOD and PM2.5 are generally co-located. Between 2003 and 2023, there is a significant negative trend for both AOD and PM2.5 over most of the United States, Europe, East Asia, and parts of the Amazon basin, the latter from reduced deforestation activity. Positive trends are noted over parts of Siberia, which are driven by increased wildfire, as well as over India and Iran, which are driven by an increase in anthropogenic emissions (Satheesh et al. 2017). The trends between 2012 and 2023 show some contrast to those between 2003 and 2023: a stronger decrease over China reflecting a decrease in anthropogenic emissions (Quaas et al. 2022), smaller decreasing trends over Amazonia, Europe, and the United States, and new increases over Bolivia and Paraguay caused by a series of years with large fire events.

Anthropogenic AOD and radiative forcing resulting from aerosol–radiation (RFari) and aerosol–cloud interactions (RFaci) are shown in Fig. 2.65 for 2023 and the period 2003-23, as computed following Bellouin et al. (2020). There was a small increase in anthropogenic AOD in 2023 compared to 2022 (0.061 versus 0.059) and, consequently, aerosol radiative forcing has become slightly more negative by an estimated 0.05 W m^{-2}. These results are in contrast to the decreasing trend in anthropogenic AOD that started in 2018, but cannot yet signify a longer-term reversal.

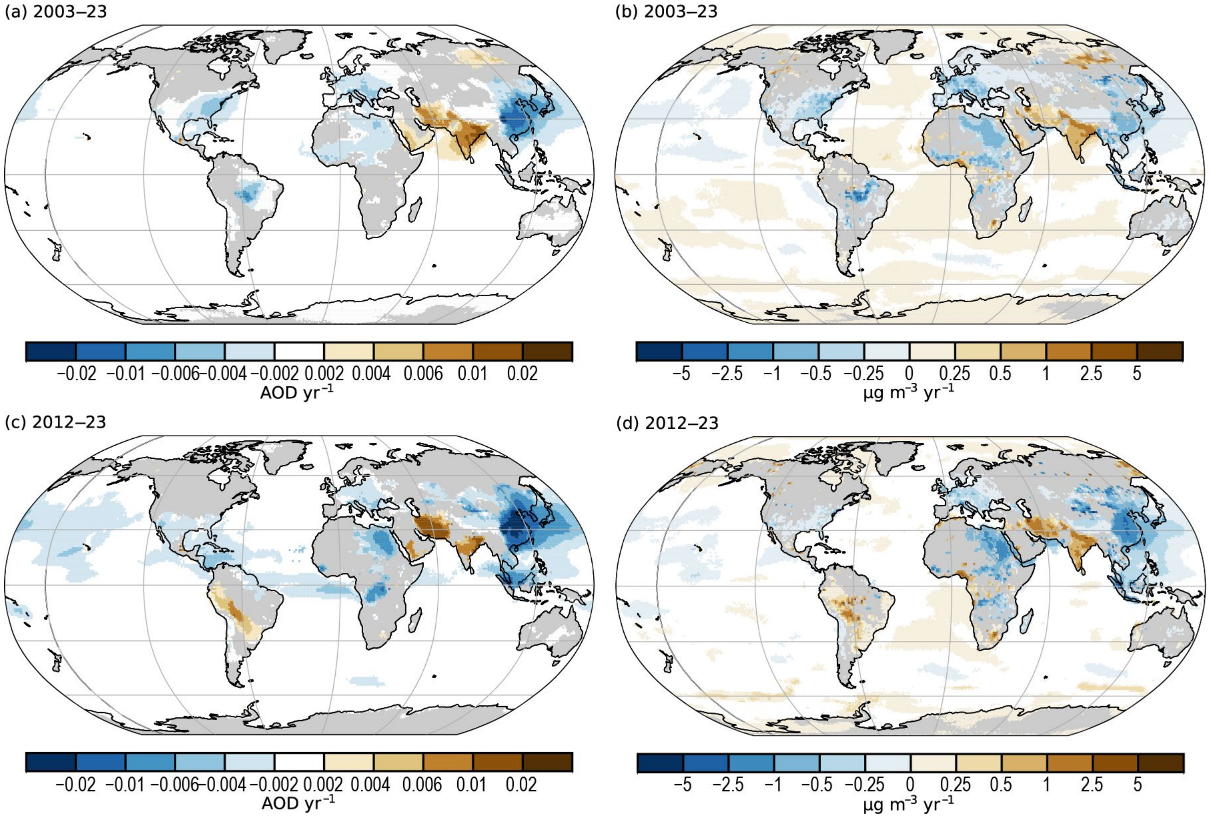

Fig. 2.64. (a),(b) Linear trends of total aerosol optical depth (AOD; AOD unit yr^{-1}) and fine particulate matter (PM2.5; µg m^{-3} yr^{-1}) for 2003–23; and (c),(d) linear trends of total AOD (AOD unit yr^{-1}) and PM2.5 (µg m^{-3} yr^{-1}) for 2012–23. Only trends that are statistically significant (95% confidence level) are shown.

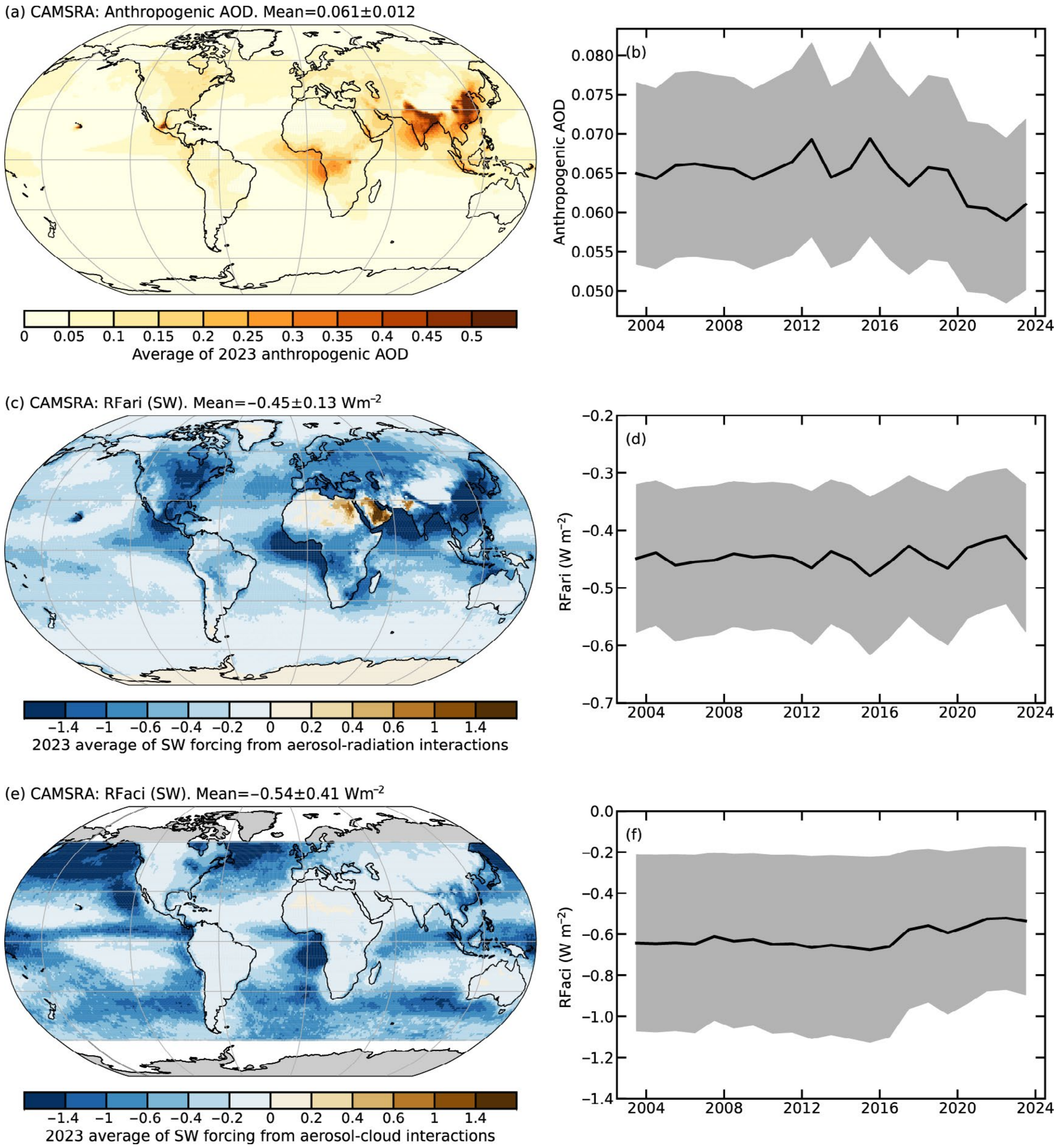

Fig. 2.65. CAMSRA (a) 2023 average of anthropogenic aerosol optical depth (AOD); (b) global annual average of anthropogenic AOD from 2003 to 2023. Radiative forcing in the shortwave (SW) spectrum due to (c),(d) aerosol-radiation (RFari) and (e),(f) aerosol-cloud interactions (RFaci). The left column shows the distributions for 2023. The right column shows time series of global averages for the period 2003–23, with the 1-σ uncertainties of these estimates shown in gray.

4. TROPOSPHERIC OZONE

—O. R. Cooper, J. R. Ziemke, and K.-L. Chang

Tropospheric ozone is a short-lived climate forcer with a global distribution that varies regionally, vertically, and on seasonal and interannual time scales (Forster et al. 2021; Szopa et al. 2021), posing a challenge for trend detection (Chang et al. 2021; Fiore et al. 2022). Atmospheric chemistry models indicate an approximately 40% increase of the tropospheric ozone burden (TOB) since the nineteenth century, and limited observations since the early and mid-twentieth century are consistent with the model estimates (Tarasick et al. 2019). Widespread in situ and satellite observations also record an increase of TOB since the mid-1990s (Gulev et al. 2021); however, new satellite-based observations suggest that the increase of TOB came to an end in 2020 in response to diminished ozone precursor emissions during the economic downturn that was triggered by the coronavirus (COVID-19) pandemic (Miyazaki et al. 2020; Ziemke et al. 2021). With three additional years (2021–23) of no growth in TOB as described below, the year 2020 may be a change point in the TOB record.

The unusual period (2020–23) of no growth in TOB (Fig. 2.66) coincides with observations of negative ozone anomalies (−5%) in the free troposphere above western North America and

Europe during 2020, which were recorded by ozonesondes, infrared spectrometers, and commercial aircraft (Steinbrecht et al. 2021; Clark et al. 2021; Chang et al. 2022, 2023). These anomalies were strongest in summer, when photochemical production is most active, and they are similar in magnitude to negative ozone anomalies detected at high-elevation rural sites in western North America and Europe (Putero et al. 2023). Model simulations of the COVID-19 period indicate that reduced emissions of ozone precursor gases across the Northern Hemisphere led to the ozone decreases (Miyazaki et al. 2020; Steinbrecht et al. 2021), reaching levels similar to those measured in the mid-1990s when ozone precursor emissions were less than 2019 levels (Chang et al. 2022). The models also indicate that the 2020 ozone anomalies were not caused by the unusual ozone depletion event that occurred above the Arctic during the spring of 2020 (Steinbrecht et al. 2021; Wang et al. 2023).

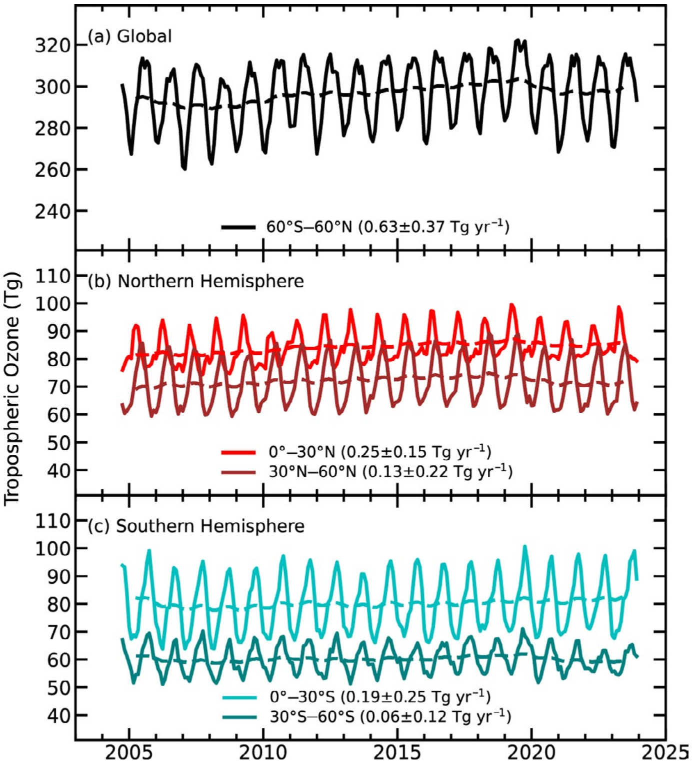

Fig. 2.66. Monthly averages (solid lines) and 12-month running means (dashed lines) of Ozone Monitoring Instrument (OMI)/Microwave Limb Sounder (MLS) tropospheric ozone burdens (Tg) from Oct 2004 through Dec 2023 for (a) 60°S–60°N (black), (b) the Northern Hemisphere tropics (red) and midlatitudes (dark red), and (c) the Southern Hemisphere tropics (blue) and midlatitudes (green). Slopes of linear fits to the data are presented with their 95% confidence-level uncertainties.

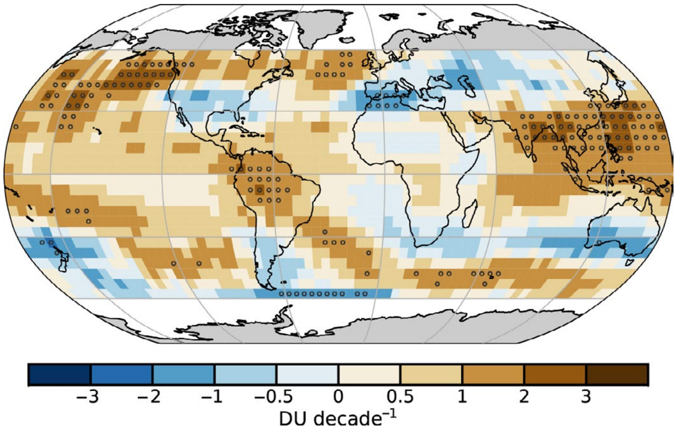

Fig. 2.67. Linear trends in Ozone Monitoring Instrument (OMI)/Microwave Limb Sounder (MLS) tropospheric column ozone (DU decade^{-1}) on a 5° × 5° grid from Oct 2004 through Dec 2023. Circles denote trends with p-values <0.05. Trends were calculated using a multivariate linear regression model (e.g., Randel and Cobb 1994 and references therein) that included a seasonal cycle fit and the Niño-3.4 index as an El Niño–Southern Oscillation proxy; trend uncertainties included autoregressive adjustment via Weatherhead et al. (1998).

The combined Aura Ozone Monitoring Instrument and Microwave Limb Sounder satellite ozone measurements (OMI/MLS) provide a continuous record of the TOB from 60°S to 60°N for the period 2004–23 (Ziemke et al. 2019). The vertical resolution of OMI/MLS monthly tropospheric column ozone is ~3 km near the tropopause with a regional precision of ~2 Dobson units (DU; 7%); trend uncertainties are about 0.5 DU decade^{-1} (1.5% decade^{-1}). Positive tropospheric column ozone anomalies were widespread across the Northern Hemisphere in 2023 (relative to 2005–22), with peak values above South Asia, East Asia, and the North Pacific Ocean, while relatively weak negative anomalies occurred above southern Africa, Australia, and New Zealand (Plate 2.1aa). Global TOB (60°S–60°N) increased at the rate of 1.06±0.48 Tg yr^{-1} for the first 15 years of the record (2004–19), equal to a total increase of ~5% (Fig. 2.66). There was a slight drop in TOB in 2020, likely due to reduced ozone precursor emissions during the COVID-19 pandemic, as described above (Fig. 2.66). The tropospheric ozone burden remained at similar levels during 2021–23, mainly driven by decreases in northern midlatitudes (Figs. 2.66a–c). Regionally, the strongest positive trends (2004–23) have occurred above South and East Asia and across much of the North Pacific Ocean, along with Amazonia (Fig. 2.67). Weak but widespread ozone decreases are present above North America, Europe, Central Asia, Siberia, northern and southern Africa, Australia, and New Zealand, with the strongest decreases above North Africa and the western Mediterranean.

Tropospheric ozone burden trends cannot be assessed from surface records because surface trends are often decoupled from the trends in the free troposphere above (Gulev et al. 2021), and the limited availability of long-term surface records precludes the construction of a data record that is globally representative; however, long-term surface records at remote locations are critical for evaluating the performance of global chemistry-climate models. Ozone trends from six such sites are reported here, based on records more than 20 years in length (Fig. 2.68; Table 2.11). Two records—those of the Mauna Loa Observatory in Hawaii, and the Barrow Atmospheric Observatory in Alaska—now span 50 years and report positive surface ozone trends of 0.93±0.39 ppbv decade^{-1} and 0.50±0.34 ppbv decade^{-1}, respectively. The 48-year record at South Pole also reports a positive albeit weaker trend of 0.32±0.34 ppbv decade^{-1}. The observations show no trend at Arrival Heights, Antarctica, since 1996. There is some evidence of a decrease at Tudor Hill, Bermuda, since 1988 (–0.81±1.10 ppbv decade^{-1}), as well as clear evidence of a decrease at Summit, Greenland, since 2000 (–2.00±0.93 ppbv decade^{-1}).

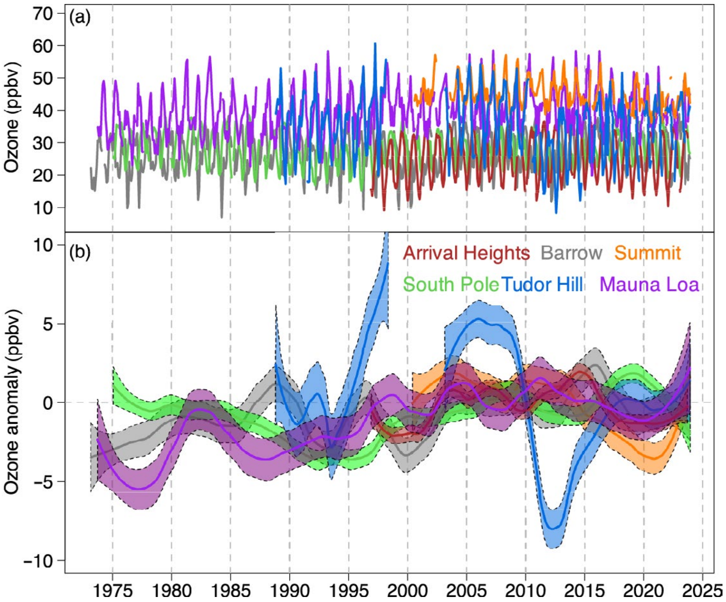

Fig. 2.68. (a) Monthly mean surface ozone (ppb) at Barrow Observatory, Alaska (gray), Summit, Greenland (orange), Tudor Hill, Bermuda (blue), Mauna Loa, Hawaii (purple), Arrival Heights, Antarctica (red), and South Pole (green). Monthly means are produced for months with at least 50% data availability using observations from all 24 hours of the day. The locations of each site are listed in Table 2.11. (b) As in panel (a), except the time series have been converted to monthly anomalies, referenced to the monthly climatological values over 2000–20, and smoothed using a locally weighted scatterplot smoothing regression.

Table 2.11. Surface ozone trends at the six baseline monitoring sites shown in Fig. 2.68 Trends are estimated by the generalized least squares method, based on monthly anomalies referenced to the monthly 2000–20 base period (Chang et al. 2021), and reported with 95% confidence intervals and *p*-values.

Site name — latitude, longitude, elevation (m)	Yrs with data	Trend, ppbv decade^{-1}	*p*-value
Summit, Greenland — 72.6°N, 38.5°W, 3238 m	2000–present	–2.00±0.93	p<0.01
Barrow Atmospheric Observatory, Alaska — 71.3°N, 156.6°W, 11 m	1973–present	0.50±0.34	p<0.01
Tudor Hill, Bermuda — 32.3°N, 64.9°W, 30 m	1988–1998, 2003–present	–0.81±1.10	p=0.14
Mauna Loa Observatory (MLO), Hawaii — 19.5°N, 155.6°W, 3397 m	1973–present	0.93±0.39	p<0.01
Arrival Heights, Antarctica — 77.8°S, 166.8°W, 50 m	1996–present	0.23±0.53	p=0.39
South Pole, Antarctica — 90.0°S, 59.0°E, 2840 m	1975–present	0.32±0.34	p=0.06

5. STRATOSPHERIC AEROSOLS

—S. Khaykin, G. Taha, T. Leblanc, T. Sakai, I. Morino, B. Liley, and S. Godin-Beekmann

Stratospheric aerosols play a large role in the chemical and radiative balance of the atmosphere (Kremser et al. 2016). Explosive volcanic eruptions may directly inject sulfur dioxide (SO_2) and ash into the stratosphere, leading to significant perturbations of stratospheric aerosol burden at hemispheric and global scales lasting from several months to several years. Another important source of particulate matter in the stratosphere is the increasingly intense wildfires (Peterson et al. 2021; Fromm et al. 2022).

Figure 2.69 shows 24 years of stratospheric aerosol optical depth (sAOD) observations by the ground-based Network for the Detection of Atmospheric Composition Change lidars at Observatoire de Haute Provence (OHP), France (43.9°N), and Lauder observatory, New Zealand (45.0°S), together with zonally averaged satellite data. These stations, antipodally located on the globe, respectively represent the northern and southern extratropics. The OHP time series (Fig. 2.69a) from 2000 to 2023 is largely modulated by several moderate volcanic eruptions as well as by the extreme British Columbia pyrocumulonimbus wildfire outbreak in August 2017 (Peterson et al. 2018), which led to a prolonged perturbation of stratospheric aerosol composition and burden. The largest impact on the NH sAOD in terms of magnitude and longevity of the perturbation was generated by the Raikoke volcanic eruption in 2019. The decay of the Raikoke sAOD perturbation appears to be longer than those of other midlatitude eruptions of similar magnitude. This is possibly due to the diabatic lofting of ash-rich Raikoke plumes that were shown to self-organize into persistent stratospheric anticyclones (Khaykin et al. 2022a). Such behavior has previously been reported for the wildfire smoke aerosols (Khaykin et al. 2020) that contain highly absorptive black carbon; however, it was unexpected for the volcanic aerosols, composed primarily of non-absorbing sulfates.

Significant sAOD perturbations in the Southern Hemisphere (SH; Fig. 2.69b) were nearly absent for more than two decades until the 2015 Calbuco volcanic eruption in Chile. The record-breaking 2019/20 "Australian New Year Super Outbreak" (ANYSO) wildfires boosted the SH sAOD to four times the background level according to Stratospheric Aerosol and Gas Experiment (SAGE) III and surpassed the Raikoke-induced NH perturbation (Khaykin et al. 2020), which was deemed

(a) OHP lidars (43.9°N) and satellites zonal/monthly means 40°N–50°N

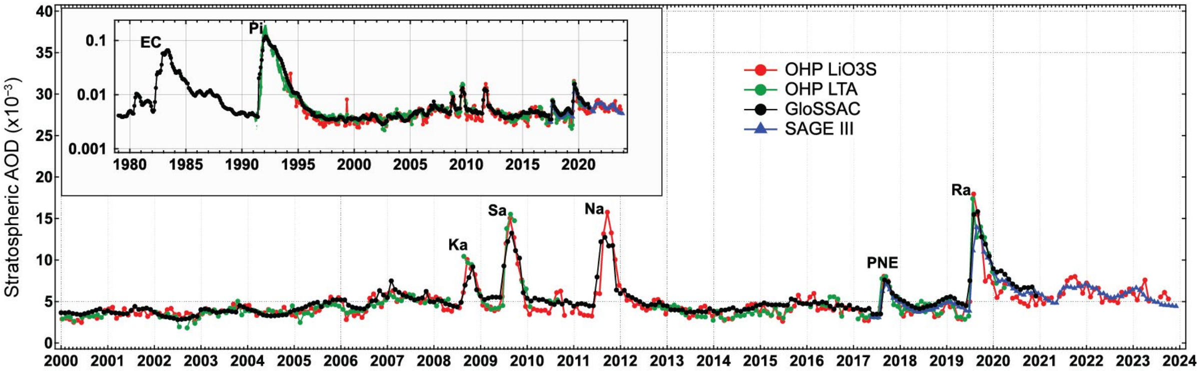

(b) Lauder lidar (45°S) and satellite zonal/monthly means 40°S–50°S

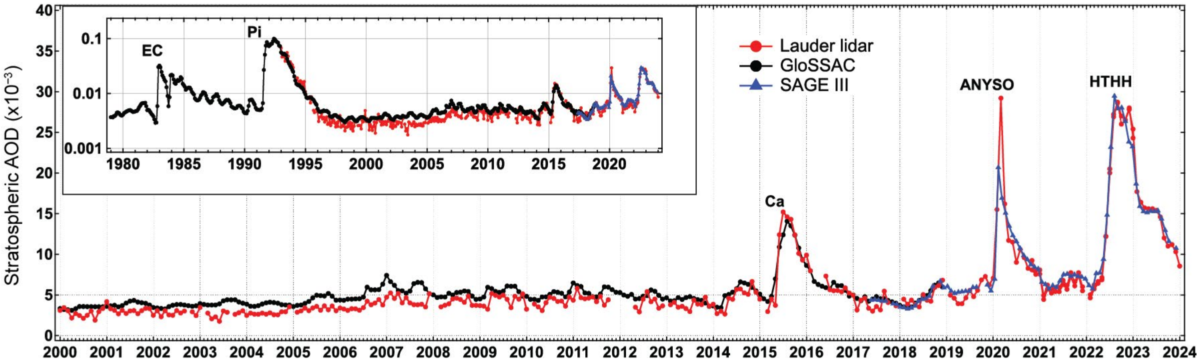

Fig. 2.69. Time series of monthly mean stratospheric aerosol optical depth (sAOD) at 532 nm of the stratospheric layer between 380 K and 1000 K potential temperature from ground-based lidars at (a) French Observatoire de Haute Provence (OHP, 43.9°N, 5.7°E, LiO$_3$S, and LTA lidars, red and green curves) and (b) New Zealand's Lauder station (45.0°S, 169.7°E, Lauder aerosol lidar, red curve) and the corresponding monthly/zonal-mean values from satellite observations within 40°N–50°N and 40°S–50°S latitude bands from the International Space Station's Stratospheric Aerosol and Gas Experiment (SAGE) III instrument (blue curves) and GloSSAC (Global Satellite-based Stratospheric Aerosol Climatology) merged satellite record (black curves). The embedded panels display the log-scaled time series from the beginning of the GloSSAC record. The literal notations indicate the most significant volcanic eruptions: El Chichon (EC), Pinatubo (Pi), Kasatochi (Ka), Sarychev (Sa), Nabro (Na), Raikoke (Ra), Calbuco (Ca), and Hunga Tonga–Hunga Haʻapai (HTHH); and wildfire events: Pacific Northwest Event (PNE; British Columbia, Canada), and Australian New Year Super Outbreak (ANYSO).

the 30-year high at that time (Leblanc et al. 2020). The ANYSO outbreak led to a prolonged perturbation in the entire SH with the decay exceeding one year.

More recently, the 30-year global sAOD record has been surpassed again, following the eruption of the Hunga Tonga–Hunga Ha'apai (HTHH) volcano on 15 January 2022, which was marked by extreme explosiveness with aerosols reaching an altitude above 50 km (Carn et al. 2022; Khaykin et al. 2022b). Aerosol layers were detected by the Ozone Mapping and Profiler Suite–Limb Profiler (OMPS-LP) instrument above 40 km, though the bulk of HHTH aerosols was bounded within the 20-km to 30-km layer (Taha et al. 2023).

The meridional evolution of the sAOD (Fig. 2.70a) shows that the HTHH-induced perturbation was mostly restricted to the tropical belt during the first four months after the eruption, although some transport into southern high latitudes occurred as early as February 2022 (Khaykin et al. 2022b). The transport of the bulk of volcanic material into the southern extratropics occurred in June 2022; however, its further penetration towards the pole was hindered by a strong transport barrier at the edge of the Antarctic stratospheric vortex that had been fully established by that time (Manney et al. 2023). By early 2023, the HTHH aerosols had spread across the entire SH and, unlike in 2022, were then entrained by the 2023 Antarctic vortex.

While the bulk of the HTHH sAOD perturbation has been restricted to the tropical belt and the SH, limited transport to the northern extratropics can be seen by tracking the anomalies in the aerosol extinction vertical profiles. Figure 2.70b displays the meridional transport of the HTHH sulfate aerosols expressed as the potential temperature of the peak extinction ratio (ER; aerosol-to-molecular extinction ratio) from OMPS-LP observations. The data suggest that the first intrusions into the northern extratropics occurred in April 2022, after which ground-based lidars in the NH extratropics started reporting weak yet distinct aerosol layers in the mid-stratosphere (Khaykin et al. 2022b). Further NH midlatitude intrusion episodes occurred during November 2022–January 2023. The vertical evolution of the peak ER (Fig. 2.70b) reveals that sedimentation of HTHH sulfate aerosols was slower in the tropics, where it is partly compensated by upwelling, and faster towards the poles.

Additional stratospheric aerosols detected in the NH mid- and high latitudes from April through November 2023 (Figs. 2.70a,b) can be traced to the eruption of Shiveluch volcano in the Kamchatka peninsula on 14 April 2023, as well as to a series of wildfire outbreaks in Canada and Siberia that led to a significant season-wide pollution of the lowermost stratosphere with smoke aerosols.

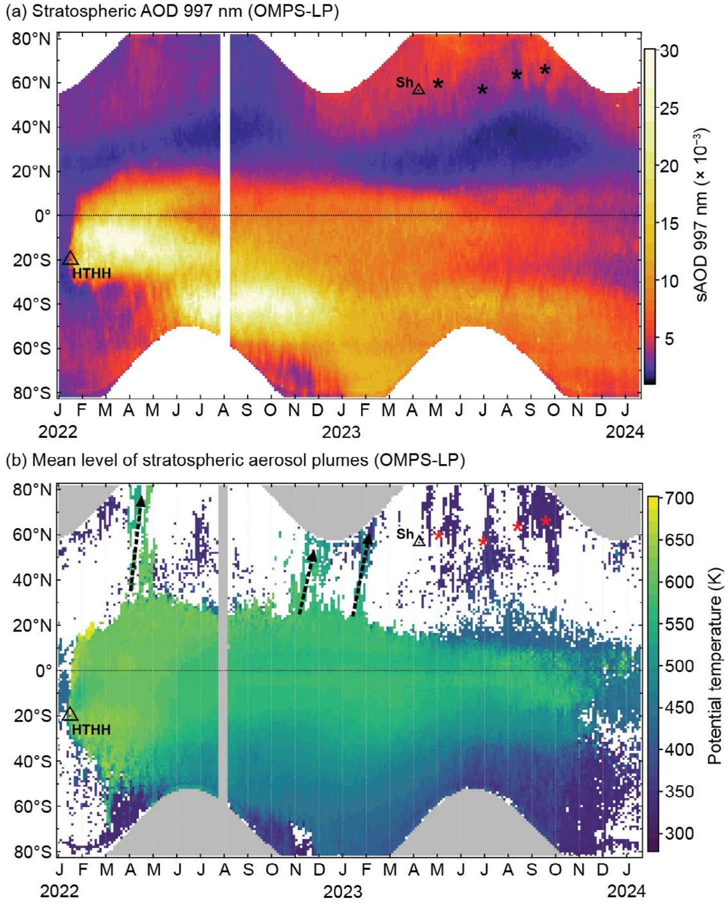

Fig. 2.70. Time–latitude evolution of the stratospheric aerosol from OMPS-LP observations at 997 nm in 2022/23. (a) Zonal-mean stratospheric aerosol optical depth (sAOD). (b) Mean potential temperature of the stratospheric peak of extinction ratio for the samples with ERmax>6, which corresponds to departures beyond ~7 sigma of the background variability in the given bin. This method allows for the detection of optically thin yet distinct aerosol layers, which are hard to spot using zonally averaged sAOD. The dashed arrows in (b) indicate the episodes of Hunga Tonga–Hunga Ha'apai (HTHH) aerosol intrusions into the Northern Hemisphere extratropics. The large and small triangles in (a) and (b) indicate the eruptions of HTHH and Shiveluch, respectively, whereas the black stars in (a) and red stars in (b) indicate wildfire events with measurable stratospheric impact in Canada and Russia during summer 2023.

6. STRATOSPHERIC OZONE

—M. Weber, W. Steinbrecht, C. Arosio, R. van der A, S. M. Frith, J. Anderson, L. M. Ciasto, M. Coldewey-Egbers, S. Davis, D. Degenstein, V. E. Fioletov, L. Froidevaux, D. Hubert, D. Loyola, A. Rozanov, V. Sofieva, K. Tourpali, R. Wang, T. Warnock, and J. D. Wild

Stratospheric ozone protects the ecosystem from harmful ultraviolet radiation. The total ozone column is an indicator of the level of protection from this radiation. About 90% of the total column amount resides in the stratosphere, and the number of ozone molecules is maximum at about 20-km to 25-km altitude (lower stratosphere), an altitude range that is called the ozone layer. Long-term changes in stratospheric ozone are governed by declining stratospheric halogens (chemistry) from man-made ozone-depleting substances (ODSs) and by the current and future greenhouse gas concentrations in the atmosphere (chemistry and circulation; WMO 2022).

In 2023, total column ozone was, on average, slightly lower compared to the 1998–2008 reference period in the NH, while in the SH from 35°S to 60°S, it was higher by up to 10 DU–15 DU (Plate 2.1ab). Antarctic total column ozone was close to the long-term mean except for in a small region south of Australia (Plate 2.1ab). The year 2023 ends a series of three years with below-average ozone values for the SH extratropics. The SH total column ozone was unusually low in 2022 (Figs. 2.71d,e), mainly due to circulation changes but also due to enhanced chemical destruction following the HTHH volcanic eruption in January 2022 (e.g., Santee et al. 2022; Evan et al. 2023; Fleming et al. 2024). In the tropics (Fig. 2.71c), total ozone was higher by a few DU compared to previous years but was within the year-to-year variability (two sigma) of the last two decades. Globally, total ozone levels

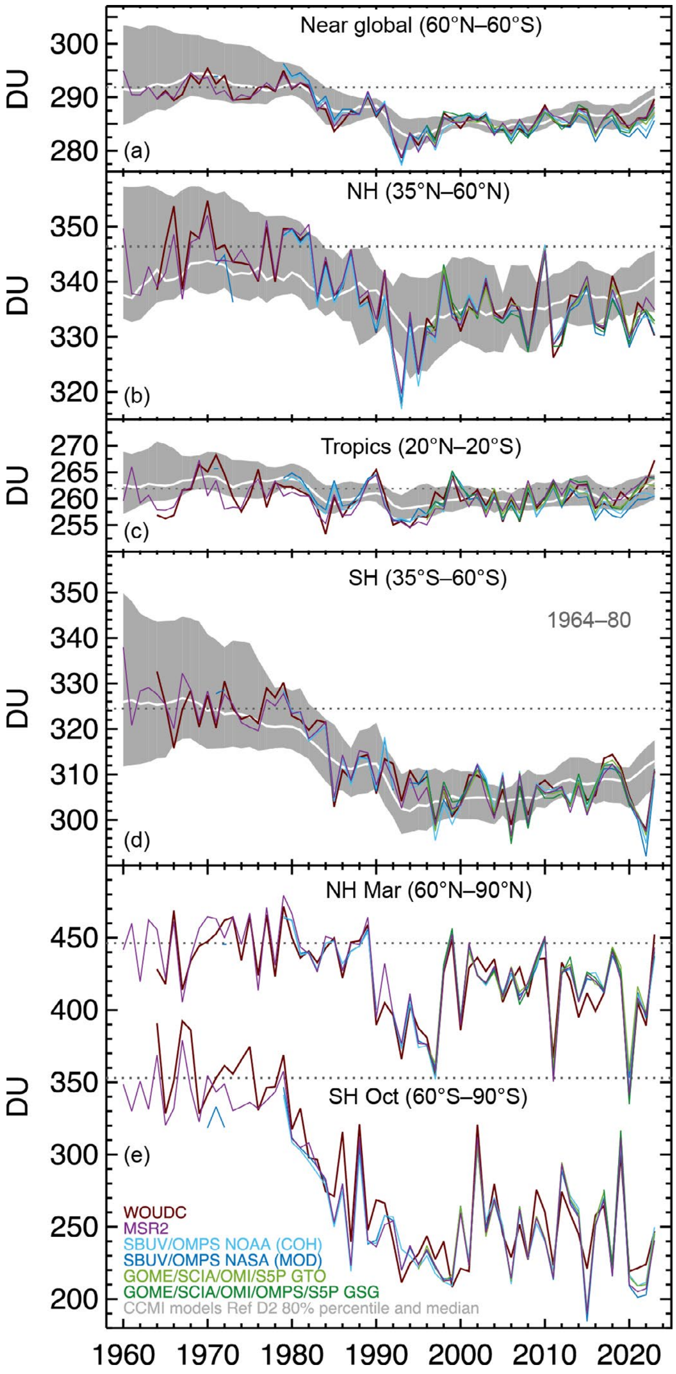

Fig. 2.71. Time series of annual mean total column ozone (DU) in (a)–(d) four zonal bands and (e) polar (60°–90°) total column ozone in Mar (Northern Hemisphere [NH]) and Oct (Southern Hemisphere [SH]), the months when polar ozone losses usually are largest. Data are from the World Ozone and Ultraviolet Radiation Data Centre (WOUDC) ground-based measurements combining Brewer, Dobson, SAOZ, and filter spectrometer data (red: Fioletov et al. 2002, 2008); the BUV/SBUV/SBUV2/OMPS merged products from NASA (V8.7; dark blue; Frith et al. 2014; 2017), and NOAA (SBUV V8.6, OMPS V4r1; light blue; Jeannette Wild, NOAA, 2024, personal communication); the GOME/SCIAMACHY/GOME-2/OMPS/TROPOMI products (GSG) from University of Bremen (dark green, Weber et al. 2022), and GTO from the EU's German Aerospace Center (DLR; light green; Coldewey-Egbers et al. 2022; Garane et al. 2018). MSR-2 (purple) assimilates nearly all ozone datasets after corrections based on the ground-based data (van der A et al. 2015). The dotted gray lines in each panel show the average total column ozone level for 1964–80 calculated from the WOUDC data. Most of the observational data for 2023 are preliminary. The thick white lines in (a)–(d) show the median from chemistry-climate CCMI-2022 ref D2 model runs (Plummer et al. 2021). The model data have been smoothed using a three-point triangle function. The gray-shaded areas provide the 80% percentile range for the model data. All datasets have been bias-corrected by subtracting individual data averages and adding the multi-instrument mean in the reference period (1998–2008).

in 2023 were close to the long-term average of the last 20 years and broadly agree with projections from chemistry-climate models (CCMs) using current scenarios of ODSs and greenhouse gases, as shown in Figs. 2.71a–d.

Figures 2.72d,e show that ozone at 50 hPa (~22-km altitude) in the tropics and northern midlatitudes behaved similarly to the total column (Figs. 2.71b,c). In 2023, the NH annual mean was nearly unchanged from previous years (Fig. 2.72d). Ozone at 50 hPa was slightly higher in the tropics in 2023 but still within the year-to-year variability of the last decade (Fig. 2.72e), and larger than in 2022 by about 5% in the SH (Fig. 2.72f), bringing it closer to the long-term average. In the upper stratosphere (2 hPa or 42-km altitude; Figs. 2.72a–c), ozone observations show a clear increase since the mid-1990s, averaging 0.2±0.15% yr^{-1}. The 2023 annual means follow the long-term trend, again in general agreement with the broad range predicted by CCMs.

In the SH midlatitude, elevated total column ozone (Plate 2.1ab; Fig. 2.71d) and ozone in lower stratosphere (Fig. 2.72f) in 2023 compared to 2022 is probably related to the strong El Niño that started to emerge in the middle of 2023. El Niños are linked to a strengthening of the Brewer-Dobson (BD) circulation and a weakening of the polar vortex, which both increase extratropical ozone by enhancing ozone transport from the tropical stratosphere to higher latitudes and by reducing the potential for the formation of widespread polar stratospheric clouds and subsequent large chemical ozone depletion in polar spring (e.g., Domeisen et al. 2022; Butchart 2014). The quasi-biennial oscillation (QBO) was in its westerly phase from September 2022 until the end of boreal summer 2023. This is associated with a weaker BD circulation and typically results in lower extratropical and higher tropical ozone columns. In the first half of 2023, this resulted in lower stratospheric ozone in the NH (e.g., Baldwin et al. 2001). The QBO turned easterly during the second half of 2023, coinciding with the strengthening of El Niño. The combined effect on SH ozone resulted in positive anomalies at southern midlatitudes (Plate 2.1ab; Figs. 2.71d,e, 2.72f).

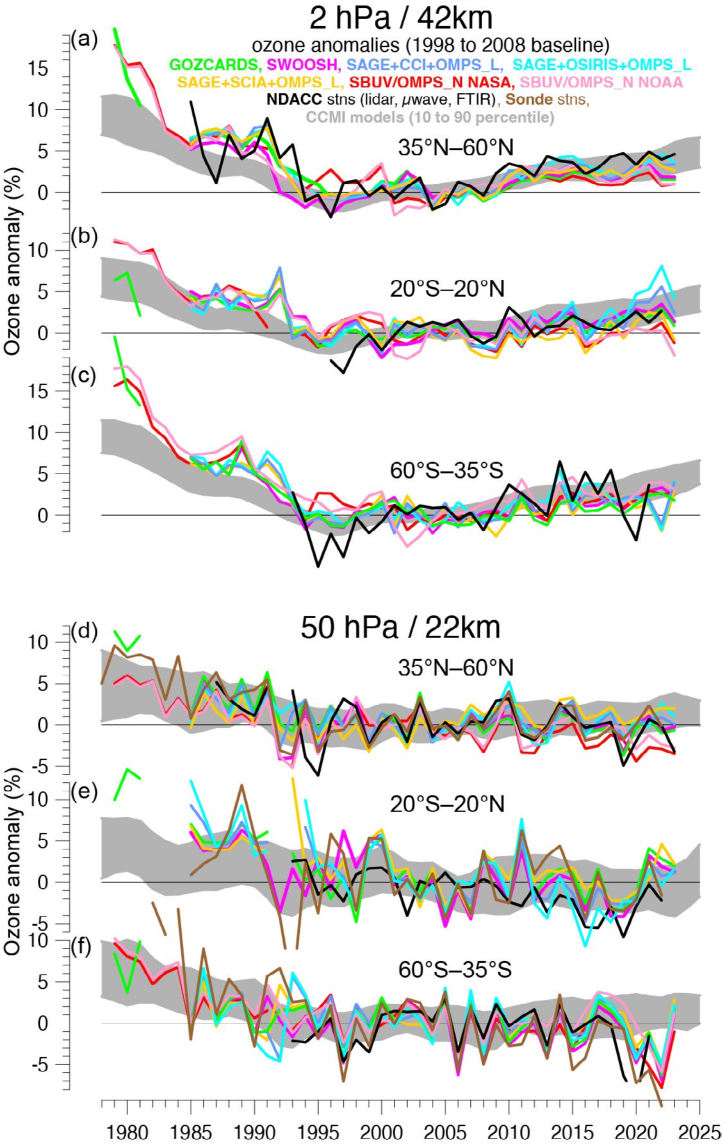

Fig. 2.72. Annual mean anomalies of ozone (%) in (a)–(c) the upper stratosphere near 42-km altitude or 2-hPa pressure, and (d)–(f) the lower stratosphere, near 22 km or 50 hPa for three zonal bands: 35°N–60°N, 20°S–20°N (tropics), and 35°S–60°S, respectively. Anomalies are with respect to the 1998–2008 baseline. Colored lines are long-term records obtained by merging different limb (GOZCARDS, SWOOSH, SAGE+CCI+OMPS_L, SAGE+OSIRIS+OMPS_L, SAGE+SCIAMACHY+OMPS_L) or nadir-viewing (SBUV, OMPS_N) satellite instruments. The nadir-viewing instruments have much coarser altitude resolution than the limb-viewing instruments. This can cause differences in some years, especially at 50 hPa. The black line is determined from merging ground-based ozone records at seven Network for the Detection of Atmospheric Composition Change (NDACC) stations employing differential absorption lidars and microwave radiometers. See Steinbrecht et al. (2017), Arosio et al. (2019), and Godin-Beekmann (2022) for details on the various datasets. Gray-shaded areas show the range of chemistry-climate model simulations from CCMI-1 refC2 (SPARC/IO3C/GAW 2019). Ozone data for 2023 are not yet complete for all instruments and are still preliminary.

7. STRATOSPHERIC WATER VAPOR

—S. M. Davis, K. H. Rosenlof, E. Asher, H. Vömel, R. M. Stauffer, and D. F. Hurst

In the aftermath of the January 2022 eruption of the Hunga Tonga–Hunga Ha'apai (HTHH) volcano (20.5°S, 175.4°W), which injected ~50 Tg–150 Tg water vapor (WV) into the stratosphere (3.5%–10% of the entire stratospheric burden; Millán et al. 2022; Vömel et al. 2022), WV concentrations remained at or near record-high levels through much of the stratosphere in 2023. By being injected into the tropical stratosphere between approximately 26 km (22 hPa) and 34 km (6 hPa), air from the eruption bypassed the tropical tropopause layer (TTL) "cold trap" that normally controls the amount of WV entering the stratosphere (Fig. 2.73a). This dramatic perturbation to WV and other stratospheric species (e.g., ozone; section 2g6) is expected to persist for years.

At the beginning of 2023, the HTHH stratospheric WV perturbation had already been transported upward within the rising branch of the Brewer-Dobson circulation in the tropics (Fig. 2.73a) and poleward into each hemisphere (Fig. 2.73b). The majority of the WV perturbation was still in the SH in January 2023. This hemispheric asymmetry was caused by the location and timing of the eruption, which was followed by strong poleward transport up to the SH polar vortex edge in the 2022 austral winter.

In 2023, the HTHH WV perturbation continued to spread poleward and downward in the NH (Figs. 2.74c,f,i). By the end of the year, elevated WV was evident in the lower stratosphere at high northern latitudes down to ~68 hPa/~19 km (Fig. 2.74i). Whereas the tropical (15°S–15°N) mean WV was at a record level in the mid-stratosphere (near ~30 hPa/24 km) for much of 2022 (relative to the 2004–21 mean), monthly WV anomalies in 2023 were at record levels in the upper stratosphere (Fig. 2.73a). For example, at and above 10 hPa/31 km, anomalies were 1.2 ppm to 1.8 ppm (parts per million, i.e., μmol mol^{-1}), corresponding to a deviation from the climatological mean of ~25%–30% (~10 std. dev.).

Even though the mid- and upper-stratospheric WV anomalies were most dramatic in 2023, lower-stratospheric WV anomalies (near 82 hPa/17 km) were also positive (wet) for all months (e.g., Figs. 2.73a,c), following a general trend towards more positive anomalies in the last five years, which is also evident in frost point measurements from the set of balloon-launching stations with long-term records (Fig. 2.75).

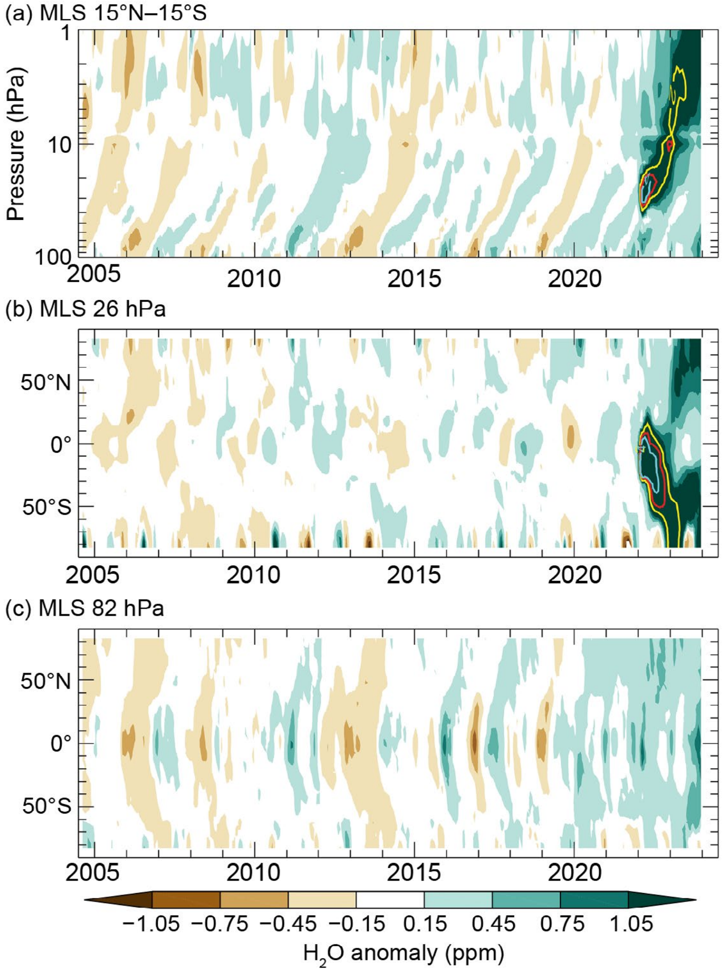

Fig. 2.73. (a) Vertical–time contour of tropical (15°S–15°N) lower-stratospheric water vapor (WV) anomalies, with the +2-, +3-, and +4-ppm values shown as yellow, red, and cyan contour lines, respectively. (b),(c) Latitude–time contour of WV anomalies at (b) 26 hPa and (c) 82 hPa, respectively. All panels are based on version 5.0 Aura Microwave Limb Sounder (MLS) data, which has collected near-global (82°S–82°N) measurements since Aug 2004. Anomalies are differences from the mean 2004–2021 water vapor mixing ratios (ppm) for each month. (a) shows the unprecedented injection of water vapor directly into the stratosphere by the Hunga Tonga–Hunga Ha'apai (HTHH) eruption, followed by its slow ascent through the tropical stratosphere. (b) shows the southward propagation of the plume at 26 hPa in 2022, followed by the downward transport of the HTHH-related anomalies in 2023, while (c) shows a more typical propagation of interannual-varying tropical lower-stratospheric WV anomalies to higher latitudes in both hemispheres following the second-warmest coldpoint and record wet tropical lower-stratospheric WV in 2023. (c) also shows the influences of dehydrated air masses from the Antarctic polar vortex as they are transported toward the Southern Hemisphere midlatitudes at the end of each year. Tick marks denote the beginning of each year.

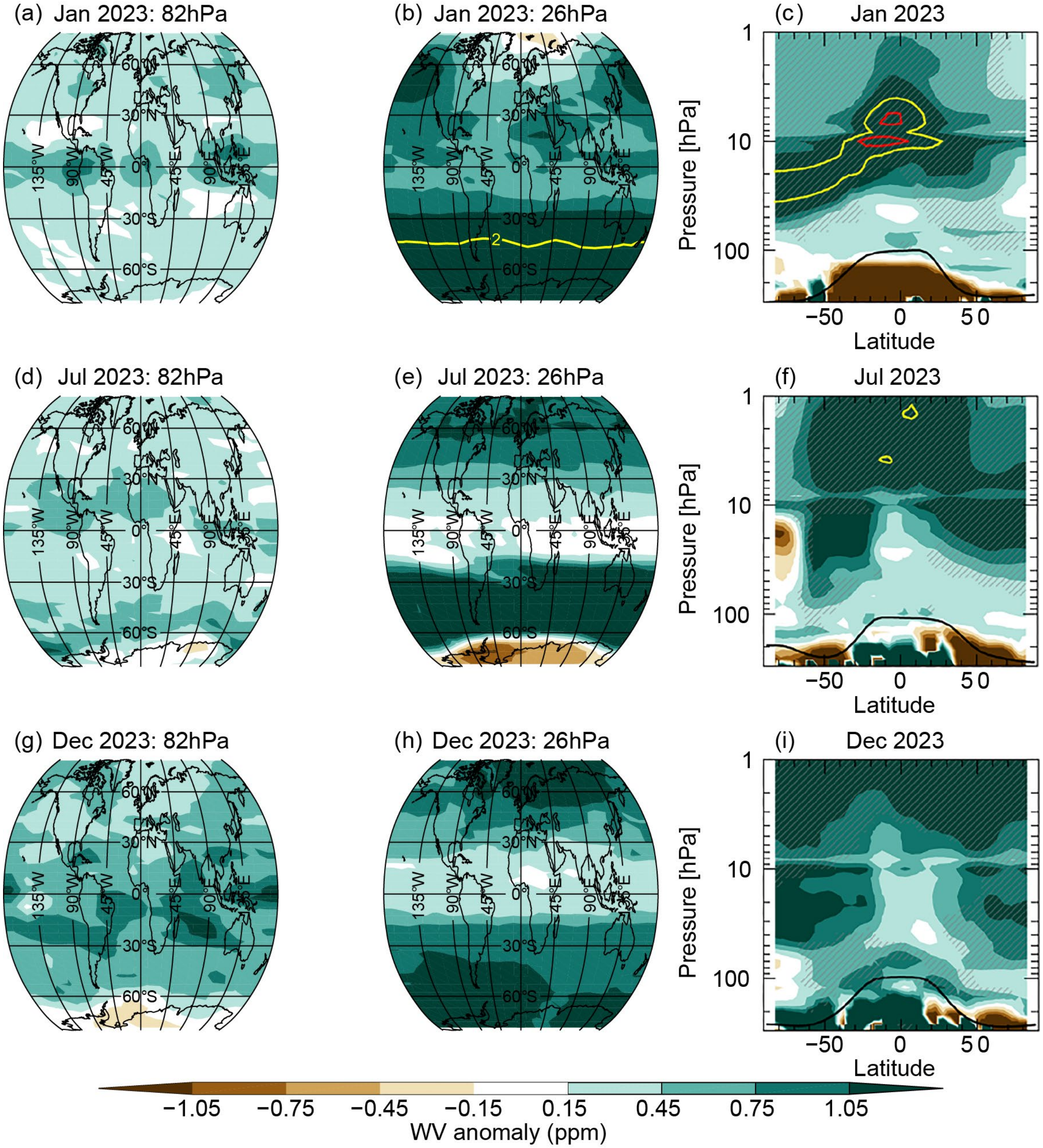

Fig. 2.74. Deseasonalized monthly lower stratospheric Aura Microwave Limb Sounder (MLS) anomalies (ppm; 2004–21 base period) at (a),(d),(g), 82 hPa and (b),(e),(h) 26 hPa. (c),(f),(i) show latitude–height cross-sections of the water vapor (WV) anomalies. Data are shown for Jan 2023 (top row), Jul 2023 (middle row), and Dec 2023 (bottom row). WV anomalies of +2 ppm and +3 ppm are shown with yellow and red contour lines, respectively. Hatching in the right column shows where the zonal-mean WV was at record values for the given month.

The 2023 WV anomalies in the lowermost tropical stratosphere are expected to be primarily caused by anomalies in tropical tropopause temperatures, although a contribution from WV-impacted air from higher latitudes via mixing is also plausible. Considering the whole time series, lower-stratospheric WV anomalies from the Aura Microwave Limb Sounder (MLS) and frost point hygrometers are highly correlated with tropical (15°S–15°N) cold-point tropopause (CPT) temperature anomalies (Figs. 2.75b,c). In 2023, tropical CPT temperatures were the second highest on record (annual mean anomaly was +0.73 K; second only to 2022, which was +0.76 K), and MLS tropical stratospheric WV entry values at 82 hPa were at their highest recorded levels in the 20-year MLS record (2023 annual mean anomaly was +0.39 ppm, compared to +0.27 ppm in 2022).

La Niña conditions were present at the beginning of 2023 (see section 4b), which during boreal winter are typified by weaker tropical lower-stratospheric upwelling and anomalously warmer CPTs (e.g., Garfinkel et al. 2021). The positive tropical lower-stratospheric WV anomalies at the beginning of 2023 are thus consistent with the expected La Niña response. Following a brief transition to neutral conditions, El Niño conditions emerged in May and strengthened through the rest of the year (see section 4b). The net effect of ENSO on water vapor is complex, but there is some evidence of moistening associated with strong El Niño events (Garfinkel et al. 2018).

The quasi-biennial oscillation (QBO) phase at 70 hPa was westerly throughout 2023 (section 2e3). The QBO westerly phase is associated with anomalously weak tropical upwelling and warm temperatures, which can impact the CPT. Thus, the QBO westerlies and La Niña likely enhanced lower-stratospheric WV at the beginning of 2023, while the effects of the strong El Niño may have contributed to the record-breaking stratospheric entry values of water vapor later in the year.

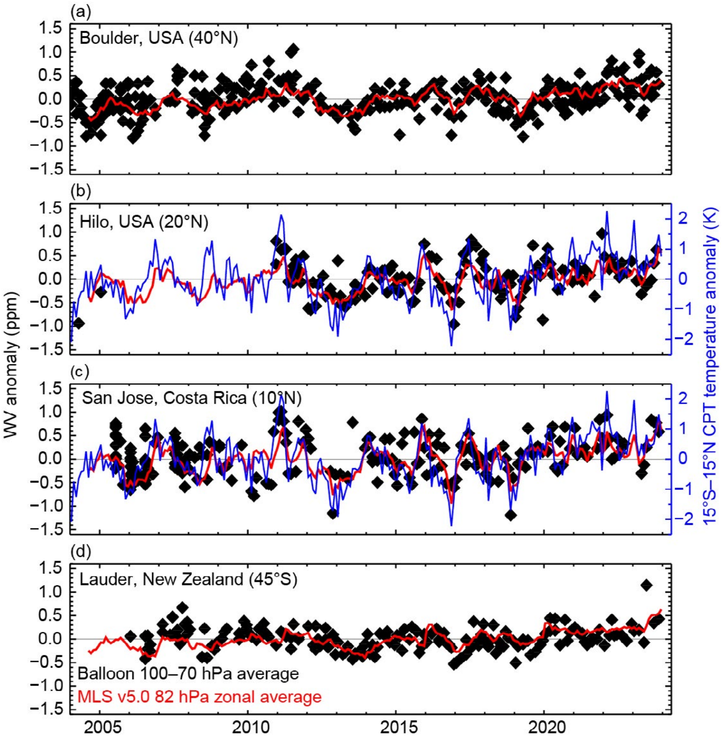

Fig. 2.75. Lower-stratospheric water vapor (WV) anomalies over four balloon-borne frost point (FP) hygrometer stations. Each panel shows the lower-stratospheric anomalies of individual FP soundings (black) and of monthly zonal averages from Microwave Limb Sounder (MLS) data at 82 hPa in the 5° latitude band containing the FP station (red). High-resolution FP vertical profile data were averaged between 70 hPa and 100 hPa to emulate the MLS averaging kernel for 82 hPa. Each MLS monthly zonal mean was determined from 2000–3000 profiles. Anomalies for MLS and FP data are calculated relative to the 2004–21 period for all sites except Hilo (2011–21). Tropical cold-point tropopause anomalies based on the MERRA-2 reanalysis ([b],[c], blue curve) are generally well correlated with the tropical lower-stratospheric WV anomalies.

8. CARBON MONOXIDE

—J. Flemming and A. Inness

The global burden of carbon monoxide (CO) increased in 2023 compared to previous years due to exceptionally high emissions from wildfires in Canada (Plate 2.1ac; Fig. 2.76; section 2h3; see Sidebar 7.1). Western Canada (i.e., Northwest Territories, Alberta) experienced increased fire frequency from May to September, and eastern Canada (i.e., Quebec) was the center of wildfires in May and June (see Sidebar 7.1). The resulting emissions led to increased total-column CO values of up to 25% in the affected areas and the outflow region over the Atlantic.

Carbon monoxide is emitted into the atmosphere by combustion processes originating from anthropogenic sources, such as road transport and energy generation, as well as from wildfires (Szopa et al. 2021). Of similar or larger size than these emissions is the chemical production of CO in the atmosphere from formaldehyde as part of the oxidation chains of methane, isoprene, and other volatile organic trace gases. Oxidation of CO by reaction with the hydroxyl radical is the main loss process for CO, resulting in an atmospheric lifetime of one to two months. The presence of CO is one of the factors that controls the abundance of tropospheric ozone, which is a short-lived pollutant and climate forcer (section 2g4).

According to the CAMS (https://atmosphere.copernicus.eu/) reanalysis of atmospheric composition (Inness et al. 2019), the global CO burden has decreased over the last 20 years (Fig. 2.76a). The decrease is likely caused by both decreased anthropogenic emissions in most parts of the world, as well as a strong decrease in fire frequency compared to the early 2000s, mainly in South America. In recent years, positive global and regional CO anomalies have occurred because of intense wildfires related to exceptional regional meteorological conditions such as the peat fires in Indonesia in 2015 that were associated with El Niño conditions, or boreal wildfires such as those in Siberia during a heatwave in 2021. The positive CO anomalies in 2023 in North America (Fig. 2.76b) and western Australia were also caused by increased wildfire activity supported by exceptionally warm and dry conditions, some possibly related to the onset of El Niño in May 2023. The main areas of seasonal savanna wildfires, such as tropical Africa and tropical South America, showed negative anomalies in 2023 (Plate 2.1ac).

CAMS has produced a retrospective analysis of CO, aerosols, and ozone since 2003 by assimilating satellite retrievals of atmospheric composition with the European Centre for Medium-Range Weather Forecasts (ECMWF) model (Inness et al. 2019). This reanalysis assimilated global thermal infrared total-column CO retrievals (V6 from 2003 to 2016; NRT V7 from January 2017 to June 2019; NRT V8 from July 2019 to present) of the Measurement of Pollution in the Troposphere (MOPITT) instrument (Deeter et al. 2014, 2017, 2019), excluding observations poleward of 65°N and 65°S, using the ECWMF four-dimensional variational assimilation (4D-VAR) data assimilation system. Anthropogenic emissions were taken from the MACCity inventory (Granier et al. 2011) that accounts for projected emission trends according to the Representative Concentration Pathways (RCP) 8.5 scenario, but COVID-19-related emissions modifications were not applied. Biomass burning emissions were taken from the Global Fire Assimilation System (v1.4; Kaiser et al. 2012; section 2h3) that is based on MODIS fire radiative power retrievals (Giglio et al. 2016). Monthly mean biogenic emissions simulated by the Model of Emissions of Gases and Aerosols from Nature version 2.1 (MEGAN2.1) model following Sindelarova et al. (2014) were used for the period 2003–17, after which a monthly-mean climatology derived from the 2003–17 simulations was applied.

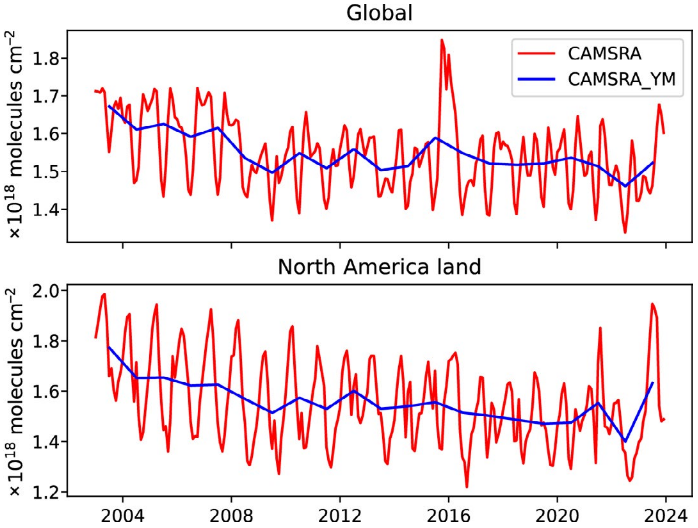

Fig. 2.76. Time series of the area-averaged monthly mean (red) and annual mean (blue, yearly mean [YM]) total column carbon monoxide (CO; × 10^{18} molecules cm^{-2}) over (a) the whole globe and (b) North America (30°N–70°N, 55°W–165°W, land points only for b) from the CAMS reanalysis for the period 2003–23.

h. Land surface properties

1. TERRESTRIAL SURFACE ALBEDO DYNAMICS

—F. Cappucci, N. Gobron, and G. Duveiller

The terrestrial surface albedo is the ratio between the solar radiation reflected by Earth's surface and the incident light. It is a key forcing parameter controlling the partitioning of radiative energy between the atmosphere and the surface. Increases in vegetation lead to a "darkening" effect, as more radiation is absorbed by plants in the visible spectrum. At the same time, the near-infrared albedo increases slightly, as healthy vegetation tends to reflect this part of the spectrum. Desertification and the related exposure of bare soil or increases in snowpack lead to a brighter surface and higher surface albedo.

In 2023, the normalized anomaly (2003–20 base period) of white-sky albedo in the visible broadband (Plate 2.1ad) indicated a notable surface darkening (values below –15%) of more than 17% of the land surface, compared to 6% recorded in 2022 (Duveiller and Gobron 2023). The darkening effect over Quebec and Nunavut and over large parts of Siberia was affected by the early melting of surface snow, starting in the second quarter of the year (section 2c5), together with the continuous decline in surface snow cover since the beginning of this century (Young 2023). The decreases in visible surface albedo recorded in central and eastern Europe, eastern China, western India, Japan, northern Australia, and sub-Saharan Africa were associated with a slight increase of the near-infrared albedo (Plate 2.1ae) as vegetation density increased over these areas (section 2h2).

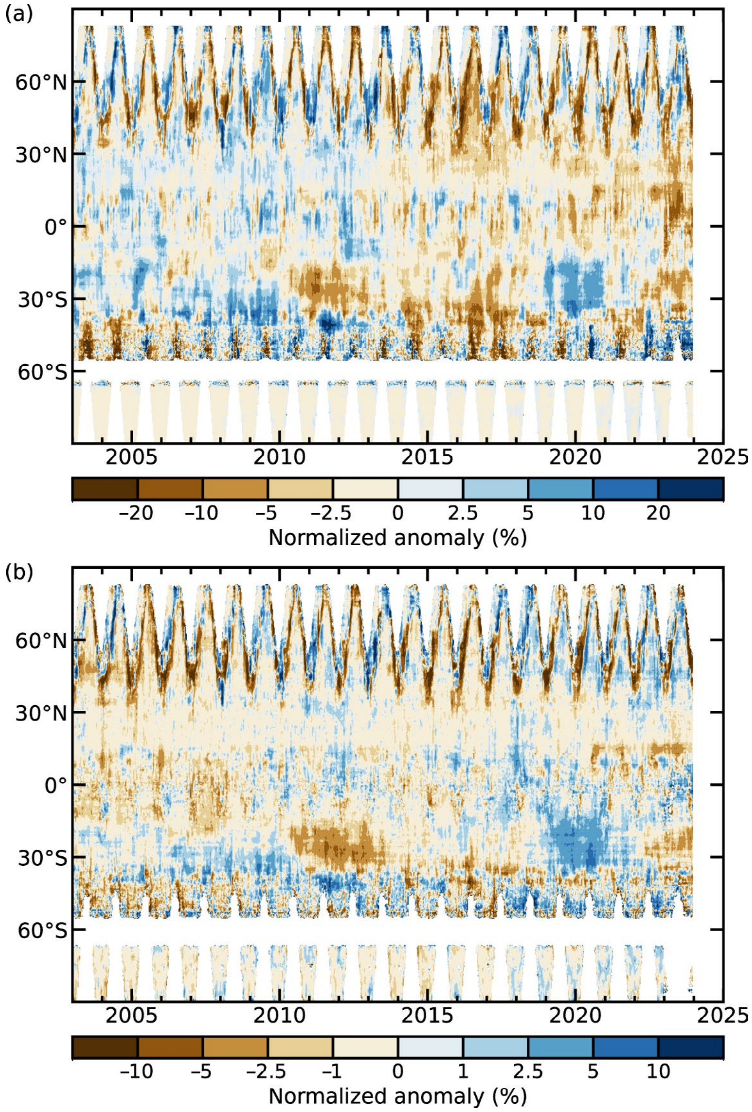

Fig. 2.77. Zonally averaged (a) white sky visible (%) and (b) near-infrared (%) broadband land surface albedo anomalies for the period 2003–23 (2003–20 base period).

In some regions, such as in eastern Australia, western Africa, and the Arabian Peninsula, 2023 displayed opposite signs of both albedo anomalies with respect to 2022. These fluctuations can be attributed to vegetation dynamics that are sensitive to water availability and temperature variations. Positive anomalies recorded over the central United States and Alaska resulted from above-average snow cover, which even extended during late spring after snowstorms in some of these regions.

The patterns of the zonally averaged albedo anomalies in the visible (Fig. 2.77a) and near-infrared (Fig. 2.77b) parts of the spectrum follow the darkening trend of previous years. Both figures show the large interannual variations related to seasonal snow in winter and spring at mid- and high-northern latitudes, but also the general trend in increased vegetation greening during summer periods. Persistent negative anomalies are noticeable for 2022 and 2023 between 15°N and 30°N in the visible albedo (with weak anomalies in the near-infrared domain), mainly due to the increase in vegetation density over China and India. Persistent negative anomalies in 2022/23 in both visible and near-infrared domains are detected between 10°S and 30°S, indicating a deviation from average conditions mainly over southern Africa and Australia.

The amplitude of the globally smoothed average anomaly (solid black line) is within

±4% in the visible domain during 2003–23 (and within ±1% for the near-infrared; Fig. 2.78). The year 2023 is characterized by a trend to more negative anomalies in both the visible and near-infrared domains, driven by the dominant contribution from the Northern Hemisphere regions.

This analysis was based on satellite products derived from the Moderate Resolution Imaging Spectroradiometer (MODIS) instrument on board the *Aqua* and *Terra* satellite platforms to generate a long-term record from 2002 to 2022 (Schaaf et al. 2002). The 2023 data are from the Visible Infrared Imaging Radiometer Suite (VIIRS) on board the Suomi NPP. Although VIIRS has been assessed as a strong candidate for the continuation of the MODIS archive (Liu at al. 2017), a small difference between VIIRS and MODIS surface albedo was noted; VIIRS 2023 data were bias-corrected accordingly. The anomalies were calculated at a 10-day frequency, based on the 2003–20 reference period.

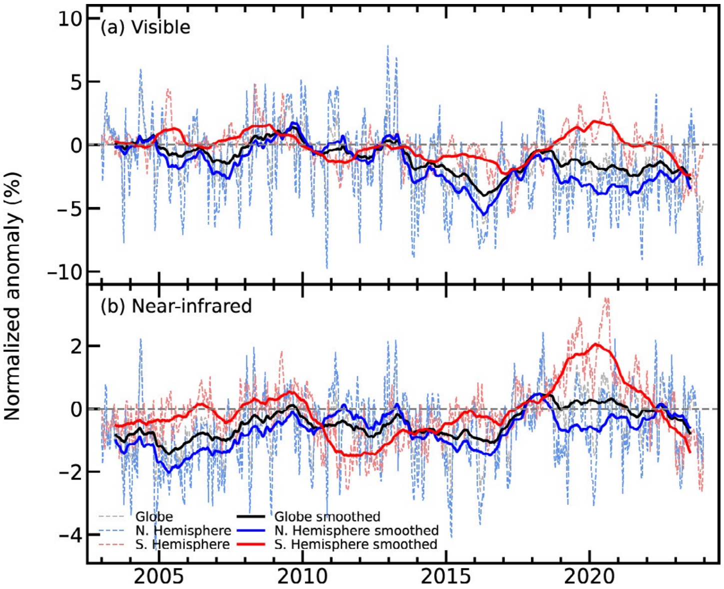

Fig. 2.78. Global (black lines), Northern Hemisphere (blue), and Southern Hemisphere (red) land surface (a) visible and (b) near-infrared broadband albedo normalized anomalies (%; 2003–20 base period) for the period 2003–23. Dotted lines denote each 10-day period; solid lines indicate the 12-month running averaged mean.

2. TERRESTRIAL VEGETATION DYNAMICS

—N. Gobron and F. Cappucci

The fraction of absorbed photosynthetically active radiation (FAPAR) reveals the amount of vegetation as well as its health and is important for assessing primary productivity and the associated fixing of atmospheric carbon dioxide by plants. FAPAR anomalies in 2023 compared to the 1998–20 average show a greater extent of positive values than negative values in the level of vegetation productivity across the world (Plate 2.1af).

Positive anomalies (increased plant photosynthesis) over the northern-central region of the United States and southern-central Canada (i.e., Great Plains) indicate that vegetation health recovered from last year due to above-average precipitation associated with higher temperatures. In contrast, fire events over the Quebec region (section 2h3) resulted in negative annual anomalies (decreased plant photosynthesis) as more than five million hectares of boreal forest burnt (see Sidebar 7.1 for details). The positive annual anomalies over Europe highlighted that Earth's surfaces continued the greening trend due to higher temperatures as well as plentiful rainfall.

Positive anomalies over southern Brazil and Paraguay were due to the transition to El Niño, which started in spring with extreme rainfall (section 2d4). In contrast, severe heatwaves, especially in Chile and southwestern Argentina (see section 7d3), impacted vegetation health, leading to negative FAPAR anomalies. The Central African Republic showed positive anomalies that were due to above-normal precipitation during the rainy seasons, whereas Namibia suffered from drought during the first half of the year (see section 7e). A major part of northern and southeastern Australia had positive FAPAR anomalies, as both precipitation and temperature were above normal (see section 7h4).

Figure 2.79 shows that all latitudes—though more markedly over the Southern Hemisphere (SH)—were affected by negative anomalies (i.e., less than −0.04) from 2002 to 2014, and that positive patterns were dominant in both hemispheres afterward. In 2023, the monthly anomalies were positive at nearly all latitudes, apart from a few places such as south of 20°S. Regions around 50°S had strong negative patterns at both the start and end of the year.

Figure 2.80 shows the global and hemispheric anomalies, with more seasonal variability in the less-landed SH than in the Northern Hemisphere (NH). FAPAR anomalies over the SH were positive before 2002, then negative until 2010. Thereafter, there were positive peaks in 2011, 2014, 2016/17, and 2022, with few negative months after 2013. The NH was positive in 1998, negative from 1999 to 2013, and positive thereafter. This trend towards positive values is linked to the trend for surface temperatures over land (see Fig. 2.1b). FAPAR annual anomalies were 0.013 (0.006) for NH (SH) in 2023 (with record values set in the NH [>0.02] at the end of the year).

Optical space sensors are used to infer FAPAR, an essential climate variable of the Global Climate Observation System (GCOS 2022). The 2023 analysis merges 26 years of global FAPAR products based on four optical sensors: Sea-Viewing Wide Field-of-View Sensor (SeaWiFS), Envisat/MERIS, Terra-Aqua/MODIS and Sentinel-3/Ocean and Land Colour Instrument (OLCI) from 1998 to 2023 (Gobron et al. 2010, 2022; Pinty et al. 2011; Gobron and Robustelli 2013). Uncertainties of each dataset were derived through error propagation techniques and comparisons against multiple proxies using ground-based measurements and radiative transfer simulations that all provide an estimate of the uncertainties and biases. This long-term FAPAR dataset has an estimated average uncertainty of ~5%–10%.

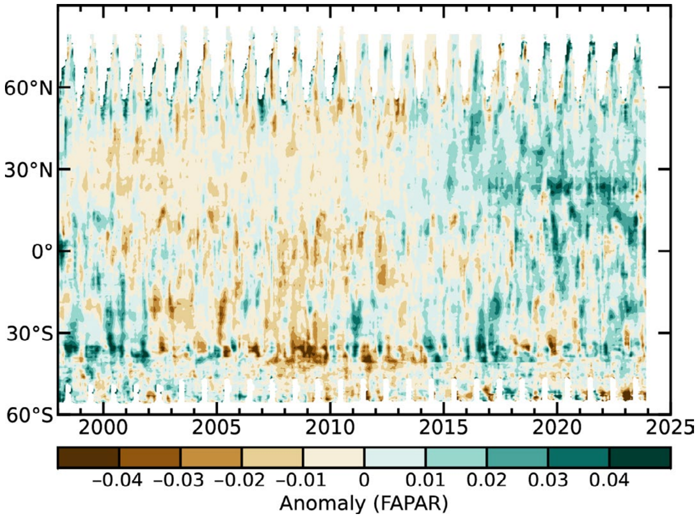

Fig. 2.79. Zonally averaged fraction of absorbed photosynthetically active radiation (FAPAR) anomalies for 1998–2023 (1998–2020 base period).

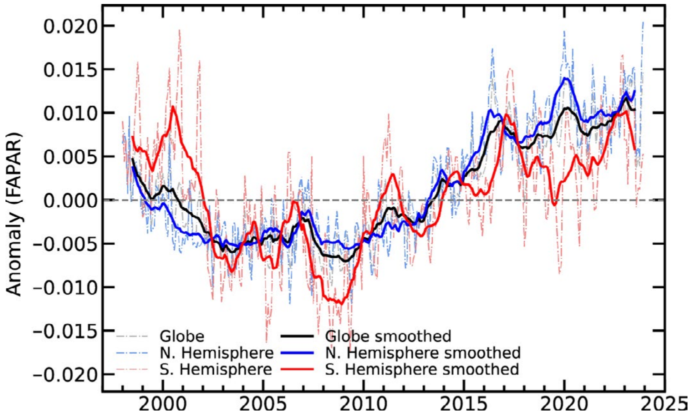

Fig. 2.80. Global (black lines), Northern Hemisphere (blue), and Southern Hemisphere (red) fraction of absorbed photosynthetically active radiation (FAPAR) anomalies for 1998–2023 (1998–2020 base period). Dotted lines denote each monthly period; solid lines indicate the six-month running averaged mean.

3. BIOMASS BURNING

—J. W. Kaiser, M. Parrington, and D. Armenteras

Two distinct trends that have emerged in global biomass burning over the last decade continued in 2023. Many savanna regions, which dominate global fire emissions, saw a decline related to agricultural expansion, while many forested regions—where climate change with severe drought periods increases the flammability of the landscape (e.g., Xing and Wang 2023 for the Arctic)—experienced longer and more intense wildfire episodes (Plate 2.1ag). The amount of biomass burning, referred to here as “fire activity” and more commonly as wildfires, is characterized here as the amount of carbon that is consumed by fire and emitted into the atmosphere. Of this, 80%–95% is emitted as carbon dioxide (CO_2), and the rest is oxidized to CO_2 in the atmosphere or released as particulate matter. In a stable ecosystem, virtually all of this CO_2 is assimilated again by the regrowth of vegetation. Currently however, 20% is estimated to contribute to the long-term build-up of atmospheric CO_2 (Zheng et al. 2023).

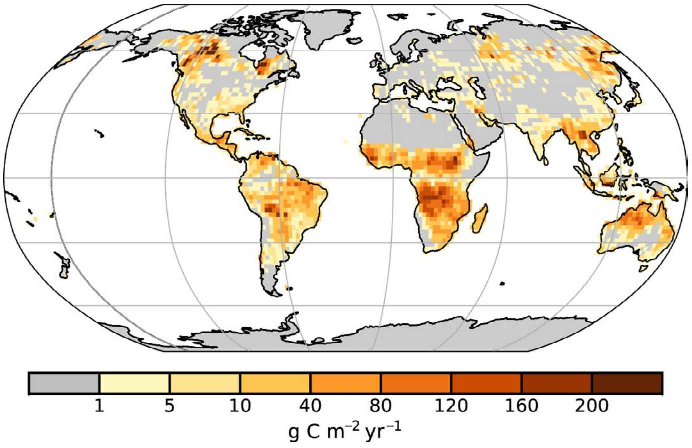

Fig. 2.81. Global map of fire activity (g C m^{-2} yr^{-1}) in 2023 in terms of carbon consumption. (Source: CAMS-GFASv1.4.)

Global annual total estimated fire emissions were close to the 2003–20 average in 2023 in the GFASv1.4 dataset (Table 2.12). However, 2022 had the lowest global emissions in GFAS, and the 2023 emissions represent an increase of 26% from 2022. The years 2019 and 2023 have similar emission budgets, and both are higher than any other year after 2015. The increase in 2023 was driven by anomalously large-scale wildfires that burned persistently in forests across Canada from May to September (Fig. 2.81; Plate 2.1ag; see Sidebar 7.1). These wildfires consumed five times more biomass than the average for the 2003–20 reference period and three times more than the previously recorded maximum (2014; cf. Fig. 2.82a). In contrast, the United States experienced its lowest annual total fire emissions on record, and wildfire emissions from boreal Eurasia were 28% below the 2003–20 average.

African fire carbon emissions accounted for roughly half of the total global emissions during the 2000s but their contribution has since shrunk to ~40%. The decreasing trend in savanna regions continued in 2023 over Northern-Hemisphere Africa with emissions 20% below the 2003–20 average, the third successive year with lower fire activity than any years in the record prior to 2019 (Fig. 2.82b). Southern-Hemisphere Africa and South America also contributed to the

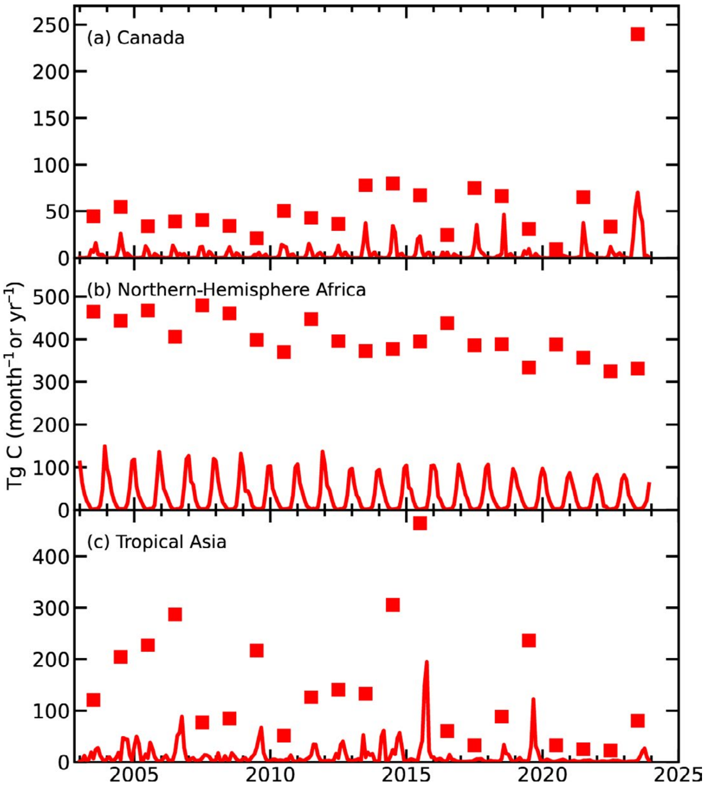

Fig. 2.82. Regional time series of monthly (lines in Tg C month^{-1}) and annual (symbols in Tg C yr^{-1}) biomass burning activity for (a) Canada, (b) Northern-Hemisphere Africa, and (c) tropical Asia.

Table 2.12. Annual continental-scale biomass burning budgets in terms of carbon emission (Tg C yr^{-1}). (Source: CAMS-GFASv1.4.)

Name of Region	Location	Biomass Burning 2003–20 Mean value (Range)	Biomass Burning 2023 Value	Biomass Burning 2023 Anomaly (%)
Global	–	2052 (1776– 2388)	1996	–53 (–3%)
North America	30°N–75°N, 190°E–330°E	88 (60–116)	265	+177 (–201%)
Central America	13°N–30°N, 190°E–330°E	49 (35–67)	53	+4 (+8%)
South America	13°N–60°S, 190°E–330°E	368 (243–540)	338	–30 (–8%)
Europe and Mediterranean	30°N–75°N, 330°E–60°E	41 (27–70)	29	–12 (–30%)
N. Hem. Africa	0°–30°N, 330°E–60°E	412 (333–479)	331	–81 (–20%)
S. Hem. Africa	0°–35°S, 330°E–60°E	486 (433–548)	459	–27 (–6%)
Northern Asia	30°N–75°N, 60°E–190°E	204 (118–446)	147	–57 (–28%)
Southeast Asia	10°N–30°N, 60°E–190°E	120 (85–157)	116	–4 (–3%)
Tropical Asia	10°N–10°S, 60°E–190°E	161 (33–464)	80	–80 (–50%)
Australia	10°S–50°S, 60°E–190°E	123 (54–226)	177	+54 (+44%)
Canada	47°N–75°N, 219°E–310°E	46 (10–80)	240	+194 (+421%)
Western United States (sub-region)	30°N–49°N, 230°E–260°E	19 (8–42)	16	–2 (–12%)

trend. Increased wildfire emissions related to warmer and drier conditions occurred in tropical regions of Australia between September and November (Plate 2.1ag). Fire activity in tropical Asia—including Indonesia—increased relative to the previous three years (Fig. 2.82c) but was significantly lower than the increased emissions of 2006, 2015, and 2019 despite the El Niño and positive Indian Ocean dipole-related conditions. In this region, extreme fires are driven by the combination of agricultural use of fires on plantations, in particular for palm oil and pulp production, and drought conditions during El Niño years, which lead to a high persistence of fires on peatlands that have become exposed by deforestation of tropical rainforest. The relatively low fire activity across the region in 2023 indicates that stricter policies by the Indonesian government that restrict the use of agricultural fires are largely effective.

While South America overall experienced moderately below-average fire activity (–8%; Plate 2.1ag), seasonal fires increased in several regions. Chile experienced its second-highest wildfire activity for any January–February period in 20 years, with almost 4 Tg C emissions (Fig. 2.81). In the same period, the Corrientes region in Argentina reached its second-highest emissions on record. The latter part of the year saw a spike in fires across Bolivia and some Brazilian states (including parts of the Amazon), which was largely driven by drought conditions in the Pantanal wetlands (section 2d11). Bolivia experienced its highest fire activity since 2010, with the peak shifting to October and November (peak monthly emissions of 30 Tg C in November) instead of the usual August and September. Fire emissions from the Brazilian Amazon continued the recent trend with below-average fire since 2003 emissions in Mato Grosso but increased fires in Amazonas (e.g., the highest for the month of June since 2007 [de Oliveira et al. 2023] and the highest for November [https://atmosphere.copernicus.eu/2023-year-intense-global-wildfire-activity]) despite decreased deforestation in the Brazilian Amazon relative to 2022 (http://www.obt.inpe.br/OBT/assuntos/programas/amazonia/prodes); this suggests that fire types other than those related to deforestation have become relatively more important in South America. The increasing wildfires indicate a possible effect of the 2023 El Niño, which favors hot and dry conditions and increases general vegetation flammability, but also a lag effect of a period of weakened enforcement of environmental laws that favored old pastures burning earlier in the dry season (de Oliveira et al. 2023).

The GFAS is operated by the Copernicus Atmosphere Monitoring Service (CAMS) and produces global fire emission estimates (Kaiser et al. 2012) in near-real-time based on the MODIS Fire Radiative Power products (Giglio et al. 2016). A combination of real-time and consistently reprocessed products by CAMS are used here, with input from MODIS Collection 6 for the entire period of 2003–23. The biases with respect to Collection 5 and between satellites have been corrected. The time series in Plate 1.1 also places GFAS in the context of GFED4s, which is primarily based on burnt area observation and dates to 1997 (van der Werf et al. 2017)

4. PHENOLOGY OF PRIMARY PRODUCERS

—D. L. Hemming, O. Anneville, Y. Aono, T. Crimmins, N. Estrella, S. -I. Matsuzaki, A. Menzel, I. Mrekaj, J. O'Keefe, A. D. Richardson, J. Rozkošný, T. Rutishauser, R. Shinohara, S. J. Thackeray, A. J. H. van Vliet, and J. Garforth.

Vegetation phenology, "the rhythm of the seasons", is strongly affected by climate variations and can influence the local and global climate via modifications in the land–atmosphere exchanges of energy, moisture, and carbon (Hassan et al. 2024). A range of satellite- and surface-based observations monitor phenological variability across space and time.

PhenoCam (http://phenocam.nau.edu/) is a network of over 800 automated digital cameras monitoring phenological changes in a wide range of ecosystems around the world (Richardson 2019; Seyednasrollah et al. 2019). The highest-density and longest-running PhenoCam sites (of which there are over 50 with more than 10 years of observations) are in the United States. Indicators of start of season (SOS_{PC}) and end of season (EOS_{PC}) were estimated from PhenoCam data and ground observation (GO) of red oak (*Quercus rubra*; SOS_{GO}, EOS_{GO}) in Harvard Forest, a deciduous forest in Massachusetts in the United States (Richardson and O'Keefe 2009; O'Keefe

2023), and from red oak observations across the northeastern United States contributed to *Nature's Notebook* (SOS_{NN}, EOS_{NN}), the USA-National Phenology Network's (USA-NPN) phenology monitoring platform (Rosemartin et al. 2014; Crimmins et al. 2022). Interannual variations in the start and end of season dates at Harvard Forest are broadly consistent with the broader-scale USA-NPN data (Figs. 2.83a,b; Table 2.13). In 2023, SOS_{PC}, SOS_{GO}, and SOS_{NN} were 6, 11, and 13 days earlier, respectively, than in 2022, while EOS_{PC}, EOS_{GO}, and EOS_{NN} were 11, 8, and 0 days later than in 2022. SOS_{PC} (EOS_{PC}) was 5 days earlier (5 days later) than the 2011–20 baseline mean, resulting in a growing season length of 177 days, 17 days longer than in 2022, and 10 days longer than the baseline (167±7 days).

The USA-NPN's extended Spring Index (SI-x), a model that reflects the onset of spring-season biological activity (Schwartz et al. 2013; Crimmins et al. 2017), estimated widespread earlier "first leaf" in 2023 across the eastern United States and later first leaf across the western United States compared with 2022 or the 2011–20 mean (Figs. 2.83a,b). These estimates were consistent with the SOS_{PC} and SOS_{GO} observations at Harvard Forest and SOS_{PC} observations from six other sites across the country (see Fig. 2.83 for details). They were more than 14 days earlier or later than recent years across many parts of the United States, largely due to warmer- (and cooler-) than-average late winter/spring 2023 temperatures across the eastern (and western) United States.

Start- and end-of-season indicators for native oak trees (*Quercus robur* and/or *Quercus petraea*) at European sites in Germany (D), Netherlands (NL), Slovakia (SK), and the United Kingdom (UK) are represented by observations of first leaf (SOS) and leaf fall or bare tree (EOS; Table 2.13; Figs. 2.84c,d). These events have been shown to be strongly influenced by spring and winter temperatures across Europe (Menzel et al. 2020). In 2023, SOS across all four European countries was later than usual. Compared to the 2000–20 mean, SOS dates in D, NL, SK, and UK were later by 3, 1, 5, and 2 days, respectively, and EOS dates were later by 8, 11, 6, and 4 days (Table 2.13). The later SOS and EOS dates across Europe were in part associated with relatively cool spring temperatures, delaying leaf out, followed by warm autumn temperatures, which

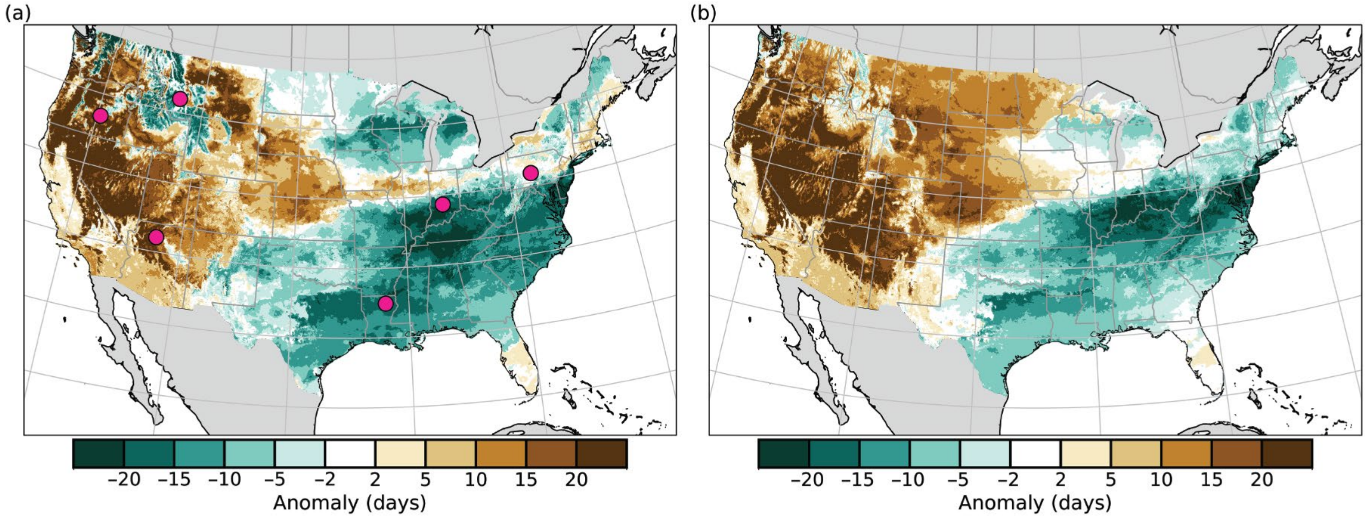

Fig. 2.83. 2023 'first leaf' date anomalies across the United States relative to (a) 2022 and (b) the 2011–20 baseline, estimated using the USA National Phenological Network's (USA-NPN) extended Spring Index (SI-x) model (Source: https://www.usanpn.org/data). Negative (green) values show earlier first leaf and positive (brown) values are later estimates for 2023. First leaf SI-x anomalies are generally consistent with start of season PhenoCam (SOS_{PC}) anomalies at the following six sites highlighted as points in (a): 1) a deciduous forest in Indiana (Morgan Monroe State Forest, SOS_{PC} = 15 days earlier than in 2022, and 6 days earlier than 2011–20); 2) a deciduous forest in Pennsylvania (Susquehanna Shale Hills Critical Zone Observatory, SOS_{PC} = 18 days earlier than in 2022); 3) a deciduous forest in Louisiana (Russell Sage State Wildlife Management Area, SOS_{PC} = 18 days earlier than in 2022); 4) a sagebrush site in Oregon (Eastern Oregon Agricultural Research Center, SOS_{PC} = 29 days later than in 2022); 5) a grassland site in Montana (Butte, SOS_{PC} = 6 days earlier than in 2022, but 1 day later than during 2011–20); and 6) a wooded shrubland site in Arizona (Grand Canyon National Park, SOS_{PC} = 12 days later than in 2022).

encouraged later leaf activity (for UK, see Kendon et al. 2023). The 2023 EOS in D was the latest since 2000, and this was associated with the warmest September temperatures on record (since 1881; Deutscher Wetterdienst [DWD] 2023; section 7f3). In SK, below-average temperatures during the end of March and April increased the prevalence of nocturnal frosts and delayed the first leaf onset, while extremely warm September and above-average October temperatures combined with ample precipitation resulted in the latest EOS dates across SK in 2023 since 2000. While the phenological timing of leaf out shifted later in the season in 2023, the length of the growing season for oak at the European locations was close to the baseline mean.

In Kyoto, Japan, full bloom dates (FBD) for a native cherry tree (*Prunus jamasakura*) have been recorded since 812 AD (Aono and Kazui 2008). For the Arashiyama district of Kyoto, these are updated with daily observations at train stations that are recorded in newspapers and on websites by railway passengers. In 2023, the FBD was the earliest on record for Arashiyama at 12 days earlier than the baseline (2000–20 mean; Table 2.13; Fig. 2.84e).

Monitoring data on lake water concentrations of the photosynthetic pigment chlorophyll-*a* were available to estimate spring phytoplankton phenology (nine Northern Hemisphere and one Southern Hemisphere lakes are reported; Fig. 2.85). The seasonal timing was estimated for start of season (SOS_L; Park et al. 2016), day of maximum concentration (DOM_L), and center of gravity (COG_L), which is an estimate of the mid-point of the plankton bloom (Edwards and Richardson 2004). The lake basins showed great interannual variation and mixed phenological behavior in 2023 relative to 2000–20. The SOS_L and COG_L occurred earlier than the baseline median for most of the lakes—7 and 8 of 10, respectively—whereas no consistent pattern was observed for DOM_L.

Table 2.13. Day of year (doy, equivalent to Julian day) and date of start of season (SOS), end of season (EOS), and full bloom date (FBD; cherry tree observations only) for land phenology records in USA (Harvard: PhenoCam, red oak, and USA National Phenology Network [USA-NPN] mean covering northeastern USA), Europe oak records (Germany, Netherlands, Slovakia, and United Kingdom), and Japan (native cherry tree observations in Japan). The baseline period is 2000–20 for all records except PhenoCam and USA-NPN which have baseline periods of 2008–22 and 2011–22, respectively, spanning the available observations. Growing season length for 2023 and the baseline mean are calculated as EOS minus SOS or FBD as appropriate for the record. Negative/positive values represent earlier/later dates for 2023 relative to the baseline mean.

Location/ Record	SOS/FBD 2023 (doy, date)	SOS/FBD Baseline (doy, date)	SOS/FBD Difference 2023 – Baseline (days)	EOS 2023 (doy, date)	EOS Baseline (doy, date)	EOS Difference 2023 – Baseline (days)	Growing season EOS–SOS 2023 (days)	Growing season EOS–SOS Baseline mean (days)
Harvard PhenoCam	123 3 May	128 8 May	–5	300 27 Oct	295 22 Oct	+5	177	167
Harvard red oak	122 2 May	128 8 May	–6	299 26 Oct	293 20 Oct	+6	177	165
Northeastern USA-NPN	113 23 Apr	125 5 May	–12	265 22 Sep	278 5 Oct	–13	152	153
Germany	121 1 May	118 28 Apr	+3	318 14 Nov	310 6 Nov	+8	197	192
Netherlands	111 21 Apr	110 20 Apr	+1	342 8 Dec	331 27 Nov	+11	231	221
Slovakia	121 1 May	116 26 Apr	+5	297 24 Oct	291 18 Oct	+6	176	175
UK	116 26 Apr	114 24 Apr	+2	339 5 Dec	335 1 Dec	+4	223	221
Japan	84 25 Mar	96 6 Apr	–12	--	--	--	--	--

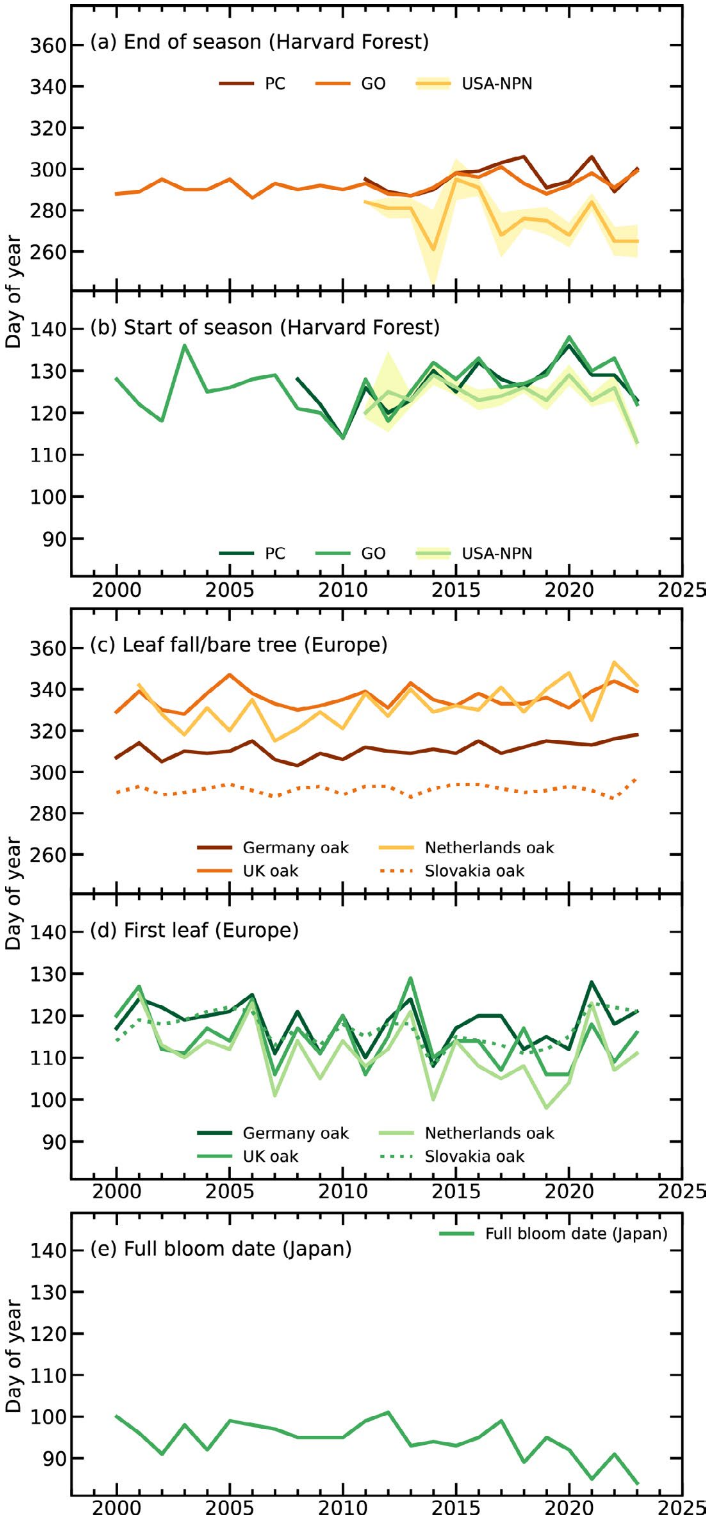

Fig. 2.84. Day of year of spring (greens) and autumn (oranges) vegetation phenology indicators for: (a),(b) Harvard Forest, Massachusetts, USA, derived from PhenoCam (PC), ground observations (GO) of red oak (Quercus rubra), and the USA-National Phenology Network (USA-NPN) regional-scale means of red oak observations (calculated across the northeastern states of Pennsylvania, New Jersey, New York, Connecticut, Rhode Island, Massachusetts, Vermont, New Hampshire, and Maine, ±1 std. error shaded); (c),(d) Germany, United Kingdom, Netherlands, and Slovakia mean of native oak observations (*Quercus robur* and/or *Quercus patrea*), and (e) Kyoto (Arashiyama district), Japan, full bloom date observations of native cherry trees (*Prunus jamasakura*).

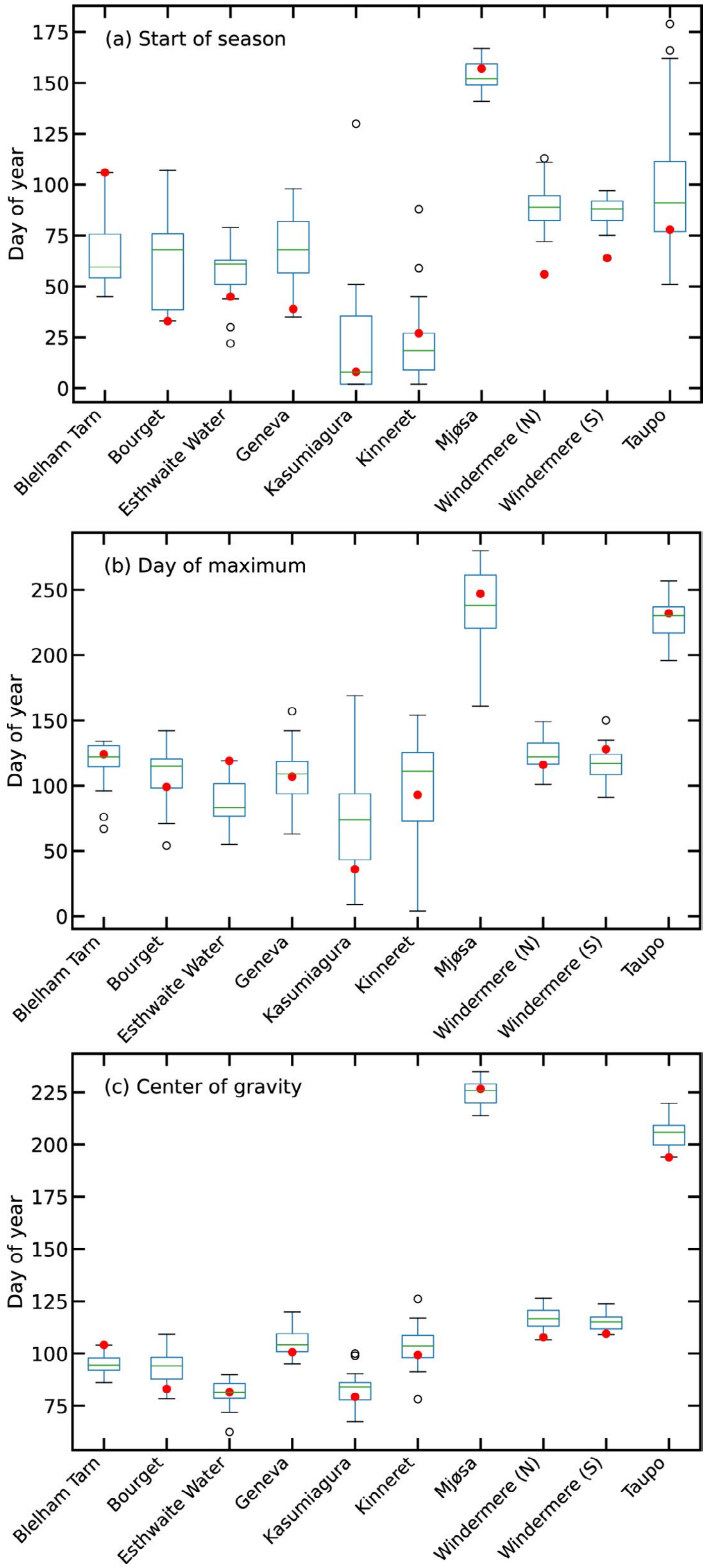

Fig. 2.85. Phenological metrics based on lake chlorophyll-*a* concentrations, as a proxy of phytoplankton biomass: (a) start of season, (b) day of maximum, and (c) center of gravity. Boxplots show variation during the 2000–20 baseline period, and red dots show 2023 values. Nine lakes are in the Northern Hemisphere (Blelham Tarn [United Kingdom], Bourget [France], Esthwaite Water [United Kingdom], Geneva [France/Switzerland], Kasumigaura [Japan], Kinneret [Israel], Mjøsa [Norway], north and south basins of Windermere [United Kingdom]), and one lake is in the Southern Hemisphere (Taupo [New Zealand]).

5. VEGETATION OPTICAL DEPTH

—R. M. Zotta, R. van der Schalie, T. Frederikse, W. Preimesberger, R. de Jeu, and W. Dorigo

Vegetation optical depth (VOD) derived from space-borne passive microwave radiometers is a non-dimensional parameter used in radiative transfer models to describe the interaction between radiance emitted from Earth's surface and vegetation and is an indicator of the water stored in plant structures. It has found utility in a wide range of studies, including drought- and vegetation-condition monitoring (Moesinger et al. 2022; Vreugdenhil et al. 2022). Positive VOD anomalies indicate above-average vegetation abundance, while negative VOD anomalies indicate underdeveloped or stressed vegetation.

Several trends resulting from land-use changes manifest prominently in VOD anomalies (Plate 2.1ah; Dorigo et al. 2021; Zotta et al. 2023), which are calculated as deviations from the 1991–2020 climatology. Notably, negative annual VOD anomalies in regions like Mongolia, Bolivia, Paraguay, and Brazil reflect the impacts of deforestation and land degradation, while positive anomalies in areas such as India and northeastern China signify agricultural intensification and reforestation efforts (Song et al. 2018). In order to exclude such long-term trends and isolate the year-to-year anomalies, we also look at the differences in VOD between 2023 and 2022 (Appendix Fig. A2.7).

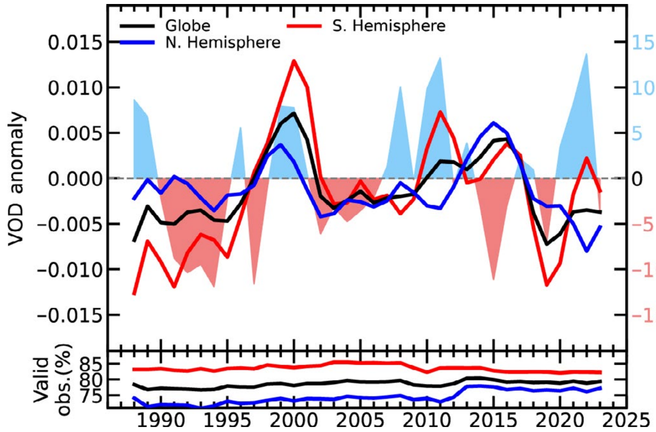

Fig. 2.86. Yearly vegetation optical depth (VOD) anomalies computed from the 1991–2020 climatology and their agreement with the Southern Oscillation Index (SOI). The SOI tracks the state of the El Nino–Southern Oscillation. (Source: VOD Climate Archive [VODCA]; http://www.bom.gov.au/climate/enso/soi/.)

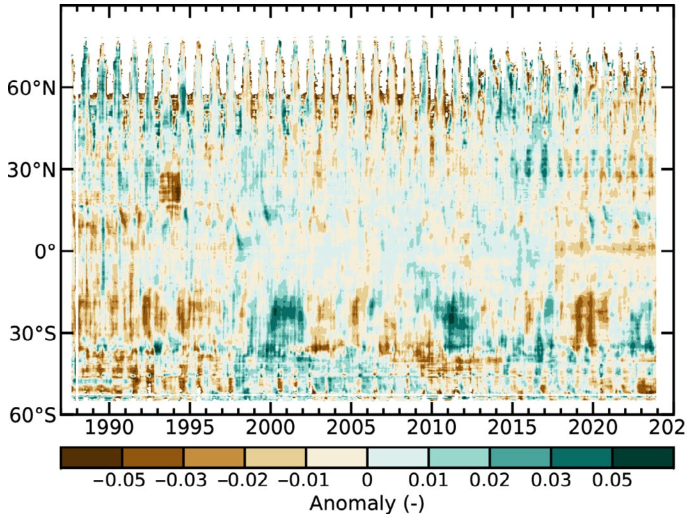

Fig. 2.87. Time–latitude diagram of vegetation optical depth (VOD) anomalies (1991–2020 base period). Data are masked where no retrieval is possible, or where the quality is not assured and flagged due to frozen soil, radio frequency interference, etc. (Source: VOD Climate Archive [VODCA].)

In 2023, annual VOD anomaly patterns differed from those in recent years (e.g., Zotta et al. 2023; Dorigo et al. 2022, 2021). In the Southern Hemisphere, where there is a clear connection between vegetation activity and variations in the El Niño–Southern Oscillation (ENSO; Miralles et al. 2014; Martens et al. 2017), overall VOD was lower than in 2022 (Figs. 2.86, 2.87).

Compared to 2022, substantial increases in VOD can be observed across regions in North America, northern Australia, and the Horn of Africa (Appendix Fig. A2.7). In northern Australia, the patterns are likely due to above-average rainfall (sections 2d4, 7h4) driving vegetation growth. In the Horn of Africa, predominantly positive annual (Plate 2.1ah) and high monthly (Appendix Fig. A2.8) VOD anomalies in November and December coincided with heavy rains associated with El Niño (section 2d4) and with the switch of the Indian Ocean dipole from negative to positive in September 2023 (see section 4f). The remarkable increases in VOD across Ethiopia, Somalia, and Kenya (Appendix Fig. A2.7) were likely due to favorable growing conditions caused by large precipitation amounts and were also captured in other satellite-borne vegetation indicators (FEWS NET 2023). In North America, the increase in VOD can likely be attributed to vegetation recovery after persistent dry conditions, which ameliorated in many regions such as the northeastern United States, the western portion of the Great Plains, California, and in parts of the Great Lakes and the Southeast (NOAA/NCEI 2023). Strong positive VOD anomalies in November and December (Appendix Fig. A2.8) support the findings of crop reports that announced favorable conditions for winter wheat across the United States and Canada, especially in Ontario and Manitoba (GeoGlam 2023).

Similar to soil moisture (section 2d10), VOD decreased substantially across southern Africa in 2023, where ENSO is one of the strongest drivers impacting agricultural production (OCHA 2023). Here, optical satellite observations of vegetation health indicate stressed vegetation (section 2h2; NOAA/NCEI 2023a). In the Maghreb (west and central north Africa) and northern Africa, where satellite observations from the Gravity Recovery and Climate Experiment (GRACE) have indicated persistently low soil moisture and groundwater (section 2d9; NOAA/NCEI 2023b), patterns of decreased VOD and negative monthly VOD anomalies across most of the year have prevailed. VOD also decreased in Central America and Mexico. An extremely dry period led to crop damage and losses observed in FAPAR anomalies (section 2h2; Toreti et al. 2023). In the Amazon basin, the decrease in VOD and the negative monthly anomalies across most of the year were likely caused by severe heatwaves and below-average rainfall linked with ENSO. In Spain, the decrease in VOD coincided with sparse rainfall and heatwaves that dominated in spring and summer (sections 2b1, 2d4).

The VOD data are from the VOD Climate Archive v2 (VODCA v2; Moesinger et al. 2020; Zotta et al. 2024a,b). VODCA merges VOD observations from several space-borne radiometers (Special Sensor Microwave/Imager [SSM/I], Tropical Rainfall Measuring Mission [TRMM], WindSat, Advanced Microwave Scanning Radiometer-Earth Observing System [AMSR-E] and Advanced Microwave Scanning Radiometer 2 [AMSR2]) through the Land Parameter Retrieval Model (Meesters et al. 2005; van der Schalie et al. 2017) into a long-term, harmonized dataset. Here, we used VODCA CXKu, a multi-frequency product that blends C-, X-, and Ku band observations, has a spatial resolution of 0.25°, and provides daily observations.

Acknowledgments

a Introduction

Robert Dunn and Kate Willett were supported by the Met Office Hadley Centre Climate Programme funded by the U.K. Department for Science, Innovation and Technology (DSIT). The editors thank the five anonymous reviewers and also Lizzie Fuller, John Kennedy, David Parker, and Ruben Urraca Valle for their insight, thoughts, and suggestions when developing this chapter. We also thank Fumi Sezaki (Japanese Meteorological Association [JMA]), Julien Nicolas (European Centre for Medium-Range Weather Forecasts [ECMWF]), and Mike Bosilovich (NASA) for their help in providing the reanalysis data used in this chapter.

b2 Lake surface temperature

Lake surface water temperatures from satellite data have been generated within the Climate Change Initiative Lakes project funded by the European Space Agency (4000125030/18/I-NB) with adaptation funded by the E.U. Copernicus Climate Change Service (C3S) programme and extensions by the U.K. Earth Observation Climate Information Service (EOCIS) project (NE/X019071/1). Part of the in situ data used for the validation of the satellite data and for this report have kindly been made publicly available by Fisheries and Oceans Canada (FOC), the National Data Buoy Center (NDBC) from NOAA, the Hungarian Meteorological Office, the Upper Great Lakes Observing System (UGLOS), and the North Temperate Lakes Long-Term Ecological Research (NTL-LTER). The authors gratefully acknowledge the late Alon Rimmer for always supplying data for Lake Kinneret. Data from Lake Zurich were provided by the City of Zurich Water Supply and by the Amt für Abfall, Wasser, Energie und Luft of the Canton of Zurich.

b3 Night marine air temperature

R. C. Cornes was supported by the NERC NC CLASS programme (NE/R015953/1) and the NERC GloSAT project (NE/S015647/2). R. Junod was supported by funding from the U.S. Department of Energy (DE-SC0023332).

b4 Surface temperature extremes

Robert Dunn was supported by the Met Office Hadley Centre Climate Programme funded by the Department for Science, Innovation and Technology (DSIT).

b5 Tropospheric temperature

Work performed by Stephen Po-Chedley at Lawrence Livermore National Laboratory (LLNL) was supported by the Regional and Global Model Analysis Program of the Office of Science at the Department of Energy (DOE) and performed under the auspices of the DOE under Contract DE- AC52-07NA27344.

c1 Permafrost temperatures and active-layer thickness

Research on James Ross Island was supported by the Czech Antarctic Research Programme and Czech Science Foundation project (GM22-28659M). The Circumpolar Active Layer Monitoring (CALM) program is funded by the National Science Foundation (NSF) Project 1836377. The Svalbard permafrost data is part the Svalbard Integrated Earth Observing System (SIOS). The Swiss Permafrost Monitoring Network (PERMOS) is financially supported by MeteoSwiss (in the framework of GCOS Switzerland), the Federal Office for the Environment, and the Swiss Academy of Sciences, and acknowledges the contribution of its partner institutions. The French Network PermaFRANCE is financially supported by the Observatoire des Sciences de l'Univers Grenoble and the French Research Infrastructure OZCAR. The Chinese Permafrost Monitoring Network is financially supported by the Chinese National Science Foundation (41931180) and Cryosphere Research Station on Qinghai-Xizang Plateau, CAS.

c2 Rock glacier velocity

Rock glacier monitoring at Hinteres Langtalkar and Dösen rock glaciers (AT) is supported by the Hohe Tauern National Park Carinthia through its long-term permafrost monitoring program. Laurichard (FR) survey is supported by Observation and Experimentation System for Environmental Research (SOERE/All'envi-OZCAR Research Infrastructure) and the PermaFrance observatory "monitoring the mountain permafrost in the French Alps" as well as the French National Research Agency in the framework of the Investissements d'Avenir programs: Risk@UGA (ANR-15-IDEX-02) and LabEx OSUG@2020 (ANR10 LABX56). The Ecrins National Park has helped field surveys since the early 2000s. The Swiss Permafrost Monitoring Network (PERMOS) is financially supported by MeteoSwiss in the framework of Global Climate Observing System (GCOS) Switzerland, the Federal Office for the Environment, and the Swiss Academy of Sciences. PERMOS acknowledges the important contribution of the partner institutions and principal investigators. The time series for Central Asian rock glaciers was compiled with the ESA Permafrost_CCI project (4000123681/18/I-NB). The time series for the Dry Andes was supported by the Centro de Estudios Avanzados en Zonas Áridas (CEAZA) and the Leading House for the Latin American Region (University of St. Gallen), grant number MOB1829.

c4 Lake ice cover

We thank Al and Sue Stangel, Alexander Mills, Ann LaLiberte, Beth Kohlman, BJ Bauer, Bob Katzenberger, Bonny Pederson, Brendan Wiltse, Brian D. Neill, Brian Vlach, John Barten, Rick Brascke, Calvin Maurer, Carl C. Nelson, Carol Wendorf, Cheryl and Dorothy Zingler, Clare and Dan Shirley, Craig Hillman, Dale Robertson, Dan Brumm, Daniel L. Anderson, Dave and Lynda J. Urshan, David Kahan, Don McClanathan, Donald and Mureil Fornasiere, Doug Fitzgerald, Douglas Pierzina, Dr. Neal D. Mundahl, Duane Williams and Edie Evarts, Duncan A. Brown, Earl Cook, Fred Buckley, Gary Teigen, Gay Alberts Ruby, Gene Cooper, George Grevich, Greg Sass, Holly Waterfield, Huaxia Yao, James and Sharon Fenner, James W. Danielson, Jan Henning L'Abée-Lund, Jeff Goelzer, Jeffrey G. Lowe, Jerry Evans, Jerry Sondreal, Jim and Judy Daugherty, Joe Jenkins, Joel Rasmussen, John and Catherine Bart, John Maier, Jonathan Ross, Dan Drumm, Dr. Lesly Knoll, Joy Krubsack, Kay and Rich Rezanka, Kay Olson, Kay Wepfer, Ken Blumenfeld, Larry and Marlene Lotto, Larry Peterson, Lars Rudstam, Lolita Olson, Lowell Dague, Marge Kellor, Mark Biller, Mark Holland, Mark J. and Rosie Peters, Mary Jane Dillingham, Mary Lou Fry, Randell Fry, Merja Pulkkanen, Michael Allen, Michael Bradley, Michael Kolecheck, Michael Traufler, Mickey and Dennis Chick, Mike, Jeff, and Thomm Backus, Molly Hibbard, Morris and Doris Whiting, Mr. and Mrs. Jay R. Mackie, Mr. and Mrs. William Bergersen, Mrs. Gale Wheeler, Mrs. Kathy Elhard, Mrs. Margery Armstrong, Myron Hagelstrom, Nancy Putnam, Nancy Steenport, Park Manager (L.C.), Patricia Bebak, Patrick Collins, Paulette Janssen, Pete Boulay, Peter Bearup, Rachel Dahlke, Raymond (Joe) Jenkins, Richard L. Tamke, Rock Anderson, Ron Pabich, Ronald Jones, Ross Swain, Sally Ketchen, Sandra Anderson, Scott Schoepp, Sharon Natzel, Shin-Ichiro Matsuzaki, Susan Reineking, Susan Verhaalen, Tana McNutt, Theodore (Ted) Peters, Thomas Sommerfeldt, Tom Stangl, Travis Campbell, Virgil Luehrs, Walt and Nancy Quillinan, Walter R. Brown, Water Dahlke III, William and Brenda Jones, and William Hanson, for their dedication and efforts to collecting and sharing in situ ice phenological records with us.

c5 Northern Hemisphere continental snow cover extent

This work is funded in part by NOAA's Climate Data Record (CDR) Program at the National Centers for Environmental Information (NCEI).

d1 Surface humidity

Kate Willett was supported by the Met Office Hadley Centre Climate Programme funded by the Department for Science, Innovation and Technology (DSIT). Adrian Simmons and David Lavers were supported by the Copernicus Climate Change Service (C3S) implemented by the European Centre for Medium-Range Weather Forecasts (ECMWF) on behalf of the European Commission.

d2 Humid-heat extremes over land

Kate Willett was supported by the U.K.-China Research and Innovation Partnership Fund through the Met Office Climate Science for Service Partnership (CSSP) China under the International Science Partnerships Fund (ISPF).

Cassandra Rogers is supported with funding from the Australian Government under the National Environmental Science Program.

Thank you to Tim Cowan from the University of Southern Queensland and Blair Trewin from the Bureau of Meteorology for providing initial reviews of the humid heat extremes over land section.

d7 Cloudiness

Clouds and Earth's Radiant Energy Systems Energy Balanced and Filled (CERES EBAF) data were obtained from the NASA Langley Research Center CERES ordering tool at https://ceres.larc.nasa.gov/data/.

d8 Lake water storage

B. M. Kraemer acknowledges support from the University of Freiburg Chair of Environmental Hydrosystems. M. F. Meyer and M. E. Harlan were supported by the United States Geological Survey (USGS) Mendenhall Fellowships from the Water Mission Area. The funders had no role in study design, data collection and analysis, decision to publish, or preparation of the manuscript. R. S. La Fuente was funded by the Irish HEA Landscape programme and Dundalk Institute of Technology (DkIT) Research Office. Any use of trade, firm, or product names is for descriptive purposes only and does not imply endorsement by the U.S. Government.

d9 Groundwater and terrestrial water storage

Work on the Groundwater and Terrestrial Water Storage section was funded by NASA's Gravity Recovery and Climate Experiment Follow-On (GRACE-FO) Science Team.

d10 Soil moisture

This study uses satellite soil moisture observations from the Copernicus Climate Change Service (C3S) Climate Data Store (CDS) (2018): Soil moisture gridded data from 1978 to present. C3S CDS. (Accessed on 16 01 2024), 10.24381/cds.d7782f18.

d11 Monitoring drought using the Self Calibrating Palmer Drought Severity Index

Jonathan Barichivich was supported by the European Research Council (ERC) under the Horizon Europe research and innovation programme (ERC-starting grant CATES, grant agreement No. 101043214). Tim Osborn received funding from the U.K. Natural Environment Research Council (NERC) (NE/S015582/1). Ian Harris received funding from U.K. National Centre for Atmospheric Science (NCAS). The research presented in the drought section was carried out on the High-Performance Computing Cluster supported by the Research and Specialist Computing Support service at the University of East Anglia.

d12 Land evaporation

D. G. Miralles acknowledges support from the European Research Council (ERC) under grant agreement no. 101088405 (HEAT). H. E. Beck is supported by the King Abdullah University of Science and Technology.

e2 Surface winds

C. Azorin-Molina was supported by CSIC-UV-GVA and funded by AICO/2021/023, LINCGLOBAL-CSIC ref. INCGLO0023, and PTI-CLIMA.

Robert Dunn was supported by the Met Office Hadley Centre Climate Programme funded by the Department for Business, Energy and Industrial Strategy (BEIS).

L. Ricciardulli was supported by NASA Ocean Vector Wind Science Team grant 80NSSC23K0984. Z. Zeng was supported by the National Natural Science Foundation of China grant 42071022.

e4 Lightning

The work of M. Füllekrug was sponsored by the Royal Society (U.K.) grant NMG/R1/180252 and the Natural Environment Research Council (U.K.) under grants NE/L012669/1 and NE/H024921/1.

E. Williams is supported for studies on global circuit response to climate change from the Physical and Dynamic Meteorology Program at the National Science Foundation (NSF) on grant no. 6942679.

C. Price was supported in his lightning research by the Israel Science Foundation (ISF) grant 2701/17, and the Ministry of Energy grant no. 220-17-002. S. Goodman was supported by NASA Grant 80NSSC21K0923 and NASA Contract 80GSFC20C044. The authors wish to thank Peter Thorne at Maynooth University in Ireland and at the European Centre for Medium Range Weather Forecast (ECMWF) for suggesting and initiating this work and for recommending that lightning be made an essential climate variable.

f1 Earth radiation budget at top-of-atmosphere

This research has been supported by the NASA Clouds and Earth's Radiant Energy Systems (CERES) project. The resources of the NASA Langley Atmospheric Sciences Data Center are utilized to process the instantaneous Single Scanner Footprint (SSF) data used as input to Energy Balance and Filled (EBAF) Ed4.2 and processes the FLASHFlux TISA version 4B. We further acknowledge the efforts of Walt Miller and Pam Mlynczak of the CERES team who monitor CERES data production and produce the FLASHFlux TISA 4B monthly averaged data products, respectively.

g3 Tropospheric aerosols

The data used for this section were provided by the European Union Copernicus Atmosphere Monitoring Service (CAMS).

g4 Tropospheric ozone

The NOAA Proving Ground and Risk Reduction (PGRR) Program supported the contributions by O. R. Cooper and K.-L. Chang. K.-L. Chang was also supported by NOAA cooperative agreement NA22OAR4320151. Funding for J. Ziemke for this research was provided in part by NASA NNH14ZDA001N-DSCOVR, NASA Suomi NPP and Joint Polar Satellite System (JPSS) Satellites Standard Products for Earth System Data Records, and Code 614 programmatic support for long-term ozone trends.

g5 Stratospheric aerosols

Lidar observations at Observatory de Haute-Provence (OHP) are funded by the French National Centre for Scientific Research (CNRS) National Institute of Sciences of the Universe (INSU) and CNES. S. Khaykin's work is supported by the ANR PyroStrat 21-CE01- 335 0007-01 project. We thank Christine David, Alain Hauchecorne, Julien Jumelet, Philippe Keckhut (LATMOS), and the lidar station operators for their contributions to long-term monitoring of stratospheric aerosol at OHP. Lidar observation at Lauder are funded in part by the Greenhouse gases Observing SATellite (GOSAT) project. We thank Richard Querel (National Institute of Water and Atmospheric Research [NIWA]), Osamu Uchino, Tomohiro Nagai (Meteorological Research Institute [MRI]) and Yushitaka Jin (MRI) for their contributions to long-term monitoring of stratospheric aerosol at Lauder.

g6 Stratospheric ozone

Carlo Arosio, Melanie Coldewey-Egbers, Diego Loyola, Viktoria Sofieva, Alexei Rozanov, and Mark Weber are grateful to the E.U. Copernicus Climate Change Service (C3S), C3S2_312a_Lot2 Ozone, and to European Space Agency's (ESA) Climate Change Initiative Ozone (CCI+) projects for supporting the generation and extension of the GTO-ECV total ozone and SAGE-CCI-OMPS data records. Carlo Arosio, Viktoria Sofieva, Kleareti Tourpali, Alexei Rozanov, and Mark Weber are grateful for the support of the ESA project Ozone Recovery from Merged Observational Data and Model Analysis (OREGANO). Stacey M. Frith is supported by the NASA Long Term Measurement of Ozone program WBS 479717. Lucien Froidevaux's contribution, with the assistance of Ryan Fuller, was performed at the Jet Propulsion Laboratory (JPL), California Institute of Technology, under contract with NASA. Jeannette Wild was supported by NOAA grant NA19NES4320002 (Cooperative Institute for Satellite Earth System Studies [CISESS]) at the University of Maryland's Earth System Science Interdisciplinary Center (ESSIC). Melanie Coldewey-Egbers and Diego Loyola acknowledge the partial support by the German Aerospace Center (DLR) projects MABAK and INPULS.

h2 Terrestrial vegetation dynamics

The authors thank the providers of the remote sensing dataset needed to perform this analysis and the Joint Research Centre's (JRC) Big Data Analytics Platform (BDAP).

h4 Phenology of primary producers

Debbie Hemming acknowledges support from the Met Office Hadley Centre Climate Programme funded by the Department for Science, Innovation and Technology (DSIT), and thanks all co-authors for their interesting and helpful contributions. Andrew Richardson acknowledges support from the National Science Foundation (NSF) Long Term Ecological Research (LTER) program (award 1832210). John O'Keefe also acknowledges support from the NSF through the LTER (award 1832210) program. Nature's Calendar (Woodland Trust) in the U.K. thanks all its volunteer recorders and support from players of People's Postcode Lottery. Theresa Crimmins and the USA National Phenology Network (USA-NPN) acknowledge support from the NSF through the Division of Biological Infrastructure (award 2031660), the US Fish and Wildlife Service (agreements F16AC01075 and F19AC00168) and the U.S. Geological Survey (G14AC00405 and G18AC00135). The USA-NPN thanks the many participants contributing phenology observations to *Nature's Notebook*. De Natuurkalender (Nature's Calendar) program in the Netherlands thanks all the volunteers and school children in the GLOBE program for their many observations. Annette Menzel and Nicole Estrella acknowledge support from the Bavarian State Ministry of Science and the Arts in the context of the Bavarian Climate Research Network (BayKlif) (Bavarian Citizen Science Portal for Climate Research and Science Communication [BAYSICS]). The Slovak Hydrometeorological Institute thanks all its volunteer observers for participating in the phenological observation program. Orlane Anneville acknowledges support from the National Institute of Agricultural Research (INRAE). Stephen Thackeray thanks Werner Eckert, Heidrun Feuchtmayr, Shin-Ichiro Matsuzaki, Ryuichiro Shinohara, Jan-Erik Thrane, Piet Verburg, Tamar Zohary and all field and lab workers associated with the provision of the lake chlorophyll-*a* data. We acknowledge funding from Vassdragsforbundet for Mjøsa med tilløpselver (https://www.vassdragsforbundet.no/om-oss/) and Natural Environment Research Council award number NE/R016429/1 as part of the U.K. Status, Change and Projections of the Environment (UK-SCAPE) programme delivering National Capability. Data for Lakes Geneva and Bourget were contributed by the Observatory of alpine LAkes (OLA), © SOERE OLA-IS, AnaEE-France, INRAE of Thonon-les-Bains, CIPEL, CISALB.

h5 Vegetation optical depth

R. M. Zotta and W. Dorigo acknowledge the TU Wien Wissenschaftspreis 2015, a personal grant awarded to W. Dorigo. We also acknowledge support from the European Space Agency (ESA) Climate Change Initiative and the Copernicus Climate Change Service (C3S).

Sidebar 2.1: Impacts of extreme temperatures in 2023

Robert Dunn and Kate Willett were supported by the Met Office Hadley Centre Climate Programme.

Appendix 1: Acronyms

4D-VAR	four-dimensional variational data assimilation
AAO	Antarctic Oscillation
AATSR	Advanced Along Track Scanning Radiometer
AEM ENTLN	Advanced Environmental Monitoring Earth Networks Total Lightning Network
ALT	active-layer thickness
AMSR2	Advanced Microwave Scanning Radiometer 2
AMSR-E	Advanced Microwave Scanning Radiometer-Earth Observing System
ANYSO	Australian New Year Super Outbreak
AOD	aerosol optical depth
ASCAT	Advanced Scatterometer
ASR	absorbed solar radiation
BD	Brewer-Dobson
C3S	Copernicus Climate Change Service
CALM	Circumpolar Active Layer Monitoring
CAMS	Copernicus Atmosphere Monitoring Service
CCI	Climate Change Initiative
CCM	chemistry climate model
CERES	Clouds and the Earth's Radiant Energy System
CFC	chlorofluorocarbon
CH_3CCl_3	methyl chloroform
CH_4	methane
CO	carbon monoxide
CO_2	carbon dioxide
COG	center of gravity
COVID-19	Coronavirus disease 2019
cp	specific heat capacity of air at constant pressure
CPT	cold-point tropopause
CRE	cloud radiative effect
DOM	day of maximum concentration
DWD	Deutscher Wetterdienst
DZAA	depth of zero annual amplitude
EBAF	Energy Balance and Filled
ECMWF	European Centre for Medium-Range Weather Forecasts
EESC	equivalent effective stratospheric chlorine
EESC(A)	equivalent effective stratospheric chlorine in the Antarctic
EESC(ML)	equivalent effective stratospheric chlorine in the midlatitudes
ENSO	El Niño–Southern Oscillation
EOCIS	Earth Observation Climate Information Service
EOF	empirical orthogonal function
EOS	end of season
ER	extinction ratio
ERB	Earth radiation budget
ERF	effective radiative forcing
ESA	European Space Agency
ET	evapotranspiration
EUR	Europe
FAPAR	fraction of absorbed photosynthetically active radiation
FBD	full bloom dates
FEWS NET	Famine Early Warning Systems Network

FF	fossil fuel
FP	frost point
GAM	General Additive Model
GCOS	Global Climate Observing System
GISS	Goddard Institute for Space Studies
GLAMOS	Glacier Monitoring Switzerland
GLD360	Global Lightning Detection Network
GLEAM	Global Land Evaporation Amsterdam Model
GLIMS	Global Land Ice Measurements from Space
GLM	Geostationary Lightning Mapper
GloSSAC	Global Satellite-based Stratospheric Aerosol Climatology
GO	ground observations
GPCC	Global Precipitation Climatology Centre
GPCP	Global Precipitation Climatology Project
GRACE	Gravity Recovery and Climate Experiment
GRACE-FO	Gravity Recovery and Climate Experiment Follow-On
GSL	Global Snow Lab
HCFC	hydrochlorofluorocarbon
HFC	hydrofluorocarbon
HTHH	Hunga Tonga–Hunga Haʻapai
INRAE	Université Grenoble Alpes
IOD	Indian Ocean dipole
IPCC	Intergovernmental Panel on Climate Change
ITCZ	Intertropical Convergence Zone
LLGHG	long-lived greenhouse gas
LSWT	lake surface water temperature
LTT	lower-tropospheric temperature
Lv	latent heat of vaporization
LWCRE	longwave cloud radiative effect
LWS	lake water storage
MC	Maritime Continent
MCM	million cubic meters
MCS	mesoscale convective system
MCS	marine cold spell
MEGAN2.1	Model of Emissions of Gases and Aerosols from Nature version 2.1
MHW	marine heatwave
MLO	Mauna Loa Observatory
MLS	Microwave Limb Sounder
MODIS	Moderate Resolution Imaging Spectroradiometer
MOPITT	Measurement of Pollution in the Troposphere
MSLP	mean sea-level pressure
N_2O	nitrous oxide
NA	North America
NAO	North Atlantic Oscillation
NDACC	Network for the Detection of Atmospheric Composition Changes
NH	Northern Hemisphere
NMAT	night marine air temperature
NN	Nature’s Notebook
O_3	tropospheric ozone
OCHA	Office for the Coordination of Humanitarian Affairs
ODGI	Ozone Depleting Gas Index
ODS	ozone-depleting substance

OHP	Observatoire de Haute Provence
OLR	outgoing longwave radiation
OMI	Ozone Monitoring Instrument
OMPS	Ozone Mapping and Profiler Suite
OMPS-LP	Ozone Mapping and Profiler Suite–Limb Profiler
ONI	Oceanic Niño Index
PC	PhenoCam
PERMOS	Swiss Permafrost Monitoring Network
PM2.5	fine particulate matter
PNA	Pacific/North American
PSA	Pacific–South American
q	specific humidity
QBO	quasi-biennial oscillation
QTP	Qinghai-Tibet Plateau
QuikSCAT	Quick Scatterometer
RCP	representative concentration pathway
RFaci	aerosol-cloud interactions
RFari	aerosol-radiation
RGIK	rock glacier inventories and kinematics
RGV	rock glacier velocity
RH	relative humidity
RSS	Remote Sensing Systems
RSW	reflected shortwave
Rx1day	one-day maximum accumulation
SAGE	Stratospheric Aerosol and Gas Experiment
SAM	Southern Annular Mode
sAOD	stratospheric aerosol optical depth
SCE	snow cover extent
scPDSI	self-calibrating Palmer Drought Severity Index
SH	Southern Hemisphere
SNAO	summer North Atlantic Oscillation
SO_2	sulfur dioxide
SOI	Southern Oscillation Index
SOS	start of season
SSM/I	Special Sensor Microwave/Imager
SSMIS	Special Sensor Microwave Imager/Sounder
SST	sea surface temperature
SSU	Stratospheric Sounding Unit
SW	shortwave
SWCRE	shortwave cloud radiative effect
T	dry-bulb air temperature
Ta	air temperature
TCWV	total column water vapor
TEC	total energy content
Teq	equivalent temperature
TLS	lower stratosphere temperature
TLT	lower tropospheric temperature
TMI	Tropical Rainfall Measuring Mission’s Microwave Imager
TOA	top-of-atmosphere
TOB	tropospheric ozone burden
Tq	latent temperature
TRMM	Tropical Rainfall Measuring Mission

TSI	total solar irradiance
TTL	tropical tropopause layer
T_w	wet-bulb temperature
TWS	terrestrial water storage
T_wX	daily maximum wet-bulb temperatures
Tx	zonal mean profiles
USA-NPN	USA National Phenology Network
UT	upper tropospheric
UTH	upper-tropospheric humidity
UW WWLLN	University of Washington's World Wide Lightning Location Network
VEI	Volcanic Explosivity Index
VIIRS	Visible Infrared Imaging Radiometer Suite
VOD	vegetation optical depth
VODCA	Vegetation Optical Depth Climate Archive
w.e.	water equivalent
WGMS	World Glacier Monitoring Service
WMO	World Meteorological Organization
WOUDC	World Ozone and Ultraviolet Radiation Data Centre
WV	water vapor

Appendix 2: Datasets and sources

Section 2b Temperature

Sub-section	General Variable or Phenomenon	Specific dataset or variable	Source
2b1	Temperature, [Near] Surface	Berkeley Earth	http://berkeleyearth.org/data/
2b1	Temperature, [Near] Surface	ERA5	https://www.ecmwf.int/en/forecasts/dataset/ecmwf-reanalysis-v5
2b1	Temperature, [Near] Surface	HadCRUT5 Global Temperature	https://www.metoffice.gov.uk/hadobs/hadcrut5/
2b1	Temperature, [Near] Surface	CRUTEM5	https://www.metoffice.gov.uk/hadobs/crutem5/
2b1, 2b3	Temperature, [Near] Surface	HadSST4	https://www.metoffice.gov.uk/hadobs/hadsst4/
2b1, 2b4	Temperature, [Near] Surface	JRA-55 Atmospheric Reanalysis	https://search.diasjp.net/en/dataset/JRA55
2b1	Temperature, [Near] Surface	JRA-3Q	https://search.diasjp.net/en/dataset/JRA3Q
2b1, 2b2	Temperature, [Near] Surface	NASA/GISS Global Temperature V4	https://data.giss.nasa.gov/gistemp/
2b1	Temperature, [Near] Surface	NOAA/NCEI NOAAGlobalTemp	https://www.ncei.noaa.gov/products/land-based-station/noaa-global-temp
2b2	Lake Temperature	Full Lake Surface Temperature Water dataset	https://cds.climate.copernicus.eu/cdsapp#!/dataset/satellite-lake-water-temperature
2b2	Lake Temperature	National Buoy Data Center Great Lakes Buoys	https://www.ndbc.noaa.gov/mobile/region.php?reg=great_lakes
2b2	Lake Temperature	Balaton Lakes	https://odp.met.hu/climate/observations_hungary/hourly/historical/
2b2	Lake Temperature	Canadian Lakes	https://www.meds-sdmm.dfo-mpo.gc.ca/isdm-gdsi/waves-vagues/data-donnees/index-eng.asp
2b2	Lake Temperature	Biel and Thun Lakes (Switzerland); Biwa and Mikata Lakes (Japan)	https://www.die3seen.ch/, https://portal.gemstat.org/applications/public.html?publicuser=PublicUser
2b2	Lake Temperature	Trout Lake	https://portal.edirepository.org/nis/mapbrowse?scope=knb-lter-ntl&identifier=116&revision=27
2b2	Lake Temperature	ESA CCI LAKES LSWT v2.0.2	https://catalogue.ceda.ac.uk/uuid/a07deacaffb8453e93d57ee214676304
2b2	Lake Temperature	Sentinel 3 Sea and Land Surface Temperature Radiometer (SLSTR)	https://sentinel.esa.int/web/sentinel/user-guides/sentinel-3-slstr/overview

Sub-section	General Variable or Phenomenon	Specific dataset or variable	Source
2b3	Nighttime marine Air Temperature	CLASSnmat	https://catalogue.ceda.ac.uk/uuid/5bbf48b128bd488dbb10a56111feb36a
2b3	Nighttime marine Air Temperature	UAHNMATv1	https://www.nsstc.uah.edu/climate/, https://doi.org/10.1002/joc.6354
2b4	Sea Surface Temperature	NOAA Optimum Interpolation Sea Surface Temperature (OISST) v2.1	https://www.ncei.noaa.gov/products/optimum-interpolation-sst
2b4	Temperature, [Near] Surface	GHCNDEX	https://www.climdex.org/
2b4	Temperature, [Near] Surface	MERRA-2	http://gmao.gsfc.nasa.gov/reanalysis/MERRA-2/
2b4, 2b5	Temperature, Upper Atmosphere	ERA5	https://www.ecmwf.int/en/forecasts/dataset/ecmwf-reanalysis-v5
2b4, 2b5	Temperature, Upper Atmosphere	JRA-55 Atmospheric Reanalysis	http://jra.kishou.go.jp/JRA-55/index_en.html
2b5	Temperature, Upper Atmosphere	MERRA-2	http://gmao.gsfc.nasa.gov/reanalysis/MERRA-2/
2b5	Temperature, Upper Atmosphere	NOAA/NESDIS/STAR MSU v5	https://www.star.nesdis.noaa.gov/data/mscat/MSU_AMSU_v5.0/Monthly_Atmospheric_Layer_Mean_Temperature/
2b5	Temperature, Upper Atmosphere	RAOBCORE, RICH	https://imgw.univie.ac.at/forschung/klimadiagnose/raobcore/
2b5	Temperature, Upper Atmosphere	RATPAC A2	https://www.ncei.noaa.gov/products/weather-balloon/radiosonde-atmospheric-temperature-products
2b5	Temperature, Upper Atmosphere	RSS v4.0	https://www.remss.com/measurements/upper-air-temperature/
2b5	Temperature, Upper Atmosphere	UAH MSU v6.0	https://www.nsstc.uah.edu/data/msu/v6.0/
2b5	Sea Surface Temperature	Niño 3.4 Index	https://psl.noaa.gov/gcos_wgsp/Timeseries/Nino34/
2b6	Temperature, Upper Atmosphere	Aura MLS	https://disc.gsfc.nasa.gov/datasets/ML2T_005/summary

Section 2c Cryosphere

Sub-section	General Variable or Phenomenon	Specific dataset or variable	Source
2c1	Permafrost	Global Terrestrial Network for Permafrost (GTN-P)	http://gtnpdatabase.org/
2c1	Permafrost	GTN-P global mean annual ground temperature data for permafrost	https://doi.org/10.1594/PANGAEA.884711
2c1	Permafrost	Permafrost Temperature at Chinese (QTP) sites	https://nsidc.org/data/GGD700/versions/1
2c1	Permafrost	Permafrost Temperature at French sites	https://permafrance.osug.fr
2c1	Permafrost	Permafrost Temperature at Norwegian sites	https://cryo.met.no/
2c1, 2c2	Permafrost	Permafrost Temperature at Swiss sites (PERMOS)	https://www.permos.ch, https://www.permos.ch/doi/permos-dataset-2022-1
2c1	Active Layer Depth	Circumpolar Active Layer Monitoring (CALM)	https://www.gwu.edu/~calm/
2c2	Rock Glacier Velocity	Regional Rock Glacier Velocity	Available from authors upon request. Austria: V. Kaufmann and A. Kellerer-Pirklbauer, Central Asia: A. Kääb, Dry Andes: S. Vivero, France: X. Bodin, D. Cusicanqui and E. Thibert, Switzerland: R. Delaloye, J. Noetzli and C. Pellet
2c3	Glacier Mass, Area or Volume	World Glacier Monitoring Service	http://dx.doi.org/10.5904/wgms-fog-2022-09
2c3	Glacier Area	Copernicus Sentinel-2 MSI image	https://sentinels.copernicus.eu/web/sentinel/user-guides/sentinel-2-msi/overview
2c4	Lake Ice	ERA5	https://www.ecmwf.int/en/forecasts/dataset/ecmwf-reanalysis-v5
2c4	Lake Ice	Lake ice clearance and formation data for Green Lakes Valley, 1968 - ongoing. ver 5. Environmental Data Initiative	https://portal.edirepository.org/nis/mapbrowse?scope=knb-lter-nwt&identifier=106&revision=6
2c4	Lake Ice	Global Lake and River Ice Phenology Database, Version 1	https://doi.org/10.7265/N5W66HP8
2c4	Lake Ice	Mountain Lake Biology, Chemistry, Physics, and Climate Data since 1959 at Castle Lake ver 1. Environmental Data Initiative	https://doi.org/10.6073/pasta/a8e3b81cfe5864731b29ad42506c65d7
2c4	Lake Ice	Great Lakes Annual Maximum Ice Cover (%)	https://www.glerl.noaa.gov/data/ice/

Sub-section	General Variable or Phenomenon	Specific dataset or variable	Source
2c4	Lake Ice	Great Lakes Ice	www.glerl.noaa.gov/data/ice
2c4	Lake Ice	Geographic variation and temporal trends in ice phenology in Norwegian lakes during a century, Dryad	https://datadryad.org/stash/dataset/doi:10.5061/dryad.bk3j9kd9x
2c4	Lake Ice	lake surface water temperature and ice cover in subalpine Lake Lunz, Austria	https://doi.org/10.1080/20442041.2017.1294332
2c4	Temperature, [Near] Surface	NASA/GISS Global Temperature	https://data.giss.nasa.gov/gistemp/
2c5	Snow Properties	Northern Hemisphere (NH) Snow Cover Extent (SCE), Version 1	doi:10.7289/V5N014G9, https://www.snowcover.org

Section 2d Hydrological cycle

Sub-section	General Variable or Phenomenon	Specific dataset or variable	Source
2d1	Humidity, [Near] Surface	ERA5	https://www.ecmwf.int/en/forecasts/dataset/ecmwf-reanalysis-v5
2d1, 2d2	Humidity, [Near] Surface	HadISDH	www.metoffice.gov.uk/hadobs/hadisdh, https://catalogue.ceda.ac.uk/uuid/251474c7b09449d8b9e7aeaf1461858f
2d1	Humidity, [Near] Surface	JRA-55 Atmospheric Reanalysis	http://jra.kishou.go.jp/JRA-55/index_en.html
2d1	Humidity, [Near] Surface	MERRA-2	https://gmao.gsfc.nasa.gov/reanalysis/MERRA-2/
2d3	Water Vapor, Total Column	COSMIC	http://cosmic-io.cosmic.ucar.edu/cdaac/index.html
2d3	Water Vapor, Total Column	ERA5	https://www.ecmwf.int/en/forecasts/dataset/ecmwf-reanalysis-v5
2d3	Water Vapor, Total Column	GNSS Ground-Based Total Column Water Vapor	https://doi.org/10.25326/68
2d3	Water Vapor, Total Column	JRA-55 Atmospheric Reanalysis	http://jra.kishou.go.jp/JRA-55/index_en.html
2d3	Water Vapor, Total Column	MERRA-2	https://gmao.gsfc.nasa.gov/reanalysis/MERRA-2/
2d3	Water Vapor, Total Column	SSM/I -AMSR-E Ocean Total Column Water Vapor	http://www.remss.com
2d4	Humidity, Upper Atmosphere	Upper Troposphere Humidity (UTH)	Available on request to Brian Soden (bsoden@miami.edu)

Sub-section	General Variable or Phenomenon	Specific dataset or variable	Source
2d4	Humidity, Upper Atmosphere	ERA5	https://www.ecmwf.int/en/forecasts/dataset/ecmwf-reanalysis-v5
2d4	Humidity, Upper Atmosphere	High Resolution Infrared Sounder (HIRS)	https://www.ncei.noaa.gov/products/climate-data-records/hirs-ch12-brightness-temperature
2d4	Temperature, Upper Atmosphere	NOAA/NESDIS/STAR MSU v5	https://www.star.nesdis.noaa.gov/pub/smcd/emb/mscat/data/MSU_AMSU_v5.0/Monthly_Atmospheric_Layer_Mean_Temperature/
2d5, 2d6	Precipitation	GPCC	www.dwd.de/EN/ourservices/gpcc/gpcc.html
2d5	Precipitation	Global Precipitation Climatology Project (GPCP) v2.3	https://www.dwd.de/EN/ourservices/gpcc/gpcc.html, https://www.ncei.noaa.gov/products/global-precipitation-climatology-project
2d6	Precipitation	HadEX3	https://www.metoffice.gov.uk/hadobs/hadex3/
2d6	Precipitation	Climate Extremes Index Component 4	https://www.ncdc.noaa.gov/extremes/cei/
2d6	Precipitation	ERA5	https://www.ecmwf.int/en/forecasts/datasets/reanalysis-datasets/era5
2d6	Precipitation	GHCNDEX	https://www.climdex.org
2d6	Precipitation	MERRA-2	https://gmao.gsfc.nasa.gov/reanalysis/MERRA-2/
2d7	Cloud properties	PATMOS-x v6.0	https://www.ncei.noaa.gov/products/climate-data-records/avhrr-hirs-cloud-properties-patmos
2d7	Cloud Properties	Aqua MODIS C6.1 MYD08_M3	https://ladsweb.modaps.eosdis.nasa.gov/missions-and-measurements/products/MYD08_M3
2d7	Cloud Properties	Clouds and the Earth's Radiant Energy System Energy Balance and Filled (CERES EBAF) v4.2	https://ceres.larc.nasa.gov/data/
2d7	Modes of Variability	Multivariate ENSO Index (MEI) v2	https://psl.noaa.gov/enso/mei/
2d8	Lake Water Storage	'GloLakes' lake and reservoir storage	https://doi.org/10.5194/essd-16-201-2024
2d9	Groundwater and terrestrial water storage	GRACE / GRACE-FO	https://podaac.jpl.nasa.gov/dataset/TELLUS_GRAC-GRFO_MASCON_CRI_GRID_RL06.1_V3
2d10	Soil Moisture	Copernicus Climate Change Service (C3S) v202012 product based on the ESA Climate Change Initiative for Soil Moisture (ESA CCI SM) v05.2 merging algorithm	https://cds.climate.copernicus.eu/cdsapp#!/dataset/satellite-soil-moisture?tab=form

Sub-section	General Variable or Phenomenon	Specific dataset or variable	Source
2d11	Drought	Climatic Research Unit gridded Time Series (CRU TS) 4.07	https://crudata.uea.ac.uk/cru/data/hrg/cru_ts_4.07/
2d12	Land Evaporation	Climatic Research Unit gridded Time Series (CRU TS) 4.07	https://www.gleam.eu/
2d1	Modes of Variability	Southern Oscillation Index	https://crudata.uea.ac.uk/cru/data/soi/

Section 2e Atmospheric circulation

Sub-section	General Variable or Phenomenon	Specific dataset or variable	Source
2e1	Modes of Variability	Antarctic Oscillation (AAO)/Southern Annular Mode (SAM)	https://ftp.cpc.ncep.noaa.gov/cwlinks/norm.daily.aao.index.b790101.current.ascii
2e1	Pressure, Sea Level or Near-Surface	ERA5	https://www.ecmwf.int/en/forecasts/dataset/ecmwf-reanalysis-v5
2e2	Modes of Variability	Antarctic Oscillation (AAO)/Southern Annular Mode (SAM)	https://ftp.cpc.ncep.noaa.gov/cwlinks/norm.daily.aao.index.b790101.current.ascii
2e2	Wind, [Near] Surface	ERA5	https://www.ecmwf.int/en/forecasts/dataset/ecmwf-reanalysis-v5
2e2	Wind, [Near] Surface	HadISD v3.3.0.2022f	https://hadleyserver.metoffice.gov.uk/hadisd/v330_2022f/index.html
2e2	Wind, [Near] Surface	Modern-Era Retrospective Analysis for Research and Applications version 2 (MERRA-2)	http://gmao.gsfc.nasa.gov/reanalysis/MERRA-2/
2e2	Wind [Near Surface]	Remote Sensing System (RSS) Merged 1-deg monthly radiometer winds	https://www.remss.com/measurements/wind/
2e2	Wind [Near Surface]	Remote Sensing System (RSS) Advanced Scatterometer (ASCAT)	https://www.remss.com/missions/ascat/
2e2	Wind [Near Surface]	Remote Sensing System (RSS) QuickScat4	https://www.remss.com/missions/qscat/
2e3	Wind [Upper Atmosphere]	Quasi biennial Oscillation (QBO)	https://www.atmohub.kit.edu/data/singapore2023.dat
2e3	Modes of Variability	Antarctic Oscillation (AAO), Southern Annular Mode (SAM)	https://www.cpc.ncep.noaa.gov/products/precip/CWlink/daily_ao_index/aao/aao.shtml, http://www.nerc-bas.ac.uk/icd/gjma/sam.html

Sub-section	General Variable or Phenomenon	Specific dataset or variable	Source
2e3	Wind [Upper Atmosphere]	ERA5 hourly data on pressure levels from 1940 to present. Copernicus Climate Change Service (C3S) Climate Data Store (CDS)	https://cds.climate.copernicus.eu/cdsapp#!/dataset/reanalysis-era5-pressure-levels?tab=overview
2e3	Wind [Upper Atmosphere]	ERA-Interim	www.ecmwf.int/en/research/climate-reanalysis/era-interim
2e3	Wind [Upper Atmosphere]	MERRA-2	http://gmao.gsfc.nasa.gov/reanalysis/MERRA-2/
2e3	Wind [Upper Atmosphere]	JRA-55 Atmospheric Reanalysis	http://jra.kishou.go.jp/JRA-55/index_en.html
2e4	Lightning	GOES-R Geostationary Lightning Mapper (GLM) Gridded Data Products V1	http://doi.org/10.7289/V5KH0KK6

Section 2f Earth's radiation budget

Sub-section	General Variable or Phenomenon	Specific dataset or variable	Source
2f1	TOA Earth Radiation Budget	CERES Energy Balanced and Filled version 4.2	https://ceres-tool.larc.nasa.gov/ord-tool/jsp/EBAFTOA42Selection.jsp
2f1	TOA Earth Radiation Budget	CERES FLASHflux version 4A	https://ceres-tool.larc.nasa.gov/ord-tool/jsp/FLASH_TISASelection.jsp
2f1	TOA Earth Radiation Budget	Community-Consensus TSI Composit	https://spot.colorado.edu/~koppg/TSI/TSI_Composite-SIST.txt
2f2	Solar Transmission, Apparent	Mauna Loa Observatory	https://www.esrl.noaa.gov/gmd/webdata/grad/mloapt/mauna_loa_transmission.dat
2f2	Cloud Aerosol	Cloud-Aerosol LIDAR and Infrared Pathfinder Satellite Observations (CALIPSO)	http://www-calipso.larc.nasa.gov
2f2	Ozone, Stratospheric	Stratospheric Aerosol and Gas Experiment (SAGE) limb sounder	https://sage.nasa.gov/sageiii-iss/browse_images/expedited/

Section 2g Atmospheric composition

Sub-section	General Variable or Phenomenon	Specific dataset or variable	Source
2g1	Trace Gases	Atmospheric Gas trends	https://gml.noaa.gov/ccgg/trends/
2g1	Trace Gases	Global Greenhouse Gas Reference Network	https://gml.noaa.gov/ccgg/about.html

Sub-section	General Variable or Phenomenon	Specific dataset or variable	Source
2g1	Trace Gases	Atmospheric Greenhouse Gas Index (AGGI)	www.esrl.noaa.gov/gmd/aggi
2g2	Trace Gases	Halocarbons and other Atmospheric Trace Species	https://gml.noaa.gov/aftp/data/hats/
2g2	Trace Gases	Advanced Global Atmospheric Gases Experiment	https://agage2.eas.gatech.edu/data_archive/global_mean/global_mean_ms.txt
2g2	Trace Gases	Ozone-Depleting Gas Index (ODGI)	www.esrl.noaa.gov/gmd/odgi
2g3	Aerosols	Advanced Along Track Scanning Radiometer (AATSR)	https://earth.esa.int/eogateway/instruments/aatsr
2g3	Aerosols	Copernicus Atmosphere Monitoring Service Reanalysis (CAMSRA)	https://ads.atmosphere.copernicus.eu/cdsapp#!/dataset/cams-global-radiative-forcing-auxilliary-variables?tab=overview
2g4	Ozone, Tropospheric	NOAA Global Monitoring Laboratory	https://gml.noaa.gov/aftp/data/ozwv/SurfaceOzone/
2g5	Stratospheric Aerosols	OHP LTA lidar	https://www-air.larc.nasa.gov/missions/ndacc/data.html?station=haute.provence/ames/lidar/
2g5	Stratospheric Aerosols	OHP LiO3S lidar	https://www-air.larc.nasa.gov/missions/ndacc/data.html?station=haute.provence/ames/lidar/
2g5	Stratospheric Aerosols	Lauder aerosol lidar	https://www-air.larc.nasa.gov/missions/ndacc/data.html?station=lauder/ames/lidar/
2g5	Stratospheric Aerosols	SAGE III v5.3	https://asdc.larc.nasa.gov/project/SAGE%20III-ISS/g3bssp_53
2g5	Stratospheric Aerosols	GloSSAC v2.	https://asdc.larc.nasa.gov/project/GloSSAC
2g5	Stratospheric Aerosols	OMPS-LP v2.1	https://disc.gsfc.nasa.gov/datasets/OMPS_NPP_LP_L2_AER_DAILY_2/summary
2g6	Ozone, Total Column and Stratospheric	GOME/SCIAMACHY/GOME2 (GSG) Merged Total Ozone	http://www.iup.uni-bremen.de/UVSAT/datasets/merged-wfdoas-total-ozone
2g6	Ozone, Total Column and Stratospheric	GOME/SCIAMACHY/GOME2 (GTO) Merged Total Ozone	https://atmos.eoc.dlr.de/gto-ecv
2g6	Ozone, Total Column and Stratospheric	GOZCARDS ozone profiles	https://www.earthdata.nasa.gov/esds/competitive-programs/measures/gozcards
2g6	Ozone, Total Column and Stratospheric	Multi Sensor Reanalysis (MSR-2) of total ozone	http://www.temis.nl/protocols/O3global.html
2g6	Ozone, Total Column and Stratospheric	NASA BUV/SBUV/OMPS v8.7 (MOD) Merged Ozone	https://acd-ext.gsfc.nasa.gov/Data_services/merged/

Sub-section	General Variable or Phenomenon	Specific dataset or variable	Source
2g6	Ozone, Total Column and Stratospheric	NOAA SBUV V8.6 OMPS V4r1 cohesive data set (COH)	ftp://ftp.cpc.ncep.noaa.gov/SBUV_CDR/
2g6	Ozone, Total Column and Stratospheric	Network for the Detection of Atmospheric Composition Change (NDACC) lidar, microwave and FTIR	https://www-air.larc.nasa.gov/missions/ndacc
2g6	Ozone, Total Column and Stratospheric	CCMI-2022 model runs	https://blogs.reading.ac.uk/ccmi/ccmi-2022/
2g6	Ozone, Total Column and Stratospheric	SAGE-CCI-OMPS	https://climate.esa.int/en/projects/ozone/data
2g6	Ozone, Total Column and Stratospheric	SAGE/OSIRIS	Bourassa et al. (2018) doi:10.5194/amt-11-489-2018
2g6	Ozone, Total Column and Stratospheric	SAGE-SCIA-OMPS	Arosio et al., (2018) doi:10.5194/amt-2018-275
2g6	Ozone, Total Column and Stratospheric	SWOOSH	www.esrl.noaa.gov/csd/groups/csd8/swoosh/
2g6	Ozone, Total Column and Stratospheric	WOUDC Ground-based Ozone	ftp.tor.ec.gc.ca; cd /pub/woudc/Projects Campaigns/ZonalMeans
2g7	Stratospheric Water Vapor	the Aura Microwave Limb Sounder version 5.0 data, as merged into SWOOSH	www.esrl.noaa.gov/csd/groups/csd8/swoosh/
2g7	Tropopause Temperature	MERRA-2	http://gmao.gsfc.nasa.gov/reanalysis/MERRA-2/
2g7	Stratospheric Water Vapor	NOAA Frostpoint Hygrometer (FPH)	https://gml.noaa.gov/aftp/data/ozwv/WaterVapor/
2g7	Stratospheric Water Vapor	Cryogenic Frostpoint Hygrometer (CFH)	https://ndacc.org
2g8	Trace Gases	Copernicus Atmosphere Monitoring Service Reanalysis (CAMSRA) for Carbon Monoxide	https://ads.atmosphere.copernicus.eu/cdsapp#!/dataset/cams-global-radiative-forcing-auxilliary-variables?tab=overview

Section 2h Land surface properties

Sub-section	General Variable or Phenomenon	Specific dataset or variable	Source
2h1	Albedo	MODIS/Terra+Aqua BRDF/Albedo Albedo Daily L3 Global 0.05Deg CMG V061	https://lpdaac.usgs.gov/products/mcd43c3v061/
2h1	Albedo	VIIRS VNP43C3 Collection 1.0	https://lpdaac.usgs.gov/products/vnp43c3v001 https://doi.org/10.5067/VIIRS/VNP43C3.001

Sub-section	General Variable or Phenomenon	Specific dataset or variable	Source
2h2	fraction of absorbed photosynthetically active radiation (FAPAR)	JRC TIP MODIS	https://fapar.jrc.ec.europa.eu
2h2	FAPAR	MERIS	https://fapar.jrc.ec.europa.eu
2h2	FAPAR	SeaWiFS FAPAR	http://fapar.jrc.ec.europa.eu/
2h2	FAPAR	OLCI	https://dataspace.copernicus.eu/
2h3	Biomass, Greenness or Burning	GFAS v1.4	https://ads.atmosphere.copernicus.eu/cdsapp#!/dataset/cams-global-fire-emissions-gfas
2h3	Biomass, Greenness or Burning	Global Fire Emissions Database	https://www.globalfiredata.org/data.html
2h3	Deforestation	PRODES Amazonia	http://www.obt.inpe.br/OBT/assuntos/programas/amazonia/prodes
2h4	Phenology	MODIS Normalized Difference Vegetative Inex	https://modis.gsfc.nasa.gov/data/dataprod/mod13.php
2h4	Temperature [Near] Surface	MERRIS-2 monthly temperature	https://goldsmr4.gesdisc.eosdis.nasa.gov/data/MERRA2_MONTHLY/M2TMNXLND.5.12.4/
2h4	Phenology	USA-National Phenology Network (NPN) phenology data	https://www.usanpn.org/data/observational
2h4	Phenology	USA-National Phenology Network (NPN) Spring Index raster data products	https://data.usanpn.org/geoserver-request-builder/
2h4	Phenology	German oak phenology data	https://opendata.dwd.de/
2h4	Phenology	Harvard Forest	https://harvardforest1.fas.harvard.edu/exist/apps/datasets/showData.html?id=hf003
2h4	Phenology	Natures Calendar	https://naturescalendar.woodlandtrust.org.uk/
2h4	Phenology	PhenoCam	http://phenocam.sr.unh.edu
2h4	Phenology	UK Cumbrian lakes data	https://catalogue.ceh.ac.uk/documents/bf30d6aa-345a-4771-8417-ffbcf8c08c28/
2h5	Vegetation Optical Depth	Global Long-term Microwave Vegetation Optical Depth Climate Archive (VODCA) v2	https://researchdata.tuwien.ac.at/records/t74ty-tcx62
2h5	Modes of Variability	Southern Oscillation Index	http://www.bom.gov.au/climate/enso/soi/

Sidebar 2.2 Near-surface equivalent temperature as a key climate change metric

Sub-section	General Variable or Phenomenon	Specific dataset or variable	Source
SB2.2	Temperature [Near] Surface	ERA5	https://www.ecmwf.int/en/forecasts/dataset/ecmwf-reanalysis-v5
SB2.2	Dewpoint	ERA5	https://www.ecmwf.int/en/forecasts/dataset/ecmwf-reanalysis-v5
SB2.2	Pressure [Near] Surface	ERA5	https://www.ecmwf.int/en/forecasts/dataset/ecmwf-reanalysis-v5
SB2.2	Humidity [Near] Surface	HadISDH	www.metoffice.gov.uk/hadobs/hadisdh, https://catalogue.ceda.ac.uk/uuid/251474c7b09449d8b9e7aeaf1461858f

Appendix 3: Supplemental materials

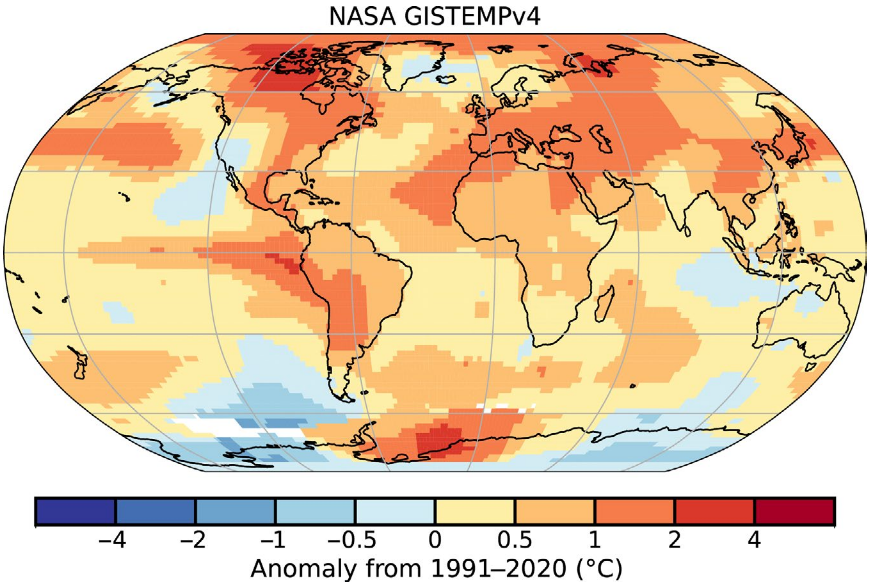

Fig. A2.1. Global surface temperature anomalies. (°C; Source: NASA-GISTEMPv4.)

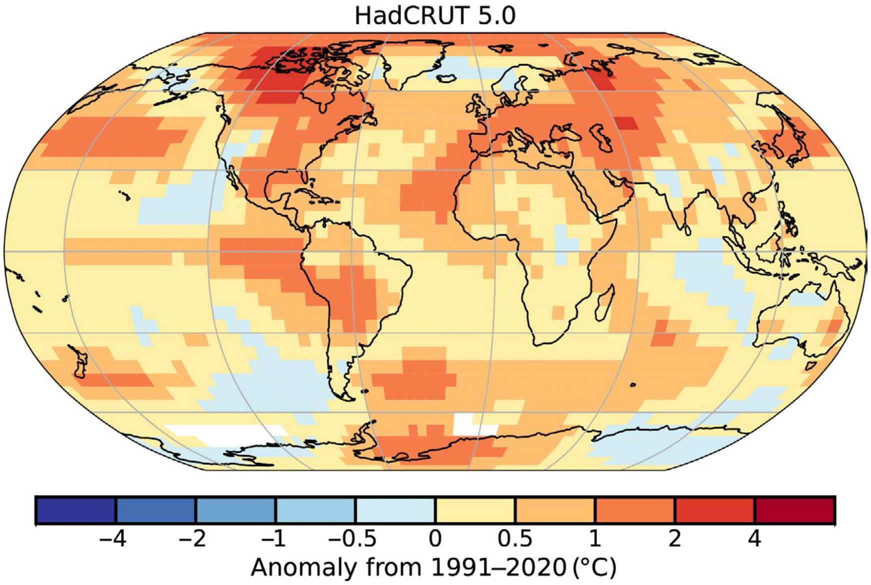

Fig. A2.2. Global surface temperature anomalies. (°C; Source: HadCRUT5.)

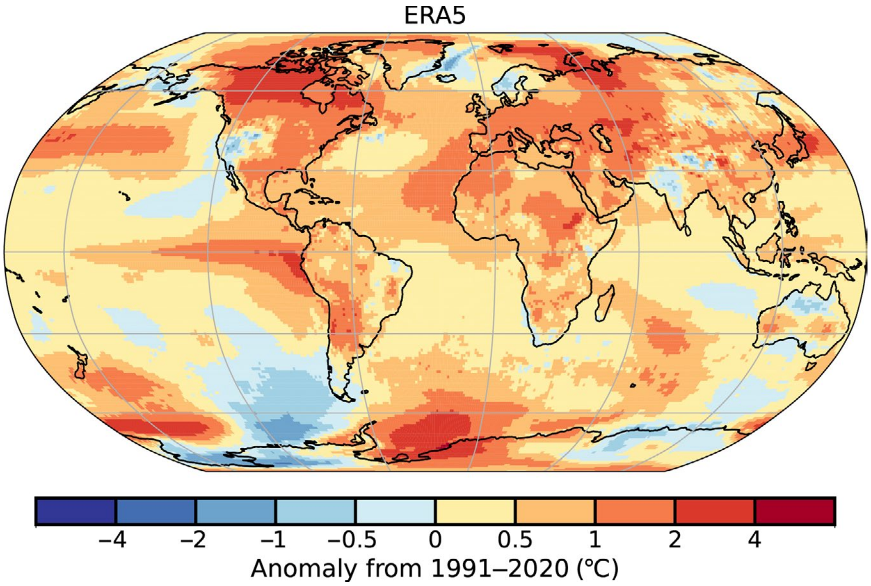

Fig. A2.3. Global surface temperature anomalies. (°C; Source: ERA5.).

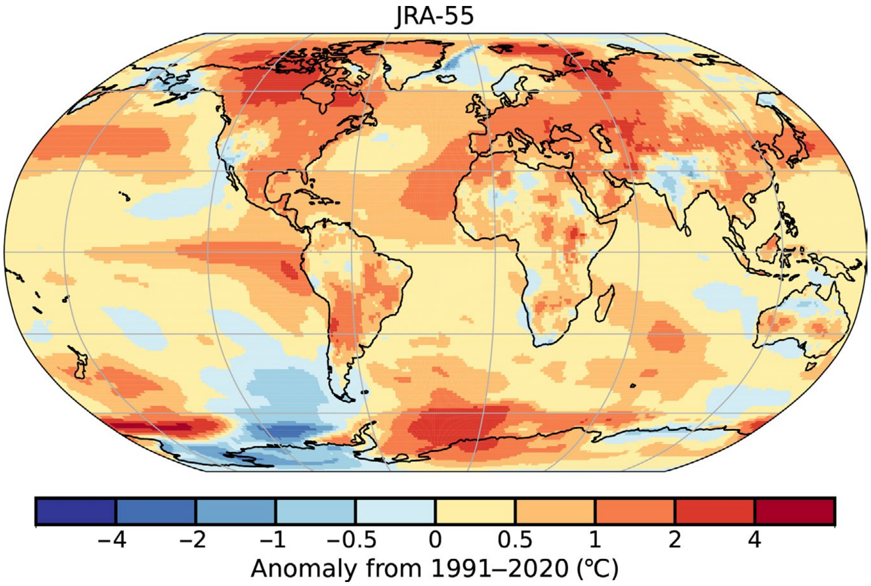

Fig. A2.4. Global surface temperature anomalies. (°C; Source: JRA-55.)

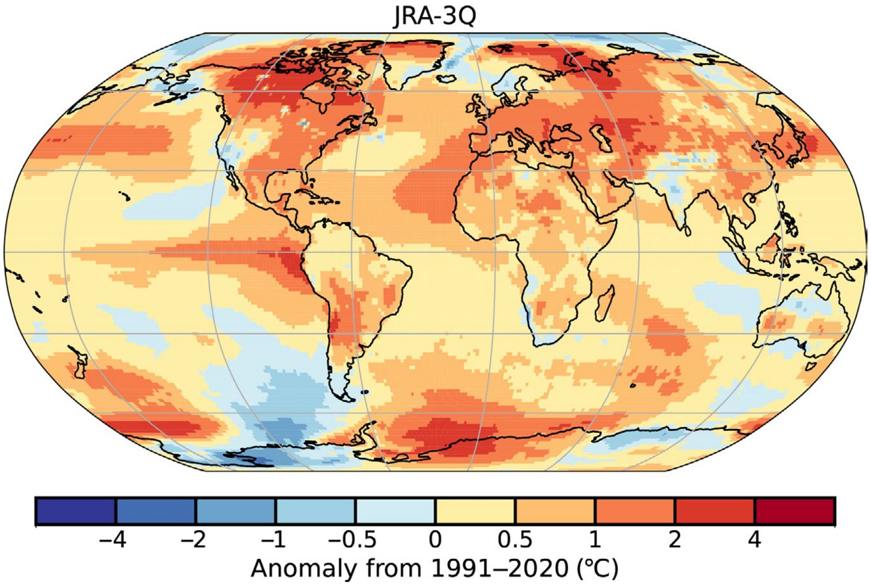

Fig. A2.5. Global surface temperature anomalies. (°C; Source: JRA-3Q.)

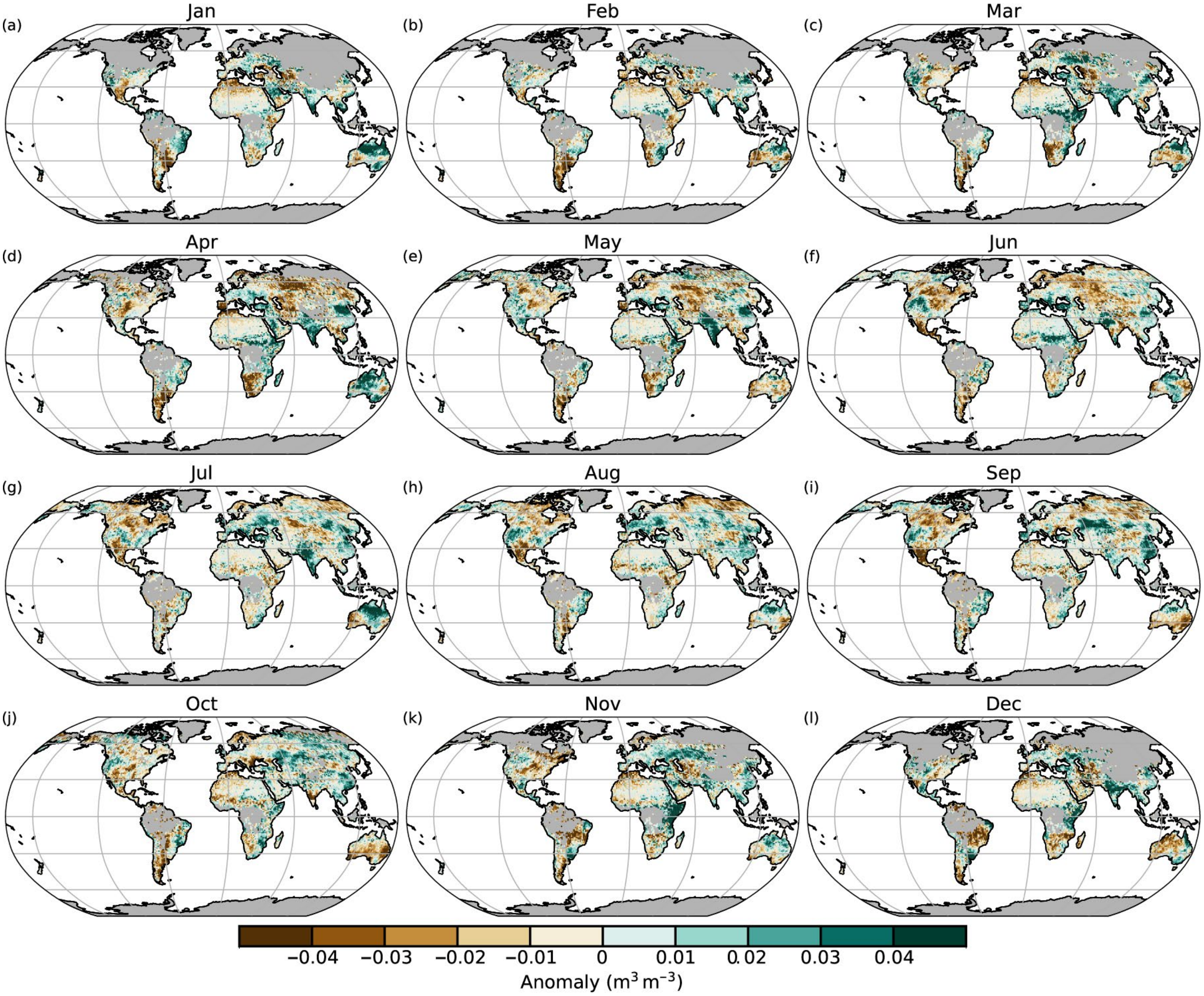

Fig. A2.6. Monthly average soil moisture anomalies for 2023 (m^3 m^{-3} ; 1991–2020 base period). Data are masked where no retrieval is possible or where the quality is not assured and flagged, for example due to dense vegetation, frozen soil, permanent ice cover, or radio frequency interference. (Source: C3S Soil Moisture.)

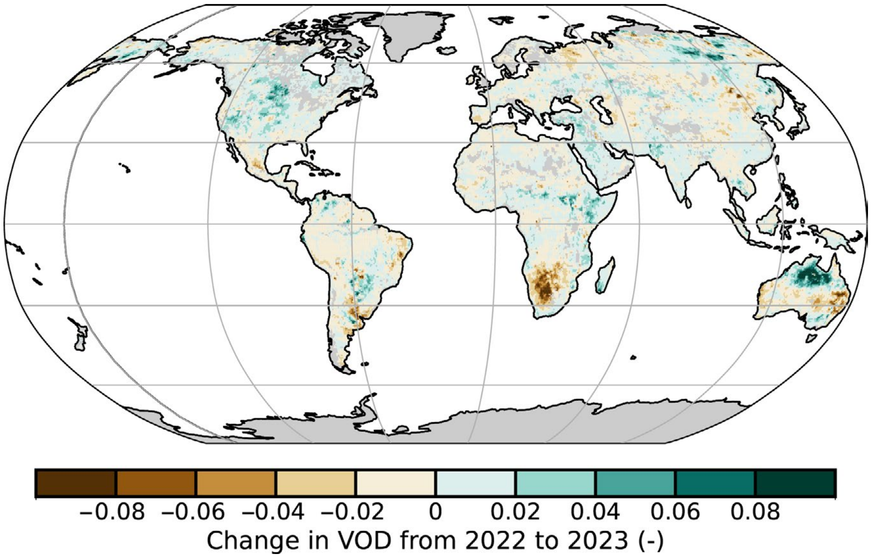

Fig. A2.7. The difference in average CXKu vegetation optical depth (VOD) between the years 2022 and 2023. Brown (green) colors indicate areas where VOD in 2023 were lower (higher) than in 2022. (Source: VODCA.)

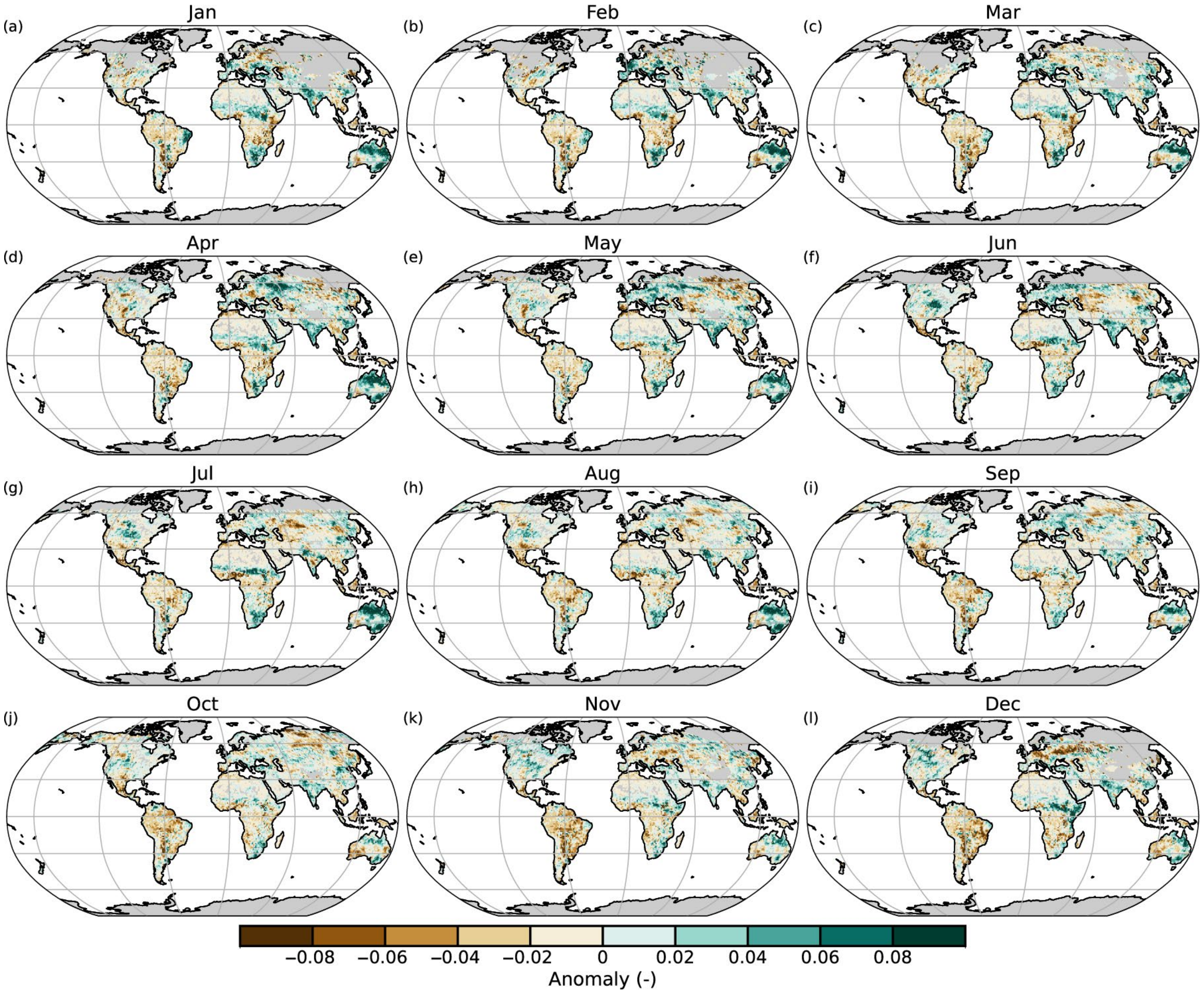

Fig. A2.8. VODCA monthly CXKu vegetation optical depth (VOD) anomalies in 2023 (1991–2020 base period). VOD cannot be retrieved over frozen or snow-covered areas, which is why they are masked out in winter.

Table A2.1. Notable precipitation events, with prior known record where long-term observations are available. (Source: GHCNDEX unless otherwise noted.)

Date	Index	Amount (mm)	Prior Record Year (Amount in mm)	Location	Reference
01/02/23	Rx5day	653.2	1987 (336.5)	Beverley Springs, Australia	
01/19/23	Rx1day	104		Antosyhihy, Madagascar	Davies (2023a)
02/14/23	Rx1day	183.8		Whangarei, New Zealand	Murray (2023)
02/14/23	Rx5day	408.7		Glenbervie Forest, Northland, New Zealand	Murray (2023)
02/14/23	Rx5day	447		The Pinnacles, New Zealand	Murray (2023)
02/19/23	Rx1day	682		Bertioga, Brazil	Davies (2023b)
02/24/23	Rx1day	672		Marromeu, Mozambique	United Nations Office for the Coordination of Humanitarian Affairs (2023)
08/03/23	Rx5day	488	1998 (264.4)	Almora Station, Australia	
09/03/23	Rx5day	421	2009 (294)	Undilla Station, Australia	Bureau of Meteorology (2024)
03/16/23	Rx1day	152.4	1962 (71.1)	Hat Creek, California, USA	
04/12/23	Rx1day	571.5	2003 (259.6)	Fort Lauderdale, Florida, USA	
05/02/23	Rx1day	182.6		Mushubati, Rwanda	World Meteorological Organization (WMO; 2023)
05/24/23	Rx1day	304.8	2018 (230.1)	Agat, Guam	
06/23/23	Rx1day	156.6		Retiro, Chile	Davies (2023c)
07/07/23	Rx5day	160.3	2001 (95.4)	Delsbo, Sweden	
07/20/23	Rx1day	198.6		Maharashtra, India	Davies (2023d)
07/28/23	Rx1day	649.8		Mulugu, India	The Watchers (2023)
08/19/23	Rx5day	371.9		Termas de Chillán, Chile	Davies (2023e)
08/22/23	Rx1day	73.7	2016 (38.1)	Rosette, Utah, USA	
08/24/23	Rx1day	123	2016 (73.6)	Harrow, Canada	
08/29/23	Rx5day	744.8		Wangjiayuan Reservoir, China	Du Yan (2023)

Date	Index	Amount (mm)	Prior Record Year (Amount in mm)	Location	Reference
09/04/23	Rx5day	1096.2		Zagora Pelion, Greece	WMO (2023)
09/05/23	Rx1day	759.6		Zagora Pelion, Greece	WMO (2023)
09/07/23	Rx1day	425	1926 (534.1)	Hong Kong Observatory	Hong Kong Observatory (2024)
09/07/23	Rx1h	158.1	2008 (145.5)	Hong Kong Observatory	Hong Kong Observatory (2024)
09/08/23	Rx1day	391.5	2013 (272)	Mobara City, Japan	Davies (2023f)
09/11/23	Rx1day	414.1		Al Badya, Libya	WMO (2023)
09/25/23	Rx1day	216		Dwarsberg, South Africa	Maswanganye (2023)
10/24/23	Rx1day	406		Al Ghadya Airport, Yemen	Davies (2023g)
10/29/23	Rx5day	1125.8	1995 (704.2)	Danang, Vietnam	
12/13/23	Rx5day	1933.8	1996 (1265.6)	Whyanbeel Valley, Australia	
12/13/23	Rx5day	1592.8	2018 (557.2)	White Cliff Point, Australia	
12/13/23	Rx5day	1295	2004 (745)	Copperlode Dam, Australia	
12/21/23	Rx5day	211.4	2022 (127)	Green Cape, Australia	

References

Adler, R., G. Gu, M. Sapiano, J. Wang, and G. Huffman, 2017: Global precipitation: Means, variations and trends during the satellite era (1979–2014). *Surv. Geophys.*, **38**, 679–699, https://doi.org/10.1007/s10712-017-9416-4.

——, and Coauthors, 2018: The Global Precipitation Climatology Project (GPCP) monthly analysis (new version 2.3) and a review of 2017 global precipitation. *Atmosphere*, **9**, 138, https://doi.org/10.3390/atmos9040138.

Alden, C. B., J. B. Miller, and J. W. C. White, 2010: Can bottom-up ocean CO_2 fluxes be reconciled with atmospheric ^{13}C observations? *Tellus*, **62B**, 369–388, https://doi.org/10.1111/j.1600-0889.2010.00481.x.

Ali, H., H. J. Fowler, and V. Mishra, 2018: Global observational evidence of strong linkage between dew point temperature and precipitation extremes. *Geophys. Res. Lett.*, **45**, 12 320–12 330, https://doi.org/10.1029/2018GL080557.

Allan, R. J., J. A. Lindesay, and D. E. Parker, 1996: El Niño Southern Oscillation and Climatic Variability. CSIRO Publishing, 405 pp.

Allan, R. P., C. Liu, M. Zahn, D. A. Lavers, E. Koukouvagias, and A. Bodas-Salcedo, 2014: Physically consistent responses of the global atmospheric hydrological cycle in models and observations. *Surv. Geophys.*, **35**, 533–552, https://doi.org/10.1007/s10712-012-9213-z.

Ammann, C. M., G. A. Meehl, W. M. Washington, and C. S. Zender, 2003: A monthly and latitudinally varying volcanic forcing dataset in simulations of 20th century climate. *Geophys. Res. Lett.*, **30**, 1657, https://doi.org/10.1029/2003GL016875.

Aono, Y., and K. Kazui, 2008: Phenological data series of cherry tree flowering in Kyoto, Japan, and its application to reconstruction of springtime temperatures since the 9th century. *Int. J. Climatol.*, **28**, 905–914, https://doi.org/10.1002/joc.1594.

Arguez, A., S. Hurley, A. Inamdar, L. Mahoney, A. Sanchez-Lugo, and L. Yang, 2020: Should we expect each year in the next decade (2019–28) to be ranked among the top 10 warmest years globally? *Bull. Amer. Meteor. Soc.*, **101**, E655–E663, https://doi.org/10.1175/BAMS-D-19-0215.1.

Arosio, C., A. Rozanov, E. Malinina, M. Weber, and J. P. Burrows, 2019: Merging of ozone profiles from SCIAMACHY, OMPS and SAGE II observations to study stratospheric ozone changes. *Atmos. Meas. Tech.*, **12**, 2423–2444, https://doi.org/10.5194/amt-12-2423-2019.

Augustine, J. A., K. O. Lantz, J.-P. Vernier, and J. E. Barnes, 2023: Mauna Loa apparent transmission record update for 2022 [in “State of the Climate in 2022”]. *Bull. Amer. Meteor. Soc.*, **104** (9), S81–S84, https://doi.org/10.1175/BAMS-D-23-0090.1.

Ayarzagüena, B., S. Ineson, N. J. Dunstone, M. P. Baldwin, and A. A. Scaife, 2018: Intraseasonal effects of El Niño–Southern Oscillation on North Atlantic climate. *J. Climate*, **31**, 8861–8873, https://doi.org/10.1175/JCLI-D-18-0097.1.

Azisov, E., M. Hoelzle, S. Vorogushyn, T. Saks, R. Usubaliev, M. Esenaman uulu, and M. Barandun, 2022: Reconstructed centennial mass balance change for Golubin glacier, Northern Tien Shan. *Atmosphere*, **13**, 954, https://doi.org/10.3390/atmos13060954.

Azorin-Molina, C., R. J. H. Dunn, L. Ricciardulli, C. A. Mears, T. R. McVicar, J. P. Nicolas, Z. Zeng, and M. G. Bosilovich, 2023a: Land and ocean surface winds [in “State of the Climate in 2022”]. *Bull. Amer. Meteor. Soc.*, **104** (9), S72–S74, https://doi.org/10.1175/BAMS-D-23-0090.1.

——, and Coauthors, 2023b: Biases in wind speed measurements due to anemometer changes. *Atmos. Res.*, **289**, 106771, https://doi.org/10.1016/j.atmosres.2023.106771.

Baldwin, J. W., T. Benmarhnia, K. L. Ebi, O. Jay, N. J. Lutsko, and J. K. Vanos, 2023: Humidity’s role in heat-related health outcomes: A heated debate. *Environ. Health Perspect.*, **131**, 055001, https://doi.org/10.1289/EHP11807.

Baldwin, M. P., and Coauthors, 2001: The quasi-biennial oscillation. *Rev. Geophys.*, **39**, 179–229, https://doi.org/10.1029/1999RG000073.

Barichivich, J., E. Gloor, P. Peylin, R. J. Brienen, J. Schöngart, J. C. Espinoza, and K. C. Pattnayak, 2018: Recent intensification of Amazon flooding extremes driven by strengthened Walker circulation. *Sci. Adv.*, **4**, eaat8785, https://doi.org/10.1126/sciadv.aat8785.

——, T. J. Osborn, I. Harris, G. van der Schrier, and P. D. Jones, 2020: Monitoring global drought using the self-calibrating Palmer Drought Severity Index [in “State of the Climate in 2019”]. *Bull. Amer. Meteor. Soc.*, **101** (8), S59–S60, https://doi.org/10.1175/BAMS-D-20-0104.1.

——, ——, ——, ——, and ——, 2021: Monitoring global drought using the self-calibrating Palmer Drought Severity Index [in “State of the Climate in 2020”]. *Bull. Amer. Meteor. Soc.*, **102** (8), S68–S70, https://doi.org/10.1175/BAMS-D-21-0098.1.

——, ——, ——, ——, and ——, 2022: Monitoring global drought using the self-calibrating Palmer Drought Severity Index [in “State of the Climate in 2021”]. *Bull. Amer. Meteor. Soc.*, **103** (8), S66–S67, https://doi.org/10.1175/BAMS-D-22-0092.1.

Bartow-Gillies, E., J. Blunden, and T. Boyer, 2023: A look at 2022: Takeaway points from the state of the climate. *Bull. Amer. Meteor. Soc.*, **104**, 810–820, https://doi.org/10.1175/BAMS-D-23-0192.1.

Basu, S., and Coauthors, 2022: Estimating emissions of methane consistent with atmospheric measurements of methane and $\delta^{13}C$ of methane. *Atmos. Chem. Phys.*, **22**, 15 351–15 377, https://doi.org/10.5194/acp-22-15351-2022.

Becker, A., P. Finger, A. Meyer-Christoffer, B. Rudolf, K. Schamm, U. Schneider, and M. Ziese, 2013: A description of the global land-surface precipitation data products of the Global Precipitation Climatology Centre with sample applications including centennial (trend) analysis from 1901–present. *Earth Syst. Sci. Data*, **5**, 71–99, https://doi.org/10.5194/essd-5-71-2013.

Behera, S. K., J. J. Luo, S. Masson, S. A. Rao, H. Sakuma, and T. Yamagata, 2006: A CGCM study on the interaction between IOD and ENSO. *J. Climate*, **19**, 1688–1705, https://doi.org/10.1175/JCLI3797.1.

Bell, B., and Coauthors, 2021: The ERA5 global reanalysis: Preliminary extension to 1950. *Quart. J. Roy. Meteor. Soc.*, **147**, 4186–4227, https://doi.org/10.1002/qj.4174.

Bell, G. D., and M. S. Halpert, 1998: Climate assessment for 1997. *Bull. Amer. Meteor. Soc.*, **79** (Suppl.), S1–S50, https://doi.org/10.1175/1520-0477-79.5s.S1.

Bellouin, N., and Coauthors, 2020: Radiative forcing of climate change from the Copernicus reanalysis of atmospheric composition. *Earth Syst. Sci. Data*, **12**, 1649–1677, https://doi.org/10.5194/essd-12-1649-2020.

Bessenbacher, V., D. L. Schumacher, M. Hirschi, S. I. Seneviratne, and L. Gudmundsson, 2023: Gap-filled multivariate observations of global land–climate interactions. *J. Geophys. Res. Atmos.*, **128**, e2023JD039099, https://doi.org/10.1029/2023JD039099.

Betts, R. A., C. D. Jones, J. R. Knight, R. F. Keeling, and J. J. Kennedy, 2016: El Niño and a record CO_2 rise. *Nat. Climate Change*, **6**, 806–810, https://doi.org/10.1038/nclimate3063.

Birkett, C., C. Reynolds, B. Beckley, and B. Doorn, 2011: From research to operations: The USDA Global Reservoir and Lake Monitor. *Coastal Altimetry*, S. Vignudelli et al., Eds., Springer, 19–50, https://doi.org/10.1007/978-3-642-12796-0_2.

Block, B. D., and Coauthors, 2019: The unique methodological challenges of winter limnology. *Limnol. Oceanogr. Methods*, **17**, 42–57, https://doi.org/10.1002/lom3.10295.

Bock, O., 2022: Global GNSS Integrated Water Vapour data, 1994–2022. AERIS, accessed 18 July 2024, https://doi.org/10.25326/68.

——, and A. C. Parracho, 2019: Consistency and representativeness of integrated water vapour from ground-based GPS observations and ERA-Interim reanalysis. *Atmos. Chem. Phys.*, **19**, 9453–9468, https://doi.org/10.5194/acp-19-9453-2019.

Bodhaine, B. A., B. G. Mendonca, J. M. Harris, and J. M. Miller, 1981: Seasonal variations in aerosols and atmospheric transmission at Mauna Loa Observatory. *J. Geophys. Res.*, **86**, 7395–7398, https://doi.org/10.1029/JC086iC08p07395.

Bowen, S., B. Kerschner, and J. Z. Ng, 2024: Natural catastrophe and climate report 2023: Data, insights and perspective. Gallagher Re, 76 pp., https://www.ajg.com/gallagherre/-/media/files/gallagher/gallagherre/news-and-insights/2024/january/natural-catastrophe-and-climate-report-2023.pdf.

Brohan, P., J. J. Kennedy, I. Harris, S. F. Tett, and P. D. Jones, 2006: Uncertainty estimates in regional and global observed temperature changes: A new data set from 1850. *J. Geophys. Res.*, **111**, D12106, https://doi.org/10.1029/2005JD006548.

Brutsaert, W., 2017: Global land surface evaporation trend during the past half century: Corroboration by Clausius-Clapeyron scaling. *Adv. Water Resour.*, **106**, 3–5, https://doi.org/10.1016/j.advwatres.2016.08.014.

Bureau of Meteorology, 2024a: Annual climate statement 2023. Accessed 15 February 2024, http://www.bom.gov.au/climate/current/annual/aus/.

——, 2024b: Tropical climate update. Accessed 15 January 2024, http://www.bom.gov.au/climate/tropical-note/.

Butchart, N., 2014: The Brewer-Dobson circulation. *Rev. Geophys.*, **52**, 157–184, https://doi.org/10.1002/2013RG000448.

Buzan, J. R., and M. Huber, 2020: Moist heat stress on a hotter Earth. *Annu. Rev. Earth Planet. Sci.*, **48**, 623–655, https://doi.org/10.1146/annurev-earth-053018-060100.

Byrne, M. P., and P. A. O'Gorman, 2013: Link between land–ocean warming contrast and surface relative humidities in simulations with coupled climate models. *Geophys. Res. Lett.*, **40**, 5223–5227, https://doi.org/10.1002/grl.50971.

——, and ——, 2018: Trends in continental temperature and humidity directly linked to ocean warming. *Proc. Natl. Acad. Sci. USA*, **115**, 4863–4868, https://doi.org/10.1073/pnas.1722312115.

Caine, T., J. Morse, and Niwot Ridge LTER, 2023: Lake ice clearance and formation data for Green Lakes Valley, 1968 – ongoing, version 6. Environmental Data Initiative, accessed 17 January 2024, https://doi.org/10.6073/pasta/e89a9a6984ebbcdbbc85c16d65298dd2.

Campos, D., and R. Rondanelli, 2023: ENSO-related precipitation variability in Central Chile: The role of large scale moisture transport. *J. Geophys. Res. Atmos.*, **128**, e2023JD038671, https://doi.org/10.1029/2023JD038671.

Capotondi, A., and Coauthors, 2015: Understanding ENSO diversity. *Bull. Amer. Meteor. Soc.*, **96**, 921–938, https://doi.org/10.1175/BAMS-D-13-00117.1.

Carn, S., N. Krotkov, B. Fisher, and C. Li, 2022: Out of the blue: Volcanic SO2 emissions during the 2021–2022 eruptions of Hunga Tonga —— Hunga Ha'apai (Tonga). Front. *Earth Sci.*, **10**, 976962, https://doi.org/10.3389/feart.2022.976962.

Carrea, L., O. Embury, and C. J. Merchant, 2015: Datasets related to in-land water for limnology and remote sensing applications: Distance-to-land, distance-to-water, water-body identifier and lake-centre co-ordinates. *Geosci. Data J.*, **2**, 83–97, https://doi.org/10.1002/gdj3.32.

——, and Coauthors, 2019: Lake surface temperature [in "State of the Climate in 2018"]. *Bull. Amer. Meteor. Soc.*, **100** (8), S13–S14, https://doi.org/10.1175/2019BAMSStateoftheClimate.1.

——, and Coauthors, 2020: Lake surface temperature [in "State of the Climate in 2019"]. *Bull. Amer. Meteor. Soc.*, **101** (8), S26–S28, https://doi.org/10.1175/BAMS-D-20-0104.1.

——, C. Merchant, B. Calmettes, and J.-F. Cretaux, 2021: Lake surface water temperature [in "State of the Climate in 2020"]. *Bull. Amer. Meteor. Soc.*, **102** (8), S28–S31, https://doi.org/10.1175/BAMS-D-21-0098.1.

——, ——, and R. I. Woolway, 2022a: Lake surface water temperature [in "State of the Climate in 2021"]. *Bull. Amer. Meteor. Soc.*, **103** (8), S28–S30, https://doi.org/10.1175/BAMS-D-22-0092.1.

——, and Coauthors, 2022b: ESA Lakes Climate Change Initiative (Lakes_cci): Lake products, version 2.0.2. NERC EDS Centre for Environmental Data Analysis[NR9][KW10], accessed March 2024, https://doi.org/10.5285/a07deacaffb8453e93d57ee214676304.

——, and Coauthors, 2023: Satellite-derived multivariate worldwide lake physical variable timeseries for climate studies. *Sci. Data*, **10**, 30, https://doi.org/10.1038/s41597-022-01889-z.

Chandra, S., E. K. Suenaga, F. Scordo, and T. A. Daniel, 2022: Mountain lake biology, chemistry, physics, and climate data since 1959 at Castle Lake, version 1. Environmental Data Initiative, accessed 17 January 2024, https://doi.org/10.6073/pasta/a8e3b81cfe5864731b29ad42506c65d7.

Chang, K.-L., M. G. Schultz, X. Lan, A. McClure-Begley, I. Petropavlovskikh, X. Xu, and J. R. Ziemke, 2021: Trend detection of atmospheric time series: Incorporating appropriate uncertainty estimates and handling extreme events. *Elementa*, **9**, 00035, https://doi.org/10.1525/elementa.2021.00035.

——, and Coauthors, 2022: Impact of the COVID-19 economic downturn on tropospheric ozone trends: An uncertainty weighted data synthesis for quantifying regional anomalies above western North America and Europe. *AGU Adv.*, **3**, e2021AV000542, https://doi.org/10.1029/2021AV000542.

——, and Coauthors, 2023: Diverging ozone trends above western North America: Boundary layer decreases versus free tropospheric increases. *J. Geophys. Res. Atmos.*, **128**, e2022JD038090, https://doi.org/10.1029/2022JD038090.

Christianson, K. R., K. A. Loria, P. D. Blanken, N. Caine, and P. T. J. Johnson, 2021: On thin ice: Linking elevation and long-term losses of lake ice cover. *Limnol. Oceanogr. Lett.*, **6**, 77–84, https://doi.org/10.1002/lol2.10181.

Christy, J. R., R. W. Spencer, W. B. Norris, W. D. Braswell, and D. E. Parker, 2003: Error estimates of version 5.0 of MSU–AMSU bulk atmospheric temperatures. *J. Atmos. Oceanic Technol.*, **20**, 613–629, https://doi.org/10.1175/1520-0426(2003)20<613:EEOVOM>2.0.CO;2.

Chung, E.-S., B. Soden, and V. O. John, 2013: Intercalibrating microwave satellite observations for monitoring long-term variations in upper- and midtropospheric water vapor. *J. Atmos. Oceanic Technol.*, **30**, 2303–2319, https://doi.org/10.1175/JTECH-D-13-00001.1.

——, ——, B. Sohn, and L. Shi, 2014: Upper-tropospheric moistening in response to anthropogenic warming. *Proc. Natl. Acad. Sci. USA*, **111**, 11 636–11 641, https://doi.org/10.1073/pnas.1409659111.

Cicoira, A., J. Beutel, J. Faillettaz, and A. Vieli, 2019: Water controls the seasonal rhythm of rock glacier flow. *Earth Planet. Sci. Lett.*, **528**, 115844, https://doi.org/10.1016/j.epsl.2019.115844.

Clark, H., and Coauthors, 2021: The effects of the COVID-19 lockdowns on the composition of the troposphere as seen by In-service Aircraft for a Global Observing System (IAGOS) at Frankfurt. *Atmos. Chem. Phys.*, **21**, 16 237–16 256, https://doi.org/10.5194/acp-21-16237-2021.

Clarke, B., and Coauthors, 2024: Climate change, not El Niño, main driver of extreme drought in highly vulnerable Amazon River Basin. World Weather Attribution, 43 pp., https://doi.org/10.25561/108761.

Coldewey-Egbers, M., D. G. Loyola, C. Lerot, and M. Van Roozendael, 2022: Global, regional and seasonal analysis of total ozone trends derived from the 1995–2020 GTO-ECV climate data record. *Atmos. Chem. Phys.*, **22**, 6861–6878, https://doi.org/10.5194/acp-22-6861-2022.

Cornes, R. C., E. C. Kent, D. I. Berry, and J. J. Kennedy, 2020: CLASSnmat: A global night marine air temperature data set, 1880–2019. *Geosci. Data J.*, **7**, 170–184, https://doi.org/10.1002/gdj3.100.

Crimmins, T. M., R. L. Marsh, J. Switzer, M. A. Crimmins, K. L. Gerst, A. H. Rosemartin, and J. F. Weltzin, 2017: USA National Phenology Network gridded products documentation. USGS Open-File Rep. 2017–1003, 34 pp., https://doi.org/10.3133/ofr20171003.

——, E. G. Denny, E. E. Posthumus, A. H. Rosemartin, R. Croll, M. Montano, and H. Panci, 2022: Science and management advancements made possible by the USA National Phenology Network's Nature's Notebook platform. *BioScience*, **72**, 908–920, https://doi.org/10.1093/biosci/biac061.

Cropper, T. E., D. I. Berry, R. C. Cornes, and E. C. Kent, 2023: Quantifying daytime heating biases in marine air temperature observations from ships. *J. Atmos. Oceanic Technol.*, **40**, 427–438, https://doi.org/10.1175/JTECH-D-22-0080.1.

C3S, 2024: 2023 is the hottest year on record, with global temperatures close to the 1.5°C limit. Copernicus Climate Change Service, 9 January, https://climate.copernicus.eu/copernicus-2023-hottest-year-record.

Cusicanqui, D., A. Rabatel, C., Vincent, X., Bodin, E. Thibert, and B. Francou, 2021: Interpretation of volume and flux changes of the Laurichard rock glacier between 1952 and 2019, French Alps. *J. Geophys. Res. Earth Surface*, **126**, e2021JF006161, https://doi.org/10.1029/2021JF006161.

Daniel, J. S., S. Solomon, and D. L. Albritton, 1995: On the evaluation of halocarbon radiative forcing and global warming potentials. *J. Geophys. Res.*, **100**, 1271–1285, https://doi.org/10.1029/94JD02516.

Davidson, E. A., 2009: The contribution of manure and fertilizer nitrogen to atmospheric nitrous oxide since 1860. *Nat. Geosci.*, **2**, 659–662, https://doi.org/10.1038/ngeo608.

Davies, R., 2023a: Madagascar – 700 homes flooded as tropical storm Cheneso makes landfall. Floodlist, 20 January, accessed 13 February 2023, https://floodlist.com/africa/madagascar-tropical-storm-cheneso-january-2023.

——, 2023b: Brazil – Death toll rises in Sao Paulo floods and landslide. Floodlist, 21 February, accessed 16 February 2024, https://floodlist.com/america/brazil-sao-paulo-floods-update-february-2023.

——, 2023c: Chile – 2 Dead, 6 missing after floods in 7 regions. Floodlist, 25 June, accessed 15 February 2024, https://floodlist.com/america/chile-floods-june-2023.

——, 2023d: India – 12 killed in landslide after heavy rain in Maharashtra. Floodlist, 20 July, accessed 16 February 2024, https://floodlist.com/asia/india-maharashtra-floods-landslide-july-2023.

——, 2023e: Chile – Over 30,000 evacuate floods in 6 regions. Floodlist, 22 August, accessed 15 February 2024, https://floodlist.com/america/chile-floods-august-2023.

——, 2023f: Japan – Floods impact Chiba, Fukushima and Ibaraki after record rain. Floodlist, 11 September, accessed 15 February 2024, https://floodlist.com/asia/japan-floods-september-2023.

——, 2023g: Yemen – Thousands displaced by floods after cyclone Tej dumps 400 mm of rain. Floodlist, 25 October, accessed 16 February 2024, https://floodlist.com/asia/yemen-floods-cyclone-tej-october-2023.

Davis, S., and Coauthors, 2023: Hunga Tonga-Hunga Ha'apai eruption [in "State of the Climate 2022"]. *Bull. Amer. Meteor. Soc.*, **104** (9), S82–S84, https://doi.org/10.1175/BAMS-D-23-0090.1.

Dee, D. P., and Coauthors, 2011: The ERA-Interim reanalysis: Configuration and performance of the data assimilation system. *Quart. J. Roy. Meteor. Soc.*, **137**, 553–597, https://doi.org/10.1002/qj.828.

Deeter, M. N., and Coauthors, 2014: The MOPITT version 6 product: Algorithm enhancements and validation. *Atmos. Meas. Tech.*, **7**, 3623–3632, https://doi.org/10.5194/amt-7-3623-2014.

——, D. P. Edwards, G. L. Francis, J. C. Gille, S. Martínez-Alonso, H. M. Worden, and C. Sweeney, 2017: A climate-scale satellite record for carbon monoxide: The MOPITT version 7 product. *Atmos. Meas. Tech.*, **10**, 2533–2555, https://doi.org/10.5194/amt-10-2533-2017.

——, and Coauthors, 2019: Radiance-based retrieval bias mitigation for the MOPITT instrument: The version 8 product. *Atmos. Meas. Tech.*, **12**, 4561–4580, https://doi.org/10.5194/amt-12-4561-2019.

Deng, K., C. Azorin-Molina, L. Minola, G. Zhang, and D. Chen, 2020: Global near-surface wind speed changes over the last decades revealed by reanalyses and CMIP6 model simulations. *J. Climate*, **34**, 2219–2234, https://doi.org/10.1175/JCLI-D-20-0310.1.

de Oliveira, G., and Coauthors, 2023: Increasing wildfires threaten progress on halting deforestation in Brazilian Amazonia. *Nat. Ecol. Evol.*, **7**, 1945–1946, https://doi.org/10.1038/s41559-023-02233-3.

DiGangi, E. A., M. Stock, and J. Lapierre, 2021: Thunder hours: How old methods offer new insights into thunderstorm climatology. *Bull. Amer. Meteor. Soc.*, **103**, E548–E569, https://doi.org/10.1175/BAMS-D-20-0198.1.

Dlugokencky, E. J., L. P. Steele, P. M. Lang, and K. A. Masarie, 1994: The growth rate and distribution of atmospheric methane. *J. Geophys. Res.*, **99**, 17 021–17 043, https://doi.org/10.1029/94JD01245.

DMC, 2023a: Monthly Climate Bulletin, June Edition (in Spanish). Dirección Meteorológica de Chile, 28 pp., https://climatologia.meteochile.gob.cl/application/publicaciones/documentoPdf/boletinClimatologicoMensual/boletinClimatologicoMensual202306.pdf.

Domeisen, D. I. V., C. I. Garfinkel, and A. H. Butler, 2019: The teleconnection of El Niño Southern Oscillation to the stratosphere. *Rev. Geophys.*, **57**, 5–47, https://doi.org/10.1029/2018RG000596.

Donat, M. G., L. V. Alexander, H. Yang, I. Durre, R. Vose, and J. Caesar, 2013: Global land-based datasets for monitoring climatic extremes. *Bull. Amer. Meteor. Soc.*, **94**, 997–1006, https://doi.org/10.1175/BAMS-D-12-00109.1.

Dorigo, W., and Coauthors, 2017: ESA CCI soil moisture for improved Earth system understanding: State-of-the art and future directions. *Remote Sens. Environ.*, **203**, 185–215, https://doi.org/10.1016/j.rse.2017.07.001.

——, L. Mösinger, R. van der Schalie, R.-M. Zotta, T. M. Scanlon, and R. De Jeu, 2021: Long-term monitoring of vegetation state through passive microwave satellites [in "State of the Climate in 2020"]. *Bull. Amer. Meteor. Soc.*, **102** (8), S110–S112, https://doi.org/10.1175/BAMS-D-21-0098.1.

——, R. Zotta, R. van der Schalie, W. Preimesberger, L. Mösinger, and R. De Jeu, 2022: Vegetation optical depth [in "State of the Climate in 2021"]. *Bull. Amer. Meteor. Soc.*, **103** (8), S108–S109, https://doi.org/10.1175/BAMS-D-22-0092.1.

——, W. Preimesberger, C. Reimer, R. van der Schalie, A. Pasik, R. De Jeu, and C. Paulik, 2023: Soil moisture gridded data from 1978 to present, v202212.0.0. Copernicus Climate Change Service (C3S) Climate Data Store (CDS), accessed 16 January 2024, https://cds.climate.copernicus.eu/cdsapp#!/dataset/satellite-soil-moisture?tab=overview.

Dudok de Wit, T., G. Kopp, C. Fröhlich, and M. Schöll, 2017: Methodology to create a new Total Solar Irradiance record: Making a composite out of multiple data records. *Geophys. Res. Lett.*, **44**, 1196–1203, https://doi.org/10.1002/2016GL071866.

Dunn, R. J. H., 2019: HadISD version 3: Monthly updates. Hadley Centre Tech. Note 103, 10 pp., www.metoffice.gov.uk/research/library-and-archive/publications/science/climate-science-technical-notes.

——, and C. P. Morice, 2022: On the effect of reference periods on trends in percentile-based extreme temperature indices. *Environ. Res. Lett.*, **17**, 034026, https://doi.org/10.1088/1748-9326/ac52c8.

——, K. M. Willett, P. W. Thorne, E. V. Woolley, I. Durre, A. Dai, D. E. Parker, and R. S. Vose, 2012: HadISD: A quality-controlled global synoptic report database for selected variables at long-term stations from 1973–2011. *Climate Past*, **8**, 1649–1679, https://doi.org/10.5194/cp-8-1649-2012.

——, ——, D. E. Parker, and L. Mitchell, 2016: Expanding HadISD: Quality-controlled, sub-daily station data from 1931. *Geosci. Instrum. Methods Data Syst.*, **5**, 473–491, https://doi.org/10.5194/gi-5-473-2016.

——, and Coauthors, 2020: Development of an updated global land in situ–based data set of temperature and precipitation extremes: HadEX3. *J. Geophys. Res. Atmos.*, **125**, e2019JD032263, https://doi.org/10.1029/2019JD032263.

——, C. Azorin-Molina, M. J. Menne, Z. Zeng, N. W. Casey, and C. Shen, 2022a: Reduction in reversal of global stilling arising from correction to encoding of calm periods. *Environ. Res. Commun.*, **4**, 061003, https://doi.org/10.1088/2515-7620/ac770a.

——, M. G. Donat, and L. V. Alexander, 2022b: Comparing extremes indices in recent observational and reanalysis products. *Front. Climate*, **4**, 989505, https://doi.org/10.3389/fclim.2022.989505.

Duveiller, G., and N. Gobron, 2023: Land surface properties: Terrestrial surface albedo dynamics [in "State of the Climate in 2022"]. *Bull. Amer. Meteor. Soc.*, **104** (9), S102–S103, https://doi.org/10.1175/BAMS-D-23-0090.1.

DWD, 2023: Deutschlandwetter im Jahr 2023. DWD, 29 December, https://www.dwd.de/DE/presse/pressemitteilungen/DE/2023/20231229_deutschlandwetter_jahr2023_news.html.

Edwards, M., and A. Richardson, 2004: Impact of climate change on marine pelagic phenology and trophic mismatch. *Nature*, **430**, 881–884, https://doi.org/10.1038/nature02808.

Ellis, H. T., and R. F. Pueschel, 1971: Solar radiation: Absence of air pollution trends at Mauna Loa. *Science*, **172**, 845–846, https://doi.org/10.1126/science.172.3985.845.

Estilow, T. W., A. H. Young, and D. A. Robinson, 2015: A long-term Northern Hemisphere snow cover extent data record for climate studies and monitoring. *Earth Syst. Sci. Data*, **7**, 137–142, https://doi.org/10.5194/essd-7-137-2015.

Etheridge, D. M., L. P. Steele, R. L. Langenfelds, R. J. Francey, J. M. Barnola, and V. I. Morgan, 1996: Natural and anthropogenic changes in atmospheric CO_2 over the last 1000 years from air in Antarctic ice and firn. *J. Geophys. Res.*, **101**, 4115–4128, https://doi.org/10.1029/95JD03410.

Etzelmüller, B., K. Isaksen, J. Czekirda, S. Westermann, C. Hilbich, and C. Hauck, 2023: Rapid warming and degradation of mountain permafrost in Norway and Iceland. *Cryosphere*, **17**, 5477–5497, https://doi.org/10.5194/tc-17-5477-2023.

Evan, S., and Coauthors, 2023: Rapid ozone depletion after humidification of the stratosphere by the Hunga Tonga Eruption. *Science*, **382**, eadg2551, https://doi.org/10.1126/science.adg2551.

Feng, L., P. I. Palmer, S. Zhu, R. J. Parker, and Y. Liu, 2022: Tropical methane emissions explain large fraction of recent changes in global atmospheric methane growth rate. *Nat. Commun.*, **13**, 1378, https://doi.org/10.1038/s41467-022-28989-z.

FEWS NET, 2023: Widespread extreme seasonal rains cause severe floods but improve agricultural productivity over eastern Horn. East Africa Seasonal Monitor, 30 November, 5 pp., https://fews.net/east-africa/seasonal-monitor/november-2023.

Fioletov, V. E., G. E. Bodeker, A. J. Miller, R. D. McPeters, and R. Stolarski, 2002: Global and zonal total ozone variations estimated from ground-based and satellite measurements: 1964–2000. *J. Geophys. Res.*, **107**, 4647, https://doi.org/10.1029/2001JD001350.

——, and Coauthors, 2008: The performance of the ground-based total ozone network assessed using satellite data. *J. Geophys. Res.*, **113**, D14313, https://doi.org/10.1029/2008JD009809.

Fiore, A. M., and Coauthors, 2022: Understanding recent tropospheric ozone trends in the context of large internal variability: A new perspective from chemistry-climate model ensembles. *Environ. Res. Climate*, **1**, 025008, https://doi.org/10.1088/2752-5295/ac9cc2.

Fisher, J. B., and Coauthors, 2017: The future of evapotranspiration: Global requirements for ecosystem functioning, carbon and climate feedbacks, agricultural management, and water resources. *Water Resour. Res.*, **53**, 2618–2626, https://doi.org/10.1002/2016WR020175.

——, and Coauthors, 2020: ECOSTRESS: NASA's next generation mission to measure evapotranspiration from the international space station. *Water Resour. Res.*, **56**, e2019WR026058, https://doi.org/10.1029/2019WR026058.

Fleming, E. L., P. A. Newman, Q. Liang, and L. D. Oman, 2024: Stratospheric temperature and ozone impacts of the Hunga Tonga-Hunga Ha'apai water vapor injection. *J. Geophys. Res. Atmos.*, **129**, e2023JD039298, https://doi.org/10.1029/2023JD039298.

Fogt, R. L., and G. J. Marshall, 2020: The Southern Annular Mode: Variability, trends, and climate impacts across the Southern Hemisphere. *Wiley Interdiscip. Rev.: Climate Change*, **11**, e652, https://doi.org/10.1002/wcc.652.

Folland, C. K., J. Knight, H. W. Linderholm, D. Fereday, S. Ineson, and J. W. Hurrell, 2009: The Summer North Atlantic Oscillation: Past, present and future. *J. Climate*, **22**, 1082–1103, https://doi.org/10.1175/2008JCLI2459.1.

Forster, P., and Coauthors, 2021: The Earth's energy budget, climate feedbacks, and climate sensitivity. Climate Change 2021: The Physical Science Basis, V. Masson-Delmotte et al., Eds., Cambridge University Press, 923–1054, https://doi.org/10.1017/9781009157896.009.

Forster, P. M., and Coauthors, 2023: Indicators of Global Climate Change 2022: Annual update of large-scale indicators of the state of the climate system and human influence. *Earth Syst. Sci. Data*, **15**, 2295–2327, https://doi.org/10.5194/essd-15-2295-2023.

Foster, M. J., C. Phillips, A. K. Heidinger, E. E. Borbas, Y. Li, W. P. Menzel, A. Walther, and E. Weisz, 2023: PATMOS-x version 6.0: 40 years of merged AVHRR and HIRS global cloud data. *J. Climate*, **36**, 1143–1160, https://doi.org/10.1175/JCLI-D-22-0147.1.

Fountain, A. G., B. Glenn, and C. McNeil, 2023: Inventory of glaciers and perennial snowfields of the conterminous USA. *Earth Syst. Sci. Data*, **15**, 4077–4104, https://doi.org/10.5194/essd-15-4077-2023.

Fowler, H. J., and Coauthors, 2021: Anthropogenic intensification of short-duration rainfall extremes. *Nat. Rev. Earth Environ.*, **2**, 107–122, https://doi.org/10.1038/s43017-020-00128-6.

Frauenfelder, R., W. Haeberli, and M. Hoelzle, 2003: Rock glacier occurrence and related terrain parameters in a study area of the Eastern Swiss Alps. Permafrost: Proceedings of the 8th International Conference on Permafrost, M. Phillips, S. M. Springman, and L. U. Arenson, Eds., A. A. Balkema, 253–258, https://www.arlis.org/docs/vol1/ICOP/55700698/Pdf/Chapter_046.pdf.

Free, M., D. J. Seidel, J. K. Angel, J. Lanzante, I. Durre, and T. C. Peterson, 2005: Radiosonde Atmospheric Temperature Products for Assessing Climate (RATPAC): A new dataset of large-area anomaly time series. *J. Geophys. Res.*, **110**, D22101, https://doi.org/10.1029/2005JD006169.

Friedlingstein, P., and Coauthors, 2023: Global carbon budget 2023. *Earth Syst. Sci. Data*, **15**, 5301–5369, https://doi.org/10.5194/essd-15-5301-2023.

Frith, S. M., N. A. Kramarova, R. S. Stolarski, R. D. McPeters, P. K. Bhartia, and G. J. Labow, 2014: Recent changes in total column ozone based on the SBUV Version 8.6 Merged Ozone Data Set. *J. Geophys. Res. Atmos.*, **119**, 9735–9751, https://doi.org/10.1002/2014JD021889.

——, R. S. Stolarski, N. A. Kramarova, and R. D. McPeters, 2017: Estimating uncertainties in the SBUV Version 8.6 merged profile ozone data set. *Atmos. Chem. Phys.*, **17**, 14 695–14 707, https://doi.org/10.5194/acp-17-14695-2017.

Fritz, S., and Coauthors, 2019: Citizen science and the United Nations sustainable development goals. *Nat. Sustainability*, **2**, 922–930, https://doi.org/10.1038/s41893-019-0390-3.

Fromm, M., R. Servranckx, B. J. Stocks, and D. A. Peterson, 2022: Understanding the critical elements of the pyrocumulonimbus storm sparked by high-intensity wildland fire. *Commun. Earth Environ.*, **3**, 243, https://doi.org/10.1038/s43247-022-00566-8.

Füllekrug, M., E. Williams, C. Price, S. Goodman, R. Holzworth, K. Virts, and D. Buechler, 2022: Lightning ["State of the Climate in 2021"]. *Bull. Amer. Meteor. Soc.*, **103** (8), S79–S81, https://doi.org/10.1175/BAMS-D-22-0092.1.

Garane, K., and Coauthors, 2018: Quality assessment of the Ozone_cci Climate Research Data Package (release 2017): 1. Ground-based validation of total ozone column data products. *Atmos. Meas. Tech.*, **11**, 1385–1402, https://doi.org/10.5194/amt-11-1385-2018.

Garfinkel, C. I., A. Gordon, L. D. Oman, F. Li, S. Davis, and S. Pawson, 2018: Nonlinear response of tropical lower-stratospheric temperature and water vapor to ENSO. Atmos. *Chem. Phys.*, **18**, 4597–4615, https://doi.org/10.5194/acp-18-4597-2018.

——, and Coauthors, 2021: Influence of the El Niño–Southern Oscillation on entry stratospheric water vapor in coupled chemistry–ocean CCMI and CMIP6 models. *Atmos. Chem. Phys.*, **21**, 3725–3740, https://doi.org/10.5194/acp-21-3725-2021.

Garrigues, S., and Coauthors, 2022: Monitoring multiple satellite aerosol optical depth (AOD) products within the Copernicus Atmosphere Monitoring Service (CAMS) data assimilation system. *Atmos. Chem. Phys.*, **22**, 14 657–14 692, https://doi.org/10.5194/acp-22-14657-2022.

GCOS, 2022: The 2022 Global Climate Observing System (GCOS) implementation plan. GCOS-244, WMO, 98 pp., https://gcos.wmo.int/en/publications/gcos-implementation-plan2022.

Gelaro, R., and Coauthors, 2017: The Modern-Era Retrospective Analysis for Research and Applications, version 2 (MERRA-2). *J. Climate*, **30**, 5419–5454, https://doi.org/10.1175/JCLI-D-16-0758.1.

GeoGlam, 2023: Global Crop Monitor December 2023. Accessed 30 January 2024, https://cropmonitor.org/index.php/cmreports/reports-archive/.

Getirana, A., S. Kumar, M. Girotto, and M. Rodell, 2017: Rivers and floodplains as key components of global terrestrial water storage variability. *Geophys. Res. Lett.*, **44**, 10 359–10 368, https://doi.org/10.1002/2017GL074684.

Giglio, L., W. Schroeder, and C. O. Justice, 2016: The collection 6 MODIS active fire detection algorithm and fire products. *Remote Sens. Environ.*, **178**, 31–41, https://doi.org/10.1016/j.rse.2016.02.054.

Gillooly, J. F., J. H. Brown, G. B. West, V. M. Savage, and E. L. Charnov, 2001: Effects of size and temperature on metabolic rate. *Science*, **293**, 2248–2251, https://doi.org/10.1126/science.1061967.

GISTEMP Team, 2024: GISS Surface Temperature Analysis (GISTEMP), v4. NASA Goddard Institute for Space Studies, accessed 14 February 2024, https://data.giss.nasa.gov/gistemp/.

GLAMOS, 2023: Swiss Glacier Volume Change, release 2023. Glacier Monitoring Switzerland, accessed 1 March 2024, https://doi.org/10.18750/volumechange.2023.r2023.

GLIMS, 2023: Glacier viewer. Accessed 2 January 2024, https://www.glims.org/maps/glims.

Gobron, N., and M. Robustelli, 2013: Monitoring the state of the global terrestrial surfaces. Proc. 2013 ESA Living Planet Symp., Edinburgh, United Kingdom, European Space Agency, JRC84937, https://publications.jrc.ec.europa.eu/repository/handle/JRC84937.

——, A. S. Belward, B. Pinty, and W. Knorr, 2010: Monitoring biosphere vegetation 1998–2009. *Geophys. Res. Lett.*, **37**, L15402, https://doi.org/10.1029/2010GL043870.

——, and Coauthors, 2022: Evaluation of Sentinel-3A and Sentinel-3B ocean land colour instrument green instantaneous fraction of absorbed photosynthetically active radiation. *Remote Sens. Environ.*, **270**, 112850, https://doi.org/10.1016/j.rse.2021.112850.

Godin-Beekmann, S., and Coauthors, 2022: Updated trends of the stratospheric ozone vertical distribution in the 60°S–60°N latitude range based on the LOTUS regression model. *Atmos. Chem. Phys.*, **22**, 11 657–11 673, https://doi.org/10.5194/acp-22-11657-2022.

Goodman, S. J., D. E. Buechler, K. Knupp, K. Driscoll, and E. W. McCaul Jr., 2000: The 1997-98 El Niño event and related wintertime lightning variations in the southeastern United States. *Geophys. Res. Lett.*, **27**, 541–544, https://doi.org/10.1029/1999GL010808.

Granier, C., and Coauthors, 2011: Evolution of anthropogenic and biomass burning emissions of air pollutants at global and regional scales during the 1980–2010 period. *Climatic Change*, **109**, 163–190, https://doi.org/10.1007/s10584-011-0154-1.

Grant, L., and Coauthors, 2021: Attribution of global lake systems change to anthropogenic forcing. *Nat. Geosci.*, **14**, 849–854, https://doi.org/10.1038/s41561-021-00833-x.

Grifoni, F., N. Cannone, P. Convey, and M. Guglielmin, 2024: A decade (2013–2022) of permafrost and active layer thickness monitoring in Antarctic Peninsula Area. Extended Abstracts, 12th Int. Conf. on Permafrost, Whitehorse, YT, Canada, 83–84, https://www.permafrost.org/proceedings-of-the-12th-international-conference-on-permafrost-icop/.

Grimm, A. M., 2003: The El Niño impact on the summer monsoon in Brazil: Regional processes versus remote influences. *J. Climate*, **16**, 263–280, https://doi.org/10.1175/1520-0442(2003)016<0263:TENIOT>2.0.CO;2.

——, and A. Natori, 2006: Climate change and interannual variability of precipitation in South America. *Geophys. Res. Lett.*, **33**, L19706, https://doi.org/10.1029/2006GL026821.

Gruber, A., W. A. Dorigo, W. Crow, and W. Wagner, 2017: Triple collocation-based merging of satellite soil moisture retrievals. *IEEE Trans. Geosci. Remote Sens.*, **55**, 6780–6792, https://doi.org/10.1109/TGRS.2017.2734070.

——, T. Scanlon, R. van der Schalie, W. Wagner, and W. Dorigo, 2019: Evolution of the ESA CCI Soil Moisture climate data records and their underlying merging methodology. *Earth Syst. Sci. Data*, **11**, 717–739, https://doi.org/10.5194/essd-11-717-2019.

Gulev, S. K., and Coauthors, 2021: Changing state of the climate system. Climate Change 2021: The Physical Science Basis, V. Masson-Delmotte et al., Eds., Cambridge University Press, 287–422, https://doi.org/10.1017/9781009157896.004.

Haimberger, L., C. Tavolato, and S. Sperka, 2012: Homogenization of the Global Radiosonde Temperature dataset through combined comparison with reanalysis background series and neighboring stations. *J. Climate*, **25**, 8108–8131, https://doi.org/10.1175/JCLI-D-11-00668.1.

Hansen, J., and S. Lebedeff, 1987: Global trends of measured surface air temperature. *J. Geophys. Res.*, **92**, 13 345–13 372, https://doi.org/10.1029/JD092iD11p13345.

——, S. Makiko, R. Ruedy, K. Lo, D. W. Lea, and M. Medina-Elizade, 2006: Global temperature change. *Proc. Natl. Acad. Sci. USA*, **103**, 14 288–14 293, https://doi.org/10.1073/pnas.0606291103.

——, R. Ruedy, M. Sato, and K. Lo, 2010: Global surface temperature change. *Rev. Geophys.*, **48**, RG4004, https://doi.org/10.1029/2010RG000345.

Harris, I., T. J. Osborn, P. D. Jones, and D. H. Lister, 2020: Version 4 of the CRU TS monthly high-resolution gridded multivariate climate dataset. *Sci. Data*, **7**, 109, https://doi.org/10.1038/s41597-020-0453-3.

Hassan, T., R. Gulzar, M. Hamid, R. Ahmad, S. A. Waza, and A. A. Khuroo, 2024: Plant phenology shifts under climate warming: A systematic review of recent scientific literature. *Environ. Monit. Assess.*, **196**, 36, https://doi.org/10.1007/s10661-023-12190-w.

Held, I. M., and B. J. Soden, 2006: Robust responses of the hydrological cycle to global warming. *J. Climate*, **19**, 5686–5699, https://doi.org/10.1175/JCLI3990.1.

Hersbach, H., and Coauthors, 2020: The ERA5 global reanalysis. *Quart. J. Roy. Meteor. Soc.*, **146**, 1999–2049, https://doi.org/10.1002/qj.3803.

Ho, S.-P., and Coauthors, 2020: The COSMIC/FORMOSAT-3 radio occultation mission after 12 years: Accomplishments, remaining challenges, and potential impacts of COSMIC-2. *Bull. Amer. Meteor. Sci.*, **101**, E1107–E1136, https://doi.org/10.1175/BAMS-D-18-0290.1.

Hobday, A. J., and Coauthors, 2016: A hierarchical approach to defining marine heatwaves. *Prog. Oceanogr.*, **141**, 227–238, https://doi.org/10.1016/j.pocean.2015.12.014.

——, and Coauthors, 2018: Categorizing and naming marine heatwaves. *Oceanography*, **31** (2), 162–173, https://doi.org/10.5670/oceanog.2018.205.

Hodnebrog, O., and Coauthors, 2020a: Updated global warming potentials and radiative efficiencies of halocarbons and other weak atmospheric absorbers. *Rev. Geophys.*, **58**, e2019RG000691, https://doi.org/10.1029/2019RG000691.

——, and Coauthors, 2020b: The effect of rapid adjustments to halocarbons and N_2O on radiative forcing. *npj Climate Atmos. Sci.*, **3**, 43, https://doi.org/10.1038/s41612-020-00150-x.

Hofmann, D. J., and S. A. Montzka, 2009: Recovery of the ozone layer: The ozone depleting gas index. *Eos, Trans. Amer. Geophys. Union*, **90** (1), 1–2, https://doi.org/10.1029/2009EO010001.

——, J. H. Butler, E. J. Dlugokencky, J. W. Elkins, K. Masarie, S. A. Montzka, and P. Tans, 2006: The role of carbon dioxide in climate forcing from 1979 to 2004: Introduction of the annual greenhouse gas index. *Tellus*, **58B**, 614–619, https://doi.org/10.1111/j.1600-0889.2006.00201.x.

Holzworth, R. H., J. B. Brundell, M. P. McCarthy, A. R. Jacobson, C. J. Rodger, and T. S. Anderson, 2021: Lightning in the Arctic. *Geophys. Res. Lett.*, **48**, e2020GL091366, https://doi.org/10.1029/2020GL091366.

Hong Kong Observatory, 2024: Ranking of air temperature and rainfall in annual in Hong Kong. Accessed 15 February 2024, https://www.hko.gov.hk/en/cis/statistic/erank.htm.

Hou, J., A. I. J. M. Van Dijk, and L. J. Renzullo, 2022: Merging Landsat and airborne LiDAR observations for continuous monitoring of floodplain water extent, depth and volume. *J. Hydrol.*, **609**, 127684, https://doi.org/10.1016/j.jhydrol.2022.127684.

——, ——, ——, and P. R. Larraondo, 2024: GloLakes: Water storage dynamics for 27,000 lakes globally from 1984 to present derived from satellite altimetry and optical imaging. *Earth Syst. Sci. Data*, **16**, 201–218, https://doi.org/10.5194/essd-16-201-2024.

Hrbáček, F., and Coauthors, 2023: Active layer and permafrost thermal regimes in the ice-free areas of Antarctica. *Earth-Sci. Rev.*, **242**, 104458, https://doi.org/10.1016/j.earscirev.2023.104458.

Hu, G., and Coauthors, 2024: Spatiotemporal characteristics and variability in the thermal state of permafrost on the Qinghai–Tibet Plateau. *Permafrost Periglacial Processes*, **35**, 143–156, https://doi.org/10.1002/ppp.2219.

Huang, B., C. Liu, V. Banzon, E. Freeman, G. Graham, B. Hankins, T. Smith, and H.-M. Zhang, 2021: Improvements of the daily optimum interpolation sea surface temperature (DOISST) version 2.1. *J. Climate*, **34**, 2923–2939, https://doi.org/10.1175/JCLI-D-20-0166.1.

Huss, M., and M. Fischer, 2016: Sensitivity of very small glaciers in the Swiss Alps to future climate change. *Front. Earth Sci*, **4**, 34, https://doi.org/10.3389/feart.2016.00034.

Ingram, W., 2010: A very simple model for the water vapour feedback on climate change. *Quart. J. Roy. Meteor. Soc.*, **136**, 30–40, https://doi.org/10.1002/qj.546.

Inness, A., and Coauthors, 2019: The CAMS reanalysis of atmospheric composition. *Atmos. Chem. Phys.*, **19**, 3515–3556, https://doi.org/10.5194/acp-19-3515-2019.

IPCC, 2013: *Climate Change 2013: The Physical Science Basis*. T. F. Stocker et al., Eds., Cambridge University Press, 1535 pp.

——, 2021: *Climate Change 2021: The Physical Science Basis*. V. Masson-Delmotte et al., Eds., Cambridge University Press, 2391 pp., https://doi.org/10.1017/9781009157896.

Irving, D., and I. Simmonds, 2016: A new method for identifying the Pacific-South American Pattern and its influence on regional climate variability. *J. Climate*, **29**, 6109–6125, https://doi.org/10.1175/JCLI-D-15-0843.1.

Jasinski, M. F., and Coauthors, 2023: ATLAS/ICESat-2 L3A Along Track Inland Surface Water Data, version 6. NASA National Snow and Ice Data Center Distributed Active Archive Center, accessed 11 January 2024, https://doi.org/10.5067/ATLAS/ATL13.006.

Jeppesen, E., and Coauthors, 2015: Ecological impacts of global warming and water abstraction on lakes and reservoirs due to changes in water level and related changes in salinity. *Hydrobiologia*, **750**, 201–227, https://doi.org/10.1007/s10750-014-2169-x.

Junod, R. A., and J. R. Christy, 2020: A new compilation of globally gridded night-time marine air temperatures: The UAHNMATv1 dataset. *Int. J. Climatol.*, **40**, 2609–2623, https://doi.org/10.1002/joc.6354.

Kääb, A., T. Strozzi, T. Bolch, R. Caduff, H. Trefall, M. Stoffel, and A. Kokarev, 2021: Inventory and changes of rock glacier creep speeds in Ile Alatau and Kungöy Ala-Too, northern Tien Shan, since the 1950s. *Cryosphere*, **15**, 927–949, https://doi.org/10.5194/tc-15-927-2021.

Kainz, M. J., R. Ptacnik, S. Rasconi, and H. H. Hager, 2017: Irregular changes in lake surface water temperature and ice cover in subalpine Lake Lunz, Austria. *Inland Waters*, **7**, 27–33, https://doi.org/10.1080/20442041.2017.1294332.

Kaiser, J. W., and Coauthors, 2012: Biomass burning emissions estimated with a global fire assimilation system based on observed fire radiative power. *Biogeosciences*, **9**, 527–554, https://doi.org/10.5194/bg-9-527-2012.

Kaplan, A., 2011: Patterns and indices of climate variability [in "State of the Climate in 2010"]. *Bull. Amer. Meteor. Soc.*, **92** (6), S20–S25, https://doi.org/10.1175/1520-0477-92.6.S1.

Keeling, C. D., and R. Revelle, 1985: Effects of El Nino/Southern Oscillation on the atmospheric content of carbon-dioxide. *Meteoritics*, **20**, 437–450.

Kellerer-Pirklbauer, A., and Coauthors, 2024: Acceleration and interannual variability of creep rates in mountain permafrost landforms (rock glacier velocities) in the European Alps in 1995–2022. *Environ. Res. Lett.*, **19**, 034022, https://doi.org/10.1088/1748-9326/ad25a4.

Kendon, M., M. McCarthy, S. Jevrejeva, A. Matthews, T. Sparks, and J. Garforth, 2023: State of the UK climate 2022. *Int. J. Climatol.*, **42** (S1), 1–80, https://doi.org/10.1002/joc.7787.

Kennedy, J. J., N. A. Rayner, C. P. Atkinson, and R. E. Killick, 2019: An ensemble data set of sea surface temperature change from 1850: The Met Office Hadley Centre HaadSST.4.0.0.0 data set. *J. Geophys. Res. Atmos.*, **124**, 7719–7763, https://doi.org/10.1029/2018JD029867.

Kenner, R., M. Phillips, J. Beutel, M. Hiller, P. Limpach, E. Pointner, and M. Volken, 2017: Factors controlling velocity variations at short-term, seasonal and multiyear time scales, Ritigraben rock glacier, western Swiss Alps. *Permafrost Periglacial Processes*, **28**, 675–684, https://doi.org/10.1002/ppp.1953.

Kent, E. C., N. A. Rayner, D. I. Berry, M. Saunby, B. I. Moat, J. J. Kennedy, and D. E. Parker, 2013: Global analysis of night marine air temperature and its uncertainty since 1880: The HadNMAT2 data set. *J. Geophys. Res. Atmos.*, **118**, 1281–1298, https://doi.org/10.1002/jgrd.50152.

Khaykin, S., and Coauthors, 2020: The 2019/20 Australian wildfires generated a persistent smoke-charged vortex rising up to 35-km altitude. *Commun. Earth Environ.*, **1**, 22, https://doi.org/10.1038/s43247-020-00022-5.

——, A. T. J. de Laat, S. Godin-Beekmann, A. Hauchecorne, and M. Ratynski, 2022a: Unexpected self-lofting and dynamical confinement of volcanic plumes: The Raikoke 2019 case. *Sci. Rep.*, **12**, 22409, https://doi.org/10.1038/s41598-022-27021-0.

——, and Coauthors, 2022b: Global perturbation of stratospheric water and aerosol burden by Hunga eruption. *Commun. Earth Environ*, **3**, 316, https://doi.org/10.1038/s43247-022-00652-x.

Kimutai, J., and Coauthors, 2023: Compounding natural hazards and high vulnerability led to severe impacts from Horn of Africa flooding exacerbated by climate change and Indian Ocean Dipole. World Weather Attribution, 30 pp., https://doi.org/10.25561/108015.

Kjellstrom, T., C. Freyberg, B. Lemke, M. Otto, and D. Briggs, 2017: Estimating population heat exposure and impacts on working people in conjunction with climate change. *Int. J. Biometeor.*, **62**, 291–306, https://doi.org/10.1007/s00484-017-1407-0.

Kobayashi, S., and Coauthors, 2015: The JRA-55 reanalysis: General specifications and basic characteristics. *J. Meteor. Soc. Japan*, **93**, 5–48, https://doi.org/10.2151/jmsj.2015-001.

Kosaka, Y., and Coauthors, 2024: The JRA-3Q reanalysis. *J. Meteor. Soc. Japan*, **102**, 49–109, https://doi.org/10.2151/jmsj.2024-004.

Kraemer, B. M., H. Dugan, S. La Fuente, and M. F. Meyer, 2023: Lake water levels [in "State of the Climate in 2022"]. *Bull. Amer. Meteor. Soc.*, **104** (9), S61–S63, https://doi.org/10.1175/BAMS-D-23-0090.1.

Kratz, D. P., P. W. Stackhouse Jr., S. K. Gupta, A. C. Wilber, P. Sawaengphokhai, and G. R. McGarragh, 2014: The Fast Longwave and Shortwave Flux (FLASHFlux) data product: Single-scanner footprint fluxes. *J. Appl. Meteor. Climatol.*, **53**, 1059–1079, https://doi.org/10.1175/JAMC-D-13-061.1.

Kremser, S., and Coauthors, 2016: Stratospheric aerosol —— Observations, processes, and impact on climate. *Rev. Geophys.*, **54**, 278–335, https://doi.org/10.1002/2015RG000511.

Lagouarde, J.-P., and Coauthors, 2018: The Indian-French Trishna Mission: Earth Observation in the thermal infrared with high spatio-temporal resolution. *IGARSS 2018 – 2018 IEEE Int. Geoscience and Remote Sensing Symp.*, Valencia, Spain, IEEE, 4078–4081, https://doi.org/10.1109/IGARSS.2018.8518720.

Lambiel, C., and R. Delaloye, 2004: Contribution of real-time kinematic GPS in the study of creeping mountain permafrost: Examples from the western Swiss Alps. *Permafrost Periglacial Processes*, **15**, 229–241, https://doi.org/10.1002/ppp.496.

Lan, X., and Coauthors, 2019: Long-term measurements show little evidence for large increases in total US methane emissions over the past decade. *Geophys. Res. Lett.*, **46**, 4991–4999, https://doi.org/10.1029/2018GL081731.

——, and Coauthors, 2021: Improved constraints on global methane emissions and sinks using δ^{13}C-CH_4. *Global Biogeochem. Cycles*, **35**, e2021GB007000, https://doi.org/10.1029/2021GB007000.

——, K. W. Thoning, and E. J. Dlugokencky, 2024a: Trends in globally-averaged CH_4, N_2O, and SF_6 determined from NOAA Global Monitoring Laboratory measurements, version 2024-06. NOAA/GML, accessed 6 June 2024, https://doi.org/10.15138/P8XG-AA10.

——, P. Tans, and K. W. Thoning, 2024b: Trends in globally-averaged CO_2 determined from NOAA Global Monitoring Laboratory measurements, version 2024-06. NOAA/GML, accessed 6 June 2024, https://doi.org/10.15138/9N0H-ZH07.

Landerer, F. W., and Coauthors, 2020: Extending the global mass change data record: GRACE Follow-On instrument and science data performance. *Geophys. Res. Lett.*, **47**, e2020GL088306, https://doi.org/10.1029/2020GL088306.

Leblanc, T., F. Chouza, G. Taha, S. Khaykin, J. Barnes, J.-P. Vernier, and L. Rieger, 2020: 2019: A 25-year high in global stratospheric aerosol loading [in "State of the Climate in 2019"]. *Bull. Amer. Meteor. Soc.*, **101** (8), S88–S89, https://doi.org/10.1175/2020BAMSStateoftheClimate.1.

Leckey, J. P., R. Damadeo, and C. A. Hill, 2021: Stratospheric Aerosol and Gas Experiment (SAGE) from SAGE III on the ISS to a free flying SAGE IV cubesat. *Remote Sens.*, **13**, 4664, https://doi.org/10.3390/rs13224664.

Lee, H.-T., and NOAA CDR Program, 2018: NOAA Climate Data Record (CDR) of monthly Outgoing Longwave Radiation (OLR), version 2.7. NOAA National Centers for Environmental Information, accessed 27 January 2024, https://doi.org/10.7289/V5W37TKD.

Legras, B., and Coauthors, 2022: The evolution and dynamics of the Hunga Tonga–Hunga Ha'apai sulfate aerosol plume in the stratosphere. *Atmos. Chem. Phys.*, **22**, 14 957–14 970, https://doi.org/10.5194/acp-22-14957-2022.

Lenssen, N. J. L., G. A. Schmidt, J. E. Hansen, M. J. Menne, A. Persin, R. Ruedy, and D. Zyss, 2019: Improvements in the GISTEMP uncertainty model. *J. Geophys. Res. Atmos.*, **124**, 6307–6326, https://doi.org/10.1029/2018JD029522.

Levy, R. C., S. Mattoo, L. A. Munchak, L. A. Remer, A. M. Sayer, F. Patadia, and N. C. Hsu, 2013: The Collection 6 MODIS aerosol products over land and ocean. *Atmos. Meas. Tech.*, **6**, 2989–3034, https://doi.org/10.5194/amt-6-2989-2013.

Lisonbee, J., and J. Ribbe, 2021: Seasonal climate influences on the timing of the Australian monsoon onset. *Wea. Climate Dyn.*, **2**, 489–506, https://doi.org/10.5194/wcd-2-489-2021.

Liu, J., and Coauthors, 2017: Contrasting carbon cycle responses of the tropical continents to the 2015–2016 El Niño. *Science*, **358**, eaam5690, https://doi.org/10.1126/science.aam5690.

Liu, P.-W., and Coauthors, 2022: Groundwater depletion in California's Central Valley accelerates during megadrought. *Nat. Commun.*, **13**, 7825, https://doi.org/10.1038/s41467-022-35582-x.

Liu, Y., and Coauthors, 2017: Evaluation of the VIIRS BRDF, Albedo and NBAR products suite and an assessment of continuity with the long term MODIS record. *Remote Sens. Environ.*, **201**, 256–274, https://doi.org/10.1016/j.rse.2017.09.020.

——, L. Zhou, Y. Qin, C. Azorin-Molina, C. Shen, R. Xu, and Z. Zeng, 2024: Impacts of anemometer changes, site relocations and processing methods on wind speed trends in China. *Atmos. Meas. Tech.*, **17**, 1123–1131, https://doi.org/10.5194/amt-17-1123-2024.

Livezey, R. E., M. Masutani, A. Leetmaa, H. Rui, M. Ji, and A. Kumar, 1997: Teleconnective response of the Pacific–North American region atmosphere to large central equatorial Pacific SST anomalies. *J. Climate*, **10**, 1787–1820, https://doi.org/10.1175/1520-0442(1997)010<1787:TROTPN>2.0.CO;2.

Loeb, N. G., B. A. Wielicki, D. R. Doelling, G. L. Smith, D. F. Keyes, S. Kato, N. Manalo-Smith, and T. Wong, 2009: Toward optimal closure of the Earth's top-of-atmosphere radiation budget. *J. Climate*, **22**, 748–766, https://doi.org/10.1175/2008JCLI2637.1.

——, S. Kato, W. Su, T. Wong, F. Rose, D. R. Doelling, and J. Norris, 2012: Advances in understanding top-of-atmosphere radiation variability from satellite observations. *Surv. Geophys.*, **33**, 359–385, https://doi.org/10.1007/s10712-012-9175-1.

——, and Coauthors, 2018: Clouds and the Earth's Radiant Energy System (CERES) Energy Balanced and Filled (EBAF) Top-of-Atmosphere (TOA) edition-4.0 data product. *J. Climate*, **31**, 895–918, https://doi.org/10.1175/JCLI-D-17-0208.1.

——, G. C. Johnson, T. J. Thorsen, J. M. Lyman, F. G. Rose, and S. Kato, 2021: Satellite and ocean data reveal marked increase in Earth's heating rate. *Geophys. Res. Lett.*, **48**, e2021GL093047, https://doi.org/10.1029/2021GL093047.

——, and Coauthors, 2022: Evaluating twenty-year trends in Earth's energy flows from observations and reanalyses. *J. Geophys. Res. Atmos.*, **127**, e2022JD036686, https://doi.org/10.1029/2022JD036686.

Lopez, L. S., A. Basu, K. Blagrave, G. Bove, K. Stewart, D. Bazely, and S. Sharma, 2024: Establishing a long-term citizen science project? Lessons learned from the Community Lake Ice Collaboration spanning over 30 yr and 1000 lakes. *Limnol. Oceanogr. Lett.*, **9**, 99–111, https://doi.org/10.1002/lol2.10336.

MacCallum, S. N., and C. J. Merchant, 2012: Surface water temperature observations of large lakes by optimal estimation. *Can. J. Remote Sens.*, **38**, 25–45, https://doi.org/10.5589/m12-010.

Magnin, F., L. Ravanel, X. Bodin, P. Deline, E. Malet, J. Krysiecki, and P. Schoeneich, 2024: Main results of permafrost monitoring in the French Alps through the PermaFrance network over the period 2010–2022. *Permafrost Periglacial Processes*, **35**, 3–23, https://doi.org/10.1002/ppp.2209.

Manney, G. L., M. L. Santee, Z. D. Lawrence, K. Wargan, and M. J. Schwartz, 2021: A moments view of climatology and variability of the Asian summer monsoon anticyclone. *J. Climate*, **34**, 7821–7841, https://doi.org/10.1175/JCLI-D-20-0729.1.

——, and Coauthors, 2023: Siege in the southern stratosphere: Hunga Tonga-Hunga Ha'apai water vapor excluded from the 2022 Antarctic polar vortex. *Geophys. Res. Lett.*, **50**, e2023GL103855, https://doi.org/10.1029/2023GL103855.

Marchant, R., C. Mumbi, S. Behera, and T. Yamagata, 2007: The Indian Ocean dipole – The unsung driver of climatic variability in East Africa. *Afr. J. Ecol.*, **45**, 4–16, https://doi.org/10.1111/j.1365-2028.2006.00707.x.

Marshall, G. J., 2003: Trends in the Southern Annular Mode from observations and reanalyses. *J. Climate*, **16**, 4134–4143, https://doi.org/10.1175/1520-0442(2003)016<4134:TITSAM>2.0.CO;2.

Martens, B., and Coauthors, 2017: GLEAM v3: Satellite-based land evaporation and root-zone soil moisture. *Geosci. Model Dev.*, **10**, 1903–1925, https://doi.org/10.5194/gmd-10-1903-2017.

——, W. Waegeman, W. A. Dorigo, N. E. C. Verhoest, and D. G. Miralles, 2018: Terrestrial evaporation response to modes of climate variability. *npj Climate Atmos. Sci.*, **1**, 43, https://doi.org/10.1038/s41612-018-0053-5.

Maswanganye, S., 2023: Putting the Western Cape September rainfall event into perspective – SAEON eNews. South African Environmental Observation Network. SAEON eNews, https://enews.saeon.ac.za/issue-05-2023/putting-the-western-cape-september-rainfall-event-into-perspective/.

Matthews, T., 2018: Humid heat and climate change. *Prog. Phys. Geogr.*, **42**, 391–405, https://doi.org/10.1177/0309133318776490.

——, M. Byrne, R. Horton, C. Murphy, R. Pielke Sr., C. Raymond, P. Thorne, and R. L. Wilby, 2022: Latent heat must be visible in climate communications. *Wiley Interdiscip. Rev.: Climate Change*, **13**, e779, https://doi.org/10.1002/wcc.779.

Mayer, M., K. E. Trenberth, L. Haimberger, and J. T. Fasullo, 2013: The response of tropical atmospheric energy budgets to ENSO. *J. Climate*, **26**, 4710–4724, https://doi.org/10.1175/JCLI-D-12-00681.1.

McCabe, M. F., B. Aragon, R. Houborg, and J. Mascaro, 2017: CubeSats in hydrology: Ultrahigh-resolution insights into vegetation dynamics and terrestrial evaporation. *Water Resour. Res.*, **53**, 10017–10024, https://doi.org/10.1002/2017WR022240.

——, D. G. Miralles, T. R. H. Holmes, and J. B. Fisher, 2019: Advances in the remote sensing of terrestrial evaporation. *Remote Sens.*, **11**, 1138, https://doi.org/10.3390/rs11091138.

McCarthy, M. P., and R. Toumi, 2004: Observed interannual variability of tropical troposphere relative humidity. *J. Climate*, **17**, 3181–3191, https://doi.org/10.1175/1520-0442(2004)017<3181:OIVOTT>2.0.CO;2.

McVicar, T. R., and Coauthors, 2012: Global review and synthesis of trends in observed terrestrial near-surface wind speeds: Implications for evaporation. *J. Hydrol.*, **416–417**, 182–205, https://doi.org/10.1016/j.jhydrol.2011.10.024.

Mears, C. A., and F. J. Wentz, 2016: Sensitivity of satellite-derived tropospheric temperature trends to the diurnal cycle adjustment. *J. Climate*, **29**, 3629–3646, https://doi.org/10.1175/JCLI-D-15-0744.1.

——, D. K. Smith, L. Ricciardulli, J. Wang, H. Huelsing, and F. J. Wentz, 2018: Construction and uncertainty estimation of a satellite-derived total precipitable water data record over the world's oceans. *Earth Space Sci.*, **5**, 197–210, https://doi.org/10.1002/2018EA000363.

Meesters, A. G., R. A. De Jeu, and M. Owe, 2005: Analytical derivation of the vegetation optical depth from the microwave polarization difference index. *IEEE Geosci. Remote Sens. Lett.*, **2**, 121–123, https://doi.org/10.1109/LGRS.2005.843983.

Menne, M. J., I. Durre, R. S. Vose, B. E. Gleason, and T. G. Houston, 2012: An overview of the global historical climatology network-daily database. *J. Atmos. Oceanic Technol.*, **29**, 897–910, https://doi.org/10.1175/JTECH-D-11-00103.1.

Menzel, A., Y. Yuan, M. Matiu, T. H. Sparks, H. Scheifinger, R. Gehrig, and N. Estrella, 2020: Climate change fingerprints in recent European plant phenology. *Global Change Biol.*, **26**, 2599–2612, https://doi.org/10.1111/gcb.15000.

Messager, M. L., B. Lehner, G. Grill, I. Nedeva, and O. Schmitt, 2016: Estimating the volume and age of water stored in global lakes using a geo-statistical approach. *Nat. Commun.*, **7**, 13603, https://doi.org/10.1038/ncomms13603.

Michel, S. E., J. R. Clark, B. H. Vaughn, M. Crotwell, M. Madronich, E. Moglia, D. Neff, and J. Mund, 2022: Stable isotopic composition of atmospheric methane (^{13}C) from the NOAA GML Carbon Cycle Cooperative Global Air Sampling Network, 1998–2021. University of Colorado, Institute of Arctic and Alpine Research (INSTAAR), accessed 15 December 2022, https://doi.org/10.15138/9p89-1x02.

Millán, L., and Coauthors, 2022: The Hunga Tonga-Hunga Ha'apai hydration of the stratosphere. *Geophys. Res. Lett.*, **49**, e2022GL099381, https://doi.org/10.1029/2022GL099381.

Miller, B. R., and Coauthors, 2010: HFC-23 (CHF_3) emission trend response to HCFC-22 ($CHClF_2$) production and recent HFC-23 emission abatement measures. *Atmos. Chem. Phys.*, **10**, 7875–7890, https://doi.org/10.5194/acp-10-7875-2010.

Minola, L., H. Reese, H. W. Lai, C. Azorin-Molina, J. A. Guijarro, S. W. Son, and D. Chen, 2022: Wind stilling-reversal across Sweden: The impact of land-use and large-scale atmospheric circulation changes. *Int. J. Climatol.*, **42**, 1049–1071, https://doi.org/10.1002/joc.7289.

Miralles, D. G., T. R. H. Holmes, R. A. M. De Jeu, J. H. Gash, A. G. C. A. Meesters, and A. J. Dolman, 2011: Global land-surface evaporation estimated from satellite-based observations. *Hydrol. Earth Syst. Sci.*, **15**, 453–469, https://doi.org/10.5194/hess-15-453-2011.

——, and Coauthors, 2014: El Niño–La Niña cycle and recent trends in continental evaporation. *Nat. Climate Change*, **4**, 122–126, https://doi.org/10.1038/nclimate2068.

Mitchell, L., E. Brook, J. E. Lee, C. Buizert, and T. Sowers, 2013: Constraints on the late Holocene anthropogenic contribution to the atmospheric methane budget (2013b). *Science*, **342**, 964–966, https://doi.org/10.1126/science.1238920.

Miyazaki, K., K. Bowman, T. Sekiya, M. Takigawa, J. L. Neu, K. Sudo, G. Osterman, and H. Eskes, 2021: Global tropospheric ozone responses to reduced NO_x emissions linked to the COVID-19 worldwide lockdowns. *Sci. Adv.*, **7**, eabf7460, https://doi.org/10.1126/sciadv.abf7460.

Moesinger, L., W. Dorigo, R. de Jeu, R. van Der Schalie, T. Scanlon, I. Teubner, and M. Forkel, 2020: The global long-term microwave Vegetation Optical Depth Climate Archive (VODCA). *Earth Syst. Sci. Data*, **12**, 177–196, https://doi.org/10.5194/essd-12-177-2020.

——, R.-M. Zotta, R. van Der Schalie, T. Scanlon, R. de Jeu, and W. Dorigo, 2022: Monitoring vegetation condition using microwave remote sensing: The Standardized Vegetation Optical Depth Index (SVODI). *Biogeosciences*, **19**, 5107–5123, https://doi.org/10.5194/bg-19-5107-2022.

Montecinos, A., M. V. Kurgansky, C. Muñoz, and K. Takahashi, 2011: Non-ENSO interannual rainfall variability in central Chile during austral winter. *Theor. Appl. Climatol.*, **106**, 557–568, https://doi.org/10.1007/s00704-011-0457-1.

Montzka, S. A., J. H. Butler, R. C. Myers, T. M. Thompson, T. H. Swanson, A. D. Clarke, L. T. Lock, and J. W. Elkins, 1996: Decline in the tropospheric abundance of halogen from halocarbons: Implications for stratospheric ozone depletion. *Science*, **272**, 1318–1322, https://doi.org/10.1126/science.272.5266.1318.

Morice, C. P., and Coauthors, 2021: An updated assessment of near-surface temperature change from 1850: The HadCRUT5 data set. *J. Geophys. Res. Atmos.*, **126**, e2019JD032361, https://doi.org/10.1029/2019JD032361.

Mühle, J., and Coauthors, 2010: Perfluorocarbons in the global atmosphere: Tetrafluoromethane, hexafluoroethane, and octafluoropropane. *Atmos. Chem. Phys.*, **10**, 5145–5164, https://doi.org/10.5194/acp-10-5145-2010.

Murray, L., 2023: Tropical Cyclone Gabrielle – Event summary February 2023. MetService Blog, accessed 14 February 2024, https://blog.metservice.com/TropicalCycloneGabrielleSummary.

Myhre, G., D. Shindell, and J. Pongratz, 2014: Anthropogenic and natural radiative forcing. *Climate Change 2013: The Physical Science Basis*, T. F. Stocker et al., Eds., Cambridge University Press, 659–740.

Naumann, G., and Coauthors, 2021: The 2019–2021 extreme drought episode in La Plata Basin. EUR 30833 EN, Publications Office of the European Union, 44 pp., https://doi.org/10.2760/773.

Newman, P. A., J. S. Daniel, D. W. Waugh, and E. R. Nash, 2007: A new formulation of equivalent effective stratospheric chlorine (EESC). *Atmos. Chem. Phys.*, **7**, 4537–4552, https://doi.org/10.5194/acp-7-4537-2007.

Nicholson, S. E., 2017: Climate and climatic variability of rainfall over eastern Africa. *Rev. Geophys.*, **55**, 590–635, https://doi.org/10.1002/2016RG000544.

Nisbet, E. G., and Coauthors, 2023: Atmospheric methane: Comparison between methane's record in 2006–2022 and during glacial terminations. *Global Biogeochem. Cycles*, **37**, e2023GB007875, https://doi.org/10.1029/2023GB007875.

NOAA/NCEI, 2023a: Global drought narrative for November 2023. Accessed 12 February 2024, https://www.ncei.noaa.gov/access/monitoring/monthly-report/global-drought/202311.

——, 2023b: Monthly drought report for annual 2023. Accessed 30 January 2024, https://www.ncei.noaa.gov/access/monitoring/monthly-report/drought/202313.

——, 2023c: Monthly national climate report for January 2023. Accessed 18 January 2024, https://www.ncei.noaa.gov/access/monitoring/monthly-report/national/202301.

——, 2024: U.S. Climate Extremes Index (CEI). Accessed 16 February 2024, https://www.ncei.noaa.gov/access/monitoring/cei/graph.

Noetzli, J., and Coauthors, 2021: Best practice for measuring permafrost temperature in boreholes based on the experience in the Swiss Alps. *Front. Earth Sci.*, **9**, 607875, https://doi.org/10.3389/feart.2021.607875.

——, H. H. Christiansen, M. Guglielmin, F. Hrbáček, K. Isaksen, S. L. Smith, L. Zhao, and D. A. Streletskiy, 2023: Permafrost temperature and active layer thickness [in "State of the Climate in 2022"]. *Bull. Amer. Meteor. Soc.*, **104** (9), S39–S41, https://doi.org/10.1175/BAMS-D-23-0090.1.

OCHA, 2023a: Mozambique: Severe Tropical Storm Freddy – Flash update No. 10 (as of 15 March 2023) – Mozambique. Reliefweb, accessed 14 February 2024, https://reliefweb.int/report/mozambique/mozambique-severe-tropical-storm-freddy-flash-update-no-10-15-march-2023.

——, 2023b: Southern Africa: El Niño, positive Indian Ocean dipole forecast and humanitarian impact (October 2023). Accessed 30 January 2024, https://reliefweb.int/report/madagascar/southern-africa-el-nino-positive-indian-ocean-dipole-forecast-and-humanitarian-impact-october-2023.

O'Gorman, P. A., 2012: Sensitivity of tropical precipitation extremes to climate change. *Nat. Geosci.*, **5**, 697–700, https://doi.org/10.1038/ngeo1568.

——, and C. J. Muller, 2010: How closely do changes in surface and column water vapor follow Clausius-Clapeyron scaling in climate change simulations? *Environ. Res. Lett.*, **5**, 025207, https://doi.org/10.1088/1748-9326/5/2/025207.

Oh, Y., and Coauthors, 2023: CarbonTracker-CH_4 2023. NOAA, accessed March 2024, https://doi.org/10.25925/40jt-qd67.

O'Keefe, J., 2023: Phenology of woody species at Harvard Forest since 1990. Harvard Forest Data Archive: HF003, accessed March 2024, https://harvardforest1.fas.harvard.edu/exist/apps/datasets/showData.html?id=HF003.

Osborn, T. J., P. D. Jones, D. H. Lister, C. P. Morice, I. R. Simpson, J. P. Winn, E. Hogan, and I. C. Harris, 2021: Land surface air temperature variations across the globe updated to 2019: The CRUTEM5 dataset. *J. Geophys. Res. Atmos.*, **126**, e2019JD032352, https://doi.org/10.1029/2019JD032352.

Park, T., and Coauthors, 2016: Changes in growing season duration and productivity of northern vegetation inferred from long-term remote sensing data. *Environ. Res. Lett.*, **11**, 084001, https://doi.org/10.1088/1748-9326/11/8/084001.

Parker, D. E., T. P. Legg, and C. K. Folland, 1992: A new daily central England temperature series, 1772–1991. *Int. J. Climatol.*, **12**, 317–342, https://doi.org/10.1002/joc.3370120402.

Peixoto, J. P., and A. H. Oort, 1992: *Physics of Climate*. American Institute of Physics, 520 pp.

Pekel, J.-F., A. Cottam, N. Gorelick, and A. S. Belward, 2016: High-resolution mapping of global surface water and its long-term changes. *Nature*, **540**, 418–422, https://doi.org/10.1038/nature20584.

Pellet, C., and Coauthors, 2023: Rock glacier velocity [in "State of the Climate in 2022"]. *Bull. Amer. Meteor. Soc.*, **104** (9), S41–S42, https://doi.org/10.1175/BAMS-D-23-0090.1.

Peng, S., and Coauthors, 2022: Wetland emission and atmospheric sink changes explain methane growth in 2020. *Nature*, **612**, 477–482, https://doi.org/10.1038/s41586-022-05447-w.

Perkins-Kirkpatrick, S., D. Barriopedro, R. Jha, L. Wang, A. Mondal, R. Libonati, and K. Kornhuber, 2024: Extreme terrestrial heat in 2023. *Nat. Rev. Earth Environ.*, **5**, 244–246, https://doi.org/10.1038/s43017-024-00536-y.

PERMOS, 2023: Swiss Permafrost Bulletin 2022. J. Noetzli and C. Pellet, Eds., Swiss Permafrost Monitoring Network, 23 pp., https://www.permos.ch/fileadmin/Files/publications/swiss_permafrost_bulletin/PERMOS_bulletin_2022.pdf.

——, 2024: Swiss Permafrost Bulletin 2023. J. Noetzli and C. Pellet, Eds., Swiss Permafrost Monitoring Network, 25 pp., https://www.permos.ch/fileadmin/Files/publications/swiss_permafrost_bulletin/PERMOS_bulletin_2023.pdf.

Peterson, D. A., J. R. Campbell, E. J. Hyer, M. D. Fromm, G. P. Kablick III, J. H. Cossuth, and M. T. DeLand, 2018: Wildfire-driven thunderstorms cause a volcano-like stratospheric injection of smoke. *npj Climate Atmos. Sci.*, **1**, 30, https://doi.org/10.1038/s41612-018-0039-3.

——, and Coauthors, 2021: Australia's Black Summer pyrocumulonimbus super outbreak reveals potential for increasingly extreme stratospheric smoke events. *npj Climate Atmos. Sci.*, **4**, 38, https://doi.org/10.1038/s41612-021-00192-9.

Phillips, C., and M. J. Foster, 2023: Cloudiness [in "State of the Climate in 2022"]. *Bull. Amer. Meteor. Soc.*, **104** (9), S60–S61, https://doi.org/10.1175/BAMS-D-23-0090.1.

Pielke, R. A., 2003: Heat storage within the Earth system. *Bull. Amer. Meteor. Soc.*, **84**, 331–336, https://doi.org/10.1175/BAMS-84-3-331.

Pinty, B., and Coauthors, 2011: Exploiting the MODIS albedos with the Two-stream Inversion Package (JRC-TIP): 2. Fractions of transmitted and absorbed fluxes in the vegetation and soil layers. *J. Geophys. Res.*, **116**, D09106, https://doi.org/10.1029/2010JD015373.

Plummer, D., and Coauthors, 2021: CCMI-2022: A new set of Chemistry-Climate Model Initiative (CCMI) Community simulations to update the assessment of models and support upcoming ozone assessment activities. *SPARC Newsletter*, No. 57, WCRP, Toronto, Ontario, Canada, 22–30, https://www.sparc-climate.org/wp-content/uploads/sites/5/2021/07/SPARCnewsletter_Jul2021_web.pdf.

Po-Chedley, S., J. R. Christy, C.-Z. Zou, C. A. Mears, and L. Haimberger, 2023: Tropospheric temperature [in "State of the Climate in 2022"]. *Bull. Amer. Meteor. Soc.*, **104** (9), S36–S38, https://doi.org/10.1175/BAMS-D-23-0090.1.

Pogliotti, P., E. Cremonese, and U. Morra di Cella, 2023: Warming permafrost in the western Alps: A further evidence of elevation dependent warming? *J. Alp. Res.*, **111** (2), https://doi.org/10.4000/rga.11784.

Popp, T., and Coauthors, 2016: Development, production and evaluation of aerosol climate data records from European satellite observations (Aerosol_cci). *Remote Sens.*, **8**, 421, https://doi.org/10.3390/rs8050421.

Prather, M. J., C. D. Holmes, and J. Hsu, 2012: Reactive greenhouse gas scenarios: Systematic exploration of uncertainties and the role of atmospheric chemistry. *Geophys. Res. Lett.*, **39**, L09803, https://doi.org/10.1029/2012GL051440.

Putero, D., and Coauthors, 2023: Fingerprints of the COVID-19 economic downturn and recovery on ozone anomalies at high-elevation sites in North America and western Europe. *Atmos. Chem. Phys.*, **23**, 15 693–15 709, https://doi.org/10.5194/acp-23-15693-2023.

Quaas, J., and Coauthors, 2022: Robust evidence for reversal of the trend in aerosol effective climate forcing. *Atmos. Chem. Phys.*, **22**, 12 221–12 239, https://doi.org/10.5194/acp-22-12221-2022.

Randel, W. J., and J. B. Cobb, 1994: Coherent variations of monthly mean total ozone and lower stratospheric temperature. *J. Geophys. Res.*, **99**, 5433–5447, https://doi.org/10.1029/93JD03454.

——, and Coauthors, 2009: An update of observed stratospheric temperature trends. *J. Geophys. Res.*, **114**, D02107, https://doi.org/10.1029/2008JD010421.

Rantanen, M., and A. Laaksonen, 2024: The jump in global temperatures in September 2023 is extremely unlikely due to internal climate variability alone. *npj Climate Atmos. Sci.*, **7**, 34, https://doi.org/10.1038/s41612-024-00582-9.

Ray, E. A., F. L. Moore, J. W. Elkins, K. H. Rosenlof, J. C. Laube, T. Röckmann, D. R. Marsh, and A. E. Andrews, 2017: Quantification of the SF_6 lifetime based on mesospheric loss measured in the stratospheric polar vortex. *J. Geophys. Res. Atmos.*, **122**, 4626–4638, https://doi.org/10.1002/2016JD026198.

Raymond, C., T. K. Matthews, and R. M. Horton, 2020: The emergence of heat and humidity too severe for human tolerance. *Sci. Adv.*, **6**, eaaw1838, https://doi.org/10.1126/sciadv.aaw1838.

——, ——, ——, E. M. Fischer, S. Fueglistaler, C. Ivanovich, L. Suarez-Gutierrez, and Y. Zhang, 2021: On the controlling factors for globally extreme humid heat. *Geophys. Res. Lett.*, **48**, e2021GL096082, https://doi.org/10.1029/2021GL096082.

Rayner, N. A., D. E. Parker, E. B. Horton, C. K. Folland, L. V. Alexander, D. P. Rowell, E. C. Kent, and A. Kaplan, 2003: Global analyses of sea surface temperature, sea ice, and night marine air temperature since the late nineteenth century. *J. Geophys. Res.*, **108**, 4407, https://doi.org/10.1029/2002JD002670.

Renwick, J. A., and M. J. Revell, 1999: Blocking over the South Pacific and Rossby wave propagation. *Mon. Wea. Rev.*, **127**, 2233–2247, https://doi.org/10.1175/1520-0493(1999)127<2233:BOTSPA>2.0.CO;2.

RGIK, 2023a: Guidelines for inventorying rock glaciers: Baseline and practical concepts (version 1.0). Tech. Rep., IPA Action Group Rock Glacier Inventories and Kinematics, 25 pp., https://doi.org/10.51363/unifr.srr.2023.002.

——, 2023b: Rock Glacier Velocity as an associated parameter of ECV Permafrost: Baseline concepts (version 3.2). Tech. Rep., IPA Action Group Rock Glacier Inventories and Kinematics, 12 pp., https://bigweb.unifr.ch/Science/Geosciences/Geomorphology/Pub/Website/IPA/CurrentVersion/Current_RockGlacierVelocity.pdf.

Ricciardulli, L., and F. J. Wentz, 2015: A scatterometer geophysical model function for climate-quality winds: QuikSCAT Ku-2011. *J. Atmos. Oceanic Technol.*, **32**, 1829–1846, https://doi.org/10.1175/JTECH-D-15-0008.1.

——, and A. Manaster, 2021: Intercalibration of ASCAT scatterometer winds from MetOp-A, -B, and -C, for a stable climate data record. *Remote Sens.*, **13**, 3678, https://doi.org/10.3390/rs13183678.

Richardson, A. D., 2019: Tracking seasonal rhythms of plants in diverse ecosystems with digital camera imagery. *New Phytol.*, **222**, 1742–1750, https://doi.org/10.1111/nph.15591.

——, and J. O'Keefe, 2009: Phenological differences between understory and overstory. *Phenology of Ecosystem Processes*, A. Noormets, Ed., Springer, 87–117.

Rodell, M., and B. Li, 2023: Changing intensity of hydroclimatic extreme events revealed by GRACE and GRACE-FO. *Nat. Water*, **1**, 241–248, https://doi.org/10.1038/s44221-023-00040-5.

——, J. S. Famiglietti, D. N. Wiese, J. T. Reager, H. K. Beaudoing, F. W. Landerer, and M.-H. Lo, 2018: Emerging trends in global freshwater availability. *Nature*, **557**, 651–659, https://doi.org/10.1038/s41586-018-0123-1.

Rogers, C. D. W., and R. A. Warren, 2024: Fast and accurate calculation of wet-bulb temperature for humid-heat extremes. ESS Open Archive, https://doi.org/10.22541/essoar.170560423.39769387/v1.

Rohde, R. A., and Z. Hausfather, 2020: The Berkeley Earth land/ocean temperature record. *Earth Syst. Sci. Data*, **12**, 3469–3479, https://doi.org/10.5194/essd-12-3469-2020.

Rosemartin, A. H., and Coauthors, 2014: Organizing phenological data resources to inform natural resource conservation. *Biol. Conserv.*, **173**, 90–97, https://doi.org/10.1016/j.biocon.2013.07.003.

Rubino, M., and Coauthors, 2019: Revised records of atmospheric trace gases CO_2, CH_4, N_2O, and $\delta^{13}C$-CO_2 over the last 2000 years from Law Dome, Antarctica. *Earth Syst. Sci. Data*, **11**, 473–492, https://doi.org/10.5194/essd-11-473-2019.

Rudlosky, S. D., and K. S. Virts, 2021: Dual geostationary lightning mapper observations. *Mon. Wea. Rev.*, **149**, 979–998, https://doi.org/10.1175/MWR-D-20-0242.1.

Saeed, W., I. Haqiqi, Q. Kong, M. Huber, J. R. Buzan, S. Chonabayashi, K. Motohashi, and T. W. Hertel, 2022: The poverty impacts of labor heat stress in West Africa under a warming climate. *Earth's Future*, **10**, e2022ef002777, https://doi.org/10.1029/2022EF002777.

Said, R., M. Cohen, and U. Inan, 2013: Highly intense lightning over the oceans: Estimated peak currents from global GLD360 observations. *J. Geophys. Res. Atmos.*, **118**, 6905–6915, https://doi.org/10.1002/jgrd.50508.

Saji, N. H., B. N. Goswami, P. N. Vinayachandran, and T. Yamagata, 1999: A dipole mode in the tropical Indian Ocean. *Nature*, **401**, 360–363, https://doi.org/10.1038/43854.

Santee, M. L., and Coauthors, 2023: Strong evidence of heterogeneous processing on stratospheric sulfate aerosol in the extrapolar Southern Hemisphere following the 2022 Hunga Tonga-Hunga Ha'apai eruption. *J. Geophys. Res. Atmos.*, **128**, e2023JD039169, https://doi.org/10.1029/2023JD039169.

Santer, B. D., and Coauthors, 2008: Consistency of modelled and observed temperature trends in the tropical troposphere. *Int. J. Climatol.*, **28**, 1703–1722, https://doi.org/10.1002/joc.1756.

Satheesh, S. K., S. Suresh Babu, B. Padmakumari, G. Pandithurai, and V. K. Soni, 2017: Variability of atmospheric aerosols over India. *Observed Climate Variability and Change over the Indian Region*, Springer, 221–248, https://doi.org/10.1007/978-981-10-2531-0_13.

Schaaf, C. B., and Coauthors, 2002: First operational BRDF, albedo nadir reflectance products from MODIS. Remote Sens. *Environ.*, **83**, 135–148, https://doi.org/10.1016/S0034-4257(02)00091-3.

Schmidt, G., 2024: Climate models can't explain 2023's huge heat anomaly —— We could be in uncharted territory. *Nature*, **627**, 467, https://doi.org/10.1038/d41586-024-00816-z.

Schwartz, M. D., T. R. Ault, and J. L. Betancourt, 2013: Spring onset variations and trends in the continental United States: Past and regional assessment using temperature-based indices. *Int. J. Climatol.*, **33**, 2917–2922, https://doi.org/10.1002/joc.3625.

Seneviratne, S. I., T. Corti, E. L. Davin, M. Hirschi, E. B. Jaeger, I. Lehner, B. Orlowsky, and A. J. Teuling, 2010: Investigating soil moisture–climate interactions in a changing climate: A review. *Earth-Sci. Rev.*, **99**, 125–161, https://doi.org/10.1016/j.earscirev.2010.02.004.

Seyednasrollah, B., A. M. Young, K. Hufkens, T. Milliman, M. A. Friedl, S. Frolking, and A. D. Richardson, 2019: Tracking vegetation phenology across diverse biomes using version 2.0 of the PhenoCam dataset. *Sci. Data*, **6**, 261, https://doi.org/10.1038/s41597-019-0270-8.

Shao, X., S.-P. Ho, X. Jing, X. Zhou, Y. Chen, T.-C. Liu, B. Zhang, and J. Dong, 2023: Characterizing the tropospheric water vapor spatial variation and trend using 2007–2018 COSMIC radio occultation and ECMWF reanalysis data. *Atmos. Chem. Phys.*, **23**, 14 187–14 218, https://doi.org/10.5194/acp-23-14187-2023.

Shi, L., and J. J. Bates, 2011: Three decades of intersatellite-calibrated high-resolution infrared radiation sounder upper tropospheric water vapor. *J. Geophys. Res.*, **116**, D04108, https://doi.org/10.1029/2010JD014847.

Simmons, A. J., 2022: Trends in the tropospheric general circulation from 1979 to 2022. *Wea. Climate Dyn.*, **3**, 777–809, https://doi.org/10.5194/wcd-3-777-2022.

Simpson, I. R., K. A. McKinnon, D. Kennedy, D. M. Lawrence, F. Lehner, and R. Seager, 2024: Observed humidity trends in dry regions contradict climate models. *Proc. Natl. Acad. Sci. USA*, **121**, e2302480120, https://doi.org/10.1073/pnas.2302480120.

Sindelarova, K., and Coauthors, 2014: Global data set of biogenic VOC emissions calculated by the MEGAN model over the last 30 years. *Atmos. Chem. Phys.*, **14**, 9317–9341, https://doi.org/10.5194/acp-14-9317-2014.

Smith, S., V. Romanovsky, K. Isaksen, K. Nyland, N. Shiklomanov, D. Streletskiy, and H. H. Christiansen, 2023: Permafrost [in "State of the Climate 2022"]. *Bull. Amer. Meteor. Soc.*, **104** (9), 302–305, https://doi.org/10.1175/BAMS-D-23-0090.1.

Smith, S. L., H. B. O'Neill, K. Isaksen, J. Noetzli, and V. E. Romanovsky, 2022: The changing thermal state of permafrost. *Nat. Rev. Earth Environ.*, **3**, 10–23, https://doi.org/10.1038/s43017-021-00240-1.

Soden, B. J., D. L. Jackson, V. Ramaswamy, M. D. Schwarzkopf, and X. Huang, 2005: The radiative signature of upper tropospheric moistening. *Science*, **310**, 841–844, https://doi.org/10.1126/science.1115602.

Solomon, S., J. S. Daniel, R. R. Neely III, J.-P. Vernier, E. G. Dutton, and L. W. Thomason, 2011: The persistently variable "background" stratospheric aerosol layer and global climate change. *Science*, **333**, 866–870, https://doi.org/10.1126/science.1206027.

Song, F., G. J. Zhang, V. Ramanathan, and L. R. Leung, 2022: Trends in surface equivalent potential temperature: A more comprehensive metric for global warming and weather extremes. *Proc. Natl. Acad. Sci. USA*, **119**, e2117832119, https://doi.org/10.1073/pnas.2117832119.

Song, X.-P., M. C. Hansen, S. V. Stehman, P. V. Potapov, A. Tyukavina, E. F. Vermote, and J. R. Townshend, 2018: Global land change from 1982 to 2016. *Nature*, **560**, 639–643, https://doi.org/10.1038/s41586-018-0411-9.

Sorg, A., A. Kääb, A. Roesch, C. Bigler, and M. Stoffel, 2015: Contrasting responses of central Asian rock glaciers to global warming. *Sci. Rep.*, **5**, 8228, https://doi.org/10.1038/srep08228.

SPARC/IO3C/GAW, 2019: SPARC/IO3C/GAW report on long-term ozone trends and uncertainties in the stratosphere. I. Petropavlovskikh et al., Eds., SPARC Rep. 9, WCRP-17/2018, GAW Rep. 241, 99 pp., https://doi.org/10.17874/f899e57a20b.

Spencer, R. W., J. R. Christy, and W. D. Braswell, 2017: UAH version 6 global satellite temperature products: Methodology and results. *Asia-Pac. J. Atmos. Sci.*, **53**, 121–130, https://doi.org/10.1007/s13143-017-0010-y.

Stackhouse, P. W., T. Wong, D. P. Kratz, P. Sawaengphokhai, A. C. Wiber, S. K. Gupta, and N. G. Loeb, 2016: Earth radiation budget at top-of-atmosphere [in "State of the Climate in 2015"]. *Bull. Amer. Meteor. Soc.*, **97** (8), S41–S43, https://doi.org/10.1175/2016BAMSStateoftheClimate.1.

Staub, B., C. Lambiel, and R. Delaloye, 2016: Rock glacier creep as a thermally-driven phenomenon: A decade of inter-annual observation from the Swiss Alps. XI Int. Conf. on Permafrost, Potsdam, Germany, Alfred Wegener Institute Helmholtz Center for Polar and Marine Research, 96–97, https://doi.org/10.2312/GFZ.LIS.2016.001.

Steinbrecht, W., and Coauthors, 2017: An update on ozone profile trends for the period 2000 to 2016. *Atmos. Chem. Phys.*, **17**, 10 675–10 690, https://doi.org/10.5194/acp-17-10675-2017.

——, and Coauthors, 2021: COVID-19 crisis reduces free tropospheric ozone across the Northern Hemisphere. *Geophys. Res. Lett.*, **48**, e2020GL091987, https://doi.org/10.1029/2020GL091987.

Steiner, A. K., and Coauthors, 2020: Observed temperature changes in the troposphere and stratosphere from 1979 to 2018. *J. Climate*, **33**, 8165–8194, https://doi.org/10.1175/JCLI-D-19-0998.1.

Stocker, M., A. K. Steiner, F. Ladstädter, U. Foelsche, and W. J. Randel, 2024: Observed impacts of the Hunga Tonga eruption on stratospheric temperature. *EGU General Assembly 2024*, Vienna, Austria, EGU, EGU24-11683, https://doi.org/10.5194/egusphere-egu24-11683.

Stoy, P. C., J. Roh, and G. T. Bromley, 2022: It's the heat and the humidity: The complementary roles of temperature and specific humidity to recent changes in the energy content of the near-surface atmosphere. *Geophys. Res. Lett.*, **49**, e2021GL096628, https://doi.org/10.1029/2021GL096628.

Stradiotti, P., and Coauthors, 2023: Soil moisture [in "State of the Climate in 2022"]. *Bull. Amer. Meteor. Soc.*, **104** (9), S65–S66, https://doi.org/10.1175/BAMS-D-23-0090.1.

Streletskiy, D., J. Noetzli, S. L. Smith, G. Vieira, P. Schoeneich, F. Hrbacek, and A. M. Irrgang, 2021: Strategy and implementation plan for the Global Terrestrial Network for Permafrost (GTN-P) 2021-2024. Zenodo, https://doi.org/10.5281/ZENODO.6075468.

Susskind, J., G. Molnar, L. Iredell, and N. G. Loeb, 2012: Interannual variability of outgoing longwave radiation as observed by AIRS and CERES. *J. Geophys. Res.*, **117**, D23107, https://doi.org/10.1029/2012JD017997.

Szopa, S., and Coauthors, 2021: Short-lived climate forcers. *Climate Change 2021: The Physical Science Basis*, V. Masson-Delmotte et al., Eds., Cambridge University Press, 817–922, https://doi.org/10.1017/9781009157896.008.

Taha, G., R. Loughman, P. R. Colarco, T. Zhu, L. W. Thomason, and G. Jaross, 2022: Tracking the 2022 Hunga Tonga-Hunga Ha'apai aerosol cloud in the upper and middle stratosphere using space-based observations. *Geophys. Res. Lett.*, **49**, e2022GL100091, https://doi.org/10.1029/2022GL100091.

Tapley, B. D., S. Bettadpur, J. C. Ries, P. F. Thompson, and M. M. Watkins, 2004: GRACE measurements of mass variability in the Earth system. *Science*, **305**, 503–505, https://doi.org/10.1126/science.1099192.

Tarasick, D. W., and Coauthors, 2019: Tropospheric Ozone Assessment Report: Tropospheric ozone from 1877 to 2016, observed levels, trends and uncertainties. *Elementa*, **7**, 39, https://doi.org/10.1525/elementa.376.

The Watchers, 2023: Extreme rainfall in Telangana results in at least 23 fatalities, India. The Watchers, 30 July, accessed 16 February 2024, https://watchers.news/2023/07/30/extreme-rainfall-in-telangana-results-in-at-least-23-fatalities-india/.

Thibert, E., and X. Bodin, 2022: Changes in surface velocities over four decades on the Laurichard rock glacier (French Alps). *Permafrost Periglacial Processes*, **33**, 323–335, https://doi.org/10.1002/ppp.2159.

Tian, H., and Coauthors, 2024: Global nitrous oxide budget (1980–2020). *Earth Syst. Sci. Data*, **16**, 2543–2604, https://doi.org/10.5194/essd-16-2543-2024.

Timmermann, A., and Coauthors, 2018: El Niño–Southern Oscillation complexity. *Nature*, **559**, 535–545, https://doi.org/10.1038/s41586-018-0252-6.

Toreti, A., and Coauthors, 2023: Drought in Central America and Mexico August 2023. JRC Tech. Rep. 135033, 17 pp., https://doi.org/10.2760/00589.

Torralba, V., F. J. Doblas-Reyes, and N. Gonzalez-Reviriegol, 2017: Uncertainty in recent near-surface wind speed trends: A global reanalysis intercomparison. *Environ. Res. Lett.*, **12**, 114019, https://doi.org/10.1088/1748-9326/aa8a58.

Ultee, L., S. Coats, and J. Mackay, 2022: Glacial runoff buffers droughts through the 21st century. *Earth Syst. Dyn.*, **13**, 935–959, https://doi.org/10.5194/esd-13-935-2022.

van der A, R. J., M. A. F. Allaart, and H. J. Eskes, 2015: Extended and refined multi sensor reanalysis of total ozone for the period 1970–2012. *Atmos. Meas. Tech.*, **8**, 3021–3035, https://doi.org/10.5194/amt-8-3021-2015.

van der Schalie, R., and Coauthors, 2017: The merging of radiative transfer based surface soil moisture data from SMOS and AMSR-E. *Remote Sens. Environ.*, **189**, 180–193, https://doi.org/10.1016/j.rse.2016.11.026.

——, and Coauthors, 2022: Soil moisture [in "State of the Climate in 2021"]. *Bull. Amer. Meteor. Soc.*, **103** (8), S64–S66, https://doi.org/10.1175/BAMS-D-22-0092.1.

van der Schrier, G., J. Barichivich, K. R. Briffa, and P. D. Jones, 2013: A scPDSI-based global dataset of dry and wet spells for 1901–2009. *J. Geophys. Res. Atmos.*, **118**, 4025–4048, https://doi.org/10.1002/jgrd.50355.

van der Werf, G. R., and Coauthors, 2017: Global fire emissions estimates during 1997–2016. *Earth Syst. Sci. Data*, **9**, 697–720, https://doi.org/10.5194/essd-9-697-2017.

Vivero, S., X. Bodin, D. Farías-Barahona, S. MacDonell, N. Schaffer, B. A. Robson, and C. Lambiel, 2021: Combination of aerial, satellite, and UAV photogrammetry for quantifying rock glacier kinematics in the Dry Andes of Chile (30°S) since the 1950s. *Front. Remote Sens.*, **2**, 784015, https://doi.org/10.3389/frsen.2021.784015.

Vömel, H., S. Evan, and M. Tully, 2022: Water vapor injection into the stratosphere by Hunga Tonga-Hunga Ha'apai. *Science*, **377**, 1444–1447, https://doi.org/10.1126/science.abq2299.

von Schuckmann, K., and Coauthors, 2023: Heat stored in the Earth system 1960–2020: Where does the energy go? *Earth Syst. Sci. Data*, **15**, 1675–1709, https://doi.org/10.5194/essd-15-1675-2023.

Vose, R. S., and Coauthors, 2021: Implementing full spatial coverage in NOAA's global temperature analysis. *Geophys. Res. Lett.*, **48**, e2020GL090873, https://doi.org/10.1029/2020GL090873.

Vreugdenhil, M., and Coauthors, 2022: Microwave remote sensing for agricultural drought monitoring: Recent developments and challenges. *Front. Water*, **4**, 1045451, https://doi.org/10.3389/frwa.2022.1045451.

Wang, M., Q. Fu, A. Hall, and A. Sweeney, 2023: Stratosphere-troposphere exchanges of air mass and ozone concentrations from ERA5 and MERRA2: Annual-mean climatology, seasonal cycle, and interannual variability. *J. Geophys. Res. Atmos.*, **128**, e2023JD039270, https://doi.org/10.1029/2023JD039270.

Wang, X., and Coauthors, 2023: Stratospheric climate anomalies and ozone loss caused by the Hunga Tonga-Hunga Ha'apai volcanic eruption. *J. Geophys. Res. Atmos.*, **128**, e2023JD039480, https://doi.org/10.1029/2023JD039480.

Wang, Z., and Coauthors, 2024: Severe global environmental issues caused by Canada's record-breaking wildfires in 2023. *Adv. Atmos. Sci.*, **41**, 565–571, https://doi.org/10.1007/s00376-023-3241-0.

Weatherhead, E. C., and Coauthors, 1998: Factors affecting the detection of trends: Statistical considerations and applications to environmental data. *J. Geophys. Res.*, **103**, 17 149–17 161, https://doi.org/10.1029/98JD00995.

Webb, E. E., A. K. Liljedahl, J. A. Cordeiro, M. M. Loranty, C. Witharana, and J. W. Lichstein, 2022: Permafrost thaw drives surface water decline across lake-rich regions of the Arctic. *Nat. Climate Change*, **12**, 841–846, https://doi.org/10.1038/s41558-022-01455-w.

Weber, M., and Coauthors, 2022: Global total ozone recovery trends attributed to ozone-depleting substance (ODS) changes derived from five merged ozone datasets. *Atmos. Chem. Phys.*, **22**, 6843–6859, https://doi.org/10.5194/acp-22-6843-2022.

Wells, N., S. Goddard, and M. J. Hayes, 2004: A self-calibrating Palmer drought severity index. *J. Climate*, **17**, 2335–2351, https://doi.org/10.1175/1520-0442(2004)017<2335:ASPDSI>2.0.CO;2.

Wentz, F. J., 1997: A well calibrated ocean algorithm for special sensor microwave/imager. *J. Geophys. Res.*, **102**, 8703–8718, https://doi.org/10.1029/96JC01751.

——, 2015: A 17-year climate record of environmental parameters derived from the Tropical Rainfall Measuring Mission (TRMM) microwave imager. *J. Climate*, **28**, 6882–6902, https://doi.org/10.1175/JCLI-D-15-0155.1.

——, L. Ricciardulli, K. Hilburn, and C. Mears, 2007: How much more rain will global warming bring? *Science*, **317**, 233–235, https://doi.org/10.1126/science.1140746.

Western, L. M., and Coauthors, 2023: Author correction: Global increase of ozone-depleting chlorofluorocarbons from 2010 to 2020. *Nat. Geosci.*, **16**, 546, https://doi.org/10.1038/s41561-023-01205-3.

WGMS, 2023: Global Glacier Change Bulletin No. 5 (2020–2021). ISC(WDS)/IUGG(IACS)/UNEP/UNESCO/WMO, World Glacier Monitoring Service, 134 pp., https://doi.org/10.5904/wgms-fog-2023-09.

Wielicki, B. A., B. R. Barkstrom, E. F. Harrison, R. B. Lee III, G. L. Smith, and J. E. Cooper, 1996: Clouds and the Earth's Radiant Energy System (CERES): An Earth observing system experiment. *Bull. Amer. Meteor. Soc.*, **77**, 853–868, https://doi.org/10.1175/1520-0477(1996)077<0853:CATERE>2.0.CO;2.

——, and Coauthors, 1998: Clouds and the Earth's Radiant Energy System (CERES): Algorithm overview. *IEEE Trans. Geosci. Remote Sens.*, **36**, 1127–1141, https://doi.org/10.1109/36.701020.

Wiese, D. N., F. W. Landerer, and M. M. Watkins, 2016: Quantifying and reducing leakage errors in the JPL RL05M GRACE mascon solution. *Water Resour. Res.*, **52**, 7490–7502, https://doi.org/10.1002/2016WR019344.

Willett, K., 2023a: HadISDH.extremes Part I: A gridded wet bulb temperature extremes index product for climate monitoring. *Adv. Atmos. Sci.*, **40**, 1952–1967, https://doi.org/10.1007/s00376-023-2347-8.

——, 2023b: HadISDH.extremes Part II: Exploring humid heat extremes using wet bulb temperature indices. *Adv. Atmos. Sci.*, **40**, 1968–1985, https://doi.org/10.1007/s00376-023-2348-7.

——, C. N. Williams Jr., R. J. H. Dunn, P. W. Thorne, S. Bell, M. de Podesta, P. D. Jones, and D. E. Parker, 2013: HadISDH: An updated land surface specific humidity product for climate monitoring. *Climate Past*, **9**, 657–677, https://doi.org/10.5194/cp-9-657-2013.

——, R. J. H. Dunn, P. W. Thorne, S. Bell, M. de Podesta, D. E. Parker, P. D. Jones, and C. N. Williams Jr., 2014: HadISDH land surface multi-variable humidity and temperature record for climate monitoring. *Climate Past*, **10**, 1983–2006, https://doi.org/10.5194/cp-10-1983-2014.

——, ——, J. Kennedy, and D. Berry, 2020: Development of the HadISDH marine humidity climate monitoring dataset. *Earth Syst. Sci. Data*, **12**, 2853–2880, https://doi.org/10.5194/essd-12-2853-2020.

——, A. J. Simmons, M. Bosilovich and D. A. Lavers, 2023: [Global climate] Surface humidity [in "State of the Climate in 2022"]. *Bull. Amer. Meteor. Soc.*, **104**, S49–S51, https://doi.org/10.1175/BAMS-D-23-0090.1.

Williams, E., and Coauthors, 2021: Evolution of global lightning in the transition from cold to warm phase preceding two super El Niño events. *J. Geophys. Res. Atmos.*, **126**, e2020JD033526, https://doi.org/10.1029/2020JD033526.

WMO, 2018: Scientific assessment of ozone depletion: 2018. Global Ozone Research and Monitoring Project Rep. 58, 588 pp., https://csl.noaa.gov/assessments/ozone/2018.

——, 2022: Scientific assessment of ozone depletion: 2022. Global Ozone Research and Monitoring Project Rep. 278, 520 pp., https://ozone.unep.org/sites/default/files/2023-02/Scientific-Assessment-of-Ozone-Depletion-2022.pdf.

——, 2023: Significant weather and climate events in 2023. Supplement to Provisional State of the Climate 2023 Rep., World Meteorological Organization, 7 pp., https://wmo.int/sites/default/files/2023-12/Supplement.pdf.

——, 2024: State of the Global Climate 2023. WMO-1347, 53 pp., https://library.wmo.int/idurl/4/68835.

Wohland, J., N.-E. Omrani, D. Witthaut, and N.-S. Keenlyside, 2019: Inconsistent wind speed trends in current twentieth century reanalyses. *J. Geophys. Res. Atmos.*, **124**, 1931–1940, https://doi.org/10.1029/2018JD030083.

Wolf, S. T., D. J. Vecellio, and W. L. Kenney, 2022: Adverse heat-health outcomes and critical environmental limits (Pennsylvania State University Human Environmental Age Thresholds project). *Amer. J. Hum. Biol.*, **35**, e23801, https://doi.org/10.1002/ajhb.23801.

Woolway, R. I., and C. J. Merchant, 2018: Intralake heterogeneity of thermal responses to climate change: A study of large Northern Hemisphere lakes. *J. Geophys. Res. Atmos.*, **123**, 3087–3098, https://doi.org/10.1002/2017JD027661.

——, and Coauthors, 2017: Lake surface temperature [in "State of the Climate in 2016"]. *Bull. Amer. Meteor. Soc.*, **98** (8), S13–S14, https://doi.org/10.1175/2017BAMSStateoftheClimate.1

——, and Coauthors, 2018: Lake surface temperature [in "State of the Climate in 2017"]. *Bull. Amer. Meteor. Soc.*, **99** (8), S13–S15, https://doi.org/10.1175/2018BAMSStateoftheClimate.1.

Xing, J., and M. Wang, 2023: Trend and drivers of satellite-detected burned area changes across Arctic region since the 21st century. *J. Geophys. Res. Atmos.*, **128**, e2023JD038946, https://doi.org/10.1029/2023JD038946.

Yan, D., 2023: This extreme rainfall in Beijing is the largest rainfall in 140 years. Beijing China News, 2 August, accessed 16 February 2024, https://web.archive.org/web/20230805112504/http://www.bj.chinanews.com.cn/news/2023/0802/91478.html.

Yang, Y., and Coauthors, 2023: Evapotranspiration on a greening Earth. *Nat. Rev. Earth Environ.*, **4**, 626–641, https://doi.org/10.1038/s43017-023-00464-3.

Yao, F., B. Livneh, B. Rajagopalan, J. Wang, J.-F. Crétaux, Y. Wada, and M. Berge-Nguyen, 2023: Satellites reveal widespread decline in global lake water storage. *Science*, **380**, 743–749, https://doi.org/10.1126/science.abo2812.

Yosef, Y., E. Aguilar, and P. Alpert, 2021: Is it possible to fit extreme climate change indices together seamlessly in the era of accelerated warming? *Int. J. Climatol.*, **41**, E952–E963, https://doi.org/10.1002/joc.6740.

Young, S. S., 2023: Global and regional snow cover decline: 2000–2022. *Climate*, **11**, 162, https://doi.org/10.3390/cli11080162.

Yu, P., and Coauthors, 2023: Radiative forcing from the 2014–2022 volcanic and wildfire injections. *Geophys. Res. Lett.*, **50**, e2023GL103791, https://doi.org/10.1029/2023GL103791.

Zeng, Z., and Coauthors, 2019: A reversal in global terrestrial stilling and its implications for wind energy production. *Nat. Climate Change*, **9**, 979–985, https://doi.org/10.1038/s41558-019-0622-6.

Zha, J., and Coauthors, 2021: Projected changes in global terrestrial near-surface wind speed in 1.5°C–4.0°C global warming levels. *Environ. Res. Lett.*, **16**, 114016, https://doi.org/10.1088/1748-9326/ac2fdd.

Zhang, G. F., and Coauthors, 2021: Uneven warming likely contributed to declining near-surface wind speeds in northern China between 1961 and 2016. *J. Geophys. Res. Atmos.*, **126**, e2020JD033637, https://doi.org/10.1029/2020JD033637.

Zhang, X., L. Alexander, G. C. Hegerl, P. Jones, A. K. Tank, T. C. Peterson, B. Trewin, and F. W. Zwiers, 2011: Indices for monitoring changes in extremes based on daily temperature and precipitation data. *Wiley Interdiscip. Rev.: Climate Change*, **2**, 851–870, https://doi.org/10.1002/wcc.147.

Zhang, Y., and W. R. Boos, 2023: An upper bound for extreme temperatures over midlatitude land. *Proc. Natl. Acad. Sci. USA*, **120**, e2215278120, https://doi.org/10.1073/pnas.2215278120.

Zhang, Y., and Coauthors, 2023: Southern Hemisphere dominates recent decline in global water availability. *Science*, **382**, 579–584, https://doi.org/10.1126/science.adh0716.

Zhang, Z., B. Poulter, A. F. Feldman, Q. Ying, P. Ciais, S. Peng, and X. Li, 2023: Recent intensification of wetland methane feedback. *Nat. Climate Change*, **13**, 430–433, https://doi.org/10.1038/s41558-023-01629-0.

Zhao, G., Y. Li, L. Zhou, and H. Gao, 2022: Evaporative water loss of 1.42 million global lakes. *Nat. Commun.*, **13**, 3686, https://doi.org/10.1038/s41467-022-31125-6.

Zhao, L., and Coauthors, 2024: Investigation, monitoring, and simulation of permafrost on the Qinghai-Tibet Plateau: A review. *Permafrost Periglacial Processes*, https://doi.org/10.1002/ppp.2227, in press.

Zhao, Y., and Coauthors, 2019: Inter-model comparison of global hydroxyl radical (OH) distributions and their impact on atmospheric methane over the 2000–2016 period. *Atmos. Chem. Phys.*, **19**, 13 701–13 723, https://doi.org/10.5194/acp-19-13701-2019.

Zheng, B., and Coauthors, 2023: Record-high CO2 emissions from boreal fires in 2021. *Science*, **379**, 912–917, https://doi.org/10.1126/science.ade0805.

Zhu, Y., M. Stock, J. Lapierre, and E. DiGangi, 2022: Upgrades of the Earth networks total lightning network in 2021. *Remote Sens.*, **14**, 2209, https://doi.org/10.3390/rs14092209.

Ziemke, J. R., and Coauthors, 2019: Trends in global tropospheric ozone inferred from a composite record of TOMS/OMI/MLS/OMPS satellite measurements and the MERRA-2 GMI simulation. *Atmos. Chem. Phys.*, **19**, 3257–3269, https://doi.org/10.5194/acp-19-3257-2019.

——, and Coauthors, 2022: NASA satellite measurements show global-scale reductions in free tropospheric ozone in 2020 and again in 2021 during COVID-19. *Geophys. Res. Lett.*, **49**, e2022GL098712, https://doi.org/10.1029/2022GL098712.

Ziese, M., A. Rauthe-Schöch, S. Hänsel, P. Finger, E. Rustemeier, and U. Schneider, 2022: GPCC full data daily version 2022 at 1.0°: Daily land-surface precipitation from rain-gauges built on GTS-based and historic data. Global Precipitation Climatology Centre, accessed 12 February 2024, https://doi.org/10.5676/DWD_GPCC/FD_D_V2022_100.

Zohary, T., and I. Ostrovsky, 2011: Ecological impacts of excessive water level fluctuations in stratified freshwater lakes. *Inland Waters*, **1**, 47–59, https://doi.org/10.5268/IW-1.1.406.

Zotta, R. M., R. van der Schalie, W. Preimesberger, L. Mösinger, R. De Jeu, and W. Dorigo, 2023: Vegetation optical depth [in "State of the Climate in 2022"]. *Bull. Amer. Meteor. Soc.*, **104**, S110–S112, https://doi.org/10.1175/BAMS-D-23-0090.1.

——, L. Moesinger, R. van der Schalie, M. Vreugdenhil, W. Preimesberger, T. Frederikse, R. De Jeu, and W. Dorigo, 2024a: VODCA v2: Multi-sensor, multi-frequency vegetation optical depth data for long-term canopy dynamics and biomass monitoring (1.0.0). TU Wien, accessed 25 January 2024, https://doi.org/10.48436/t74ty-tcx62.

——, ——, ——, ——, ——, ——, ——, and ——, 2024b: VODCA v2: Multi-sensor, multi-frequency vegetation optical depth data for long-term canopy dynamics and biomass monitoring. *Earth Syst. Sci. Data Discuss.*, https://doi.org/10.5194/essd-2024-35.

Zou, C.-Z., H. Xu, X. Hao, Q. Liu, 2023: Mid-tropospheric layer temperature record derived from satellite microwave sounder observations with backward merging approach. *J. Geophys. Res. Atmos.*, **128**, e2022JD037472, https://doi.org/10.1029/2022JD037472.